Universidade do Porto
Faculdade de Engenharia
FEUP

Laboratory for Process, Environmental and Energy Engineering

Purification of Propylene using Functionalized Inorganic Membranes and Membrane Reactors

Miguel Mourão Teixeira

Dissertation submitted to obtain the degree of
Doctor of Philosophy in Chemical and Biological Engineering
by the
UNIVERSITY OF PORTO

SUPERVISORS

Adélio Miguel Magalhães Mendes, Associate Professor
Luís Miguel Palma Madeira, Assistant Professor
José Manuel Ribeiro de Sousa, Assistant Professor

Department of Chemical Engineering, Faculty of Engineering
Porto, April 2011

Ciência Inovação 2010
Programa Operacional Ciência e Inovação 2010

ABSTRACT

Propylene is one of the most important petrochemical intermediates. Produced in oil refining and natural gas processing, it is used as feedstock for the production of polypropylene, acrylonitrile, propylene oxide and cumene, among others. The traditional purification process of propylene in the petrochemical industry includes the selective hydrogenation of propyne and propadiene impurities in catalytic reactors and the alkene separation from propane in large distillation columns. This thesis studies membrane-based processes for propylene purification.

Two classes of membranes were studied for propylene/propane separation (zeolites and carbon molecular sieve membranes). The separation of propylene from propane by distillation is an energy and capital intensive process, thus there is a demand towards the development of cheaper technologies.

Faujasite (Y) zeolite membranes were synthesized hydrothermally on top of α–Al_2O_3 supports and permeation studies were carried out before and after ion-exchange with silver (Ag^+); a transition metal known to establish selective π–complexation bonds with propylene. In single gas permeation experiments, the zeolite membranes were more permeable to the least adsorbed species (propane) because it diffuses faster in the pores. However, in mixed gas permeation experiments, the zeolite membranes were selective towards the most highly adsorbed species (propylene) since it blocked the access of propane to the pores, hence decreasing its permeance. In the silver functionalized zeolites the sorption affinity towards the hydrocarbons was higher hence the pore blocking effect was more significant. Consequently, the propylene/propane separation factors obtained for the silver ion-exchanged membranes (1.7 to 6.0) were higher than those obtained for the non-exchanged zeolite membranes (1.3 to 2.4). The best performing zeolite membrane (propylene/propane separation factor of 6.0 and permeability towards propylene of 712 barrer) surpassed the upper bound curve

for polymer membranes. Yet, the performance of the zeolite membranes decreased quickly as silver reduced and it could only be partially recovered upon regeneration in an oxidizing atmosphere.

Composite carbon molecular sieve membranes were prepared in a single stage by dip coating a composite dispersion onto an α-Al_2O_3 support and subsequent carbonization at 550 ºC. The composite dispersions were prepared by loading one (boehmite) or two (boehmite and silver) inorganic fillers to a commercial phenolic resin (cheap polymer precursor). After carbonization, the boehmite nanoparticles originated nanowires of alumina 10-30 nm long and 1-2 nm in diameter while silver formed nanoparticles of around 30 nm in diameter, both being well dispersed in the carbon matrix. The performance of the composite membranes for propylene/propane separation was analyzed by adsorption equilibrium isotherms, uptake experiments and permeation runs. The composite carbon molecular sieve membranes exhibited small adsorption selectivities towards propylene yet high kinetic selectivities. Carbon-alumina-silver membranes were more selective and less permeable than carbon-alumina membranes for propylene/propane; the separation factors and permeabilities towards propylene of the best performing membranes ranged from 5.1-13.6 and 89-196 barrer for carbon-alumina membranes and 14.1-20.5 and 46.5-168.5 barrer for carbon-alumina-silver membranes. The differences observed were attributed to small variations in the pore size distribution of the composite material. The performances of the composite carbon membranes largely surpassed the upper bound curve for polymer membranes and perform better than the zeolite membranes tested, besides originating more reproducible membranes. These membranes experienced aging in the presence of oxygen and required regeneration procedures to restore their permeation.

The final part of the thesis focused on the development of a 1-D mathematical model to evaluate a new membrane reactor configuration for the removal of propyne from propylene streams. It was proposed to load a propyne hydrogenation catalyst over a propyne permselective membrane. The mathematical model was used to ascertain the conditions in which this membrane reactor could outperform a conventional fixed bed catalytic reactor. It was concluded that the catalytic selectivity of the membrane reactor was much higher and that it could perform the desired purification (achieve propyne concentrations below 5 ppm) with membranes exhibiting a minimum selectivity towards propyne of 15.

SUMÁRIO

O propileno é um dos mais importantes intermediários na indústria petroquímica. O propileno é produzido por refinação de petróleo ou gás natural e é utilizado como matéria-prima para a produção de polipropileno, acrilonitrilo, óxido de propileno e cumeno, entre outros. O processo tradicional de purificação do propileno na indústria petroquímica inclui a hidrogenação selectiva do propino e propadieno em reactores catalíticos e a posterior remoção do propano em grandes colunas de destilação. Esta tese foca-se no uso de processos por membranas para a purificação de correntes de propeno.

Foram estudados dois tipos de membranas (zeolíticas e membranas de peneiro molecular de carbono) para a separação propeno/propano. O processo tradicional de separação destes hidrocarbonetos por destilação acarreta custos muitos elevados, havendo portanto um grande interesse em que se desenvolvam tecnologias alternativas mais baratas.

Foram sintetizadas membranas zeolíticas (zeólito Y) suportadas em membranas tubulares de α-Al_2O_3 e foram realizados estudos de permeação antes e após a funcionalização das membranas zeolíticas com iões de prata (Ag^+). A prata na forma iónica é conhecida por estabelecer ligações do tipo π-complexante com o propileno. Em experiências de permeação monocomponente, as membranas zeolíticas foram mais permeáveis à espécie química menos adsorvida (propano), uma vez que esta se difundia mais rapidamente nos poros. No entanto, em experiências de permeação bicomponente, as membranas zeolíticas foram selectivas à espécie mais adsorvida (propileno), que bloqueia parcialmente o acesso do propano aos poros, diminuindo assim a sua permeabilidade. Nas membranas funcionalizadas com prata a adsorção dos hidrocarbonetos foi superior, bem como o efeito de bloqueio. Consequentemente, as selectividades bicomponente propileno/propano obtidas com membranas funcionalizadas com prata (selectividades entre 1,7 e 6,0) foram superiores às obtidas com membranas

não funcionalizadas (selectividades entre 1,3 e 2,4). A membrana que apresentou melhor desempenho (selectividade bicomponente 6,0 e permeabilidade ao propileno de 712 barrer) ultrapassou o desempenho das melhores membranas poliméricas. No entanto, verificou-se uma diminuição rápida no desempenho das membranas zeolíticas devida à redução da prata. Através de regeneração em atmosfera oxidante conseguiu-se obter uma recuperação parcial de desempenho.

Foram preparadas membranas compósitas de peneiro molecular de carbono numa única etapa, por deposição de uma película de resina fenólica comercial contendo nanoparticulas inorgânicas e posterior carbonização a 550 ºC. Foram usados dois tipos de dispersões compósitas, uma contendo nanopartículas de boehmite e outra contendo nanopartículas de boehmite e um sal de prata. Após a carbonização, a boehmite originou nanopartículas de alumina com 10-30 nm de comprimento e 1-2 nm de diâmetro e o sal de prata originou nanopartículas com cerca de 30 nm de diâmetro; ambos os tipos de partículas apresentaram-se bem dispersos na matriz de carbono. O desempenho das membranas compósitas de carbono relativamente à separação propileno/propano foi analisado tendo em conta as isotérmicas de equilíbrio de adsorção, cinéticas de transporte de massa (ensaios de carga) e ensaios de permeação. As membranas compósitas de peneiro molecular de carbono apresentaram selectividades de adsorção ao propileno baixas, mas elevadas selectividade cinéticas. As membranas de carbono-alumina-prata foram mais selectivas e menos permeáveis do que as membranas de carbono-alumina na separação propileno/propano; a selectividade bicomponente e permeabilidade ao propileno variou entre 5,1-13,6 e 89-196 barrer para as membranas de carbono-alumina e 14,1-20,5 e 46,5-168,5 barrer para as membranas de carbono-alumina-prata, respectivamente. As diferenças observadas foram atribuídas a pequenas variações na distribuição de tamanho dos poros do material compósito. O desempenho das membranas compósitas de carbono ultrapassou claramente o limite superior da curva de desempenho das

membranas poliméricas e foi igualmente superior ao desempenho das membranas zeolíticas testadas, para além de terem sido igualmente mais reprodutíveis. Estas membranas evidenciaram algum envelhecimento na presença de oxigénio tendo, no entanto, sido possível a sua quase completa regeneração.

Na parte final da tese desenvolveu-se um modelo matemático a uma dimensão (1-D) para avaliar o desempenho de uma nova configuração de reactor de membranas para a remoção do propino de correntes industriais de propileno. Propôs-se um reactor de membranas no qual um catalisador selectivo à hidrogenação do propino era depositado sobre a superfície do permeado de uma membrana selectiva ao propino. O modelo matemático foi usado para verificar em que condições este reactor de membranas superava o desempenho de um reactor catalítico convencional (leito fixo). Concluiu-se que a selectividade catalítica do reactor de membranas era muito superior e que se podia realizar a purificação desejada (obter concentrações de propino inferiores a 5 ppm) com membranas com selectividade ao propino superiores a 15.

SOMMAIRE

Propylène est un des intermédiaires pétrochimiques les plus importants. Produit dans le raffinage du pétrole et du traitement du gaz naturel, il est utilisé comme matière première pour la production de polypropylène, l'acrylonitrile, l'oxyde de propylène et le cumène, entre autres. Le procédé de purification traditionnel de propylène dans l'industrie pétrochimique inclut l'hydrogénation sélective des impuretés de propyne et de propadiène dans des réacteurs catalytiques et de la séparation de propane dans des colonnes de distillation. Cette thèse étudie processus de membranes pour la purification de propylène.

Deux classes de membranes ont été étudiées pour la séparation du propane/propylène (zéolithes et membranes de tamis moléculaire de carbone). La séparation du propylène à partir du propane par distillation est un processus très cher, donc il a une demande pour le développement de technologies plus économiques.

Des membranes zéolithes ont été synthétisés dessus des supports de α–Al_2O_3 et études de perméation ont été effectuées avant et après l'échange d'ions d'argent (Ag^+) ; un métal de transition capable d'établir des liaisons sélectives π–complexation avec le propylène. Dans des expériences de perméation de gaz monocomposant, les membranes zéolithes sont plus perméables à l'espèce moins adsorbé (propane), parce qu'elle se diffuse rapidement dans les pores. Toutefois, dans des expériences de perméation de gaz bicomposant, les membranes zéolithes ont été sélectives pour l'espèce plus fortement adsorbé (propylène), parce qu'elle a bloquée l'accès de propane pour les pores, diminuant ainsi sa perméabilité. Pour les membranes zéolithes fonctionnalisées l'affinité de sorption vers les hydrocarbures a été supérieur d'où l'effet de blocage des pores est plus importante. Par conséquence, les facteurs de séparation propylène/propane obtenus pour les membranes fonctionnalisés (1,7 à 6,0) ont été plus élevés que

ceux obtenus pour les non-fonctionnalisés membranes zéolithe (1,3 à 2,4). La membrane zéolithe avec la meilleure performance (facteur de séparation propylène/propane de 6,0 et de perméabilité vers propylène le 712 barrer) dépasse la courbe de limite supérieure pour les membranes de polymère. Cependant, la performance des membranes de zéolithe a diminué rapidement en raison de la réduction d'argent; et elle fut partiellement récupérée lors de la régénération dans une atmosphère oxydante.

Des membranes de tamis moléculaire de carbone composites ont été préparés dans une seule étape par trempage dans une dispersion composite sur un support α-Al_2O_3 et de carbonisation subséquente à 550 ºC. Les dispersions composites ont été préparées par le chargement d'un (boehmite) ou deux (boehmite et de l'argent) inorganiques à une résine phénolique commerciale (précurseur de polymère à bas prix). Après carbonisation, les nanoparticules des boehmite originent des nanofils d'alumine avec 10-30 nm de longueur et avec 1-2 nm de diamètre, alors que l'argent forme des nanoparticules d'environ 30 nm de diamètre; les deux étant bien dispersés dans la matrice de carbone. La performance des membranes composites pour la séparation propylène/propane ont été analysées par isothermes d'équilibre d'adsorption, des expériences cinétiques et des expériences de perméation. Les membranes composites ont présentés des petits sélectivités d'adsorption vers le propylène mais des sélectivités cinétiques hautes. Des membranes de carbone-alumine-argent ont été plus sélectives et moins perméables que les membranes en carbone-alumine pour la séparation propylène/propane; les facteurs de séparation et la perméabilité au propylène des meilleures membranes ont varié entre 5,1 et 13,6 et entre 89 et 196 barrer pour les membranes carbone-alumine. Pour les membranes de carbone-alumine-argent les perméabilités au propylène ont varié entre 14,1 et 20,5 et entre 46,5 et 168,5 barrer. Les différences observées ont été attribués à des petites variations dans la distribution de la taille des pores du matériau composite. La

performance des membranes de carbone a largement dépassée la courbe de limite supérieure pour les membranes polymériques et avec un meilleur rendement que les membranes zéolithes testées, de plus elles ont étés également plus reproductibles. Ces membranes ont connu un vieillissement en présence d'oxygène et ayant malgré été possible sa régénération presque complète.

La dernière parte de la thèse a développé un modèle mathématique 1-D pour évaluer l'élaboration d'une nouvelle configuration pour un réacteur de membrane pour la suppression du propyne des cours de propylène. Le réacteur proposé consiste dans la déposition d'un catalyseur d'hydrogénation du propyne sur la superficie d'une membrane sélectif au propyne du côté du permeát. Le modèle mathématique a été utilisé pour déterminer les conditions dans lesquelles ce réacteur de membrane pourrait surpasser la performance d'un réacteur catalytique conventionnel. Il a été conclu que la sélectivité catalytique du réacteur de membrane est beaucoup plus élevé et qu'il pourrait effectuer la purification souhaité (obtenir concentrations de propyne inférieures à 5 ppm) avec des membranes présentant une sélectivité minimale vers le propyne de 15.

ACKNOWLEDGEMENTS

First I would like to acknowledge my supervisors, Prof. Adélio Mendes, Prof. Miguel Madeira and Prof. José Sousa, for allowing me to carry out my PhD work. To Prof. Adélio Mendes, my main supervisor, I am grateful for the enthusiasm, dedication, for having patience in the right moments and particularly grateful for the countless hours spent discussing the most adequate strategies for my PhD. To Prof. Miguel Madeira I am grateful for the fruitful discussions and for the serene presence. To Prof. José Sousa I am grateful for all the help in the modelling development and in assembling the experimental setup.

I also thank LEPAE, DEQ and FEUP for providing excellent infrastructures for scientific research and to FCT for my PhD grant (SFRH/BD/24768/2005).

I would also like to express my gratitude to all my lab mates at LEPAE for the scientific suggestions and for providing an excellent work environment. Particularly, I have to thank Marta Campo and Alfredo Tanaka for the enormous help they gave me when they welcomed me into their research area. As they know so well, that ended up providing a turning point in my PhD and I can not overstate the importance of that gesture.

I would also like to thank Rafael Ferro for reviewing the sommaire.

I have to give a very special thank you to the colleagues from my graduation year that also decided to make a PhD: César Águia, Diogo Mendes, Filipe Madureira, João Ferra, Paulo Gomes, José Costa and Tiago Regala. It was with them that I shared most of the good and bad moments in my PhD journey (particularly the first year) and we all helped each other overcome them. It was a tough road for us all, but we can now look back at those days with a smile and even some nostalgia.

I also would like to acknowledge all my friends outside the academic world for all the wonderful moments, which were essential to my emotional balance during these years.

Finally and most importantly I would like to thank my parents and my brother. The people closest to you are always the ones that endure the most when one decides to make a lonely journey such as a PhD work. Throughout my years as a PhD student, you provided support and encouragement and were always present with an extra dose of patience. This thesis is especially dedicated to you.

TABLE OF CONTENTS

Abstract iii
Sumário vii
Sommaire xi
Acknowledgements xv
Table of Contents xvii
List of Tables xxii
List of Figures and Illustrations xxv

PART I: INTRODUCTION

CHAPTER 1: INTRODUCTION 3
1.1 Propylene/Propane Separation 6
1.1.1 Membranes 7
1.1.2 Zeolites 17
1.1.2.1 Zeolite Structure 18
1.1.2.2 Zeolite Synthesis 19
1.1.3 Carbon Molecular Sieve Membranes (CMSMs) 20
1.1.3.1 Precursor Selection 22
1.1.3.2 Membrane Preparation 23
1.1.3.3 Pre-Treatment 24
1.1.3.4 Carbonization 24
1.1.3.5 Post-Treatment 26
1.2 Propylene/Propadiene/Propyne Separation 27
1.2.1 Catalytic Membrane Reactors (CMRs) 27
1.3 Outline 28
1.4 List of Acronyms 30
1.5 References 31

PART II: ZEOLITE MEMBRANES

CHAPTER 2: SILVER FUNCTIONALIZED FAUJASITE ZEOLITE MEMBRANES FOR PROPYLENE/PROPANE SEPARATION..... 43
2.1 Abstract 43
2.2 Introduction 44
2.3 Experimental 45

2.3.1 Adsorbent and Membrane Synthesis 45
2.3.2 Adsorption Equilibrium Experiments 46
2.3.3 Permeation Experiments 46
2.4 Results 49
2.4.1 SEM 49
2.4.2 Adsorption Equilibrium Isotherms 50
2.4.3 Permeation Experiments 51
2.4.3.1 Effect of Feed Composition 60
2.4.4 Membrane Aging 62
2.5 Conclusions 63
2.6 Nomenclature 64
2.7 Acknowledgments 66
2.8 References 66

PART III: CARBON MOLECULAR SIEVE MEMBRANES

CHAPTER 3: COMPOSITE PHENOLIC RESIN-BASED CARBON MOLECULAR SIEVE MEMBRANES FOR GAS SEPARATION... 73
3.1 Abstract 73
3.2 Introduction 73
3.3 Experimental 75
3.3.1 Materials 75
3.3.2 Preparation of the Composite Precursor 76
3.3.3 Pyrolysis 77
3.3.4 Morphological and Structural Characterization 78
3.3.4.1 Thermogravimetric analyses (TGA) 78
3.3.4.2 X-ray and microscopic analyses 78
3.3.4.3 Pore Size Characterization 79
3.3.5 Permeation Experiments 79
3.4 Results 81
3.4.1 Thermogravimetric analyses 81
3.4.2 X-ray and microscopic analyses 83
3.4.3 Porosity Assessment 85
3.4.4 Permeation Experiments 90
3.5 Conclusions 94
3.6 Acknowledgments 94
3.7 Nomenclature 95
3.8 References 97

CHAPTER 4: CARBON-AL_2O_3-AG COMPOSITE CARBON MOLECULAR SIEVE MEMBRANES FOR GAS SEPARATION. 101
4.1 Abstract 101
4.2 Introduction 101
4.3 Experimental 102
4.3.1 Materials 102
4.3.2 Membrane Preparation 103
4.3.3 Morphological and Structural Characterization 103
4.3.4 Permeation Experiments 104
4.4 Results 105
4.4.1 Microporosity analysis 105
4.4.2 Thermogravimetric analyses (TG) 106
4.4.3 X-ray and microscopic analyses 107
4.4.4 Permeation Experiments 110
4.5 Conclusions 114
4.6 Acknowledgements 114
4.7 Nomenclature 115
4.8 References 116

CHAPTER 5: COMPOSITE CARBON MOLECULAR SIEVE MEMBRANES – ADSORPTION, KINETIC AND PERMEATION STUDIES – PART I 117
5.1 Abstract 117
5.2 Introduction 118
5.3 Experimental 118
5.3.1 Membrane Synthesis 118
5.4 Morphological and structural characterization of the membranes. 119
5.4.1 Adsorption isotherms/uptake experiments 119
5.4.2 Permeation Experiments 120
5.5 Results and Discussion 121
5.5.1 Thermogravimetric analysis 121
5.5.2 SEM/EDS 122
5.5.3 Adsorption Isotherms and Uptakes 123
5.5.3.1 Adsorption of O_2, N_2 and CO_2 123
5.5.3.2 Adsorption of C_3H_8 and C_3H_6 131
5.5.4 Permeation experiments 135
5.5.4.1 Experimental and predicted permeabilities 135
5.5.4.2 Effect of composition of c-CMSM on gas permeation properties 138
5.5.5 Stability in air and Regeneration 142
5.6 Conclusions 142
5.7 Appendix – Permeability expressions 144
5.7.1 Darken-SIPS (N_2) 144

5.7.2 Chen-Yang (CO_2, O_2) 144
5.7.3 Darken-Toth (C_3H_8, C_3H_6) 145
5.8 Nomenclature 146
5.9 Acknowledgments 148
5.10 References 148

CHAPTER 6: COMPOSITE CARBON MOLECULAR SIEVE MEMBRANES – ADSORPTION, KINETIC AND PERMEATION STUDIES – PART II 151
6.1 Abstract 151
6.2 Introduction 152
6.3 Experimental 153
6.3.1 Membrane Synthesis 153
6.3.2 Morphological and Structural Characterization 154
6.3.3 Permeation Experiments 154
6.3.4 Adsorption Isotherms/Uptake Experiments 155
6.4 Results 155
6.4.1 Thermogravimetric analyses 155
6.4.2 XRD 156
6.4.3 SEM/EDS 158
6.4.4 Permeation experiments 159
6.5 Adsorption Isotherms and Uptakes 162
6.5.1 O_2, N_2 and CO_2 163
6.5.2 C_3H_6 and C_3H_8 167
6.6 Conclusions 170
6.7 Acknowledgements 171
6.8 Nomenclature 171
6.9 References 173

PART IV: CATALYTIC MEMBRANE REACTORS

CHAPTER 7: IMPROVING PROPYNE REMOVAL FROM PROPYLENE STREAMS USING A CATALYTIC MEMBRANE REACTOR – A THEORETICAL STUDY 177
7.1 Abstract 177
7.2 Introduction 178
7.3 Model 180
7.3.1 Mass Balances 182
7.3.1.1 Partial and Total Mass Balances to the Retentate Side 182
7.3.1.2 Partial and Total Mass Balances to the Permeate Side. 183
7.3.2 Mass Balances – Dimensionless Form 183

7.3.2.1 Partial and Total Mass Balances for the Retentate Side184
7.3.2.2 Partial and Total Mass Balances for the Permeate Side184
7.3.3 Solution of the model equations 185
7.3.4 Model Reaction System and Parameters 185
7.3.5 Reaction Kinetics 187
7.3.6 Propyne/Propylene Separation Factor ($L^*_{C_3H_4}$) 188
7.3.7 Reaction Rate Ratio (R_r) 189
7.3.8 Hydrogen/Propyne Molar Inlet Ratio (Ψ) 190
7.4 Results and Discussion 190
7.4.1 Model Validation 190
7.4.2 Fixed Bed Catalytic Reactor (FBCR) 191
7.5 Membrane Separation System (MS) 192
7.6 Membrane Reactor (MR) 194
7.6.1 Effect of Membrane Permeability Coefficients 194
7.6.2 Hydrogen/Propyne Ratio Effect 197
7.6.3 Damköhler-Separation factor-Stage Cut Trade-Off 199
7.7 Conclusions 201
7.8 Acknowledgements 203
7.9 Nomenclature 203
7.10 References 205

CHAPTER 8: CONCLUSIONS AND FUTURE WORK 209
8.1 General Conclusions 209
8.2 Overview and Future Work 214

APPENDIX A: GAS PERMEATION EXPERIMENTAL APPARATUS 217

LIST OF TABLES

Table 1.1 – Physical and chemical properties of propane and propylene [9-10]. 6

Table 1.2 – Main advantages and disadvantages of inorganic membranes when compared to polymer membranes [48-49]. 13

Table 2.1 – Parameters for the adsorption isotherm of N_2, C_3H_6 and C_3H_8 on Na-Y and Ag-Y at 293 K. 51

Table 2.2 – Knudsen + surface diffusion contribution to the overall flux of N_2 on faujasite zeolite membranes. 55

Table 2.3 – C_3H_6/C_3H_8 separation factor as a function of temperature, for membranes M1, M2 and M3, using an equimolar feed of C_3H_8 and C_3H_6. 60

Table 2.4 – Effect of the composition of the feed stream on the permeance of pristine and functionalized membranes M1 and M3 towards C_3H_6 and on C_3H_6/C_3H_8 separation factor (T = 298 K, P_{feed} = 120 kPa; P_p = 1 kPa; O_2 content = 1%; composition balanced with He). 61

Table 3.1 – Mass composition of the composite boehmite + resin film, before and after carbonization. 83

Table 3.2 – Structural parameters determined from the DR fit, the Stoeckli correlations and He pycnometry. 88

Table 3.3 – Physical properties of the CMS. 88

Table 3.4 – Permselectivities for gas pairs as a function of the relative feed pressure at 293 K. 91

Table 4.1 – Structural parameters determined from the DR and Stoeckli equations. 106

Table 4.2 – Permeability of the c-CMSM for gas probe species. 111

Table 4.3 – Ideal selectivities of the c-CMSMs for gas pairs of interest. 111

Table 5.1 – Composition of the precursors used to prepare the c-CMSM. 119

Table 5.2 – Burn off of several c-CMSM prepared with different phenolic resin and boehmite contents in a 20-900 ºC run under N_2 atmosphere. 122

Table 5.3 – Fitting parameters of the adsorption experimental data with the Langmuir and SIPS equations and corresponding fitting errors and MSC values..... 125

Table 5.4 – Model parameters determined from fitting the experimental adsorption isotherms. 132

Table 5.5 – Diffusivity coefficients at zero loading and activation energies determined from uptake experiments..... 134

Table 5.6 – Contribution of entropic and enthalpic selectivities to the overall C_3H_6/C_3H_8 diffusion selectivity. 134

Table 5.7 – Permeabilities and permselectivities of membrane M1 towards O_2, N_2, C_3H_6 and C_3H_8 determined by permeation and adsorption/diffusion experiments (293 K, feed pressure 400 kPa and permeate pressure 100 kPa)... 137

Table 5.8 – Permeability of membranes M1 to M6 towards probe gases at 293 K (feed pressure = 400 kPa; permeate pressure = 100 kPa). 138

Table 5.9 – Ideal selectivity of membranes M1 to M6 for gas pairs of interest at 293 K (feed pressure = 400 kPa; permeate pressure = 100 kPa). 138

Table 5.10 – C_3H_6 permeability and C_3H_6 /C_3H_8 separation factor of membranes M2, M3 and M6 using an equimolar feed of C_3H_6 and C_3H_8 (293K, mixture feed pressure = 400 kPa). 141

Table 6.1 – Mass composition of the dispersion precursors and the resulting composite membranes..... 153

Table 6.2 – Ag cluster size in membranes M1 to M6 determined from XRD refinement. 157

Table 6.3 – C_3H_6 permeability and C_3H_6/C_3H_8 separation factor of membranes M2 and M3 using an equimolar feed of C_3H_6 and C_3H_8 (293K, mixture feed pressure = 400 kPa). 161

Table 6.4 – Fitting parameters of the adsorption experimental data with the SIPS equations and the corresponding fitting errors..... 163

Table 6.5 – Model parameters obtained fitting the diffusion coefficients at different loadings for N_2, O_2 and CO_2 at 293 K..... 166

Table 6.6 – Toth equation parameters for the adsorption of propane and propylene on a carbon- Al_2O_3-Ag sample. 168

Table 6.7 – Diffusion parameters of C_3H_6 and C_3H_8 in the temperature range 293-453 K. 169

Table 7.1 – Parameter ranges used in the simulations. 186

Table 7.2 – Reported data on kinetics of alkynes and alkenes hydrogenations under different operating conditions and using different catalysts. 187

LIST OF FIGURES AND ILLUSTRATIONS

Figure 1.1 – Worldwide polymer grade/chemical grade propylene demand in 2004 [4]. 3

Figure 1.2 – Scheme depicting the separation units used in the process of propylene purification following steam cracking of naphata and LPGs. 4

Figure 1.3 – Propylene world supply market through the years [8]. 5

Figure 1.4 – Schematic of orbital interactions of metal M(silver) and an olefin in a π-complexation mechanism (adapted from [31]). 10

Figure 1.5 – Mass transport mechanisms in porous and nonporous inorganic membranes. 12

Figure 1.6 – Comparison of performance of zeolites and CMSM with the upper bound curve for polymer membranes. 15

Figure 1.7 – Scheme depicturing the basic building unit of zeolites, the tetrahedron (A) and two tetrahedra linked by T-O-T bonds (B). 18

Figure 1.8 – Channel structure of MFI with intersecting straight and sinusoidal channels. 19

Figure 1.9 – 2-D Schemes of graphitizable (left) and non-graphitizable (right) carbons, proposed by Franklin (adapted from [95-96]). 21

Figure 1.10 – Molecular sieve carbon membranes (A) and adsorption selective carbon membranes (B). 25

Figure 2.1 – Illustration of the VTI microbalance used for adsorption experiments. 46

Figure 2.2 – Scheme of the experimental set up assembled for gas permeation measurements. 47

Figure 2.3 – SEM images of the top view of the zeolite layer formed using a clear solution precursor (A) or a gel (B) precursor, cross sectional view of the zeolite layer obtained after three hydrothermal synthesis cycles when using a clear solution precursor (C); top view of the selective layer of a membrane after ion-exchange with Ag^+ (D). 49

Figure 2.4 – N_2, C_3H_8 and C_3H_6 adsorption isotherms on NaY and AgY zeolite powders at 293 K; points – experimental values; lines – SIPS model fitting.....50

Figure 2.5 – Permeance of membranes M1 to M4 towards N_2 at 293 K, as a function of the average pressure across the membrane (symbols – experimental data; lines – linear fitting with equation (2.9)). 54

Figure 2.6 – Qualitative variation of the permeance of a gas in micropores with temperature (adapted from [44]).....56

Figure 2.7 – TPP of several gases in membranes M1 (A) and M2 (B) before and after Ag functionalization (solid lines – before ion exchange; dashed lines – after ion exchange). The feed pressure was set at 120 kPa and the permeate pressure at 3 kPa. 58

Figure 2.8 – Effect of temperature on the permeance and separation factor of membrane M1 towards an equimolar C_3H_6/C_3H_8 feed, before and after functionalization. 59

Figure 2.9 – Comparison of the mixed gas permeation results of membranes M1 and M3 with the upper bound plot derived by Burns and Koros. Next to each experimental point we can find the C_3H_6/C_3H_8 molar composition of the feed stream (%) (T=298 K; P_{feed} = 130 kPa). 62

Figure 2.10 – Images depicting AgM3 before (A) and after (B) reoxidation.....63

Figure 3.1 – Particle size distribution of the 10 wt.% boehmite dispersion. 76

Figure 3.2 – Sketch of the preparation steps of the c-CMSM. 77

Figure 3.3 – Scheme of the experimental setup used for the gas permeation experiments.....80

Figure 3.4 – Characteristic curves of the phenolic resin (A) and bohemite dispersion (B).....81

Figure 3.5 – TGA plot and correspondent derivate curve for a boehmite+resin film containing 12.5 wt.% of resin and 0.5 wt.% of boehmite (wet basis).....82

Figure 3.6 – Proximate analysis of a boehmite+resin film.....83

Figure 3.7 – XRD diffraction pattern for the boehmite + resin film sample.....83

Figure 3.8 – SEM picture of a cross sectional region of a CMS..... 84

Figure 3.9 – TEM pictures of the composite unsupported membranes. (A) Low magnification view. (B) HRTEM image of one of the Al_2O_3 fibers, the inset depicts the digital diffractogram of the fiber showing the periodicities associated to the lattice fringes of Al_2O_3..... 85

Figure 3.10 – Meso/macro porosity of c-CMSM obtained by mercury porosimetry. 86

Figure 3.11 – CO_2 characteristic curve for the c-CMSM at 273 K (points – experimental data; line – DR fitting). 87

Figure 3.12 – Micropore size distribution of the c-CMS sample..... 89

Figure 3.13 – Permeability as a function of the relative feed pressure for permanent gases (A) and hydrocarbons (B) at 293 K (symbols – experimental data; lines – trend lines). 91

Figure 3.14 – Permeability as a function of the kinetic diameter of the permeant species. 92

Figure 3.15 – Comparison of the experimental results achieved with the c-CMSM (at 400 kPa feed pressure) and the state of the art plots for O_2/N_2 and C_3H_6/ C_3H_8 separations (lines – state of the art plots; symbols – experimental data)..... 93

Figure 4.1 – DR plots for C-Al and C-Al-Ag samples. 106

Figure 4.2 – TGA of carbon-Al_2O_3 and carbon-Al_2O_3-Ag c-CMSMs..... 107

Figure 4.3 – X-ray diffraction spectrum of two composite membrane samples; dark line – C-Al; grey line – C-Al-Ag. 108

Figure 4.4 – SEM pictures of the cross sectional region of the c-CMSMs; A – C-Al membrane; B – C-Al-Ag membrane. 109

Figure 4.5 – HRTEM pictures of C-Al-Ag membrane; (A) Low magnification view; (B) High magnification view..... 109

Figure 4.6 – Effect of kinetic diameter on the permeability of the c-CMSMs: dashed lines – C-Al; solid lines – C-Al-Ag. 111

Figure 4.7 – Hypothetical size distribution of the ultramicropores in the c-CMSMs (C-Al, dashed line; C-Al-Ag, solid line). 112

Figure 4.8 – Gas permeation results for 4 gas pairs of interest in C-Al and C-Al-Ag membranes and comparison with the respective upper bound plots. 113

Figure 5.1 – Scheme depicting the permeation setup. 120

Figure 5.2 – Characteristic curves for two sets of membranes. In Figure 5.2A the boehmite composition is constant and the phenolic resin content is changed from 10 to 15 wt.% (wet basis). In Figure 5.2B the resin content remains at 12.5 wt.% while boehmite content is varied from 0.5 to 1.2 wt.% (wet basis). 121

Figure 5.3 – SEM images of the cross-section of membrane M3, after pyrolysis; (A) 10 000 x magnification (B) 25 000 x magnification. In (B) it is displayed the concentration profile of alumina throughout the membrane. 123

Figure 5.4 – Adsorption isotherms of N_2, O_2 and CO_2 at 293 K and corresponding fittings. The experimental values are represented by symbols and the SIPS fit model by lines. 124

Figure 5.5 – Experimental and model fittings for the uptake curves of N_2 at P = 15 kPa(A), CO_2 at P = 15 kPa (B) and O_2 (C) at P = 35 kPa (micropore diffusion model – solid line; LDF model – dotted line). 126

Figure 5.6 – Uptake chemisorption history of O_2 for three different pressure values; symbols – experimental data; lines – Elovich kinetic law ($1.31 < \zeta < 4.49$; $2.7\text{x}10^{-6} < \xi < 1.8\text{x}10^{-5}$ s^{-1}). 127

Figure 5.7 – O_2 adsorption /desorption equilibrium isotherm at 293 K. 128

Figure 5.8 – Dependence of diffusivities of N_2, O_2 and CO_2 with pressure; symbols – experimental diffusivities with the micropore diffusion model; lines – fitting models ($D_0^{N_2} = 9.20x10^{-12}$; $D_0^{O_2} = 2.86\text{x}10^{-11}$; $\lambda = 1.63$; $D_0^{CO_2} = 8.19\text{x}10^{-12}$; $\lambda = 0.62$) 130

Figure 5.9 – Pressure dependence of the ratio of adsorption and diffusion coefficients for pairs O_2/N_2 and CO_2/N_2. Lines were added for readability. 130

Figure 5.10 – Adsorption isotherms of C_3H_6 (A) and C_3H_8 (B) in c-CMSM1 at 293, 343, 393 and 453 K. The symbols refer to experimental data, the solid lines the fitting by the Toth equation and the dotted lines the fitting by the SIPS equation. 131

Figure 5.11 – Uptake curves of C_3H_8 and C_3H_6 in the c-CMSM M1 sample at 293 K ($P \approx 120$ kPa); points – experimental data; lines – micropore diffusion model. 133

Figure 5.12 – Predicted permselectivities of c-CMSM1 as a function of feed pressure (permeate pressure = 100 kPa); (A) O_2/N_2 and CO_2/N_2 at 293 K; (B) C_3H_6/C_3H_8 permselectivities at different temperatures. 136

Figure 5.13 – Dependence of the membrane permeabilities and ideal selectivities with the precursor content of boehmite (A and B, respectively) and phenolic resin (C and D, respectively) at 293K. Lines are used for readability. 139

Figure 5.14 – Comparison of permeation results of membranes M1 to M6 with upper bound curves for O_2/N_2 and C_3H_6/C_3H_8 separations [19-20]. 140

Figure 6.1 – Characteristic curves for membranes M1, M2, M4 and M6..... 155

Figure 6.2 - Mass derivative curves for membranes M1, M3, M4 and M5. 156

Figure 6.3 – XRD diffraction spectra of membranes M1, M2, M3 and M4. 157

Figure 6.4 – SEM images of the cross-section of membranes M1, M2, M3 and M5. 158

Figure 6.5 – Effect of the content of Ag on the permeabilities towards He, N_2, O_2, CO_2, C_3H_8, C_3H_6 (A) and on the O_2/N_2, He/N_2, CO_2/N_2 and C_3H_6/C_3H_8 permselectivities (B) (feed pressure = 500 kPa; permeate pressure = 100 kPa, T=293 K). 159

Figure 6.6 – Comparison of permeation results of membranes M2 and M3 with upper bound curves for O_2/N_2 and C_3H_6/C_3H_8 separations (A) and He/N_2 and CO_2/N_2 separations (B) [12-13]. 161

Figure 6.7 – Permeation results of membranes M2 and M3 for C_3H_6/C_3H_8 separation in single gas and mixed gas experiments. 162

Figure 6.8 – Adsorption isotherms of N_2, O_2 and CO_2 at 293 K (symbols) and correspondent SIPS model fittings (dashed lines). 163

Figure 6.9 – Experimental uptake curves of N_2, O_2 and CO_2 with the respective fit by the micropore diffusion equation ($P \approx 130$ kPa). 164

Figure 6.10 – Diffusivity coefficients as a function of the N_2, O_2 and CO_2 pressure. Symbols represent the experimental diffusivities determined with the micropore diffusion model and the lines the fitting models. 165

Figure 6.11 – O_2/N_2 and CO_2/N_2 ideal permselectivities determined from equation (5.26) as a function of the feed pressure (permeate pressure = 100 kPa); black – carbon-Al_2O_3-Ag sample; grey – carbon-Al_2O_3 sample analyzed in Chapter 5..... 166

Figure 6.12 – Adsorption isotherms of C_3H_6 (A) and C_3H_8 (B) at 293, 343, 393 and 453 K (symbols – experimental data; solid lines – Toth equation). 167

Figure 6.13– Experimental fractional uptake values of C_3H_8 and C_3H_6 in the carbon-Al_2O_3-Ag at 343 K and $P \approx 120$ kPa (experimental points – symbols; model – lines). 168

Figure 7.1 – Schematic diagram of the membrane reactor (MR). 180

Figure 7.2 – Comparison between experimental [3] conversion of propyne and ethyne as a function of CO content (A) and the ratio $H_2/(C_2H_2 + C_3H_4)$ (B) (symbols) and the results of the model (lines). The parameters determined from optimization of the experimental data were $Da = 2.1\text{x}10^{-4}$; $Rr = 0.09$; $Rr_2 = 14.18$; $Rr_3 = 1.3$. 191

Figure 7.3 – Propyne retentate molar fraction (A) and propane molar fraction (B) as a function of the *Da* number, for different hydrogen/propyne molar feed ratios (Ψ), in the FBCR with a reaction rate ratio (*Rr*) value of 0.1..... 192

Figure 7.4 – Propyne retentate concentration as a function of the dimensionless contact time, for different propyne/propylene separation factor values, in a membrane based separation system (MS) for Ψ = 1. 193

Figure 7.5 – Propyne retentate molar fraction (A and B) and propyne permeate molar fraction (C and D) as a function of Γ, for different values of L^*_{C3H4}. Figures A and C are relative to the low *Da* region and Figures B and D to the high *Da* region. $R_r = 0.1$, Ψ = 1. The other parameters used have the values listed in Table 7.1. 195

Figure 7.6 - Propyne retentate profiles (A) and propyne conversion curves (B) illustrating the effect of hydrogen/propyne molar flow ratio for a MR with separation factor 100 and R_r=10. In Figure 7.6B only the high *Da* region is represented since little effect is felt at lower *Da* values. 198

Figure 7.7 - Minimum Damköhler (*Da*) numbers to achieve 5 ppm of propyne on the retentate stream as a function of Γ, for different separation factors. 200

Figure A.1 - Picture of the gas permeation apparatus assembled……..... 217

Figure A.2 - Picture of the membrane cell and permeate tank immersed in the thermostatic bath. The arrows depict the direction of flow: green – feed/retentate stream; blue – permeate stream…..... 219

Figure A.3 - Pictures of the heating system assembled (left – top view; right – bottom view). The resistances were placed inside a conical metal structure and are seen in the bottom view picture. The thermocouple (whose slot is seen in the pictures) was connected to a temperature controller …..... 219

Figure A.4 - Membrane permeation cell from various views (A) and ceramic zeolite membranes used (B) ……..... 220

PART I:

INTRODUCTION

Chapter 1: **Introduction**

Propylene is one of the most valuable petrochemical feedstocks. By 2008, the global market for propylene had reached about 70 million tonnes [1], generating over 90 billion US dollars [2]. Propylene is supplied commercially in three distinct purity grades: RG (refinery grade, 70 %), CG (chemical grade, 95 %) and PG (polymer grade, 99.5 %). The latter is particularly relevant, because it is used to manufacture polypropylene, which accounts for roughly two thirds of the world propylene consumption. Polypropylene is widely used to make packages, textiles, plastic parts and household products [3]. Other notable derivatives of propylene include acrylonitrile, propylene oxide, acrylic acid, oxo alcohols (2-ethylhexanol, n-butanol) and cumene. Figure 1.1 shows the main derivatives of propylene in terms of their worldwide demand.

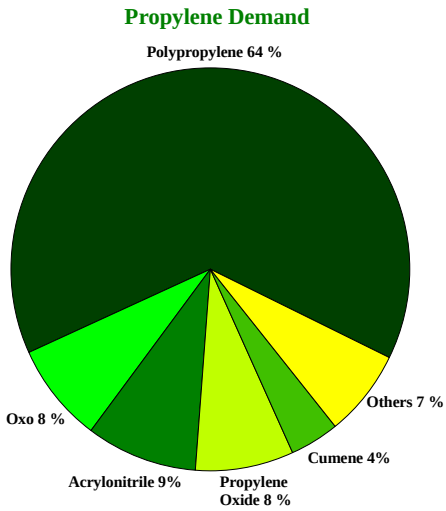

Figure 1.1 – Worldwide polymer grade/chemical grade propylene demand in 2004 [4].

Propylene is usually produced as a by-product from steam cracking of crude oil derived feedstocks such as naphtha (cycloalkanes) and LPGs (liquified petroleum gases). In a stream cracker, saturated hydrocarbons are diluted with steam and

heated in a furnace at high temperatures (ca. 700-900 ºC). Within a few miliseconds, these hydrocarbons are broken into smaller hydrocarbons. The main product arising from the steam cracking of naphta and LPGs is ethylene, but upon changing the cracking severity (the extent to which the feed mixture is broken down) and/or feedstock, it is possible to increase the propylene/ethylene ratio formed [5]. The cracked gas that exits the pyrolysis furnaces is then purified in fractionation units. A deethanizer column is typically employed to separate a C_2^- cut (hydrocarbons with 2 or less carbons) from a C_3^+ cut (hydrocarbons with 3 or more carbons). From this last cut C_4^+ hydrocarbons are removed by distillation, originating a C_3 cut consisting of propylene (about 90 %) as well as propane, propadiene and propyne. Propadiene and propyne are then typically removed in hydrogenation reactors and propane separated from propylene by distillation. The purified propylene is then used as feedstock in polypropylene plants. The process of propylene purification is schematized in Figure 1.2.

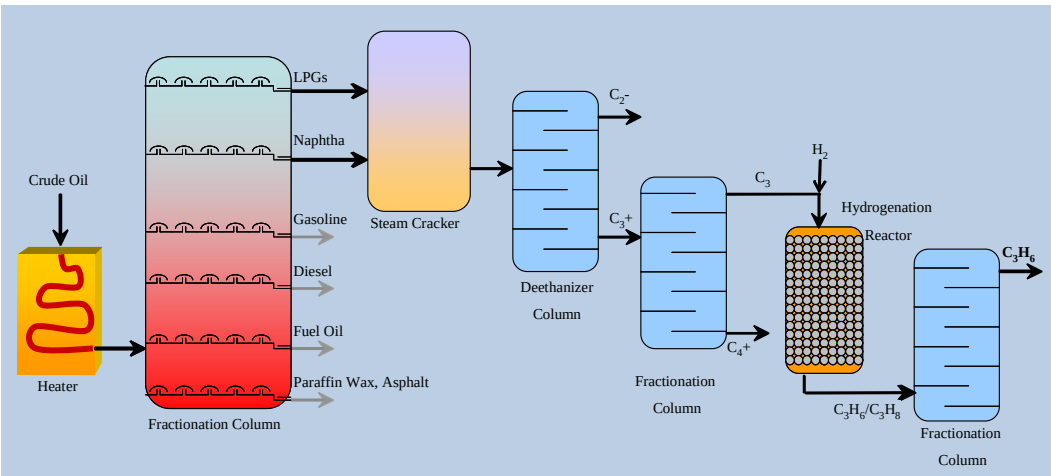

Figure 1.2 – Scheme depicting the separation units used in the process of propylene purification following steam cracking of naphata and LPGs.

The steam cracker's selectivity towards propylene is low and the supply of this olefin is supplemented by other technologies. The other widely used industrial approach is to recover propylene in RG purity from the off gases produced in

fluidized catalytic cracking (FCC) units in refineries. If higher purity grades are desired, purification in fractionation units must also be conducted. Clearly, propylene's supply market (illustrated in Figure 1.3) derives essentially from crude oil processing. Yet, as the prices of crude oil continue to rise the search for alternative approaches is intensifying. Natural gas processes (steam cracking of alkanes, propane dehydrogenation (PDH) and methanol-to-olefins processes) appear as alternatives. Recently, many ethane steam crackers (which do not produce propylene) are being built in the Middle East, where ethane is available at competitive prices [6]. This is helping to meet ethylene demands, but as the ratio of ethane to naphtha crackers increases, it creates a deficit in propylene, whose annual market growth (5 %) has been outpacing ethylene's for years. In order to cover that deficit, "on-purpose" technologies like PDH and metathesis (the catalytic conversion of ethylene and butene-2 into propylene) [7] will become progressively more significant.

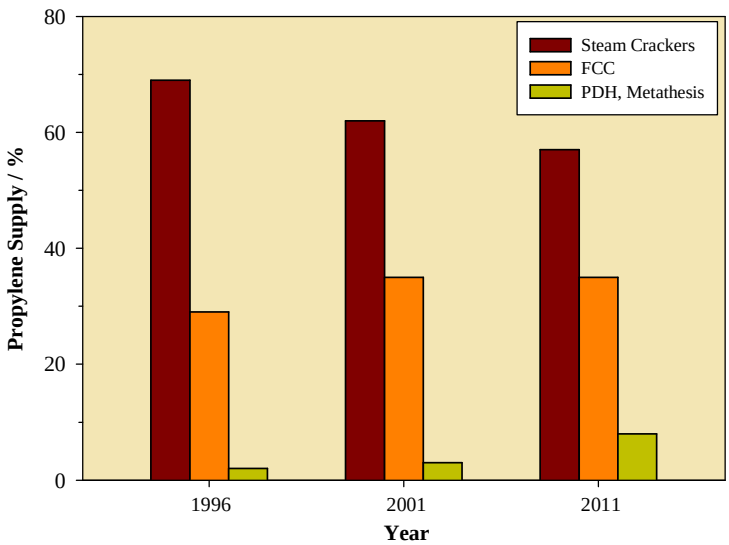

Figure 1.3 – Propylene world supply market through the years [8].

1.1 Propylene/Propane Separation

The purification of propylene is a very important process in the petrochemical industry because of its market size and expectations for future growth. In this purification process, the separation of propylene from propane is particularly difficult due to their similar physical and chemical properties (cf. Table 1.1).

Table 1.1 – Physical and chemical properties of propane and propylene [9-10].

Property	Propane	Propylene
Molecular mass ($g \cdot mol^{-1}$)	44.10	42.08
Boiling Point (ºC)	-42.1	-47.8
Fusion Point (ºC)	-187.7	-185.3
Gas Density ($kg \cdot m^{-3}$)[a]	1.91	1.81
Vapor Pressure (MPa)[b]	0.86	1.03
Gas Viscosity ($\mu Pa \cdot s$)[a]	8.1	8.5
Lennard-Jones Diameter (nm)	0.51	0.47

[a] at 293 K and 101 kPa
[b] at 293 K

This separation, carried out in both traditional (steam cracking) and on-purpose (PDH) plants, has been performed in the last 60 years by low temperature cryogenic distillation [11]. The volatilities of propane and propylene are very similar and columns containing over 200 trays (up to 100 m tall) and operating with reflux ratios greater than 10 are used [12-13]. Consequently, the energy expenses (estimated by the US Department of Energy to be 1.2×10^{14} kJ [14] per year) and capital costs related to this separation are enormous [15]. Despite the high costs, distillation remains so far unchallenged because of its reliability. However, the potential economic impact of a breakthrough in this separation has motivated researchers to find cheaper alternative technologies. Technologies currently being targeted to replace distillation include adsorption processes [11-16], membrane processes [14] and hydrid membrane-distillation processes

[17]. This thesis focuses on the use of membranes to tackle the issue of propylene purification. In order for membrane-based technologies to replace distillation, very highly selective membranes towards propylene have to be achieved. While this might not happen in a near future, some niche applications of enormous impact are closer to industrial implementation. One of these applications is the treatment of propane vent gas streams in polypropylene plants. In a typical polypropylene plant, a high-pressure reactor is used to polymerize propylene and the reaction product is transferred to a tank where residual monomer and other gases are released. Propane build up in the polymerization reactor is controlled by removing a fraction of the propylene recycle stream as a purge, which is subsequently flared. For every mol of propane purged, 2-3 mol of propylene are lost, translating into a loss of about 1-3 million dollars per year and per plant [18-19]. The use of membranes to recover and recycle propylene back to the reactor appears as an attractive potential first application because a membrane with low selectivity (3 to 5) is adequate to perform the required purification [18].

1.1.1 Membranes

According to the International Union of Pure and Applied Chemistry (IUPAC), a membrane is a structure that has lateral dimensions much greater than its thickness, through which mass transfer may occur under a variety of driving forces. When submitted to the action of a driving force it serves as a selective barrier between two phases, remaining impermeable or less permeable to specific particles, molecules, or substances, than to others. Membranes can be classified by their nature into biological (living or non living) and synthetic. Synthetic membranes can be subdivided into organic (polymer or liquid) and inorganic (ceramic, metallic, glass, zeolite and carbon). Membranes can present a homogeneous or heterogeneous structure and can be classified according to their pore dimensions as macroporous (pore diameter > 50 nm), mesoporous

(2 nm < pore diameter < 50 nm), microporous (0.3 nm < pore diameter < 2 nm) and dense membranes (pore diameter < 0.3 nm). The lower boundary for microporous membranes is not normally defined in literature but since the smallest species have a kinetic diameter of ca. 0.3 nm, this value is suggested for the pertinent boundary. The morphology, structure and chemistry of the membrane is what ultimately determines its separation mechanism and applications [20].

The use of synthetic membranes can be traced back to the nineteenth and early twentieth centuries where they were used as laboratory tools. Membranes found their first significant application in post-world war II Germany as filters for drinking water [21-22]. Nonetheless, the transition from laboratory to semi commercial production was long and strenuous. Membranes were unreliable, not very selective, and the manufacturing process was too expensive.

However, in the early 1960's, Loeb and Sourirajan [23] provided the breakthrough that bridged membrane based separations from laboratory to the industry. They proposed that an ultrathin selective layer could be deposited on a thick and permeable microporous support, which would provide mechanical strength to the membrane, without having a negative impact on the flux. Thereby, defect-free and high-flux membranes became possible. These membranes were 10 times more permeable than any other membranes then available and immediately made reverse osmosis a practical process for desalting water. The commercialization of reverse osmosis membranes benefited ultrafiltration, microfiltration and electrodialysis, which by 1980 had themselves become industrially established for a series of applications. Around the same time, Permea (now a part of Air Products) launched the first industrial gas separation membrane process using polysulfone hollow fiber membranes to separate hydrogen from purge gas streams of ammonia plants [24]. Their membranes were highly successful and motivated other companies to follow on their footsteps. By the mid-1980's, Dow, Cynara and Separex were using used cellulose acetate

membranes to remove carbon dioxide from natural gas and Generon had implemented a membrane for nitrogen/oxygen separation [25]. The membrane use for gas separations has been growing ever since and by 2002 membrane based gas separations had become a $150 million/year business [18].

At the moment, most gas separation applications use polymer membranes because of their reasonable performances, good reproducibility, low thickness and processability into efficient modular arrangements. In polymer membranes, the mass transport mechanism generally accepted is the so-called solution-diffusion model, where solutes permeate the membrane by sorbing in the membrane and diffusing across it due to a concentration gradient. In such materials, separation occurs because of differences in sorption equilibrium and mobilities of the different solutes in the membrane [21]. While polymer membranes have become a cost-competitive alternative to traditional separation methods in some markets (e.g., oxygen/nitrogen separation) they still only represent a fraction of the potential applications in refineries and chemical industries [26]. Under the harsh environments of industrial streams polymer membranes suffer from chemical and thermal instability. Moreover, when exposed to organic vapors they suffer plasticization (swelling) and lose selectivity. Hence, pre-treatment of these streams is required if polymer membranes are to be used. For propylene/propane separation, polymer membranes are frequently reported to exhibit good single gas selectivities but lower mixed gas selectivities because of propylene plasticization [27]. Also, the polymer membranes that exhibit some selectivity display small permeabilities [27-28] and the highly permeable polymer membranes exhibit small selectivities [27]. This trade-off between permeability and selectivity, represented by an upper bound curve first proposed by Robeson [29], is acknowledged as the graphical representation of the state of the art for this separation [17].

One of these strategies to overcome this trade-off curve is the use of facilitated transport membranes (FTMs), where the transport of propylene is augmented or

facilitated by an agent/carrier (typically a metal cation) that binds selectively to it. Among the carriers used to bind to propylene, silver (Ag^+) has been the most widely investigated because it forms reversible π–complexation bonds with propylene. According to Dewar [30] these complexes are formed from two-way donor-acceptor interactions; charge donation from the filled π-orbital of the ligand into the vacant orbital of the metal and back donation from the *d* orbital of the metal to the vacant π* orbital of the ligand, as illustrated in Figure 1.4. Consequently, those bonds are stronger than the Van der Waals bonds characteristic of the physisorption mechanism that occurs for paraffins. Yet, they are weak enough to be easily broken through mild changes in temperature or pressure.

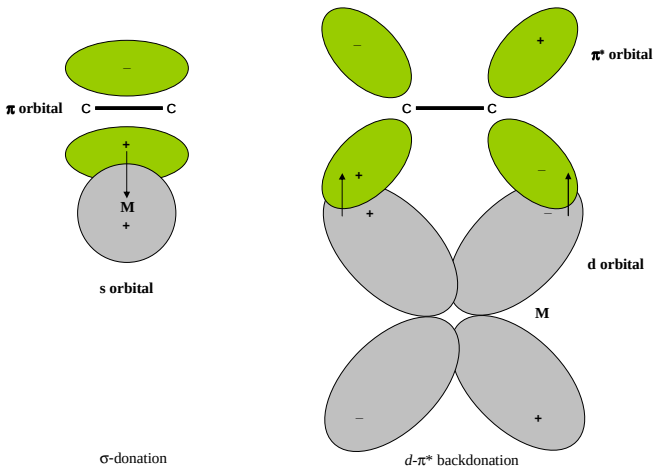

Figure 1.4 – Schematic of orbital interactions of metal M(silver) and an olefin in a π-complexation mechanism (adapted from [31]).

FTMs for olefin purification initially focused on liquid membranes that contained a dissolved carrier agent held by capillary action in the pores of a microporous polymer film [32-33]. The carrier reacted with the target molecule on the feed side, diffused across the membrane and released it on the permeate side. However, evaporation of the aqueous carrier solution (with consequent decrease

in performance) and limited solubility of the carrier in the membrane were observed. This fact combined with the increasing performance of polymer gas separation membranes in the 1980s decreased the interest in FTMs [21]. Its resurgence began upon the discovery of the potential of dispersing the carrier agent in solid polymer films [34-35]. In solid polymer membranes, the carrier is anchored (has limited mobility around its equilibrium position) and the permeant species binds at one site and hops to the next in the direction of the concentration gradient via the “hopping” mechanism. Solid polymer membranes exhibited high separation factors [36-37] but the reduction of the metal carrier hindered their long-term performances [38]. To prevent carrier reduction, ion-exchange membranes, such as Nafion, started to be intensively studied [39-41]. The sulfonate groups of Nafion bind to silver ions, thereby preventing their reduction [42]. Notwithstanding, humidification has to be supplied to the membranes for maintaining their selectivity. More recently, room temperature ionic liquids have been proposed. Because room temperature ionic liquids do not show any measurable vapour pressure they might overcome the stability problems of supported liquid membranes. Additionally, the improved wetting properties of ionic liquids enhance the mechanical stability of supported liquid membranes. While promising results have been attained [42-46] room temperature ionic liquids are very expensive for the time being.

The performance of FTMs is significantly higher than the performance of “plain” polymer membranes but the issue of stability has not been solved. The stability problems associated with polymer membranes (“plain” and functionalized) have motivated research in inorganic membranes.

Inorganic membranes can be classified in terms of their structure as porous or nonporous. In nonporous inorganic membranes (metallic, metal alloys) gas species diffuse throughout their crystal lattices but in porous membranes (zeolites, carbon, glass and oxides) diffusion occurs within their pores. The mechanisms responsible for mass transports in porous and nonporous inorganic

membranes are illustrated in Figure 1.5. In nonporous membranes, mass transport occurs by the sorption-diffusion mechanism (as in polymer materials) but in porous inorganic membranes the mass transport mechanism depends on the size of the pores. In pores larger than 100 nm transport occurs essentially by viscous (Poiseuille) flow. This flow is driven by total pressure gradient and no separation occurs as all species travel at the same speed [47]. When the pores are smaller than 100 nm (the pore diameter is the same size or smaller than the mean free path of the gas) mass transport becomes governed by Knudsen diffusion [21]. Species start to collide with each other more often than with the pore walls and the transport rate of a gas is inversely proportional to the square root of its molecular weight. Hence, high selectivities can only be achieved for species with very different molecular weights.

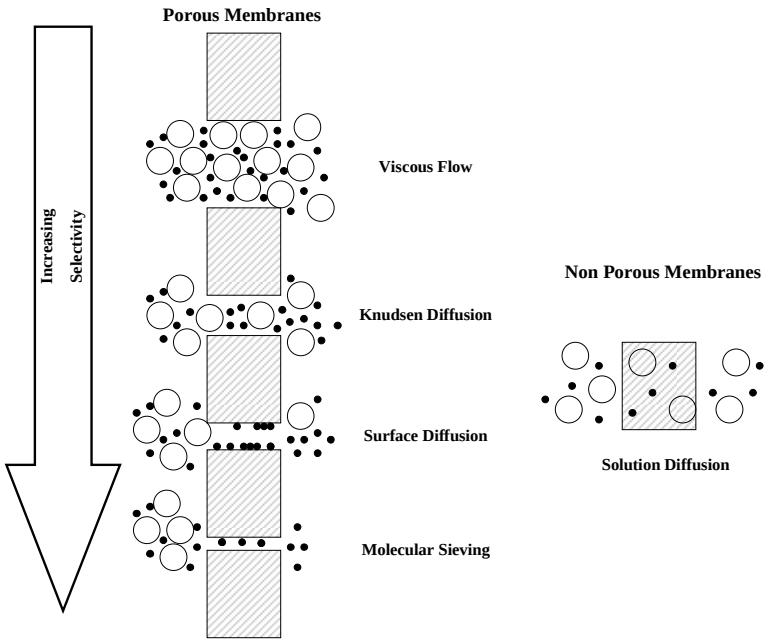

Figure 1.5 – Mass transport mechanisms in porous and nonporous inorganic membranes.

In smaller pores (0.5–2 nm) molecules are also separated by surface diffusion. Different species exhibit different adsorption rates on the surface of the pore, which affects the diffusion rates along that same surface. Finally, when the size

of the penetrant molecule is very similar to the size of the pore (~ 0.3–0.5 nm), molecules can also be separated by molecular sieving. For small enough pores, some molecules can be excluded and very high selectivities can be achieved. When compared to polymer membranes, inorganic membranes present some advantages and disadvantages (cf. Table 1.2).

Table 1.2 – Main advantages and disadvantages of inorganic membranes when compared to polymer membranes [48-49].

Advantages of Inorganic Membranes	Disadvantages of Inorganic Membranes
Thermal stability	High capital costs
Resistance to harsh environments	Brittleness
Can withstand higher pressure differences	Low membrane surface per module volume
Easy cleanability after fouling	Complex preparation methods
Do not possess swelling problems	Difficult membrane-to-module sealing at high temperatures
Inertness to microbiological degradation	Difficult to scale up
Superior permeability-selectivity relation	Poor reproducibility

Inorganic membranes exhibit higher thermal and chemical stability at high-temperatures (i.e., are able to withstand the harsh environments of petrochemical streams) as well as solvent stability and bioresistance [48]. However, their modest reproducibility, brittleness, difficult membrane-to-module sealing at high temperatures and high capital costs are arguments against their use. While those higher costs make them economically unfeasible for many separations, they yield promise for propylene/propane because of the challenging nature of that separation.

Research on inorganic membranes for propylene/propane separation has intensified in the last 20 years. Nair *et al.* prepared alumina-silica microporous membranes and tested them for propylene/propane separation. However, the selectivities were very low (below 1.8) [50-51]. Tiscornia *et al.* reported the

synthesis of high quality titanosilicate membranes [52-53] and separation factors between 3 and 7 were observed. Nikolakis *et al.* [54] reported the synthesis of faujasite zeolites on alumina supports; the propylene/propane separation factor was 6.2 and the permeance towards propylene was 2.8×10^{-8} $mol \cdot m^{-2} \cdot s^{-1} \cdot Pa^{-1}$. Giannokopoulos *et al.* [55-56] also studied faujasite type zeolites and reported even better performances; the maximum separation factor for propylene/propane was 13.7 and the permeance towards propylene was 7×10^{-9} $mol \cdot m^{-2} \cdot s^{-1} \cdot Pa^{-1}$.

Since some of these results are promising, it is surprising to see that very few studies have been reported on inorganic facilitated transport membranes. To the best of the author's knowledge, Stoitsas *et al.*'s work on Ag^{+}-SiO_2 membranes [57] is the one featuring an inorganic FTM for propylene/propane separation; a separation factor of 7.7 was reported but permeances were very low ($4\text{-}5 \times 10^{-11}$ $mol \cdot m^{-2} \cdot s^{-1} \cdot Pa^{-1}$). Nonetheless, some researchers have shown that the adsorption selectivity of zeolite adsorbents increase after functionalization [58-63].

Carbon molecular sieve membranes (CMSMs), which result from the carbonization of a polymer precursor under controlled conditions, have also been shown to display excellent olefin/paraffin selectivities [64-70]. Hayashi *et al.* [64] reported a propylene/propane separation factor of 54 at 35 ºC on a carbonized composite BPDA-pp'ODA polyimide membrane. Okamoto *et al.* [65] achieved separation factors of 12-14 for a polyimide hollow fiber membrane carbonized at 560-625 ºC while Suda and Haraya achieved propylene/propane permselectivities above 100 at 35 ºC on carbonized Kapton polyimide films [69]. Steel and Koros [68] reported permselectivities above 100 for a 6FDA/BPDA-DAM polyimide carbonized at 550 ºC and Islam *et al.* [67] maximum permselectivities of 34 on NTDA membranes carbonized at 450 ºC. Fuertes and Menendez [70] obtained permselectivities of 54 in a phenolic resin-based CMSM, but only after post-treatment of the membrane by chemical vapour deposition and oxidation. More recently, Chng *et al.* [66] used low-temperature carbonization (450 ºC) on a

PAEK/Azide precursor and propylene/propane permselectivities of 48 and separation factors of 32 were achieved.

Zeolites and CMSMs exhibit higher permeabilities and/or selectivities towards propylene/propane than polymer membranes, overcoming by far the upper bound curve of polymer membranes (see Figure 1.6). This is essentially due to their narrow pore size distribution, which makes them able to discriminate molecules based on small differences in size and shape.

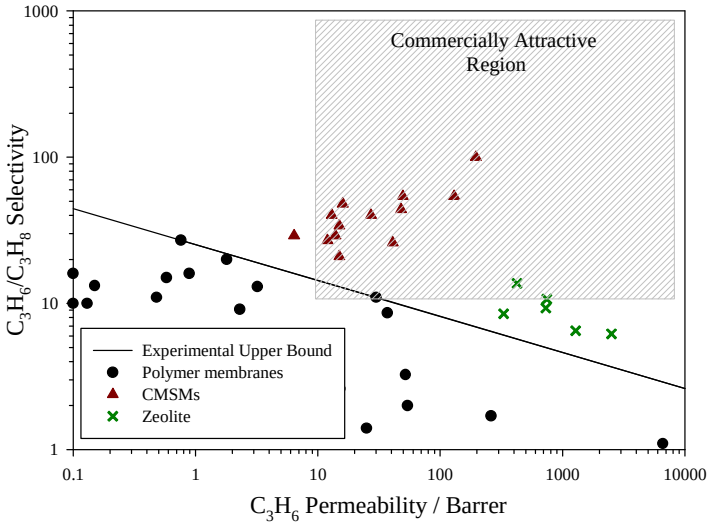

Figure 1.6 – Comparison of performance of zeolites and CMSM with the upper bound curve for polymer membranes.

It was under these circumstances that the concept of mixed matrix membranes (MMMs) appeared. In MMMs the processability of the polymer is combined with the superior gas separation performance of an inorganic filler, which is loaded into the polymer matrix [71]. The physical, thermal and mechanical properties of the membranes are all enhanced through filler incorporation, making them more suitable for operation with aggressive feeds [72]. Moreover, the infrastructure costs of MMMs are similar to those of conventional fabrication methods for polymer materials [26]. The concept of MMMs was first introduced for hybrid organic/inorganic membranes, but has been recently extended to composite

carbon/inorganic membranes. Adding inorganic nanofillers to the carbon matrix enhances the mechanical strength and reduces the brittleness of the carbon membrane while improving even further its permeability/selectivity. Successful studies on composite carbon membranes (c-CMSM) have been performed introducing metals [73-76], alkali metal ions [77], silica particles [78-79] and zeolites [80-82] in polymer precursors.

Barsema *et al.* [73] prepared P84-derived c-CMSM with Ag nanoparticles (50 nm) dispersed in the carbon matrix; the Ag/P84 membrane exhibited a 60 % increase in O_2/N_2 selectivity. The same researchers also prepared c-CMSMs from Ag/P84/SPEEK precursors [74] and an even higher O_2/N_2 selectivity (13.5) was attained. The increase in selectivity and permeability was attributed to the formation of selective bypasses around the silver nanoparticles.

Xiao *et al.* [75] reported permeability enhancements by 100 fold after loading silver to a SPAEK precursor, as well as increases in H_2/N_2 and CO_2/CH_4 selectivities. Yoda *et al*. [76] observed that the selectivity towards H_2 increased markedly upon loading Pt and Pd in polyimide precursors. Kim *et al.* [77] prepared CMSMs from Li^+, Na^+ and K^+ substituted sulfonated polyimide, and observed that the permeabilities increased with the ionic radius of the metal. Park *et al*. [78-79] realized that silica c-CMSMs revealed good performances due to the fast diffusion in silica microporous domains. Yin *et al.* [80] and Liu *et al.* [81] reported an enhancement in gas permeation in zeolite/carbon composite membranes, which they attributed to the observed increase in pore volume. On the other hand, Zeng *et al.* [82] reported an enhancement in O_2/N_2 selectivity but a decrease in permeability upon loading of zeolite NaA in a phenolic resin precursor. Since c-CMSMs have shown better results for several gas separations, it is reasonable to assume that highly performing propylene/propane membranes can also be prepared.

This thesis focuses on the use of two classes of inorganic materials for propylene/propane separation:

- zeolite membranes, more specifically silver-functionalized zeolite membranes;
- carbon molecular sieve membranes, more specifically composite carbon molecular sieve membranes.

1.1.2 Zeolites

A zeolite is classically defined as a crystalline, porous aluminosilicate built by a 3D framework of SiO_4 and AlO_4 tetrahedra (Figure 1.7A), with oxygen atoms connecting neighbouring tetrahedral – Figure 1.7B [20]. However, this definition has been broadened to include recent discoveries of oxide structures with elements other than silicon and aluminium (e.g. P) that also have well-defined pore structures due to a high degree of crystallinity. In aluminosilicates, silicon's oxidation state is +4, thus SiO_2 tetrahedra are neutral, but aluminium's oxidation state is +3, so the framework of aluminosilicates is negatively charged. Hence, alumina tetrahedra can not be placed adjacently due to strong repulsive forces and then Si/Al molar ratio in zeolites ranges from 1 to ∞ (total silicious structure). Moreover, extraframework cations are required to maintain the neutrality of the framework [83]. These cations are rather loosely held and can readily be exchanged for others in the presence of a contact solution, which sets up many of the current applications of zeolites. Cations such as sodium can be exchanged for magnesium and calcium and thus act as excellent water softeners; protons give the zeolite a strong acid nature, enabling their use for many catalytic applications. Due to the crystalline nature of their framework, zeolites possess a narrow microporous structure, which is capable of discriminating molecules due to differences in size or shape, hence they are used in gas and liquid separations.

1.1.2.1 Zeolite Structure

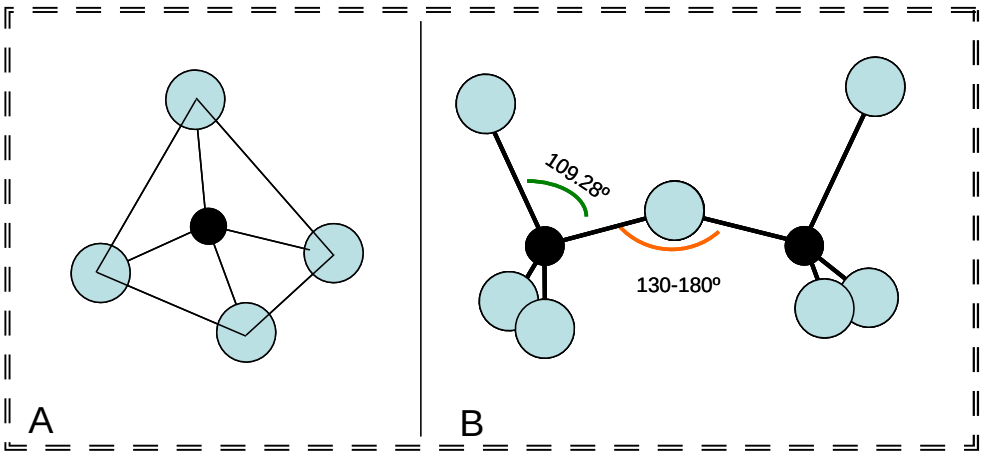

Figure 1.7 – Scheme depicturing the basic building unit of zeolites, the tetrahedron (A) and two tetrahedra linked by T-O-T bonds (B).

The tetrahedron is the basic building unit (BBU) of zeolites and their frameworks are built by tetrahedral linkage in T-O-T bonds (T refers to the metal species and O to oxygen) – Figure 1.7B. While the T-O angles in both tetrahedra remain fairly rigid, the T-O-T bonds oscilate between 130-180 ºC [84], thus allowing the formation of a great variety of more complex building units (CBUs) of the zeolite structure. The simplest of these complex structures are n-rings, where n is the number of tetrahedra. More CBUs result from the stacking of several layers of n-rings in different stacking sequences up to 12 layers. In the final zeolite structure, several pores will extend infinitely in one dimension with a minimum n-ring aperture size. Such a pore is called a channel and the 3D zeolite porous structure is a series of channels, which might intersect to form two and three dimensional channel systems [85]. The porous structure of MFI (shown in Figure 1.8) is an example of a zeolite featuring two intersecting 10-ring channel structures, one composed of straight channels and another of sinusoidal channels. Structures with 8-ring, 10-ring, or 12-ring channel apertures are the most common and are usually known as small-, medium-, and large-pore zeolites.

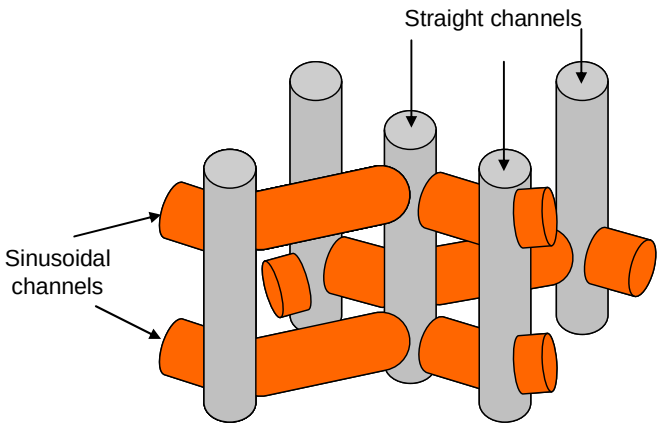

Figure 1.8 – Channel structure of MFI with intersecting straight and sinusoidal channels.

The free diameter (size of the molecules that can penetrate a particular channel) is 0.40 nm for 8-ring channels, 0.56 nm for 10-ring channels and 0.76 nm for 12-ring channels. However, the free diameter is only an approximate measure of the pore aperture. The exact dimensions of the pore depend on the particular structure and composition of the zeolite in question, the extraframework cations (which can coordinate at the channel windows and reduce the effective size of the opening [86]), the guest molecules (that are known to deform the zeolite structure), and temperature (which affects the effective aperture of the channel [87]).

1.1.2.2 Zeolite Synthesis

Zeolites are known to occur in nature since the discovery of stilbite, in 1756, by Swedish mineralogist Cronstedt [88]. However, naturally occurring zeolites are impure and have low surface areas, thus they are excluded from many important commercial applications where uniformity and purity are essential. Consequently, the focus has been mostly on synthetic zeolites. The first non-mineral zeolite was only synthetized in 1948 by Richard Barrer [36-38] but interest in zeolites rapidly escalated and by 1953, 20 zeolites had been synthesized [89]. As of today, 194

different zeolite structures (also referred as frameworks) are acknowledged by the zeolite scientific community [90]. Zeolites are synthesized by hydrothermal processes with a silica source, an alumina source, a mineralizing agent and for high Si/Al ratios, a structure directing agent [91]. The two most frequent synthesis techniques employed are *in-situ* crystallization and secondary growth method [92]. In *in-situ* crystallization the support is contacted with a gel or solution containing the zeolite precursors. Nucleation of the crystals occurs in the support, followed by crystallization until a continuous zeolite layer is formed on top of the of the support surface. The seeded or secondary growth technique decouples the nucleation and crystallization steps. Initially, a small layer of seed crystals are placed on top of the substrate and subsequently the seeds are exposed to hydrothermal growth conditions where the seed crystals grow into a continuous film. This technique gives greater flexibility, as the possibility of manipulating the morphology and orientation of the seed crystals allows manipulation of the morphology of the membrane. After hydrothermal synthesis, good intergrown crystals should be obtained, thus minimizing the undesired intercrystalline pores, which constitute low selectivity routes for gas transport. The sealing of those intercrystalline voids remains one of the biggest challenges in zeolite synthesis [93]. Additionally, in zeolite synthesis, small deviations in synthesis conditions (composition, temperature, etc.) can lead to completely different topologies, hence zeolite reproducibility is hard to achieve. The complexity of zeolite membrane synthesis makes the scale-up for industrial membrane production challenging [94].

1.1.3 Carbon Molecular Sieve Membranes (CMSMs)

Carbon has 4 outer electrons capable of multi-bonding (sp-linear, sp^2-in ring, sp^3-in diamond) so it is very versatile in the way it can organize itself. The most thermodynamically stable phase of carbon at standard conditions is graphite, an

anisotropic solid composed of hexagonal arrangement layers of carbon atoms (graphene layers) stacked in ABABAB sequence. Carbons are characterized in terms of their structural order as graphitizable or non-graphitizable. Figure 1.9 shows drawings made by Franklin in 1950 and 1951 [95-96] depicting the main differences between these structures.

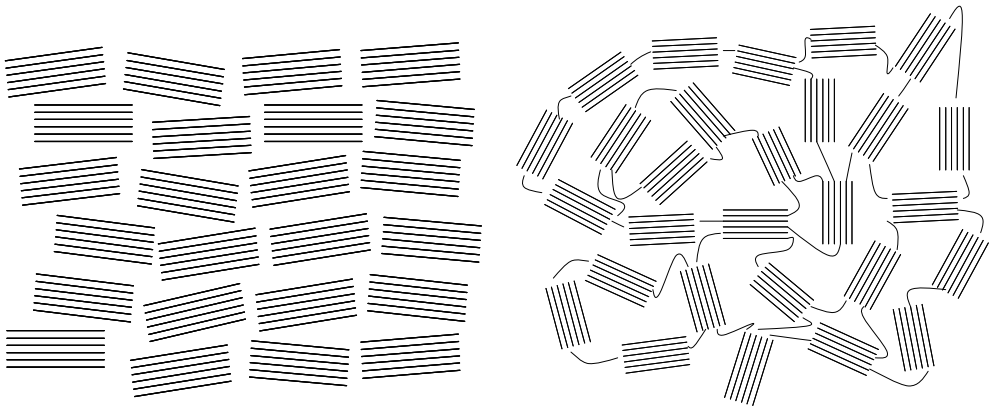

Figure 1.9 – 2-D Schemes of graphitizable (left) and non-graphitizable (right) carbons, proposed by Franklin (adapted from [95-96]).

Graphitizable carbons are structures that upon heating can become graphitic, featuring well-stacked graphene layers which exhibit long-range parallelism. Non-graphitizible carbons do not obey this ABABAB stacking, and the imperfect packing creates voids or pores in the carbon structure [97]; CMSMs are an example of non-graphitizable (porous) carbons. CMSMs are produced by the carbonization of a precursor under controlled conditions. CMSMs present a tunable pore size distribution; the pore network can be desirably tailored to suit a certain application by adequately choosing the polymer precursor and optimizing carbonization conditions such as heating rate, end temperatures, soaking times, gas atmosphere or even combining several pre- or post-carbonization treatments. The success in preparing good quality carbon membranes depends on being able to prepare a good quality polymer precursor. The synthesis of CMSMs can be divided into five steps: precursor selection, polymer membrane preparation,

precursor pre-treatment, carbonization and post-treatment of carbonized membranes [98].

1.1.3.1 Precursor Selection

The choice of a suitable precursor is essential to guarantee a crack-free carbon membrane. Polymer precursors have been shown to be preferable, because of their thermoresistance and good arrangement at molecular level [98]. Up to now, many polymer precursors have been extensively studied, namely polyimide [99-101], phenolic resin [70, 102], polyfurfuryl alcohol (PFA) [103-104] and polyacrylonitrile (PAN) [105-106]. Research has focused on thermosetting polymer precursors, which do not liquefy or soften up to the carbonization temperatures [107].

Polyimides are probably the most widely used precursor, either used as it is or blended with polyethylene glycol (PEG). They are thermally stable (up to 300 ºC), have high transition temperature, high-melting point and are easy to process. They are formed through condensation reactions with dyanhydrides and diamines and different types of dyanhydrides and diamines are used to achieve the desired separation properties. Several polyimides are commercially available, such as Matrimid, Kapton or PEI but their high prices have triggered the search for more economical precursors. An example of an economical precursor that has been gaining popularity are phenolic resins. These low cost precursors are high carbon yield polymers, with simple preparation methods [108-109] and provide carbon films with molecular sieve properties [109]. Another widely used precursor is polyfurfuryl alcohol (PFA), which leads to carbon membranes with narrow pore size distributions [107]. As PFAs are liquid at room temperature, all membranes made from this precursor are supported [104]. However, its low mechanical and elastic properties do not allow the formation of thin films on rigid

supports. Polyacrylonitriles (PANs) have been mainly used in the area of carbon fiber production. PAN fibers form thermally stable, highly oriented molecular structures when subject to a low temperature heat pre-treatment, which remain mostly undisrupted during carbonization [107]. Hence, carbon fibers have good mechanical properties, thus preventing brittleness, a common problem to carbon membranes.

Clearly, all precursors have attractive features and drawbacks. Ultimately, the choice of the precursor depends on the gas mixture to separate, the operating conditions and on the membrane geometry. The chosen precursor should provide good separation performance in the entire range of operating conditions at an affordable price.

1.1.3.2 Membrane Preparation

CMSM can be prepared as unsupported membranes (flat, hollow fibers or capillaries) or supported in flat-sheet or tubular porous inorganic membranes [110]. In most cases, due to the poor mechanical stability of unsupported membranes, supported ones are favoured. Supported membranes can be formed by ultrasonic deposition, dip coating, vapour deposition, spin coating and spray coating. Regardless of the method used, the material should be uniformly distributed. Several times, because the polymer shrinks upon pyrolization, the coating procedure has to be repeated until no defects can be detected in the carbon layer. Additionally, the support material must also be carefully chosen; it should be thermally stable during the carbonization process, very permeable, mechanically stable, allow compact packing, provide a good adhesion to the selective layer and have a low cost.

1.1.3.3 Pre-Treatment

The most frequently employed pre-treatment is heat-assisted oxidation. Oxidation leads to crosslinking of the polymer chains, so the polymer structure becomes stiffer, thus less prone to relaxation during carbonization. Hence, the precursor becomes more capable of withstanding the high temperatures of carbonization. The oxidation pre-treatment has to be optimized for each particular precursor but improvements in the CMS membrane properties are frequently reported [67, 112, 114-115]. While oxidation pre-treatment is almost always used, some times it is combined with other pre-treatment techniques to achieve the desired final membrane properties, including: (1) immersing membranes in chemical solutions, which helps to prevent clogging of the pores; (2) the use of carbonization catalysts, to allow carbonization to be carried out at lower temperatures and faster heating rates; (3) stretching, used to remove surface defects and attenuate variations in filament diameter in carbon hollow fiber membranes [107].

1.1.3.4 Carbonization

Carbonization is the process through which a polymer precursor is heated in a controlled atmosphere, yielding a carbon membrane. As the polymer matrix decomposes, volatiles are released and at the end of the carbonization a carbon matrix consisting of disordered graphene layers is formed. The spaces between these graphene layers form micropores, which are responsible for the sieving properties of carbon membranes. The porous network of CMSM is typically slit-like, and a possible pore size distribution is illustrated in Figure 1.10. It consists of relatively wide openings (micropores – D_1, D_2 and D_3 in Figure 1.10) with narrow constrictions (ultra micropores – d_c in Figure 1.10) [49]. At the constrictions, when the pore size is close to the diameter of the permeating species, repulsive forces are dominant and the permeating species requires

activation energy to pass through the constriction. Because of this, molecules with very similar sizes can be separated at these constrictions by molecular sieving. The pore openings are larger and are responsible for the adsorption capacity of a CMSM. The more easily condensable gases are preferentially adsorbed and impairing the diffusion of the less adsorbable gases [70]. Thus, the ultramicropores are responsible for the sieving properties of the carbon membrane, while the larger micropores assure there is a considerably high flux of the penetrants [107]. Depending on the controlling gas transport mechanism, carbon membranes can be separated into molecular sieve carbon membranes (Figure 1.10A) or adsorption-selective carbon membranes (Figure 1.10B).

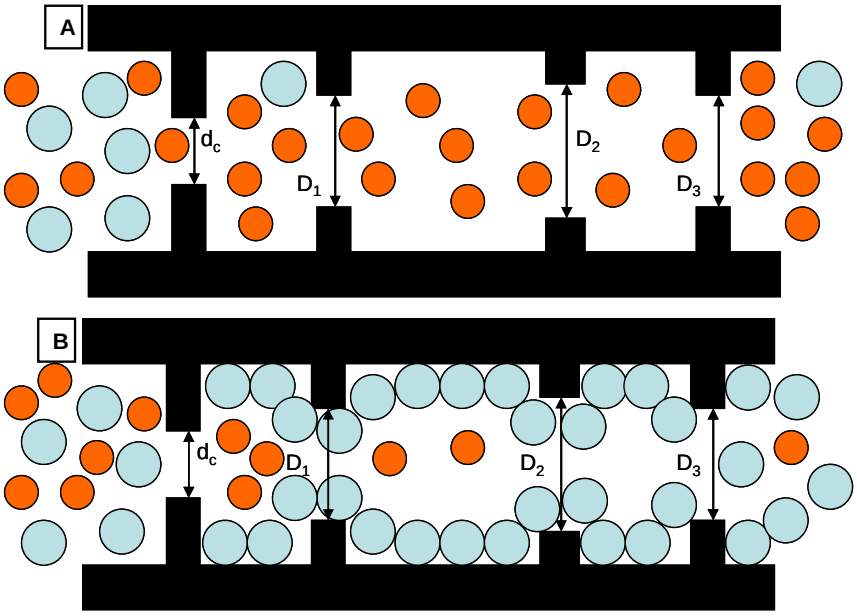

Figure 1.10 – Molecular sieve carbon membranes (A) and adsorption selective carbon membranes (B).

The final porous network depends strongly on several carbonization parameters, namely the carbonization temperature, heating rate, thermal soak time (time held at the carbonization temperature), carbonization atmosphere and, most noticeably during inert gas carbonization, the gas flow rate. The carbonization temperature

used lies between the decomposition temperature of the carbonaceous precursor and its graphitization temperature. Higher carbonization temperatures lead to CMSM with higher compactness, crystallinity and density, and smaller average interplanar spacing between the graphite-like layers of the carbon [111]; in most cases that translates into lower permeabilities and higher selectivities. Heating rates can range from 0.1 to 13.3 ºC [107, 110] and are associated with the rate of release of volatiles from the membrane. Higher heating rates may lead to the formation of pinholes and cracks so generally lower heating rates are preferable. The thermal soak time only induces some microstructural rearrangement, potentially affecting the pore size distribution of carbon membranes and its chemical stability (lower chemisorption capacity). Frequently, larger soak times cause pore sintering [112], thus decreasing the permeability. Carbonization has to be carried out either in vacuum or inert atmosphere to avoid undesired burn off and chemical damage of the membrane precursor. The use of inert gas generally leads to a more open porous network, because the flow of gas removes by-products from the polymer decomposition away from the carbon membrane [110].

1.1.3.5 Post-Treatment

Post-treatments can be used to either open or narrow the pore size distribution or to remove cracks or other defects [98]. When one desires to open the pores, low-temperature oxidation is performed [110], because it removes carbon atoms from the pore walls. When a narrower pore size distribution is the goal then chemical vapour deposition should be performed. Through carbonization of an organic species previously adsorbed in the pore system, carbon deposits on the pores, thus shrinking their aperture. Also, when a membrane presents cracks one might repair it through coating of the surface.

1.2 Propylene/Propadiene/Propyne Separation

This thesis also focuses on the removal of propyne from propylene streams (albeit to a lesser degree than propylene/propane separation). As previously mentioned, before propylene is separated from propane in a fractionation column, propadiene and propyne must be removed. Typically, this is carried out in hydrogenation reactors. However, the selectivity of this hydrogenation is not very high and the over-hydrogenation to propane is a problem that, if avoided, would decrease the costs of the subsequent distillation process. This work proposes to alternatively perform this separation in a catalytic membrane reactor, where a membrane selective towards propyne and propadiene is coupled with a hydrogenation catalyst in the permeate side of the membrane.

1.2.1 Catalytic Membrane Reactors (CMRs)

The concept of a CMR consists on coupling a membrane with a catalyst in a single unit to enhance conversion and or/ catalytic selectivity. A CMR is preferable over the conventional arrangement of a chemical reactor followed by a separation unit [113], since combining the reaction and separation in a single stage significantly reduces plant volume and increases the hydrogenation reaction selectivity [114]. The interest in using membrane reactors has increased among the scientific community, with most applications focusing on dehydrogenation reactions [115-121], hydrogenation reactions [113, 122-123] and oxidative coupling [124-126]. Three distinct classes of membrane reactors can be distinguished [123, 127-129]:

- When a membrane is used to remove a reaction product from the reactor in order to increase the yield compared to conventional reactors it is known as an extractor. Notable applications include improving the conversion in equilibrium-limited reactions or enhancing the selectivity towards an intermediate in consecutive reactions.

- When the membrane is used to control the addition of a reactant so as to limit side reactions it is called distributor. This configuration aims to avoid undesired side reactions by maintaining a very low concentration of the distributed reactant. This configuration only increases the selectivity towards an intermediate product when the reaction order of the distributed reactant on the desired reaction is the lowest. Yet, lower partial pressures of the distributed reactant lead to lower reaction rates in the membrane reactor and the gain in yield due to increased selectivity may be offset by a decrease in conversion.
- When the membrane keeps the reactants segregated on either side is known as an active contactor. This is useful to confine the reaction to a finite zone inside the membrane structure. Moreover, because the reactants reach the catalyst at stoichiometric ratio, undesirable side reactions might also be minimized [114].

In conclusion, CMRs lead to improvements in yield or simply in reaction conversion or selectivity. This can decrease downstream separation costs [130], expand the range of temperature and pressure for a given reaction [131] and provide more efficient purifications.

When the manufacturing costs of the membrane and its lifetime are successfully addressed one expects this concept to find large-scale industrial applications [130, 132].

1.3 Outline

The enormous energy and capital savings that membrane based technologies could have on propylene purification provided the motivation to this work.

The thesis is divided into four main parts: the first presents an introduction to the work, the next two concern the use of inorganic membranes for olefin/paraffin

separation, more specifically propylene/propane. The final part presents a theoretical work on the use of a CMR for propyne removal from propylene industrial streams.

Part II (Chapter 2) focuses on the use of silver-functionalized faujasite zeolite membranes for propylene/propane separation. The performance of the membranes was analyzed by mono and bicomponent permeation and the stability of the membranes was studied.

Part III (Chapters 3 to 6) reports the use of carbon molecular sieve membranes for gas separation, particularly propylene/propane. In Chapter 3 it is proposed a composite carbon membrane made from the carbonization of a phenolic resin loaded with boehmite nanoparticles. The porous network of this composite material was studied and its use for gas separation analyzed. Chapter 4 relates to the synthesis of a carbon matrix with two inorganic nanofillers, boehmite and silver. The distribution of the two fillers in the carbon matrix was analyzed and the effect of silver on the separation properties of the membrane assessed. Chapter 5 focuses on the optimization of the boehmite content in a carbon/alumina composite membrane for gas separation. Moreover, it also provides a kinetic and adsorption study of the composite material for some gas pairs, notably for propylene/propane. Finally, Chapter 6 provides a kinetic, adsorption and permeation study of carbon/alumina/silver membranes with different amounts of silver.

Part IV (Chapter 7) features a simulation work on the use of a catalytic membrane reactor for propylene streams purification by selectively hydrogenating propyne. A new membrane reactor configuration is proposed and its advantages relative to a conventional hydrogenation reactor are presented.

Finally, Chapter 8 presents the main conclusions of this work, discusses the main strengths and areas of improvement of each strategy herein discussed and ideas for future research directions are presented.

Appendix A provides a detailed description of the permeation unit that was assembled in the framework of this thesis.

1.4 List of Acronyms

Acronyms	Definition
BBU	Basic Building Unit
CBU	Complex Building Unit
c-CMSM	Composite Carbon Molecular Sieve Membrane
CG	Chemical Grade
CMR	Catalytic Membrane Reactor
CMSM	Carbon Molecular Sieve Membrane
FCC	Fluidized Catalytic Cracking
FTM	Facilitated Transport Membrane
LPG	Liquified Petroleum Gas
MMM	Mixed Matrix Membrane
RG	Refinery Grade
PAN	Polyacrylonitrile
PEG	Polyethylene Glycol
PFA	Polyfurfuryl Alcohol
PG	Polymer Grade
PDH	Propane Dehydrogenation

1.5 References

[1] World Light Olefins Analysis, CMAI Completes 2008.
[2] The Propylene Market Recovers, Study by Ceresana Research, http://www.chemeurope.com/en/news/130793/the-propylene-market-recovers.html, acessed in April 2011.
[3] Z. Ziaka, S. Vasileiadis, New Integrated Catalytic Membrane Processes for Enhanced Propylene and Polypropylene Production, Separ Sci Technol, 46 (2011) 224-233.
[4] T.E. Swaty, Global refining industry trends: the present and future, Hydrocarb Process, 84 (2005) 35-46.
[5] Z. Kotanjac, Development of packed bed membrane reactor for the oxidative dehydrogenation of propane (PhD Thesis), 2009.
[6] T. Ren, M. Patel, K. Blok, Olefins from conventional and heavy feedstocks: Energy use in steam cracking and alternative processes, Energy, 31 (2006) 425-451.
[7] K. Buker, S. Donnermeyer, H. Gehrke, M. Heinritz-Adrian, STAR Process (R) for the On-purpose Production of Propylene, Oil Gas-Eur Mag, 36 (2010) 40-44.
[8] M. Walther, Refinery sources will fill the future 'propylene gap', Oil Gas J, 101 (2003) 52-54.
[9] http://encyclopedia.airliquide.com/encyclopedia.asp, Air Liquide Website, acessed in April 2011.
[10] R.C. Reid, J.M. Prausnitz, B.E. Poling, The properties of gases and liquids, 4th ed. / Robert C. Reid, John M. Prausnitz, Bruce E. Poling. ed., McGraw-Hill, New York ; London, 1987.
[11] S.U. Rege, J. Padin, R.T. Yang, Olefin/paraffin separations by adsorption: pi-complexation vs. kinetic separation, Aiche Journal, 44 (1998) 799-809.
[12] G.E. Keller, A.E. Marcinkowsky, S.K. Verma, K.D. Williamson, Olefin recovery and purification via silver complexation, in: N.N. Li, J.M. Calo (Eds.) Sep Purif Technol, Dekker, New York, N.Y., 1992.
[13] M.T. Ravanchi, T. Kaghazchi, A. Kargari, M. Soleimani, A novel separation process for olefin gas purification: Effect of operating parameters on separation performance and process optimization, J Taiwan Inst Chem E, 40 (2009) 511-517.
[14] R.B. Eldridge, Olefin Paraffin Separation Technology - a Review, Ind Eng Chem Res, 32 (1993) 2208-2212.
[15] D.J. Safarik, R.B. Eldridge, Olefin/paraffin separations by reactive absorption: A review, Ind Eng Chem Res, 37 (1998) 2571-2581.
[16] P.S. Gomes, N. Lamia, A.E. Rodrigues, Design of a gas phase simulated moving bed for propane/propylene separation, Chemical Engineering Science, 64 (2009) 1336-1357.

[17] R.L. Burns, W.J. Koros, Defining the challenges for C_3H_6/C_3H_8 separation using polymeric membranes, J Membrane Sci, 211 (2003) 299-309.
[18] R.W. Baker, Future directions of membrane gas separation technology, Ind Eng Chem Res, 41 (2002) 1393-1411.
[19] P. Bernardo, E. Drioli, Membrane gas separation progresses for process intensification strategy in the petrochemical industry, Petrol Chem+, 50 (2010) 271-282.
[20] M. Mulder, Basic Principles of Membrane Technology, Kluwer Academic Publishers, 1996.
[21] R.W. Baker, Membrane technology and applications, 2nd ed., J. Wiley, Chichester ; New York, 2004.
[22] R.D. Noble, S.A. Stern, Membrane Separations Technology - Principles and Applications, Elsevier Science, (1995).
[23] S. Loeb, S. Sourirajan, Sea Water Demineralization by Means of an Osmotic Membrane, , Saline Water Conversion-II, Advances in Chemistry Series Number 38 , American Chemical Society, (1963) 117-132.
[24] J.M. Henis, Commercial and Pratical aspects of gas separation membranes, in: D.R. Paul, Y.P. Yampol'skii (Eds.) Polymeric gas separation membranes, CRC Press, Boca Raton, Fla. ; London, 1994, pp. 441-530.
[25] R.W. Spillman, Economics of Gas Separation Membranes, Chem Eng Prog, 85 (1989) 41-62.
[26] P. Bernardo, E. Drioli, G. Golemme, Membrane Gas Separation: A Review/State of the Art, Ind Eng Chem Res, 48 (2009) 4638-4663.
[27] K. Tanaka, A. Taguchi, J.Q. Hao, H. Kita, K. Okamoto, Permeation and separation properties of polyimide membranes to olefins and paraffins, J Membrane Sci, 121 (1996) 197-207.
[28] J.J. Krol, M. Boerrigter, G.H. Koops, Polyimide hollow fiber gas separation membranes: preparation and the suppression of plasticization in propane/propylene environments, J Membrane Sci, 184 (2001) 275-286.
[29] L.M. Robeson, Correlation of Separation Factor Versus Permeability for Polymeric Membranes, J Membrane Sci, 62 (1991) 165-185.
[30] J.S. Dewar, A Review of the Pi-Complex Theory, B Soc Chim Fr, 18 (1951) 71-79.
[31] N. Chen, R.T. Yang, Ab initio molecular orbital study of adsorption of oxygen, nitrogen, and ethylene on silver-zeolite and silver halides, Ind Eng Chem Res, 35 (1996) 4020-4027.
[32] M. Teramoto, H. Matsuyama, T. Yamashiro, Y. Katayama, Separation of Ethylene from Ethane by Supported Liquid Membranes Containing Silver-Nitrate as a Carrier, J Chem Eng Jpn, 19 (1986) 419-424.
[33] M. Teramoto, H. Matsuyama, T. Yamashiro, S. Okamoto, Separation of Ethylene from Ethane by a Flowing Liquid Membrane Using Silver-Nitrate as a Carrier, J Membrane Sci, 45 (1989) 115-136.

[34] H. Nishide, H. Kawakami, Y. Sasame, K. Ishiwata, E. Tsuchida, Facilitated Transport of Molecular-Oxygen in Cobaltporphyrin Poly(1-Trimethylsilyl-1-Propyne) Membrane, J Polym Sci Pol Chem, 30 (1992) 77-82.
[35] H. Nishide, H. Kawakami, T. Suzuki, Y. Azechi, Y. Soejima, E. Tsuchida, Effect of Polymer Matrix on the Oxygen Diffusion Via a Cobalt Porphyrin Fixed in a Membrane, Macromolecules, 24 (1991) 6306-6309.
[36] S. Sunderrajan, B.D. Freeman, C.K. Hall, I. Pinnau, Propane and propylene sorption in solid polymer electrolytes based on poly(ethylene oxide) and silver salts, J Membrane Sci, 182 (2001) 1-12.
[37] S.U. Hong, J.H. Jin, J. Won, Y.S. Kang, Polymer-salt complexes containing silver ions and their application to facilitated olefin transport membranes, Adv Mater, 12 (2000) 968-971.
[38] B. Jose, J.H. Ryu, B.G. Lee, H. Lee, Y.S. Kang, H.S. Kim, Effect of phthalates on the stability and performance of $AgBF_4$-PVP membranes for olefin/paraffin separation, Chem Commun, (2001) 2046-2047.
[39] O.I. Eriksen, I.B. Vik, I.M. Dahl, M.L. Posey, Separation of ethene from ethane with permeators based on silver ion-exchanged nafion hollow fibers., Abstr Pap Am Chem S, 214 (1997) 61.
[40] R. Rabago, D.L. Bryant, C.A. Koval, R.D. Noble, Evidence for parallel pathways in the facilitated transport of alkenes through Ag+-exchanged nafion films, Ind Eng Chem Res, 35 (1996) 1090-1096.
[41] T. Yamaguchi, C. Baertsch, C.A. Koval, R.D. Noble, C.N. Bowman, Olefin separation using silver impregnated ion-exchange membranes and silver salt/polymer blend membranes, J Membrane Sci, 117 (1996) 151-161.
[42] S. Jung, J. Palgunadi, J.H. Kim, H. Lee, B.S. Ahn, M. Cheong, H.S. Kim, Highly efficient metal-free membranes for the separation of acetylene/olefin mixtures: Pyrrolidinium-based ionic liquids as acetylene transport carriers, J Membrane Sci, 354 (2010) 63-67.
[43] J.M. Lee, J. Palgunadi, J.H. Kim, S. Jung, Y.S. Choi, M. Cheong, H.S. Kim, Selective removal of acetylenes from olefin mixtures through specific physicochemical interactions of ionic liquids with acetylenes, Phys Chem Chem Phys, 12 (2010) 1812-1816.
[44] J. Palgunadi, H.S. Kim, J.M. Lee, S. Jung, Ionic liquids for acetylene and ethylene separation: Material selection and solubility investigation, Chem Eng Process, 49 (2010) 192-198.
[45] S.W. Kang, K. Char, Y.S. Kang, Novel application of partially positively charged silver nanoparticles for facilitated transport in olefin/paraffin separation membranes, Chem Mater, 20 (2008) 1308-1311.
[46] S.W. Kang, J. Hong, K. Char, J.H. Kim, J. Kim, Y.S. Kang, Correlation between anions of ionic liquids and reduction of silver ions in facilitated olefin transport membranes, Desalination, 233 (2008) 327-332.
[47] D.D. Do, Adsorption analysis: equilibria and kinetics, Imperial College Press, London, 1998.

[48] J. Caro, M. Noack, P. Kolsch, R. Schafer, Zeolite membranes - state of their development and perspective, Micropor Mesopor Mat, 38 (2000) 3-24.
[49] A.F. Ismail, L.I.B. David, A review on the latest development of carbon membranes for gas separation, J Membrane Sci, 193 (2001) 1-18.
[50] B.N. Nair, K. Keizer, W.J. Elferink, M.J. Gilde, H. Verweij, A.J. Burggraaf, Synthesis, characterisation and gas permeation studies on microporous silica and alumina-silica membranes for separation of propane and propylene, J Membrane Sci, 116 (1996) 161-169.
[51] B.N. Nair, K. Keizer, H. Verweij, A.J. Burggraaf, Surface selective approach to separation of propylene from propane, Separ Sci Technol, 31 (1996) 1907-1914.
[52] I. Tiscornia, S. Irusta, C. Tellez, J. Coronas, J. Santamaria, Separation of propylene/propane mixtures by titanosilicate ETS-10 membranes prepared in one-step seeded hydrothermal synthesis, J Membrane Sci, 311 (2008) 326-335.
[53] I. Tiscornia, Z. Lin, J. Rocha, C. Tellez, J. Coronas, J. Santamaria, Preparation of titanosilicate ETS-10 and vanadosilicate AM-6 membranes, Studies in Surface Science and Catalysis, 158 (2005) 423-430.
[54] V. Nikolakis, G. Xomeritakis, A. Abibi, M. Dickson, M. Tsapatsis, D.G. Vlachos, Growth of a faujasite-type zeolite membrane and its application in the separation of saturated/unsaturated hydrocarbon mixtures, J Membrane Sci, 184 (2001) 209-219.
[55] I.G. Giannakopoulos, K. Kalambaliki, V. Dracopoulos, V. Nikolakis, Synthesis of faujasite membranes for the separation of propane/propylene mixtures, Studies in Surface Science and Catalysis, 158 (2005) 137-144.
[56] I.G. Giannakopoulos, V. Nikolakis, Separation of propylene/propane mixtures using faujasite-type zeolite membranes, Ind Eng Chem Res, 44 (2005) 226-230.
[57] K.A. Stoitsas, A. Gotzias, E.S. Kikkinides, T.A. Steriotis, N.K. Kanellopoulos, M. Stoukides, V.T. Zaspalis, Porous ceramic membranes for propane-propylene separation via the pi-complexation mechanism: unsupported systems, Micropor Mesopor Mat, 78 (2005) 235-243.
[58] E.I. Basaldella, J.C. Tara, G.A. Armenta, M.E.P. Iglesias, Cu/SBA-15 as adsorbent for propane/propylene separation, J Porous Mat, 14 (2007) 273-278.
[59] E.I. Basaldella, J.C. Tara, G.A. Armenta, M.E. Patino-Iglesias, E. Castellon, Propane/propylene separation by selective olefin adsorption on Cu/SBA-15 mesoporous silica, J Sol-Gel Sci Techn, 37 (2006) 141-146.
[60] N.V. Choudary, P. Kumar, T.S.G. Bhat, S.H. Cho, S.S. Han, J.N. Kim, Adsorption of light hydrocarbon gases on alkene-selective adsorbent, Ind Eng Chem Res, 41 (2002) 2728-2734.
[61] J. Padin, R.T. Yang, C.L. Munson, New sorbents for olefin/paraffin separations and olefin purification for C_4 hydrocarbons, Ind Eng Chem Res, 38 (1999) 3614-3621.

[62] A. van Miltenburg, W. Zhu, F. Kapteijn, J.A. Moulijn, Zeolite based separation of light olefin and paraffin mixtures, Studies in Surface Science and Catalysis, 158 (2005) 979-986.
[63] A. van Miltenburg, W. Zhu, F. Kapteijn, J.A. Moulijn, Adsorptive separation of light olefin/paraffin mixtures, Chem Eng Res Des, 84 (2006) 350-354.
[64] J. Hayashi, H. Mizuta, M. Yamamoto, K. Kusakabe, S. Morooka, S.H. Suh, Separation of ethane/ethylene and propane/propylene systems with a carbonized BPDA-pp'ODA polyimide membrane, Ind Eng Chem Res, 35 (1996) 4176-4181.
[65] K. Okamoto, S. Kawamura, M. Yoshino, H. Kita, Y. Hirayama, N. Tanihara, Y. Kusuki, Olefin/paraffin separation through carbonized membranes derived from an asymmetric polyimide hollow fiber membrane, Ind Eng Chem Res, 38 (1999) 4424-4432.
[66] M.L. Chng, Y.C. Xiao, T.S. Chung, M. Toriida, S. Tamai, Enhanced propylene/propane separation by carbonaceous membrane derived from poly (aryl ether ketone)/2,6-bis(4-azidobenzylidene)-4-methyl-cyclohexanone interpenetrating network, Carbon, 47 (2009) 1857-1866.
[67] M.N. Islam, W.L. Zhou, T. Honda, K. Tanaka, H. Kita, K. Okamoto, Preparation and gas separation performance of flexible pyrolytic membranes by low-temperature pyrolysis of sulfonated polyimides, J Membrane Sci, 261 (2005) 17-26.
[68] K.M. Steel, W.J. Koros, An investigation of the effects of pyrolysis parameters on gas separation properties of carbon materials, Carbon, 43 (2005) 1843-1856.
[69] H. Suda, K. Haraya, Alkene/alkane permselectivities of a carbon molecular sieve membrane, Chem Commun, (1997) 93-94.
[70] A.B. Fuertes, I. Menendez, Separation of hydrocarbon gas mixtures using phenolic resin-based carbon membranes, Sep Purif Technol, 28 (2002) 29-41.
[71] W.J. Koros, R. Mahajan, Pushing the limits on possibilities for large scale gas separation: which strategies?, J Membrane Sci, 175 (2000) 181-196.
[72] Q. Hu, E. Marand, S. Dhingra, D. Fritsch, J. Wen, G. Wilkes, Poly(amide-imide)/TiO_2 nano-composite gas separation membranes: Fabrication and characterization, J Membrane Sci, 135 (1997) 65-79.
[73] J.N. Barsema, J. Balster, V. Jordan, N.F.A. van der Vegt, M. Wessling, Functionalized Carbon Molecular Sieve membranes containing Ag-nanoclusters, J Membrane Sci, 219 (2003) 47-57.
[74] J.N. Barsema, J. Balster, N.F.A. Van der Vegt, G.H. Koops, V. Jordan, M. Wessling, Ag functionalized Carbon Molecular Sieves membranes for separating O_2 and N_2, Membranes-Preparation, Properties and Applications, 752 (2003) 207-212.
[75] Y.C. Xiao, M.L. Chng, T.S. Chung, M. Toriida, S. Tamai, H.M. Chen, Y.C.J. Jean, Asymmetric structure and enhanced gas separation performance induced by in situ growth of silver nanoparticles in carbon membranes, Carbon, 48 (2010) 408-416.

[76] S. Yoda, A. Hasegawa, H. Suda, Y. Uchimaru, K. Haraya, T. Tsuji, K. Otake, Preparation of a platinum and palladium/polyimide nanocomposite film as a precursor of metal-doped carbon molecular sieve membrane via supercritical impregnation, Chem Mater, 16 (2004) 2363-2368.
[77] Y.K. Kim, H.B. Park, Y.M. Lee, Carbon molecular sieve membranes derived from metal-substituted sulfonated polyimide and their gas separation properties, J Membrane Sci, 226 (2003) 145-158.
[78] H.B. Park, C.H. Jung, Y.K. Kim, S.Y. Nam, S.Y. Lee, Y.M. Lee, Pyrolytic carbon membranes containing silica derived from poly(imide siloxane): the effect of siloxane chain length on gas transport behavior and a study on the separation of mixed gases, J Membrane Sci, 235 (2004) 87-98.
[79] H.B. Park, S.Y. Lee, Y.M. Lee, Pyrolytic carbon membranes containing silica: morphological approach on gas transport behavior, J Mol Struct, 739 (2005) 179-190.
[80] X.Y. Yin, J.Q. Wang, N.B. Chu, J.H. Yang, J.M. Lu, Y. Zhang, D.H. Yin, Zeolite L/carbon nanocomposite membranes on the porous alumina tubes and their gas separation properties, J Membrane Sci, 348 (2010) 181-189.
[81] Q.L. Liu, T.H. Wang, J.S. Qiu, Y.M. Cao, A novel carbon/ZSM-5 nanocomposite membrane with high performance for oxygen/nitrogen separation, Chem Commun, (2006) 1230-1232.
[82] C.F. Zeng, L.X. Zhang, X.H. Cheng, H.T. Wang, N.P. Xu, Preparation and gas permeation of nano-sized zeolite NaA-filled carbon membranes, Sep Purif Technol, 63 (2008) 628-633.
[83] P. Payra, P.K. Dutta, Zeolites: A Primer, in: S.M. Auerbach, K.A. Carrado, P.K. Dutta (Eds.) Handbook of Zeolite Science and Technology, CRC Press, 2003, pp. 1-19.
[84] W.H. Baur, Straight Si-O-Si Bridging Bonds Do Exist in Silicates and Silicon Dioxide Polymorphs, Acta Crystallogr B, 36 (1980) 2198-2202.
[85] D.W. Breck, Zeolite Molecular Sieves, Krieger Publishing Company, 1974.
[86] D.R. Corbin, L. Abrams, G.A. Jones, M.L. Smith, C.R. Dybowski, J.A. Hriljac, J.B. Parise, Entrapment and Controlled-Release of Xenon in Cd^{2+}-Exchanged Zeolite Rho, J Chem Soc Chem Comm, (1993) 1027-1029.
[87] K.D. Hammonds, V. Heine, M.T. Dove, Rigid-unit modes and the quantitative determination of the flexibility possessed by zeolite frameworks, J Phys Chem B, 102 (1998) 1759-1767.
[88] A. Cronstedt, Rön och Beskrifning Om en oberkant bärg art, som kallas Zeolites, Kongliga Vetenskaps Academiens Handlingar, 17 (1756) 120-123.
[89] C.S. Cundy, P.A. Cox, The hydrothermal synthesis of zeolites: History and development from the earliest days to the present time, Chemical Reviews, 103 (2003) 663-701.
[90] http://www.iza-online.org/, International Zeolite Association website, acessed in November 2010.

[91] R. Singh, P.K. Dutta, MFI: A Case Study of Zeolite Synthesis, in: S.M. Auerbach, K.A. Carrado, P.K. Dutta (Eds.) Handbook of Zeolite Science and Technology, CRC Press, 2003, pp. 21-64.
[92] S. Nair, M. Tsapatis, Synthesis and Properties of Zeolitic Membranes, in: S.M. Auerbach, K.A. Carrado, P.K. Dutta (Eds.) Handbook of Zeolite Science and Technology, CRC Press, 2003, pp. 867-920.
[93] H.P. Hsieh, Inorganic Membranes for Separation and Reaction, Elsevier Science, 1996.
[94] J. Choi, H.K. Jeong, M.A. Snyder, J.A. Stoeger, R.I. Masel, M. Tsapatsis, Grain Boundary Defect Elimination in a Zeolite Membrane by Rapid Thermal Processing, Science, 325 (2009) 590-593.
[95] R.E. Franklin, The Interpretation of Diffuse X-Ray Diagrams of Carbon, Acta Crystallogr, 3 (1950) 107-121.
[96] R.E. Franklin, The Structure of Graphitic Carbons, Acta Crystallogr, 4 (1951) 253-261.
[97] H. Marsh, F. Rodríguez-Reinoso, Activated Carbon, Elsevier Science, 2006.
[98] A.F. Ismail, K. Li, From Polymeric Precursors to Hollow Fiber Carbon and Ceramic Membranes, in: R. Mallada, M. Menéndez (Eds.) Inorganic Membranes Synthesis, Characterization and Applications, Elsevier Science, 2008.
[99] V.C. Geiszler, W.J. Koros, Effects of polyimide pyrolysis conditions on carbon molecular sieve membrane properties, Ind Eng Chem Res, 35 (1996) 2999-3003.
[100] K.M. Steel, W.J. Koros, Investigation of porosity of carbon materials and related effects on gas separation properties, Carbon, 41 (2003) 253-266.
[101] K. Wang, H. Suda, K. Haraya, The characterization of CO_2 permeation in a CMSM derived from polyimide, Sep Purif Technol, 31 (2003) 61-69.
[102] F.K. Katsaros, T.A. Steriotis, A.K. Stubos, A. Mitropoulos, N.K. Kanellopoulos, S. Tennison, High pressure gas permeability of microporous carbon membranes, Microporous Mater, 8 (1997) 171-176.
[103] M.B. Shiflett, H.C. Foley, Reproducible production of nanoporous carbon membranes, Carbon, 39 (2001) 1421-1425.
[104] Y.D. Chen, R.T. Yang, Preparation of Carbon Molecular-Sieve Membrane and Diffusion of Binary-Mixtures in the Membrane, Ind Eng Chem Res, 33 (1994) 3146-3153.
[105] L.I.B. David, A.F. Ismail, Influence of the thermastabilization process and soak time during pyrolysis process on the polyacrylonitrile carbon membranes for O_2/N_2 separation, J Membrane Sci, 213 (2003) 285-291.
[106] V.M. Linkov, R.D. Sanderson, E.P. Jacobs, Highly Asymmetrical Carbon Membranes, J Membrane Sci, 95 (1994) 93-99.
[107] S.M. Saufi, A.F. Ismail, Fabrication of carbon membranes for gas separation - a review, Carbon, 42 (2004) 241-259.
[108] T.A. Centeno, A.B. Fuertes, Supported carbon molecular sieve membranes based on a phenolic resin, J Membrane Sci, 160 (1999) 201-211.

[109] T.A. Centeno, A.B. Fuertes, Carbon molecular sieve membranes derived from a phenolic resin supported on porous ceramic tubes, Sep Purif Technol, 25 (2001) 379-384.
[110] P.J. Williams, W.J. Koros, Gas Separation by Carbon Membranes, in: N.N. Li, A.G. Fane, W.S. Ho, T. Matsuura (Eds.) Advanced Membrane Tecnology and Applications, Wiley-AIChE, 2008, pp. 599-632.
[111] N. Tanihara, H. Shimazaki, Y. Hirayama, S. Nakanishi, T. Yoshinaga, Y. Kusuki, Gas permeation properties of asymmetric carbon hollow fiber membranes prepared from asymmetric polyimide hollow fiber, J Membrane Sci, 160 (1999) 179-186.
[112] K. Steel, Carbon Membranes for Challenging Separations (PhD Thesis), in, University of Texas, Austin, 2000.
[113] J.M. Sousa, A. Mendes, Consecutive-parallel reactions in nonisothermal polymeric catalytic membrane reactors, Ind Eng Chem Res, 45 (2006) 2094-2107.
[114] R. Mallada, M. Menendez, Inorganic membranes: synthesis, characterization and applications, Elsevier, Amsterdam ; Oxford, 2008.
[115] V. Diakov, A. Varma, Methanol oxidative dehydrogenation in a packed-bed membrane reactor: yield optimization experiments and model, Chemical Engineering Science, 58 (2003) 801-807.
[116] R. Dittmeyer, V. Hollein, P. Quicker, G. Emig, G. Hausinger, F. Schmidt, Factors controlling the performance of catalytic dehydrogenation of ethylbenzene in palladium composite membrane reactors, Chemical Engineering Science, 54 (1999) 1431-1439.
[117] A.G. Dixon, Analysis of intermediate product yield in distributed-feed nonisothermal tubular membrane reactors, Catalysis Today, 67 (2001) 189-203.
[118] K. Georgieva, I. Mednev, D. Handtke, J. Schmidt, Influence of the operating conditions on yield and selectivity for the partial oxidation of ethane in a catalytic membrane reactor, Catalysis Today, 104 (2005) 168-176.
[119] C.M. O'Neill, E.E. Wolf, Yield improvements in membrane reactors for partial oxidation reactions, Ind Eng Chem Res, 45 (2006) 2697-2706.
[120] S. Assabumrungrat, T. Rienchalanusarn, P. Praserthdam, S. Goto, Theoretical study of the application of porous membrane reactor to oxidative dehydrogenation of n-butane, Chem Eng J, 85 (2002) 69-79.
[121] M. Sheintuch, R.M. Dessau, Observations, modeling and optimization of yield, selectivity and activity during dehydrogenation of isobutane and propane in a Pd membrane reactor, Chemical Engineering Science, 51 (1996) 535-547.
[122] L. Brandao, D. Fritsch, A.M. Mendes, L.M. Madeira, Propylene hydrogenation in a continuous polymeric catalytic membrane reactor, Ind Eng Chem Res, 46 (2007) 5278-5285.
[123] L. Brandao, L.M. Madeira, A.M. Mendes, Propyne hydrogenation in a continuous polymeric catalytic membrane reactor, Chemical Engineering Science, 62 (2007) 6768-6776.

[124] Y.K. Kao, L. Lei, Y.S. Lin, Optimum operation of oxidative coupling of methane in porous ceramic membrane reactors, Catalysis Today, 82 (2003) 255-273.
[125] X. Tan, Z. Pang, S. Liu, Catalytic perovskite hollow fibre membrane reactors for methane oxidative coupling, J Membrane Sci, 302 (2007) 109-114.
[126] H.H. Wang, Y. Cong, W.S. Yang, Oxidative coupling of methane in $Ba_{0.5}Sr_{0.5}Co_{0.8}Fe_{0.2}O_3$-delta tubular membrane reactors, Catalysis Today, 104 (2005) 160-167.
[127] C. Godinez, A.L. Cabanes, G. Villora, Experimental-Study of the Front-End Selective Hydrogenation of Steam-Cracking C_2-C_3 Mixture, Chem Eng Process, 34 (1995) 459-468.
[128] A. Julbe, D. Farrusseng, C. Guizard, Porous ceramic membranes for catalytic reactors - overview and new ideas, J Membrane Sci, 181 (2001) 3-20.
[129] S. Miachon, J.A. Dalmon, Catalysis in membrane reactors: what about the catalyst?, Top Catal, 29 (2004) 59-65.
[130] S.S. Ozdemir, M.G. Buonomenna, E. Drioli, Catalytic polymeric membranes: Preparation and application, Applied Catalysis a-General, 307 (2006) 167-183.
[131] J.N. Armor, Catalysis with Permselective Inorganic Membranes, Applied Catalysis, 49 (1989) 1-25.
[132] E. Drioli, E. Fontananova, Membrane Reactors, in: N.N. Li, A.G. Fane, W.S. Ho, T. Matsuura (Eds.) Advanced Membrane Tecnology and Applications, Wiley-AIChE, 2008, pp. 703.

PART II:

ZEOLITE MEMBRANES

Chapter 2: **Silver Functionalized Faujasite Zeolite Membranes for Propylene/Propane Separation**

(Teixeira, M., Machado, A., Lin, Z., Madeira, L.M., Sousa, J., Trindade, T., Mendes, A., to be submitted)

2.1 Abstract

This chapter focuses on the separation of C_3H_6 from C_3H_6/C_3H_8 feed streams using faujasite Y zeolite membranes functionalized with Ag^+. This work was done in collaboration with CICECO/Aveiro University (under the framework of a FCT funded project, ref. POCI/EQU/59344/2004), which was responsible for the synthesis and morphological characterization of the membranes. Zeolites were prepared in powder form, for adsorption equilibrium analysis, and supported in tubular α-Al_2O_3 membranes, for gas permeation experiments.

Monocomponent permeances towards N_2, C_3H_8 and C_3H_6 in the temperature range 20-180 ºC were measured to assess the controlling mass transfer phenomena during permeation. The membrane's permeances and separation factors for C_3H_6/C_3H_8 mixed streams were also determined. The most promising membranes were ion-exchanged with Ag^+ and the impact of Ag^+ on the performance of the membrane for C_3H_6/C_3H_8 gas separation was assessed; the C_3H_6/C_3H_8 separation factor at 25 ºC increased from 1.3-2.4 to 1.7-6.0 upon Ag^+ loading. The membranes exhibited constant C_3H_6/C_3H_8 separation factors for over one week of continuous exposure to mixed C_3H_6/C_3H_8 streams.

2.2 Introduction

C_3H_6/C_3H_8 separation is regarded as one of the most important processes in today's petrochemical industry. C_3H_6 has a broad use nowadays, namely in the production of plastics such as polypropylene and chemicals such as cumene [1-2]. For a long time, cryogenic and extractive distillations have been used to perform this separation. However, due to the similar volatility of C_3H_8 and C_3H_6, distillation is very energy demanding, making it only attractive for streams containing high amounts of C_3H_6 [1, 3]. Separation technologies based on adsorbents or membranes have been suggested in the last few years as energy-saving alternatives. They take advantage of other properties of the solutes, namely their molecular size or the ability of the olefins to selectively form π-complexes with Ag^+ ion, showing enhanced separation factors. Several studies have been performed with Ag^+ functionalized polymer membranes [4-12] as well as plain and Ag^+ functionalized adsorbents [13-19]. The use of inorganic membranes [20-24] is scarcer, despite being chemically and thermally more stable than polymer ones [25]. This study focuses on the use of Ag^+ functionalized faujasite zeolite membranes, which, to be best of the authors knowledge, have not been previously proposed for this separation.

Faujasite-type (Y) zeolite membranes were prepared hydrothermally on tubular α-Al_2O_3 supports by seeding and secondary growth method. Al_2O_3 tubes were used as supports to provide a better intergrowth between the support and the faujasite (aluminosilicate) zeolite layer. The selected Y-zeolite-α-Al_2O_3 membranes, based on scanning electron microscopy and mono component gas permeance results, were functionalized with Ag^+. Permeance and C_3H_6/C_3H_8 separation factor values before and after Ag^+ incorporation were obtained and compared to assess the effect of the facilitated transport on the overall performance of the membranes.

2.3 Experimental

2.3.1 Adsorbent and Membrane Synthesis

The synthesis of the zeolite powders/membranes was performed by the research partner CICECO (Centro de Investigação em Materiais Cerâmicos e Compósitos, Universidade de Aveiro) in the framework of a FCT joint project (reference POCI/EQU/59344/2004).

Zeolite powders were synthesized according to procedures described in the literature [26]. Zeolite membranes were synthesized hydrothermally by the seeding and secondary growth method. To increase their mechanical strength, they were supported on cylindrical α-Al_2O_3 tubes with 1000 nm pore size, internal and external diameters of approximately 7 and 10 mm, respectively, and 7 cm length (Inopor). Initially, the porous support was coated with an aqueous solution of NaX seed crystals and dried at 423 K for 20 minutes. Afterwards, the support tubes were placed in an autoclave, with their outside wrapped in Teflon tape, and filled with an aluminosilicate precursor.

Both gel and clear solutions, with molar compositions (Al_2O_3:5SiO_2:7Na_2O:415H_2O) and (Al_2O_3:9SiO_2:80Na_2O:5000H_2O), respectively, were used as aluminosilicate sources. Hydrothermal synthesis was carried out in an oven at 353 K for 24 hours and the synthesis procedure was repeated three times to minimize intercrystalline defects. Ag^+ functionalized faujasite membranes were prepared by ion-exchange with a 0.1 M aqueous $AgNO_3$ solution, for one hour. The amount of Ag^+ on the final membrane ranged from 1/10 to 1/12 of the zeolite weight. The faujasite membranes were characterized by scanning electron microscopy (SEM) using a Hitachi S4100 microscope. SEM provided information regarding the morphology, thickness and uniformity of the zeolite film.

2.3.2 Adsorption Equilibrium Experiments

Adsorption isotherms of C_3H_8 and C_3H_6 in powder Y zeolite samples with Ag^+ (coded as Ag-Y) and without Ag^+ (coded as Na-Y) were determined at 293 K in a VTI gravimetric sorption analyzer (GHP-50), sketched in Figure 2.1. This fully automated analyzer consists of a microbalance, a vacuum system and a water-cooled furnace. Below 343 K, the temperature is controlled with a water bath and above 343 K the software closes the water bath valve and the temperature becomes controlled by an electric furnace. The adsorbent samples were degassed under helium conditions, at 573 K, for 6 hours.

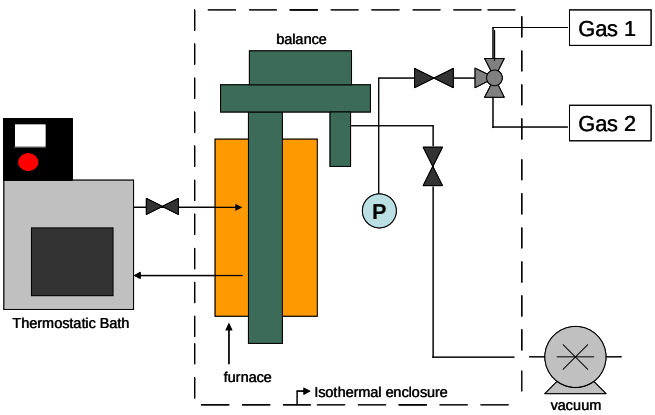

Figure 2.1 – Illustration of the VTI microbalance used for adsorption experiments.

2.3.3 Permeation Experiments

The permeability of a membrane is expressed as:

$$L_i = \frac{F_i/A_P}{\left(p_i^h - p_i^l\right)/\delta} \tag{2.1}$$

where F is the gas flow rate, A_P the permeation area of the membrane, p the partial pressure and δ the membrane thickness. The subscript refers to species i and superscripts h and l refer to high and low pressure side of the membrane,

respectively. When the membrane thickness is unknown, the membrane permeance is used instead (Π_i). This parameter is given by:

$$\Pi_i = \frac{L_i}{\delta} \tag{2.2}$$

The ideal selectivity or permselectivity $(S_{i,j})$ is the ratio of the membrane permeability towards two gas species (*i* and *j*), and indicates the membrane ability to separate the two components:

$$S_{i,j} = \frac{L_i}{L_j} \tag{2.3}$$

When the feed gas stream is a mixture, ratio of the permeabilities gives the real selectivity or separation factor $(S_{f\ i,j})$, and can be expressed by:

$$S_{f\ i,j} = \frac{y_i / y_j}{x_i / x_j} \tag{2.4}$$

where *y* refers to the molar fraction in the permeate stream and *x* to the molar fraction in the retentate stream. Permeation measurements were performed in the setup schematized in Figure 2.2.

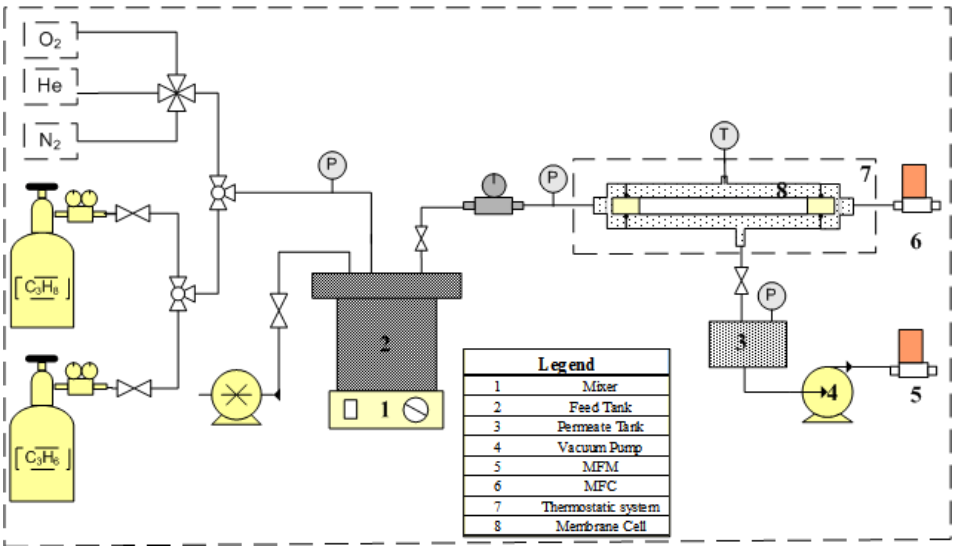

Figure 2.2 – Scheme of the experimental set up assembled for gas permeation measurements.

Ceramic tubular membranes were sealed in a custom-made stainless steel permeation cell with PTFE o-rings. Before permeation experiments, Na-Y membranes were degassed up to 180 °C (maximum temperature imposed by the o-rings) with N_2 flow across the membrane and vacuum on the permeate side, for up to 24 hours. Ag^+-Y membranes were degassed with air flow across the membrane and 30 kPa on the permeate side to minimize Ag^+ reduction by intrazeolitic water and lattice O_2 [27].

Gas permeances were determined with either pressure sensors or mass flow meters. For low flow rate values, the mass flow meters used offered lower precision so permeances were determined by monitoring the increase in permeate pressure, from initial vacuum conditions (pressure increment method). When the flow rate values were higher, permeances were determined by feeding a gas/mixture at constant pressure to the tube side, while applying vacuum to shell side, and measuring the permeating mass flow rate.

In mixed gas experiments, the feed stream was prepared in a 5 L stainless steel tank with agitation. The compositions of the feed and permeate were determined in a GC, equipped with a FID detector.

The thermostatic control of the permeation cell, for temperatures in the range 273-368 K, was achieved with a water bath. For higher temperatures, it was used a thermostatic system assembled in-house, which consisted of two resistances and a fan, and the temperature was set by a temperature controller. This system and its operation are described more thoroughly in Appendix A, as well as more details regarding the experimental setup, its assembly and the equipment used.

2.4 Results

2.4.1 SEM

Figure 2.3 shows SEM images of a zeolite membrane, before and after ion-exchange with silver. Figure 2.3A and Figure 2.3B show a zeolite layer formed with a clear solution (Figure 2.3A) or a gel (Figure 2.3B) used as precursor.

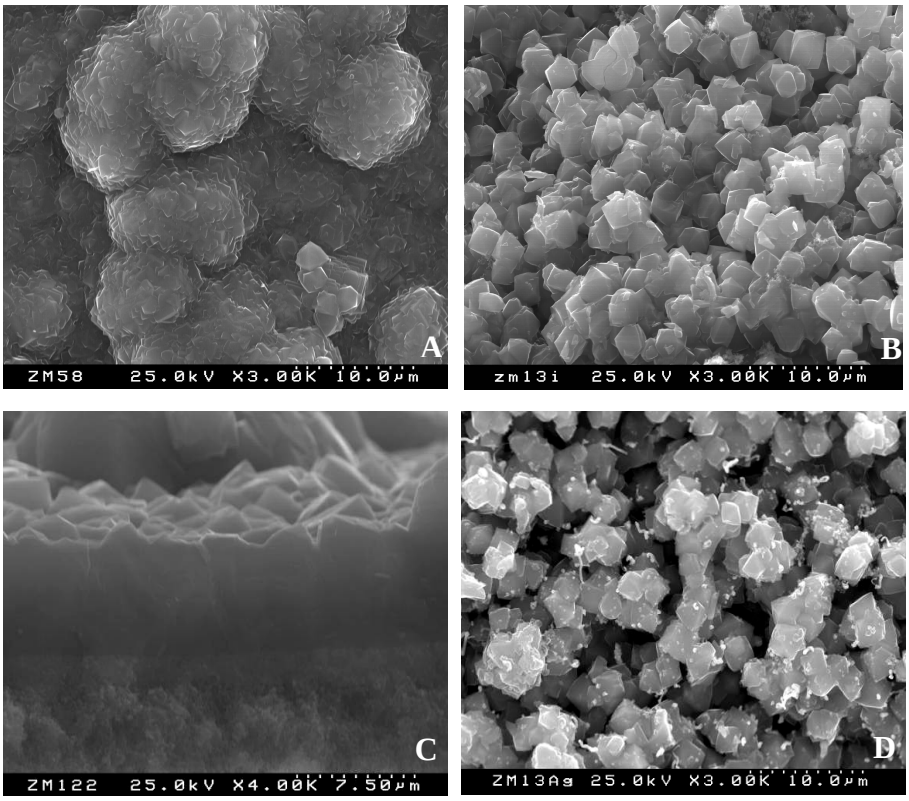

Figure 2.3 – SEM images of the top view of the zeolite layer formed using a clear solution precursor (A) or a gel (B) precursor, cross sectional view of the zeolite layer obtained after three hydrothermal synthesis cycles when using a clear solution precursor (C); top view of the selective layer of a membrane after ion-exchange with Ag^+ (D).

Clear solutions were shown to be more adequate as aluminosilicate precursors than gels, as they prevented the undesired formation of a second zeolite phase,

zeolite P (detected by XRD, data not shown). The growth of zeolite P occurs after prolonged hydrothermal exposure (more than 2 synthesis cycles) at the expense of crystals that make the zeolite film. This decreases the final membrane thickness, making it more defect prone. Zeolite P membrane is also easy to crack. The clear solution precursor led to well intergrown zeolite crystals. Figure 2.3C shows a SEM image of the cross sectional view of the supported zeolite layer obtained for the clear precursor solution; a continuous and smooth faujasite zeolite layer of ca. 7 μm can be observed. The morphology of the zeolite membrane after Ag^+ ion-exchange was also analyzed by SEM, as observed in Figure 2.3D. Ag^+ (white dots) is shown to be present as clusters, distributed across the zeolite layer.

2.4.2 Adsorption Equilibrium Isotherms

The adsorption equilibrium curves determined are shown in Figure 2.4. For Na-Y, the adsorption isotherm of N_2 was also determined for reference.

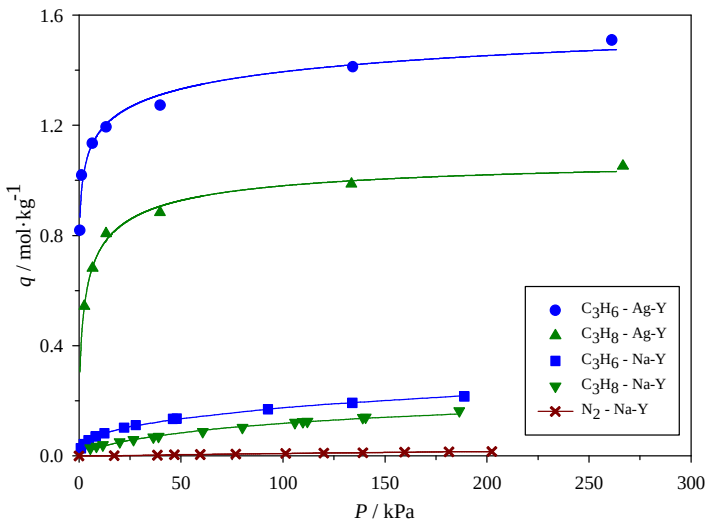

Figure 2.4 – N_2, C_3H_8 and C_3H_6 adsorption isotherms on NaY and AgY zeolite powders at 293 K; points – experimental values; lines – SIPS model fitting.

The SIPS and Henry equations (eq. (2.5) and (2.6), respectively) were used to fit the experimental adsorption data of the hydrocarbons and of N_2, respectively:

$$q = q^{\max} \frac{(bP)^{1/n}}{1+(bP)^{1/n}} \tag{2.5}$$

$$q = KP \tag{2.6}$$

where q is the surface concentration, q^{max} is the maximum surface concentration, b an affinity parameter, n the SIPS parameter and K the Henry constant. The fitting parameters are shown in Table 2.1. Figure 2.4 shows that Na-Y is selective towards C_3H_6 but its adsorption capacity for all gases is very small, particularly for N_2. The C_3H_6 / C_3H_8 adsorption selectivity of Na-Y ranges from 1.4 to 2.3 for $5 < P < 200$ kPa. For the same pressure range, Ag-Y exhibits similar adsorption selectivity (1.4 to 1.8). However, its adsorption capacity towards both hydrocarbons is much higher as compared to the Na-Y zeolite (cf.Table 2.1). The adsorption isotherms show that the Ag^+-exchanged form of the faujasite zeolite is more promising for C_3H_6/C_3H_8 separation.

Table 2.1 – Parameters for the adsorption isotherm of N_2, C_3H_6 and C_3H_8 on Na-Y and Ag-Y at 293 K.

Gas - Adsorbent	**SIPS**			**Henry**
	q^{max} **(mol·kg^{-1})**	b**(kPa^{-1})**	n	K **(mol·kg^{-1}·kPa^{-1})**
C_3H_6 - NaY	0.36	7.3×10^{-3}	2.03	-
C_3H_8 - NaY	0.29	4.1×10^{-3}	1.66	-
N_2 - NaY	-	-	-	6.33×10^{-5}
C_3H_6 – AgY	1.98	0.61	4.70	-
C_3H_8 – AgY	1.12	0.35	1.81	-

2.4.3 Permeation Experiments

Gas transport in porous membranes such as zeolites results from the contribution of different mass transport mechanisms (activated, Knudsen and molecular

diffusions and Poiseuille (viscous) flow [28-33]). For pore radius between 1 nm and 50 nm (zeolite pore size is usually close to the lower limit of this range) Knudsen diffusion is usually the predominant mass transfer mechanism [28-29, 34-36]. The molar Knudsen flux (J^K) is described by the following equation [33, 37-40]:

$$J^K = -\frac{\varepsilon}{\tau}\frac{2r_p}{3\Re T}\sqrt{\frac{8\Re T}{\pi M}}\frac{dP}{dx} \tag{2.7}$$

where M is the molar mass of the gas, T is the absolute temperature, P is the pressure, $\Re$ is the ideal gas constant, x is the distance along the direction of flow and ε, τ and r_p are the porosity, tortuosity and pore radius of the porous matrix, respectively.

Viscous flow (J^V), described by the Poiseuille equation, is present whenever there is a total pressure gradient across the porous membrane, and is characteristic of large pores (e.g., large intercrystalline defects) [37-40]:

$$J^V = -\frac{1}{\Re T}\frac{\varepsilon}{\tau}\frac{r_p^2}{8\mu}P\frac{dP}{dx} \tag{2.8}$$

where μ is the viscosity of the gas.

Surface diffusion is relevant when micropores are present and for species that adsorb significantly. The flux due to surface diffusion (J^{SD}) can be described by the following equation [28, 33]:

$$J^{SD} = -\frac{1-\varepsilon}{\tau}\rho_s D^S\frac{dq}{dx} \tag{2.9}$$

where ρ_s is the solid density, q is the surface concentration and D^S is the surface diffusion coefficient, expressed by:

$$D^S = D_C^S\Gamma \tag{2.10}$$

Where D_C^S is the corrected diffusion coefficient and Γ the thermodynamic correction factor:

$$\Gamma = \frac{\partial \ln P}{\partial \ln q} \tag{2.11}$$

When the size of the pores is similar to the size of the penetrant, molecular sieving occurs. However, the pore width of a Y zeolite is 0.74 nm [41], which is significantly higher than the kinetic diameter of all species analyzed (He – 0.26 nm, N_2 – 0.364 nm; C_3H_6 – 0.45 nm, C_3H_8 - 0.43 nm) [42]. Hence, molecular sieving should not be significant for these gases in this zeolite.

A zeolite can be characterized by performing single gas permeation experiments. For a gas which exhibits a linear adsorption isotherm (such as N_2 – cf. Figure 2.4), Γ=1 and the activated surface diffusion flux can be re-written as:

$$J^{SD} = -\frac{1-\varepsilon}{\tau}\rho_s D^S K \frac{dP}{dx} \tag{2.12}$$

where K refers to Henry's constant. In this case, the total flux results from the contribution of the Knudsen and surface diffusions and viscous flow, and a global permeance coefficient (Π_g) can be derived, expressed by equation (2.13) for steady state operation:

$$\Pi_g = \frac{J^{tot}}{P^h - P^l} = \frac{\varepsilon}{\tau}\frac{2r_p}{3\delta\Re T}\sqrt{\frac{8\Re T}{\pi M}} + \frac{1-\varepsilon}{\tau}\frac{\rho_s D^S K}{\delta} + \frac{1}{\Re T}\frac{\varepsilon}{\tau}\frac{r_p^2}{8\mu\delta}\frac{\left(P^h + P^l\right)}{2} = \alpha + \beta P_{avg} \tag{2.13}$$

where α and β are the coefficients relative to Knudsen+surface diffusion and viscous flow, respectively. It should be noted that this equation is derived integrating equations (2.7), (2.8) and (2.12) assuming slab geometry (constant integration area). The zeolite membranes used were prepared on top of cylindrical Al_2O_3 supports. Since the radius of the cylindrical support is very large compared to the selective layer thickness, the assumption of slab geometry is reasonable. The content of large defects in the membranes prepared was assessed performing N_2 permeation experiments at different feed pressures. The zeolite membrane exhibits a linear adsorption isotherm towards N_2 and parameters α and β were

determined by fitting experimental permeance values at different pressures with equation (2.13). Afterwards, the fraction of Knudsen + surface diffusion was computed at average pressure 100 kPa. A high ratio Knudsen + surface flow/total flow is a good indicator of membrane quality; a membrane is deemed promising when Knudsen+surface diffusion contribution is close to 100 %. Figure 2.5 shows the N_2 permeation results achieved for four Na-Y membranes and the corresponding parameters. Membranes M1, M2 and M3 exhibit a high fraction of Knudsen+surface flow, indicating that no large intercrystalline defects should be present in their structure.

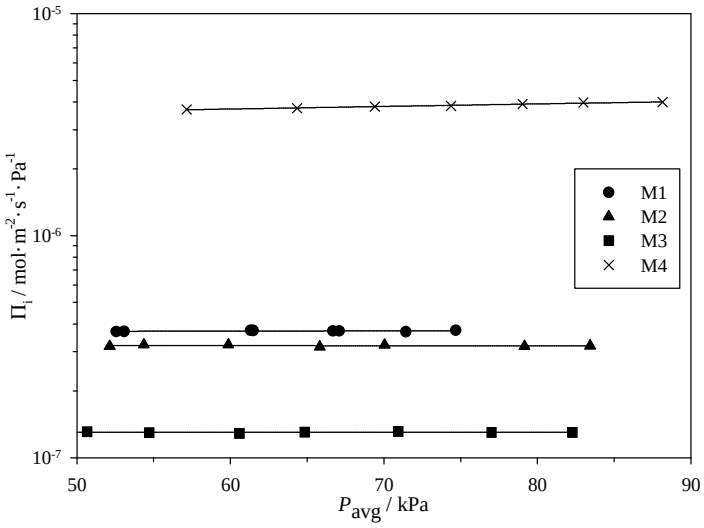

Figure 2.5 – Permeance of membranes M1 to M4 towards N_2 at 293 K, as a function of the average pressure across the membrane (symbols – experimental data; lines – linear fitting with equation (2.9)).

Table 2.2 shows that membrane M2 exhibits a Knudsen + surface diffusion contribution slightly above 100 %, which should be related to experimental errors. Membrane M4, synthesized from 2 zeolite layers, exhibits higher permeance values and a high content of large intercrystalline defects. Clearly, defect-free membranes require 3 zeolite layers. So, membranes M1, M2 and M3 were tested for He, N_2, C_3H_8 and C_3H_6 permeation at different temperatures,

before and after Ag^+ exchange.

Table 2.2 – Knudsen + surface diffusion contribution to the overall flux of N_2 on faujasite zeolite membranes.

Membrane	Zeolite Layers	α	β x P_{avg}	Knudsen + Surface Diffusion (%)
M1	3	3.66×10^{-7}	8.11×10^{-9}	97.8
M2	3	3.24×10^{-7}	-6.22×10^{-9}	101.9
M3	3	1.30×10^{-7}	2.62×10^{-10}	99.8
M4	2	3.11×10^{-6}	1.03×10^{-6}	75.1

The effect of temperature on the permeance towards a certain gas results from its combined effect on Knudsen and surface diffusion (viscous flow was shown to be negligible for membranes M1, M2 and M3). Considering an Arrehnius-type dependence for the surface diffusivity, the permeance dependence with temperature for a gas with linear isotherm (N_2) can be expressed by:

$$\Pi_g = \frac{\varepsilon}{\tau}\frac{2r_p}{3\delta\Re T}\sqrt{\frac{8\Re T}{\pi M}} + \frac{1-\varepsilon}{\tau}\frac{\rho_s D^S_{C,\infty} K_\infty}{\delta} exp\left(\frac{-\left(E_a - \left(-\Delta H\right)\right)}{RT}\right) \quad (2.14)$$

where $D^S_{C,\infty}$ is the corrected surface diffusivity at very high temperatures, E_a is the activation energy of surface diffusion, K_∞ is Henry's constant at very high temperatures and ($-\Delta H$) the heat of adsorption. For C_3H_6 and C_3H_8 (SIPS isotherm) the expression becomes:

$$\Pi_g = \frac{\varepsilon}{\tau}\frac{2r_p}{3\delta\Re T}\sqrt{\frac{8\Re T}{\pi M}} + \frac{1-\varepsilon}{\tau}\frac{\rho_s D^S_{C,\infty}}{\delta} exp\left(\frac{-E_a}{RT}\right) nq^{max} ln\left(\frac{1+\left(b_\infty exp\left(\frac{-\Delta H}{RT}\right)P^h\right)^{1/n}}{1+\left(b_\infty exp\left(\frac{-\Delta H}{RT}\right)P^l\right)^{1/n}}\right) \quad (2.15)$$

where b_∞ is the affinity parameter at very high temperatures. The temperature dependence of the Knudsen flux is the same for all gases ($\sim T^{-0.5}$) but for surface diffusion flux it is determined by the values of E_a and ($-\Delta H$), different for each gas. In general terms, the dependence of the membrane permeance towards a certain gas with temperature is known to exhibit the behaviour shown in Figure 2.6 [43-44].

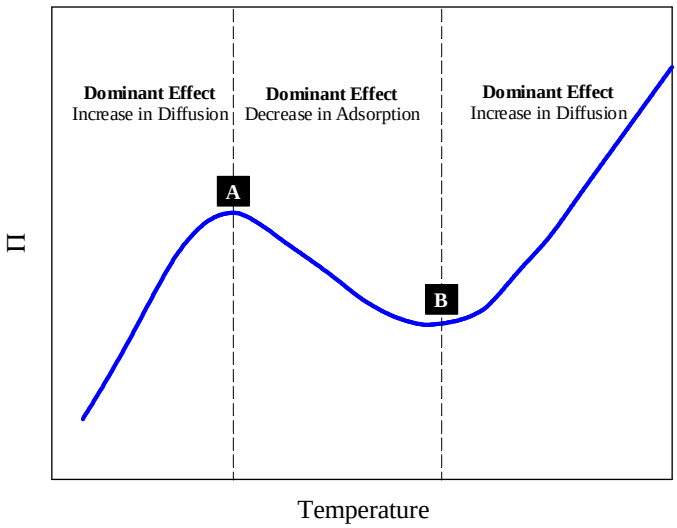

Figure 2.6 – Qualitative variation of the permeance of a gas in micropores with temperature (adapted from [44]).

As the temperature increases, the amount of adsorbed species decreases, yet their mobility is enhanced. Initially, the increase in mobility is the dominant effect and the overall effect is an increase in permeance. Eventually, desorption becomes dominant and permeance starts to decrease (point A in Figure 2.6). This trend shifts again when adsorption becomes negligible (point B). From that point on, permeance increases again due to activated diffusion in the pores. Clearly, an analysis of a Temperature Programmed Permeation (TPP) curve is a reliable way to assess the dominant transport mechanism of each gas at a certain temperature. TPP curves for N_2, He, C_3H_8 and C_3H_6 on membranes M1 and M2, before and

after functionalization with Ag^+, are plotted in Figure 2.7A and Figure 2.7B, respectively. The results of TPP for membrane M3 are not shown because the results were qualitatively similar to those of membranes M1 and M2. Figure 2.7B shows that the permeance towards He decreases slightly with temperature. He is not adsorbed by the zeolite (i.e., no contribution from surface diffusion) and the decrease of permeance with temperature (18 % for $303 < T < 435$ K) correlates well with Knudsen diffusion flux decrease ($\sim T^{-0.5}$ - cf. equation (2.7)). By applying equation (2.7) to the experimental He permeation results it was estimated the ratio porosity/tortuosity (0.1), assuming that the average pore radius of the Ag-Y zeolite membrane is roughly 0.74 nm (it is probably slightly inferior).

The permeance towards N_2 is also monotically decrescent but the reduction is more significant, which according to equation (2.14) means that there must be some surface diffusion flux (despite the low affinity of the zeolite towards N_2). Contrarily, for C_3H_8 and C_3H_6, the permeating flux initially increases with temperature. This implies that the surface diffusion flux is increasing with temperature. It is also observed that the controlling mechanism shifts from diffusion to desorption (point A in Figure 2.6). For C_3H_8, this shift occurs at 380 K (for membrane M1) and 400 K (for membrane M2). For C_3H_6, point A is above 440 K for both membranes; the exact value could not be determined because the o-rings started to deform at temperatures above 440 K. The permeance of membranes M1 and M2 towards N_2 at ~293 K is higher than the permeance towards C_3H_8 and C_3H_6. Since the adsorption affinity of the zeolite towards N_2 at that temperature is significantly smaller than the affinity towards the hydrocarbons (cf. Figure 2.4) it can be inferred that N_2 diffuses faster in the zeolite pores. For the same reason, the diffusivity of C_3H_8 is higher than the diffusivity of C_3H_6. The C_3H_6/C_3H_8 ideal selectivity is below 1 for the entire range of temperatures, being particularly low for lower temperatures. The

C_3H_6/C_3H_8 ideal selectivity in the functionalized membranes is also below 1. Figure 2.7 also shows that the permeance towards C_3H_6 and C_3H_8 decreases after functionalization ca. an order of magnitude. Since the occupancy increased markedly (cf. Figure 2.4), this decrease can be attributed to a decrease in diffusivity (due to pore constriction by Ag^+) more significant than the increase in adsorption. Another possible contributing factor is the difficulty of desorbing C_3H_6 and C_3H_8 at the permeate side of the membrane (the adsorption isotherms of C_3H_6 and C_3H_8 in AgY are very favourable).

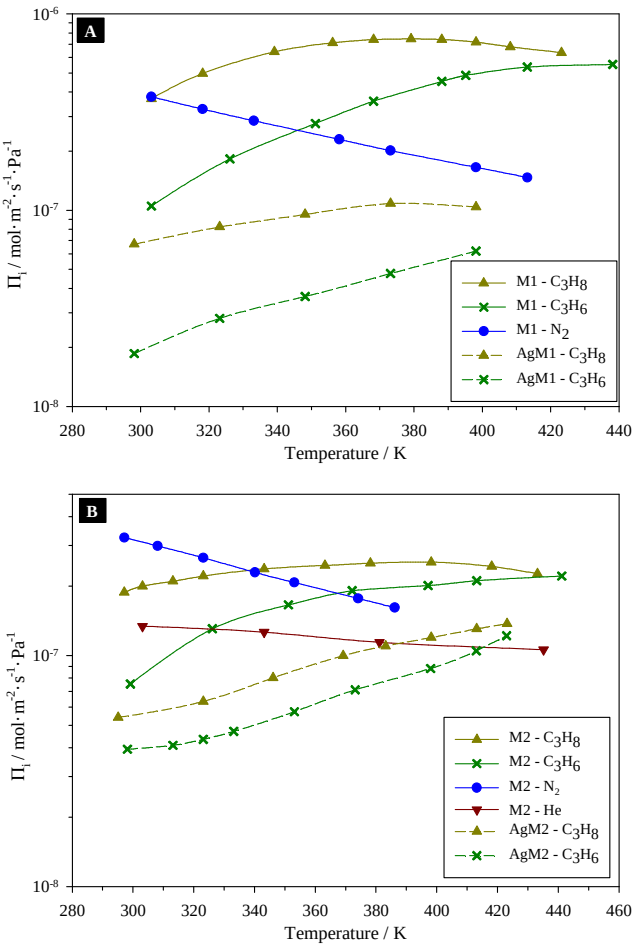

Figure 2.7 – TPP of several gases in membranes M1 (A) and M2 (B) before and after Ag functionalization (solid lines – before ion exchange; dashed lines – after ion exchange). The feed pressure was set at 120 kPa and the permeate pressure at 3 kPa.

Afterwards, bi-component experiments were performed by feeding equimolar C_3H_6/C_3H_8 streams to zeolite membranes, before and after functionalization with Ag^+. A small amount of O_2 (around 1 % molar) was added to the hydrocarbon feed stream to help prevent Ag^+ reduction, while having a negligible impact on C_3H_6/C_3H_8 separation. Figure 2.8 shows the effect of temperature on the permeance and separation factor of membrane M1 towards an equimolar C_3H_6/C_3H_8 feed, before and after Ag^+ functionalization.

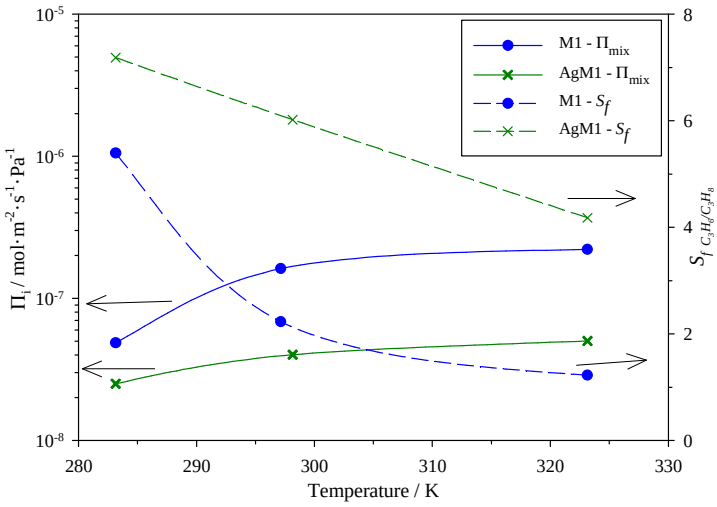

Figure 2.8 – Effect of temperature on the permeance and separation factor of membrane M1 towards an equimolar C_3H_6/C_3H_8 feed, before and after functionalization.

Table 2.3 shows the C_3H_6/C_3H_8 separation factors at three different temperatures for membranes M1, M2 and M3, before and after Ag^+ load. Membranes M1 to M3 exhibit bi-component C_3H_6/C_3H_8 selectivity (i.e., values are always above 1). The selectivity is higher at lower temperatures, where adsorption is stronger and C_3H_6 is more likely to block the adsorption of C_3H_8 (pore blocking effect). As C_3H_6 adsorbs much more in the functionalized zeolite, the separation factor is higher for functionalized membranes.

Table 2.3 – C_3H_6/C_3H_8 separation factor as a function of temperature, for membranes M1, M2 and M3, using an equimolar feed of C_3H_8 and C_3H_6.

Membrane	$S_{f\ C_3H_6/C_3H_8}$ **- Na-Y**			$S_{f\ C_3H_6/C_3H_8}$ **- Ag-Y**		
	283 K	**298 K**	**323 K**	**283 K**	**298 K**	**323 K**
M1	5.4	2.4	1.2	7.2	6.0	4.2
M2	1.4	1.3	1.2	1.9	1.7	1.8
M3	-	1.9	1.7	-	2.7	2.3

This increase in separation factor is followed by a decrease in permeance, because of the above mentioned pore aperture reduction after Ag^+ loading. At temperatures below 298 K, the Na-Y zeolite exhibits good separation results. At 283 K the separation factor is higher (increased from 2.4 to 5.4 in membrane M1) but the mixture permeance (productivity) decreases 400 %. Moreover, for future industrial applications, one should focus on ambient temperatures or slightly above. At 298 K, the improvement in C_3H_6/C_3H_8 separation factor by loading Ag^+ in faujasite zeolite membranes is significant, 2.4 to 6.0 in membrane M1 and 1.9 to 2.7 in membrane M3. Membranes M1, M2 and M3 all managed to sustain the selectivity values reported for more than one week of continuous mixture exposure.

2.4.3.1 Effect of Feed Composition

The impact of diluting with helium equimolar C_3H_6/C_3H_8 feed streams on the separation performance of the membranes was studied. Table 2.4 summarizes the results achieved. When progressively lower hydrocarbon partial pressures are used, the fraction of pores occupied by both C_3H_6 and C_3H_8 decreases. Because this decrease is more noticeable for C_3H_8 (cf. isotherms – Figure 2.4) higher C_3H_6/C_3H_8 separation factors can be achieved. Moreover, the zeolite membrane adsorption concentration of C_3H_6 adsorbs is high even at low pressures at 3 kPa

the adsorption concentration of C_3H_6 is 75 % of its value at 100 kPa (cf. Figure 2.4). Hence, it can restrict the permeation of C_3H_8, which adsorbs less, and the permeate stream becomes enriched with C_3H_6. Thus, the permeance of C_3H_6 also increases.

Table 2.4 – Effect of the composition of the feed stream on the permeance of pristine and functionalized membranes M1 and M3 towards C_3H_6 and on C_3H_6/C_3H_8 separation factor (T = 298 K, P_{feed} = 120 kPa; P_p = 1 kPa; O_2 content = 1%; composition balanced with He).

Membrane	**C_3H_6/C_3H_8 (%)**	**$\Pi_{C_3H_6}$ ($mol \cdot m^{-2} \cdot s^{-1} \cdot Pa^{-1}$)**	**$S_{f\ C_3H_6/C_3H_8}$**
AgM1	50/50	3.46×10^{-8}	6.0
AgM1	10/10	8.17×10^{-8}	8.0
AgM3	50/50	7.54×10^{-8}	2.7
AgM3	20/20	6.55×10^{-8}	3.2
AgM3	10/10	9.88×10^{-8}	4.2
AgM3	3/3	1.44×10^{-7}	5.0

Finally, the results of the zeolite membranes were compared to the best performing polymer membranes. Robeson [45] proposed that the performance of all polymer membranes is below an upper bound plot relating separation factor and permeance towards the gas of interest. These upper bound plots are widely acknowledged as the state of the art for each gas separation. In 2003, Burns and Koros devised such a plot for the C_3H_6/C_3H_8 separation [46]. The results of the Ag^+-faujasite zeolite membranes were plotted together with the results of the best performing polymer membranes. Figure 2.9 shows that Ag^+ functionalized membranes M1 and M3 surpass the upper bound plot, while their non-exchanged forms do not. The best results were achieved for the most diluted streams, yet membrane M1 also surpasses the upper bound line for undiluted equimolar C_3H_6/C_3H_8 feeds.

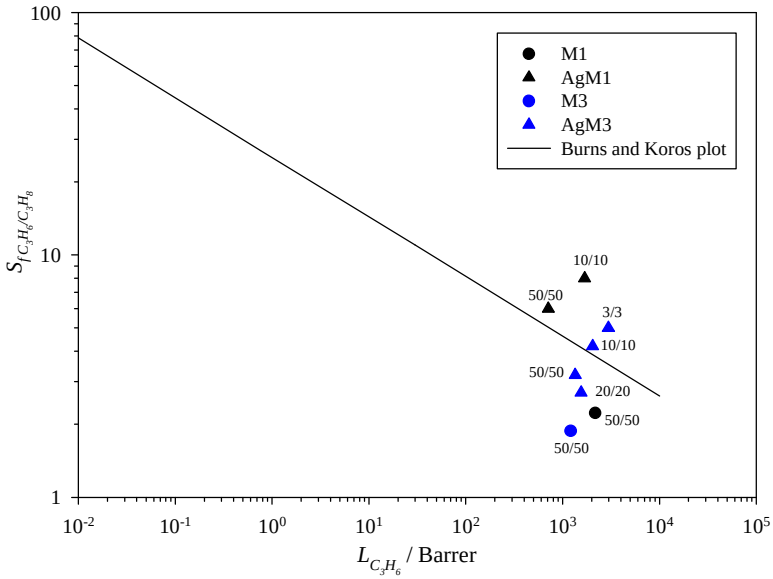

Figure 2.9 – Comparison of the mixed gas permeation results of membranes M1 and M3 with the upper bound plot derived by Burns and Koros. Next to each experimental point we can find the C_3H_6/C_3H_8 molar composition of the feed stream (%) (T=298 K; P_{feed} = 130 kPa).

2.4.4 Membrane Aging

After the permeation tests, membranes AgM1, AgM2 and AgM3 were stored in a dark environment under air atmosphere. During the following three months, the membranes became progressively darker (indicative of Ag^+ reduction to Ag^0). The membranes were tested after this three month period; a 40 % loss in C_3H_6/C_3H_8 selectivity was observed for AgM3 (from 2.7 to 1.6). It was attempted to restore the membrane performance by re-oxidizing Ag^+, following the procedure proposed by Jayaraman et al. [47]: AgM3 was heated in an oven at 523 K for three hours with a 30 mL·min^{-1} flowing stream of 13 % O_2/87 % He. After reoxidation, it acquired a yellow coloration, consistent with a partial reoxidation. Figure 2.10 depicts membrane AgM3 before and after reoxidation. AgM3 was re-tested for C_3H_6/C_3H_8 separation and although the selectivity

improved (from 1.6 to 2.0), the initial selectivity value (2.7) could not be restored.

A **B**

Figure 2.10 – Images depicting AgM3 before (A) and after (B) reoxidation.

2.5 Conclusions

Faujasite zeolite particles and membranes were hydrothermally synthesized and tested for C_3H_6/C_3H_8 separation. These particles and membranes were ion-exchanged with Ag^+ and their separation performance for C_3H_6/C_3H_8 assessed (before and after ion-exchange). The Na^+-form faujasite had low adsorption affinity towards C_3H_8 and C_3H_6, being selective towards the latter. Ag^+-exchanged faujasite samples were also selective towards C_3H_6, but had more adsorption affinity towards the hydrocarbons.

Defect-free membranes were achieved after 3 synthesis cycles. The C_3H_6/C_3H_8 permselectivity was below one for both the Na^+ and Ag^+-forms of the zeolite because C_3H_8 diffused faster on the zeolite membrane. In bi-component experiments, C_3H_6 (the more adsorbed species) blocked the permeation of C_3H_8 and C_3H_6/C_3H_8 separation factor of 6 were achieved at 298 K for equimolar

feeds. The use of lower temperatures increased the separation factors but the productivity decreased. When C_3H_6/C_3H_8 feeds were diluted, higher separation factors and higher C_3H_6 permeance values were obtained. The performance of Ag^+-faujasite membranes deteriorated over time, as Ag^+ reduced. Following reoxidation, a partial recovery in performance was observed.

2.6 Nomenclature

Variables	Definition	Units
A	Permeation area	m^{-2}
b	SIPS equation coefficient	Pa^{-1}
b_∞	SIPS equation coefficient at very high temperatures	Pa^{-1}
D^S	Surface diffusivity	$m^{-2} \cdot s^{-1}$
D_C^S	Corrected surface diffusivity	$m^{-2} \cdot s^{-1}$
$D_{C,\infty}^S$	Corrected surface diffusivity at very high temperatures	$m^{-2} \cdot s^{-1}$
E_a	Diffusion activation energy	$J \cdot mol^{-1}$
F	Molar flow rate	$mol \cdot s^{-1}$
H	Heat of adsorption	$J \cdot mol^{-1}$
J^K	Knudsen diffusion flux	$mol \cdot m^{-2} \cdot s^{-1}$
J^V	Viscous diffusion flux	$mol \cdot m^{-2} \cdot s^{-1}$
J^{SD}	Surface diffusion flux	$mol \cdot m^{-2} \cdot s^{-1}$
K	Henry's constant	$mol \cdot kg^{-1} \cdot Pa^{-1}$
K_∞	Henry's constant at high temperatures	$mol \cdot kg^{-1} \cdot Pa^{-1}$
L	Permeability	$mol \cdot m \cdot m^{-2} \cdot s^{-1} \cdot Pa^{-1}$
M	Membrane	-
n	SIPS equation parameter	-

p	Partial pressure	Pa
P_{avg}	Average Pressure	Pa
P	Total pressure	Pa
q	Surface Concentration	$mol \cdot kg^{-1}$
q^{max}	Maximum surface concentration	$mol \cdot kg^{-1}$
r_p	Pore radius	m
S	Permselectivity	-
S_f	Separation factor	-
T	Temperature	K
x	Molar fraction retentate	-
y	Molar fraction permeate	-

Greek Symbols	**Definition**	**Units**
α	(Knudsen+surface) diffusion fraction	-
β	Viscous flow fraction	-
μ	Viscosity	$kg \cdot m^{-1} \cdot s^{-1}$
ε	Porosity	-
Γ	Thermodynamic correction factor	-
τ	Tortuosity	-
δ	Membrane thickness	m
Π	Permeance	$mol \cdot m^{-2} \cdot s^{-1} \cdot Pa^{-1}$
ρ_s	Solid Density	$mol \cdot kg^{-3}$

2.7 Acknowledgments

Miguel Teixeira is grateful to the Portuguese Foundation for Science and Technology (FCT) for his doctoral grant (reference SFRH/BD/24768/2005). The authors also acknowledge financing from FCT through the projects POCTI/EQU/59344/2004 and POCTI/EQU/59345/2004.

2.8 References

[1] K. Nymeijer, T. Visser, R. Assen, M. Wessling, Super selective membranes in gas-liquid membrane contactors for olefin/paraffin separation, J Membrane Sci, 232 (2004) 107-114.
[2] S. Sridhar, A.A. Khan, Simulation studies for the separation of propylene and propane by ethylcellulose membrane, J Membrane Sci, 159 (1999) 209-219.
[3] C.L. Yu, Q.J. Ge, H.Y. Xu, W.Z. Li, Effects of Ce addition on the Pt-Sn/γ-Al_2O_3 catalyst for propane dehydrogenation to propylene, Applied Catalysis a-General, 315 (2006) 58-67.
[4] M. Teramoto, S. Shimizu, H. Matsuyama, N. Matsumiya, Ethylene/ethane separation and concentration by hollow fiber facilitated transport membrane module with permeation of silver nitrate solution, Sep Purif Technol, 44 (2005) 19-29.
[5] T. Yamaguchi, C. Baertsch, C.A. Koval, R.D. Noble, C.N. Bowman, Olefin separation using silver impregnated ion-exchange membranes and silver salt/polymer blend membranes, J Membrane Sci, 117 (1996) 151-161.
[6] S. Hess, C. Staudt-Bickel, R.N. Lichtenthaler, Propene/propane separation with copolyimide membranes containing silver ions, J Membrane Sci, 275 (2006) 52-60.
[7] L. Liu, A. Chakma, X.S. Feng, Sorption, diffusion, and permeation of light olefins in poly(ether block amide) membranes, Chemical Engineering Science, 61 (2006) 6142-6153.
[8] J.H. Kim, J. Won, Y.S. Kang, Olefin-induced dissolution of silver salts physically dispersed in inert polymers and their application to olefin/paraffin separation, J Membrane Sci, 241 (2004) 403-407.
[9] A. Sungpet, J.D. Way, C.A. Koval, M.E. Eberhart, Silver doped Nafion-poly(pyrrole) membranes for facilitated permeation of liquid-phase olefins, J Membrane Sci, 189 (2001) 271-279.

[10] O.I. Eriksen, I.B. Vik, I.M. Dahl, M.L. Posey, Separation of ethene from ethane with permeators based on silver ion-exchanged nafion hollow fibers., Abstr Pap Am Chem S, 214 (1997) 61.
[11] W.S. Ho, D.C. Dalrymple, Facilitated Transport of Olefins in Ag+-Containing Polymer Membranes, J Membrane Sci, 91 (1994) 13-25.
[12] S.W. Kang, J.H. Kim, K. Char, J. Won, Y.S. Kang, Nanocomposite silver polymer electrolytes as facilitated olefin transport membranes, J Membrane Sci, 285 (2006) 102-107.
[13] A. Takahashi, R.T. Yang, C.L. Munson, D. Chinn, Cu(I)-Y-zeolite as a superior adsorbent for diene/olefin separation, Langmuir, 17 (2001) 8405-8413.
[14] R.T. Yang, Adsorbents: fundamentals and applications, Wiley-Interscience, Hoboken, N.J.; [Great Britain], 2003.
[15] M.A. Granato, T.J.H. Vlugt, A.E. Rodrigues, Molecular simulation of propane-propylene binary adsorption equilibrium in zeolite 4A, Ind Eng Chem Res, 46 (2007) 321-328.
[16] D.H. Olson, X.B. Yang, M.A. Camblor, ITQ-12: A zeolite having temperature dependent adsorption selectivity and potential for propene separation, J Phys Chem B, 108 (2004) 11044-11048.
[17] W. Zhu, F. Kapteijn, J.A. Moulijn, Shape selectivity in the adsorption of propane/propene on the all-silica DD3R, Chem Commun, (1999) 2453-2454.
[18] H. Jarvelin, J.R. Fair, Adsorptive Separation of Propylene Propane Mixtures, Ind Eng Chem Res, 32 (1993) 2201-2207.
[19] I. Tiscornia, S. Irusta, P. Pradanos, C. Tellez, J. Coronas, J. Santamaria, Preparation and characterization of titanosilicate Ag-ETS-10 for propylene and propane adsorption, J Phys Chem C, 111 (2007) 4702-4709.
[20] K.A. Stoitsas, A. Gotzias, E.S. Kikkinides, T.A. Steriotis, N.K. Kanellopoulos, M. Stoukides, V.T. Zaspalis, Porous ceramic membranes for propane-propylene separation via the pi-complexation mechanism: unsupported systems, Micropor Mesopor Mat, 78 (2005) 235-243.
[21] B.N. Nair, K. Keizer, W.J. Elferink, M.J. Gilde, H. Verweij, A.J. Burggraaf, Synthesis, characterisation and gas permeation studies on microporous silica and alumina-silica membranes for separation of propane and propylene, J Membrane Sci, 116 (1996) 161-169.
[22] V. Nikolakis, G. Xomeritakis, A. Abibi, M. Dickson, M. Tsapatsis, D.G. Vlachos, Growth of a faujasite-type zeolite membrane and its application in the separation of saturated/unsaturated hydrocarbon mixtures, J Membrane Sci, 184 (2001) 209-219.
[23] I.G. Giannakopoulos, V. Nikolakis, Separation of propylene/propane mixtures using faujasite-type zeolite membranes, Ind Eng Chem Res, 44 (2005) 226-230.
[24] J.W. Chang, T.R. Marrero, H.K. Yasuda, Continuous process for propylene/propane separation by use of silver nitrate carrier and zirconia porous membrane, J Membrane Sci, 205 (2002) 91-102.

[25] J. Padin, S.U. Rege, R.T. Yang, L.S. Cheng, Molecular sieve sorbents for kinetic separation of propane/propylene, Chemical Engineering Science, 55 (2000) 4525-4535.
[26] H.E. Robson, Verified syntheses of zeolitic materials, 2nd rev. ed. ed., Elsevier, Amsterdam ; London, 2001.
[27] P.A. Jacobs, J.B. Uytterhoeven, Some Unusual Properties of Activated and Reduced Agnaa Zeolites, J Chem Soc Farad T 1, 75 (1979) 56-64.
[28] R.S.A. de Lange, K. Keizer, A.J. Burggraaf, Analysis and theory of gas transport in microporous sol-gel derived ceramic membranes, Journal of Membrane Science, 104 (1995) 81-100.
[29] M.B. Rao, S. Sircar, Performance and pore characterization of nanoporous carbon membranes for gas separation, Journal of Membrane Science, 110 (1996) 109-118.
[30] R. Krishna, J.A. Wesselingh, The Maxwell-Stefan approach to mass transfer, Chem Eng Sci, 52 (1997) 861-911.
[31] E.U. Schlunder, J. Yang, A. Seidel-Morgenstern, Competitive diffusion and adsorption in Vycor glass membranes - A lumped parameter approach, Catal Today, 118 (2006) 113-120.
[32] A.J. Burggraaf, Single gas permeation of thin zeolite (MFI) membranes: theory and analysis of experimental observations, Journal of Membrane Science, 155 (1999) 45-65.
[33] A. Tuchlenski, P. Uchytil, A. Seidel-Morgenstern, An experimental study of combined gas phase and surface diffusion in porous glass, Journal of Membrane Science, 140 (1998) 165-184.
[34] J.C. Jansen, K. Friess, E. Drioli, Organic vapour transport in glassy perfluoropolymer membranes: A simple semi-quantitative approach to analyze clustering phenomena by time lag measurements, Journal of Membrane Science, 367 (2011) 141-151.
[35] B.J. Hinds, N. Chopra, T. Rantell, R. Andrews, V. Gavalas, L.G. Bachas, Aligned multiwalled carbon nanotube membranes, Science, 303 (2004) 62-65.
[36] J. Gilron, A. Soffer, Knudsen diffusion in microporous carbon membranes with molecular sieving character, Journal of Membrane Science, 209 (2002) 339-352.
[37] P. Uchytil, O. Schramm, A. Seidel-Morgenstern, Influence of the transport direction on gas permeation in two-layer ceramic membranes, Journal of Membrane Science, 170 (2000) 215-224.
[38] J.W. Veldsink, G.F. Versteeg, W.P.M. van Swaaij, An experimental study of diffusion and convection of multicomponent gases through catalytic and non-catalytic membranes, Journal of Membrane Science, 92 (1994) 275-291.
[39] K. Keizer, R.J.R. Uhlhorn, R.J. Van vuren, A.J. Burggraaf, Gas separation mechanisms in microporous modified [gamma]-al2o3 membranes, Journal of Membrane Science, 39 (1988) 285-300.

[40] S. Thomas, R. Schäfer, J. Caro, A. Seidel-Morgenstern, Investigation of mass transfer through inorganic membranes with several layers, Catal Today, 67 (2001) 205-216.
[41] P. Payra, P.K. Dutta, Zeolites: A Primer, in: S.M. Auerbach, K.A. Carrado, P.K. Dutta (Eds.) Handbook of Zeolite Science and Technology, CRC Press, 2003, pp. 1-19.
[42] D.W. Breck, Zeolite Molecular Sieves, Krieger Publishing Company, 1974.
[43] W.J.W. Bakker, L.J.P. vandenBroeke, F. Kapteijn, J.A. Moulijn, Temperature dependence of one-component permeation through a silicalite-1 membrane, Aiche Journal, 43 (1997) 2203-2214.
[44] M.P. Bernal, J. Coronas, M. Menendez, J. Santamaria, Characterization of zeolite membranes by temperature programmed permeation and step desorption, J Membrane Sci, 195 (2002) 125-138.
[45] L.M. Robeson, Correlation of Separation Factor Versus Permeability for Polymeric Membranes, J Membrane Sci, 62 (1991) 165-185.
[46] R.L. Burns, W.J. Koros, Defining the challenges for C_3H_6/C_3H_8 separation using polymeric membranes, J Membrane Sci, 211 (2003) 299-309.
[47] A. Jayaraman, R.T. Yang, C.L. Munson, D. Chinn, Deactivation of pi-complexation adsorbents by hydrogen and rejuvenation by oxidation, Ind Eng Chem Res, 40 (2001) 4370-4376.

PART III:

CARBON MOLECULAR SIEVE MEMBRANES

Chapter 3: **Composite phenolic resin-based carbon molecular sieve membranes for gas separation**

(Teixeira, M., Campo, M., Tanaka, D., Llosa, M., Magen, C., Mendes, A., Carbon, In Press, Accepted Manuscript, Available online 12 June 2011)

3.1 Abstract

Composite carbon molecular sieve membranes (c-CMSM) were prepared from phenolic resin loaded with boehmite by a single dipping-drying-pyrolysis step. The composite membrane was analyzed by SEM, HR-TEM, XRD, TG, mercury porosimetry, CO_2 adsorption and permeation experiments. It was produced a 2 μm thick composite uniform layer on top of a α-Al_2O_3 support. The composite top layer exhibited nanowires of Al_2O_3 1-2 nm thick and 10-30 nm long well dispersed in a microporous carbon matrix. The micropores network accounted for 63 % of the total pore volume (DR isotherm). The c-CMSM exhibited ideal O_2/N_2 and C_3H_6/C_3H_8 permselectivities of 5 and 15, respectively. The performance of the c-CMSM for pair C_3H_6/C_3H_8 was above the upper bound curve for polymeric membranes, making it a promising vehicle for olefin purification.

3.2 Introduction

The first use of carbon membranes for gas separation can be traced back to the early 1970's, when Ash *et al.* [1-2] compressed nonporous graphited carbon into a plug, named a carbon membrane. However, the interest in carbon membranes only rose after Koresh and Suffer [3-4] reported in the 1980's the synthesis of crack free molecular sieving hollow fiber carbon membranes. At the same time,

polymer membranes, which had been widely used in many industrial applications because of their reproducibility and reasonable performance, reached a limit for their permeability/selectivity trade-off. Since then, carbon molecular sieve membranes (CMSM) have been seen as a promising alternative for some applications, because of their higher permeability and selectivity combined with greater thermal and chemical stability [5-6].

Carbon membranes result from the thermo degradation of a polymer precursor. As polymer degrades the pore network of the CMSM is created, consisting of relatively wide openings (larger pores) with narrow constrictions (smaller pores) [5]. The smaller micropores are responsible for the sieving properties of the carbon membrane, while the larger micropores assure that there is a high flux of the penetrants [6]. Moreover, carbon membranes present a tunable pore size distribution (PSD); the pore network of CMSM can be desirably tailored to suit a certain application by optimizing pyrolysis conditions such as heating rate, end temperatures, soaking times, gas atmosphere or even combining several pre- or post-pyrolysis treatments.

Up to now, many polymer precursors have been extensively studied, namely polyimide [7-9], phenolic resin [10-11], polyfurfuryl alcohol [12-13] and cellulose [14-15]. Phenolic resin is a particularly desirable precursor because it is a low cost and high carbon yield polymer [16-17]. Despite the great progress in the field of CMSM, the permeation and selectivity of the membranes have to be improved. To tackle this issue, new composite materials have been developed. Thus far, it has been reported that the performance of CMSM improves upon introducing metals [18-21], silica particles [22-23] and zeolites [24-26] in polymer precursors.

This work proposes the incorporation of relatively low cost ceramic nanoparticles of boehmite in phenolic resin to originate a defect-free and highly permeable composite carbon membrane (c-CMSM) in a single dipping-drying-carbonization

step over a ceramic porous support. Previous experiments using pure resin resulted in an uneven coating layer that penetrated into the membrane support, originating a supported membrane with very low permeability and selectivity. Dipping was performed by vacuum assisted dip coating, where the precursor solution penetrates into the openings beneath the surface of the support. This leads to thinner selective layers much less prone to cracks than traditional methods such as slip casting [27]. During the carbonization step the polymer decomposed giving place to the carbon matrix with dispersed Al_2O_3 nanofillers derived from the dehydration of the boehmite nanoparticles.

Dry films of the composite top layer were prepared and a structural and morphological characterization of the material was performed by TG, XRD, SEM, HRTEM, mercury porosimetry and subcritical CO_2 adsorption. The c-CMSM was evaluated by gas permeation. The permeability towards several gas species (He, CO_2, O_2, N_2, C_3H_6, C_3H_8) was determined, as well as the ideal selectivities for separations of industrial relevance. The performance of the membrane was compared to the state of the art of polymeric membranes.

3.3 Experimental

3.3.1 Materials

A resol phenolic resin (supplied by Euroresinas – Industrias Químicas, S.A.) was used as precursor. To avoid polymerization, the industrial resin was diluted in NMP (*N*-Methyl-2-pyrrolidone). Boehmite nanoparticles were dispersed in diluted solutions of phenolic resin to prepare all the coating solutions used. Figure 3.1 shows the particle size distribution of the dispersion of boehmite nanoparticles (planar geometry). The chemicals used were supplied by Acros Organics (*N*-Methyl-2-pyrrolidone, for analysis) and Kawaken Fine Chemicals Co., Ltd (10 % Boehmite solution, particle size 8-20 nm). The permanent gases

used in this work were supplied by Air Liquide (99.999 % pure). C_3H_8 and C_3H_6 were supplied by Praxair (99.5 % pure).

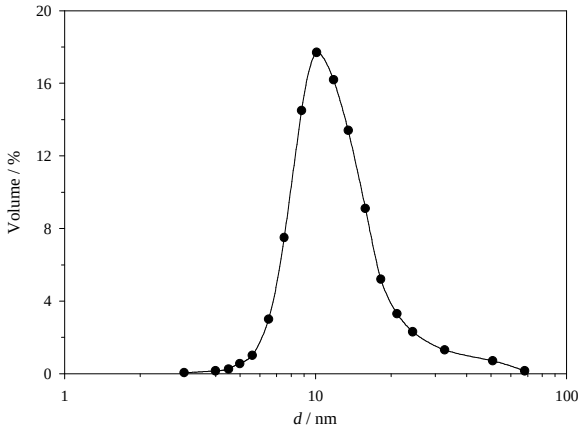

Figure 3.1 – Particle size distribution of the 10 wt.% boehmite dispersion.

3.3.2 Preparation of the Composite Precursor

Carbon membranes were prepared over 10 mm diameter, 70 mm length α-Al_2O_3 supports (200 nm average pore size – supplied by Inopor). The ends of the α-Al_2O_3 supports were attached to nonporous Al_2O_3 tubes (Omega Engineering Limited) and sealed with a glass sealant (Nippon Electric Glass GA-13N/325) at 1150 ºC, leaving an effective length for dip-coating of approximately 50 mm. Supported membranes were obtained by vacuum-assisted dip coating of the composite solution (12.5 wt.% of resin, 0.5 wt.% of boehmite in NMP) over α-Al_2O_3 support tubes. The remaining precursor solution was placed in a teflon dish to make unsupported composite films (needed for morphological characterization and adsorption experiments). Both supported and unsupported membranes were dried in an oven at 40 ºC for two hours to assure that the solvent was released from the composite films in a controlled manner, thus avoiding defects or crack formation. Afterwards, the membranes were left at 90 ºC overnight. Figure 3.2 summarizes the preparation steps of the supported

c-CMSM. The unsupported films were either crushed into small flakes or milled prior to being used in morphological characterization.

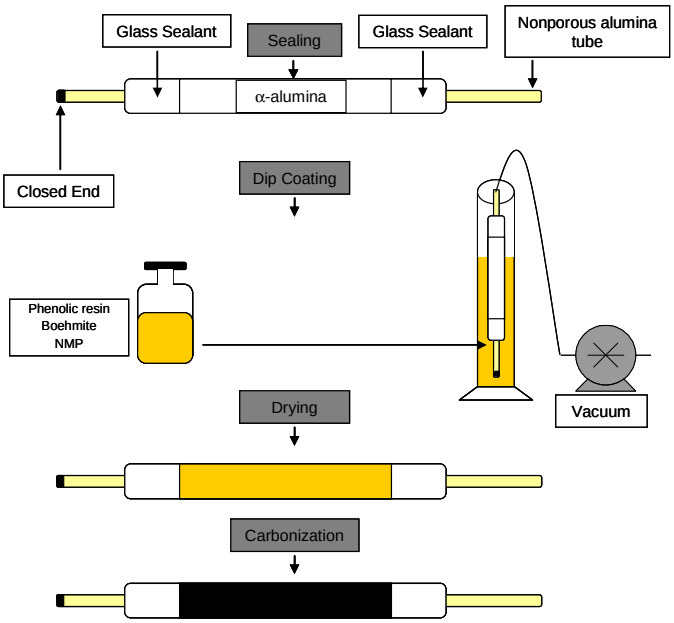

Figure 3.2 – Sketch of the preparation steps of the c-CMSM.

3.3.3 Pyrolysis

After the drying step, the supported/unsupported membranes were put on top of a stainless steel porous grid, which was placed in a quartz tube (80 mm diameter and 1.5 m in length) inside a tubular Termolab TH horizontal furnace. The temperature of the furnace was controlled by means of 3 separate heating elements (one in the center of the furnace and two on the side). Temperature homogeneity inside the oven was achieved by setting different PID heating control parameters in the three elements. The maximum temperature gradient across the tube during pyrolysis was ca. 1 ºC [14]. Before carbonization, a 1.5 $L \cdot min^{-1}$ stream of N_2 was allowed to flow inside the quartz tube for 3 hours, to remove all traces of O_2. Carbonization was performed under N_2 atmosphere, with a heating rate of 1 $ºC \cdot min^{-1}$ up to 550 ºC and a soaking time of 2 hours at this

final temperature. The literature refers carbonization temperatures for phenolic resins between 500 °C and 1000 ºC and more often between 500 °C and 700 ºC [6]. At higher temperatures the carbon atoms at the surface become more stable, less prone to O_2 chemisorption and, thus, less vulnerable to aging effects [28]. However, membranes become mechanically weaker and this compromises their integrity. For this reason, the carbonization temperature was set to 550 ºC. The slow heating rate (1 ºC·min^{-1}) used helps also to prevent membrane crack formation.

3.3.4 Morphological and Structural Characterization

3.3.4.1 Thermogravimetric analyses (TGA)

Thermogravimetric analyses were carried in a Netzsch TG 209 F1 Iris thermogravimetric balance (resolution 0.1 μg). It was analyzed the industrial phenolic resin, a 10 wt.% boehmite dispersion in water and a resin+boehmite dry film. The boehmite dispersion and the resin+boehmite film were dried overnight at 90 ºC to remove most of the solvent. Characteristic curves under N_2 were determined from 20 to 900 ºC with a heating rate of 10 ºC·min^{-1}. Proximate analysis was conducted to determine the amount of fixed carbon and Al_2O_3, following a protocol reported elsewhere [14, 29]. It consists of an initial temperature rise up to 110 ºC to remove all humidity, followed by a rise up to 950 ºC under N_2 to remove volatiles, and a final burning step at 950 ºC under O_2 atmosphere.

3.3.4.2 X-ray and microscopic analyses

X-ray diffraction (XRD) microanalyses were performed on crushed composite films to assess the crystallinity of the structure. Scanning electron microscopy

(SEM) was used to analyze the cross section of the carbonized membranes and determine the thickness of the composite layer. Energy dispersive X-ray spectroscopy (EDS) was conducted to attain a qualitative elemental composition of the membranes. EDS/SEM was performed in a FEI Quanta 400 FEG/EDAX Genesis X4M with 1.2 nm resolution and XRD analyses in a PAN'Alytical X'Pert Pro, radiation CuKα, detector X'Celerator, secondary monochromator.

High resolution transmission electron microscopy (HRTEM) was performed on milled dry films in a FEI Titan Cubed microscope equipped operated at 300 kV. This instrument is equipped with an image aberration corrector that provides 0.8 Å resolution. This technique showed the dispersion of the Al_2O_3 nanoparticles embebbed in the membrane.

3.3.4.3 Pore Size Characterization

To characterize the meso and macroporosity of the carbon material mercury intrusion porosimetry was performed in a QuantaChrome Poremaster 60. The microporosity of the material was assessed from the CO_2 adsorption isotherm at 273 K, determined in a Rubotherm® magnetic suspension balance ($\pm 10^{-5}$ mg precision) as described elsewhere [30].

3.3.5 Permeation Experiments

Permeability (L_i) characterizes the membrane concerning the permeating transport of a given gas species and it was obtained as follows:

$$L_i = F_i \frac{\delta}{\Delta p_i} \tag{3.1}$$

where i refers to a gas species, F is the permeating flux, Δp is the partial pressure difference between the retentate and permeate and δ is the membrane thickness (determined by SEM). The permeability was expressed in barrer, which equals to

3.36×10^{-16} $mol \cdot m \cdot m^{-2} \cdot s^{-1} \cdot Pa^{-1}$. The ideal selectivity or permselectivity (*S*) expressed the ratio of the permeability of two components in pure gas streams (*i* and *j*):

$$S = \frac{L_i}{L_j} \tag{3.2}$$

Monocomponent permeabilities were determined in a shell and tube membrane apparatus as sketched in Figure 3.3..

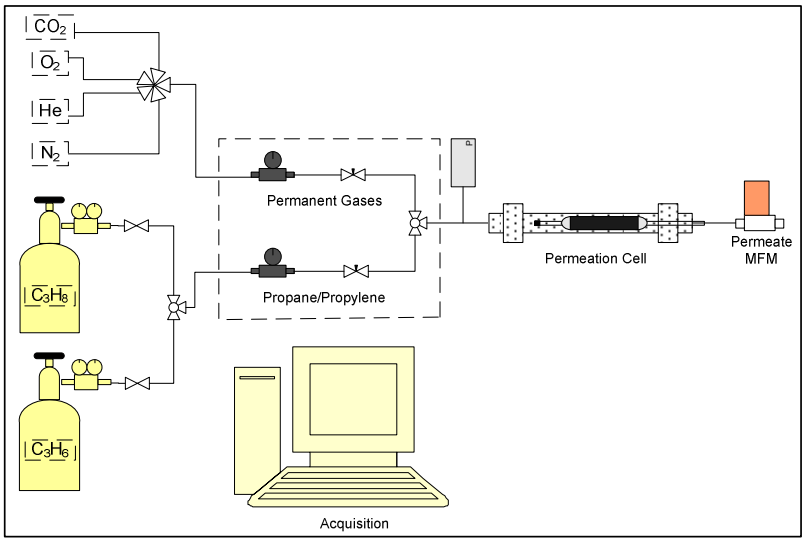

Figure 3.3 – Scheme of the experimental setup used for the gas permeation experiments.

A three-way valve controlled whether a hydrocarbon or a permanent gas is fed, while a 5-way valve determined the permanent gas to feed. The selected gas was introduced at the shell side and permeated through the membrane at a flow rate determined by one of three mass flow meters (El-Flow Bronkhorst, ranges: 0-1, 0-10 and 0-100 $mL_{NPT} \cdot min^{-1}$). Furthermore, a pressure controller (Horiba Stec, model UR-7340) was used to maintain the permeation cell at 100-400 kPa relative pressure, while the permeate side was at atmospheric pressure.

3.4 Results

3.4.1 Thermogravimetric analyses

Thermogravimetric analyses were performed on the phenolic resin, on the aqueous dispersion of boehmite nanoparticles (previously dried to remove most water) and on the boehmite+resin dry film. TG graphs and correspondent mass derivative curves for the phenolic resin and the dried aqueous boehmite dispersion are seen in Figure 3.4A-B.

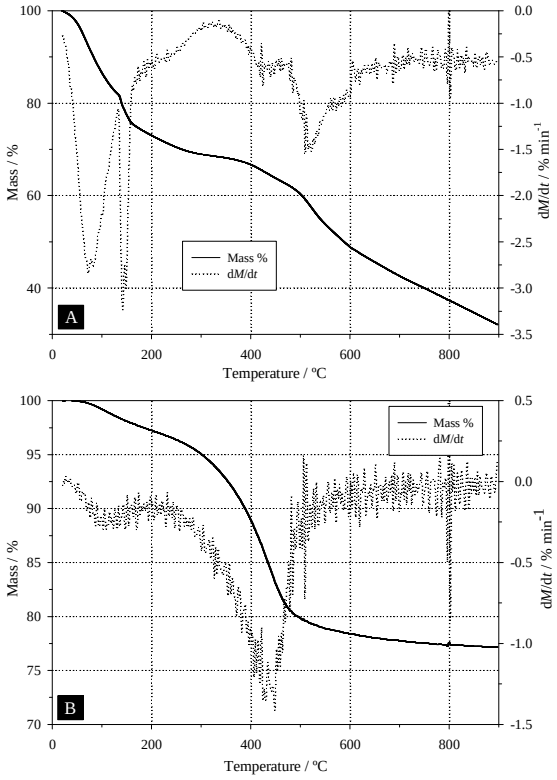

Figure 3.4 – Characteristic curves of the phenolic resin (A) and bohemite dispersion (B).

The release of volatiles from the resin takes place predominantly at 80 ºC and 150 ºC and the degradation of the polymer occurs between 470 ºC and 600 ºC. On the other hand, most of mass loss of the boehmite dispersion occurs from 300 ºC

to 500 ºC. This mass loss is attributed to the dehydroxylation of boehmite yielding Al_2O_3. After 500 ºC the mass loss is very small and can be attributed to the sintering of Al_2O_3.

An example of a boehmite+resin film TGA graph is shown in Figure 3.5. A wide peak in the mass derivative curve is observed between 375 and 600 ºC.

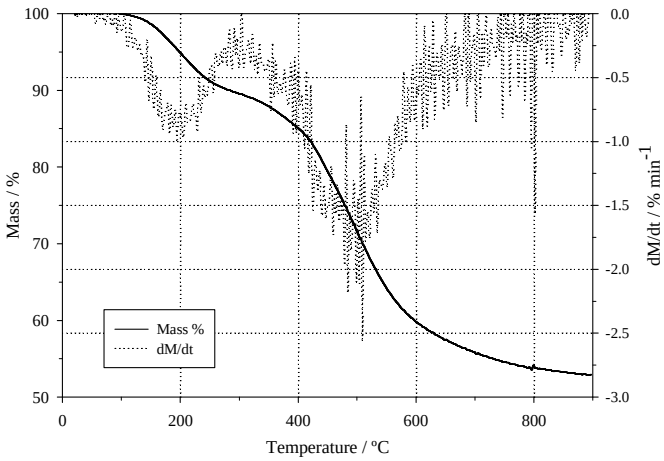

Figure 3.5 – TGA plot and correspondent derivate curve for a boehmite+resin film containing 12.5 wt.% of resin and 0.5 wt.% of boehmite (wet basis).

This peak results from the superposition of the peak related to the degradation of the polymer and the peak related to the transformation of boehmite to Al_2O_3. Proximate analysis was also performed to determine humidity, volatiles, fixed carbon and ash content. In Figure 3.6 it is plotted the mass and temperature histories. Table 3.1 offers a summary of the results obtained. It was concluded that the boehmite + resin film exhibits a high carbon yield (around 47.5 wt.% in dry basis) and Al_2O_3 content (ash) of 6.5 wt.%. The Al_2O_3 content in the final carbon film was 12 wt %.

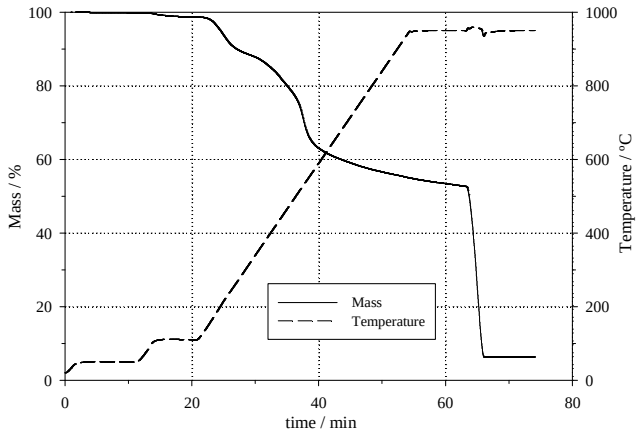

Figure 3.6 – Proximate analysis of a boehmite+resin film.

Table 3.1 – Mass composition of the composite boehmite + resin film, before and after carbonization.

Precursor (wt.%)				Carbon Film (wt.%)	
Humidity	Volatiles	Carbon	Ash	Carbon	Al_2O_3
1.4	45.9	46.4	6.4	88.0	12.0

3.4.2 X-ray and microscopic analyses

The crystallinity of the sample was analyzed by XRD. Figure 3.7 shows the XRD spectra obtained.

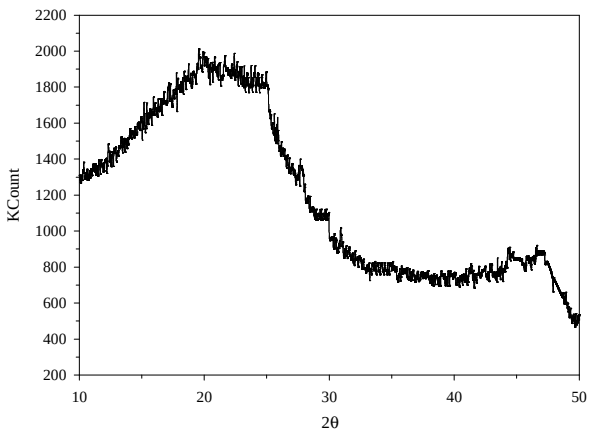

Figure 3.7 – XRD diffraction pattern for the boehmite + resin film sample.

Very wide peaks (2θ≈20º and ≈45º), characteristic of amorphous carbon, were observed. The d-spacing (d_{002}) value, calculated from Bragg's equation, was 0.447 nm. No crystalline peaks referring to Al_2O_3 could be detected.The morphology of the sample was observed by SEM. Figure 3.8 shows that a 2 μm thick carbon membrane was uniformly formed on top of the α-Al_2O_3 support tube.

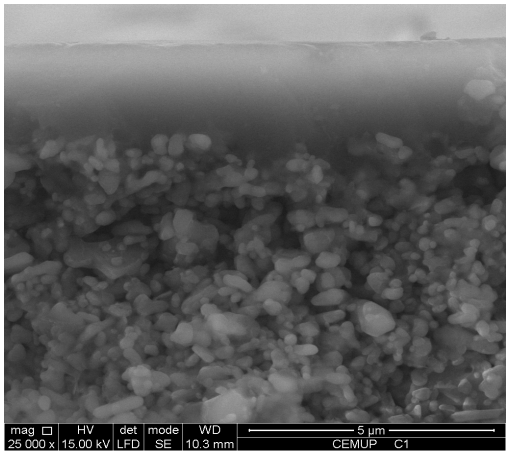

Figure 3.8 – SEM picture of a cross sectional region of a CMS.

The synthesis procedure was replicated and the prepared membranes had approximately the same thickness. EDS analysis (not shown) revealed a uniform carbon and Al_2O_3 composition along the layer thickness.

To better understand the morphology of the composite layer, HRTEM images were obtained (cf. Figure 3.9). Figure 3.9A shows that the membrane is composed of amorphous carbon flakes filled with small particles, few of them rounded, most of them fibers (1-2 nm wide and 10-30 nm long). Analysis of HRTEM images demonstrates that the fibers are crystalline and present the lattice fringes of Al_2O_3. For instance, in the example shown in Figure 3.9B, the Al_2O_3 crystal is oriented along the (111) plane and the main periodicities of 1.45 Å correspond to set of {220} planes.

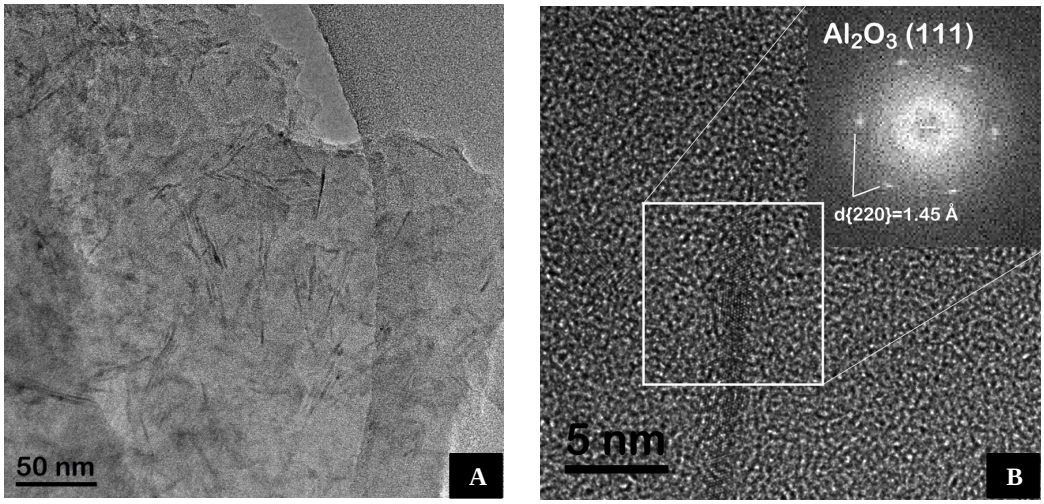

Figure 3.9 – TEM pictures of the composite unsupported membranes. (A) Low magnification view. (B) HRTEM image of one of the Al_2O_3 fibers, the inset depicts the digital diffractogram of the fiber showing the periodicities associated to the lattice fringes of Al_2O_3.

3.4.3 Porosity Assessment

The skeleton density of the c-CMSM was determined by He pycnometry in a Rubotherm® magnetic suspension balance.

$$\rho_s = \frac{m_s}{V_s} \tag{3.3}$$

To assess the macro and mesoporosity of the material, mercury intrusion porosimetry was performed on a c-CMSM sample milled in small flakes; previously, it has been demonstrated that milling a sample does not affect its macroporosity [30]. Figure 3.10 shows the differential intrusion volume as a function of the pore diameter. It can be seen that the material does not exhibit macroporosity, having only some mesoporosity. The total intruded volume (volume of pores greater than 3.6 nm, meso and macropores (V_{mp})) was 0.089 $cm^3 \cdot g^{-1}$.

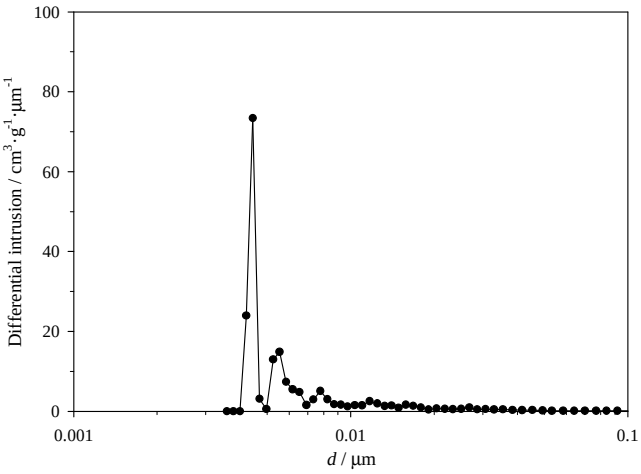

Figure 3.10 – Meso/macro porosity of c-CMSM obtained by mercury porosimetry.

The microporosity of the material was studied by adsorption of a probe gas. The most frequently used probe gas is N_2 at 77 K. Because N_2 is unable to access narrow micropores (smaller than 0.6 nm) due to diffusional limitations [31] this work uses the adsorption isotherm of CO_2 at 273 K for the description of the microporous structure of the material. In micropores, the mechanism of adsorption is known as micropore filling and has been well described by Dubinin and co-workers [32-34]. Even though it does not follow Henry's law for very small pressures [35] the Dubinin-Raduschkevisch (DR) equation is frequently used to describe the adsorption in micropores – (eq. (3.4)):

$$\theta = \frac{W}{W_0} = e^{\left[-\left(\frac{\phi}{E}\right)^2\right]} \qquad (3.4)$$

where W is the micropore volume filled at pressure P, W_0 is the total micropore volume, θ the fraction of micropore volume filled, ϕ the potential energy and E the characteristic energy. When the temperature of the gas is well below its critical temperature, the adsorbate is assumed to be in a dense state, similar to the liquid state, and the potential energy becomes:

$$\phi = \Re T \ln \frac{P_0}{P} \tag{3.5}$$

where P_0 is the vapor pressure of the free liquid, P is the pressure of the gas phase, $\Re$ is the gas constant and T is the absolute temperature. The characteristic curve for the CMS (presented in Figure 3.11) shows that the DR equation fits very well the experimental data; the micropore volume and characteristic energy were determined from the slope and the intercept, respectively. Furthermore, empiric correlations developed by Stoeckli were used to estimate the average micropore width (ℓ) and the total surface area of micropores ($A_{\mu p}$).

$$\ell = \frac{10.8}{E_0 - 11.4} \tag{3.6}$$

$$A_{\mu p} = 2000 \frac{W_0}{\ell} \tag{3.7}$$

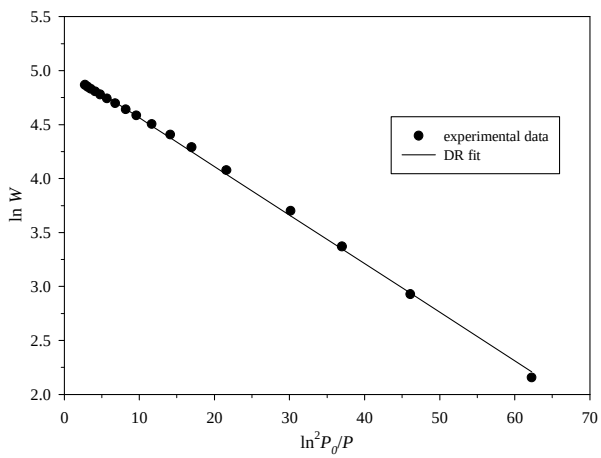

Figure 3.11 – CO_2 characteristic curve for the c-CMSM at 273 K (points – experimental data; line – DR fitting).

Table 3.2 offers a summary of the structural parameters determined from the characteristic curve and the Stoeckli correlations.

Table 3.2 – Structural parameters determined from the DR fit, the Stoeckli correlations and He pycnometry.

Parameter	Value
W_0 ($cm^3 \cdot g^{-1}$)	0.150
E_0 ($kJ \cdot mol^{-1}$)	30.2
ℓ (nm)	0.58
$A_{\mu p}$ ($m^2 \cdot g^{-1}$)	522

It can be concluded that the micropore volume obtained is similar to other values reported in the literature for carbon materials [14, 30, 36-37]. After determining the material density and micropore and meso/macropore volume the apparent material density can be obtained - eq. (3.8).

$$\rho_{app} = \frac{m_s}{V_s + W_0 + V_{mp}} \tag{3.8}$$

The total porosity of the material (ε) the micropore porosity ($\varepsilon_{\mu p}$) and the micropore volume fraction ($f_{\mu p}$) were also determined. Table 3.3 offers a summary of the physical properties of the c-CMSM. The values of total porosity (ε=0.26) and micropore porosity ($\varepsilon_{\mu p}$=0.16) are in line with literature values [30, 36].

Table 3.3 – Physical properties of the CMS.

Parameter	Value
ρ_s $\left(g \cdot cm^{-3}\right)$	1.49
ρ_{app} $\left(g \cdot cm^{-3}\right)$	1.10
$A_{mp>3.6nm}$ $\left(m^2 \cdot g^{-1}\right)$	42
$f_{\mu p}$	0.63
ε	0.26
$\varepsilon_{\mu p}$	0.16
τ	2.10

A more detailed knowledge of the microporosity of the c-CMSM required the assessment of the micropore size distribution (PSD). The PSD was determined

using the structure-based method developed by Nguyen *et al.* [30, 38-39]. This model states that the amount adsorbed, $q_{pore}(P, r)$, at any pressure P within a pore of radius r can be calculated from:

$$q_{pore}(P,r) = q_{pore}^{m}(r)\frac{b_{pore}(r)P_{pore}(r)}{1+b_{pore}(r)P_{pore}(r)} \tag{3.9}$$

where $q_{pore}^{\max}$ refers to the maximum adsorbed amount and b to Langmuir constant. The overall amount adsorbed at a certain pressure P ($q_{exp}(P)$), results from the contribution of every pore:

$$q_{\exp}(P) = \int_{0}^{\infty} q_{pore}(P,r)\,f(r)dr \tag{3.10}$$

Finally, the experimental adsorption data of CO_2 at 273 K was used to determine the fraction of pores $f(r)$ associated with each pore width dimension. The resulting pore size distribution can be seen in Figure 3.12. This CMSM exhibits both small micropores (0.35-0.45 nm) and larger micropores (0.5-0.8 nm) and the mean pore width found for this material was ℓ = 0.58 nm.

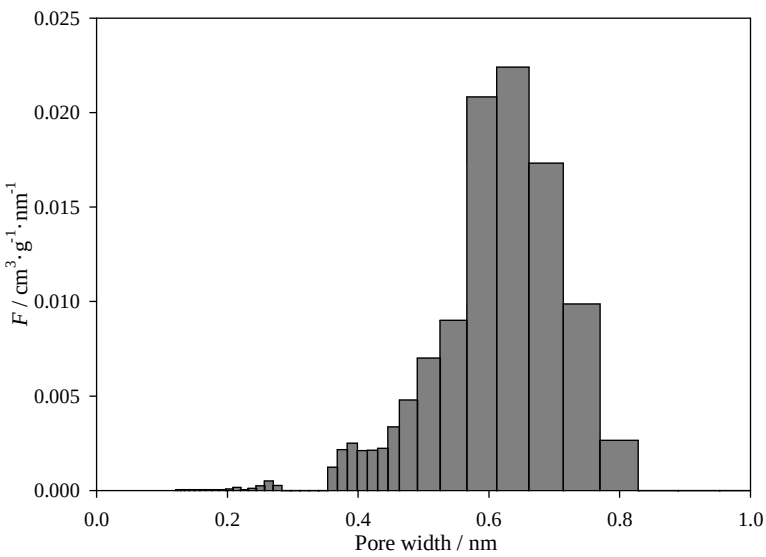

Figure 3.12 – Micropore size distribution of the c-CMS sample.

Nonetheless, the PSD shown in Figure 3.12 should be taken with some care. CO_2 adsorbs essentially on the walls of the pores and the adsorption capacity of the constrictions (smaller) is almost insignificant [8]. Thus, the PSD does not accurately reflect the amount and size distribution of the constrictions, which are essential for the sieving properties of the material. So, it is possible to expect sieving behaviour for pairs such as O_2/N_2, despite the fact that almost all pores in Figure 3.12 exhibit dimensions equal to or superior to the penetrants mentioned.

3.4.4 Permeation Experiments

Monocomponent permeabilities were determined at 293 K. The feed pressure was varied between 100-400 kPa (relative pressure) while permeate was kept at 100 kPa (atmospheric pressure). Figure 3.13 summarizes the steady state permeability results for He, CO_2, O_2, N_2, C_3H_6 and C_3H_8. The slowest diffusion species (C_3H_8) required up to 24 hours to reach steady state. Between experiments, N_2 was passed through the membrane for up to two hours to remove traces of the previously adsorbed gas. The permeability values were computed considering that the membrane thickness was uniform and approximately 2-µm thick. It is observed that the permeability towards all gases, except He, is pressure dependent, decreasing slightly with the feed pressure. This can be attributed to the interactions between the adsorbed molecule and the CMS membrane. The gases which exhibit the greater pressure dependence (CO_2, C_3H_8 and C_3H_6) are the ones with a greater adsorption affinity towards the membrane [36].

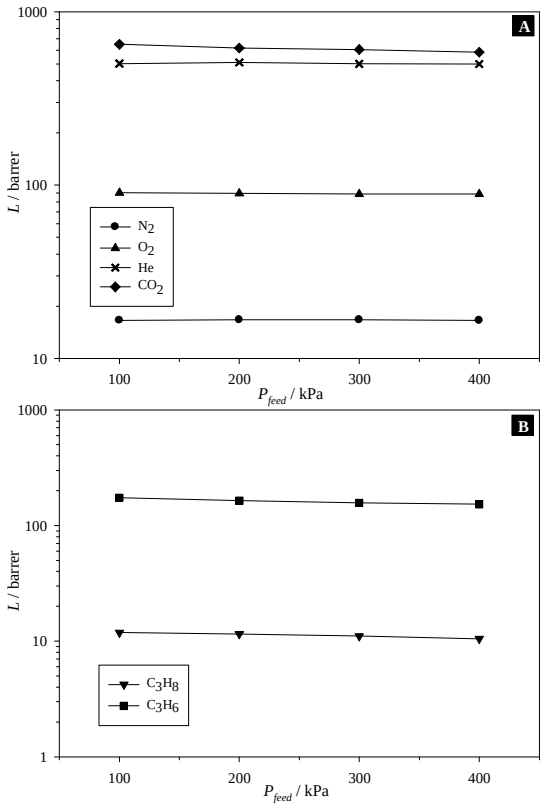

Figure 3.13 – Permeability as a function of the relative feed pressure for permanent gases (A) and hydrocarbons (B) at 293 K (symbols – experimental data; lines – trend lines).

The impact of the feed pressure on the ideal selectivities for several gas pairs of interest was also analyzed and is shown in Table 3.4. Clearly, the feed pressure has a small impact on the permselectivities for all gas pairs considered.

Table 3.4 – Permselectivities for gas pairs as a function of the relative feed pressure at 293 K.

P_{feed} (kPa)	S_{O_2/N_2}	S_{He/N_2}	S_{CO_2/N_2}	$S_{C_3H_6/C_3H_8}$
100	5.4	35.2	29.6	14.6
200	5.3	33.9	29.9	14.2
300	5.4	33.7	30.4	14.2
400	5.4	33.0	31.1	14.6

Figure 3.14 displays the dependence of the permeability of the membrane as a function of the diameter of the probe species.

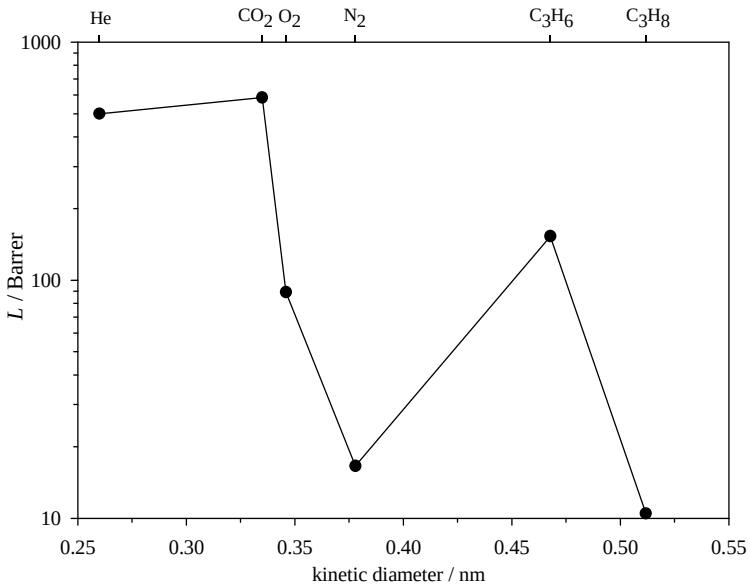

Figure 3.14 – Permeability as a function of the kinetic diameter of the permeant species.

The kinetic diameter is used for the permanent gases, but not for C_3H_6 and C_3H_8. The C_3H_6/ C_3H_8 permselectivity in carbons is not reflected by their different kinetic diameters (4.5 and 4.3, respectively for C_3H_6 and C_3H_8) as has been discussed elsewhere [8], but rather is related to their Lennard-Jones diameters (4.7 and 5.1 nm, respectively). Figure 3.14 shows that there is not a straightforward relation between permeability and the kinetic diameter of the permeant species. This fact is consistent with a gas transport that combines sieving effect at the smaller micropores (constrictions) with the adsorption and diffusion of the permeant gases on the larger pores. This explains why C_3H_8 and C_3H_6 have higher permeance values than N_2, even though their Lennard Jones diameters (4.7 nm and 5.1 nm) are much larger than N_2's (3.6 nm). For the same reason, the permeability towards CO_2 is greater than for N_2. For gases weakly

adsorbed (He, O_2 and N_2) the molecular sieving effect is controlling, and there is a declining trend in permeability as a function of the molecular size.

The ability of a membrane to effectively separate one gas from a binary mixture depends on the membrane permeability and selectivity. Robeson [40] realized that the performance of polymeric membranes for several binary gas separations of interest was below an upper bound curve; an increase in selectivity is always obtained at the expense of a decrease in permeability and vice-versa. This upper bound curve is seen as the state-of-the-art curve for each separation (for polymeric membranes). Robeson's work did not include a study of the gas pair C_3H_6/ C_3H_8 but Burns and Koros [41] conducted in 2003 a similar analysis for this separation. Figure 3.15 compares the single component permeation results achieved with this membrane with the state-of-the-art plots for O_2/ N_2 and C_3H_6/C_3H_8. It can be seen that the membrane performs as well as the best membranes for O_2/N_2 separation and significantly above the best membranes for C_3H_6/ C_3H_8 separation.

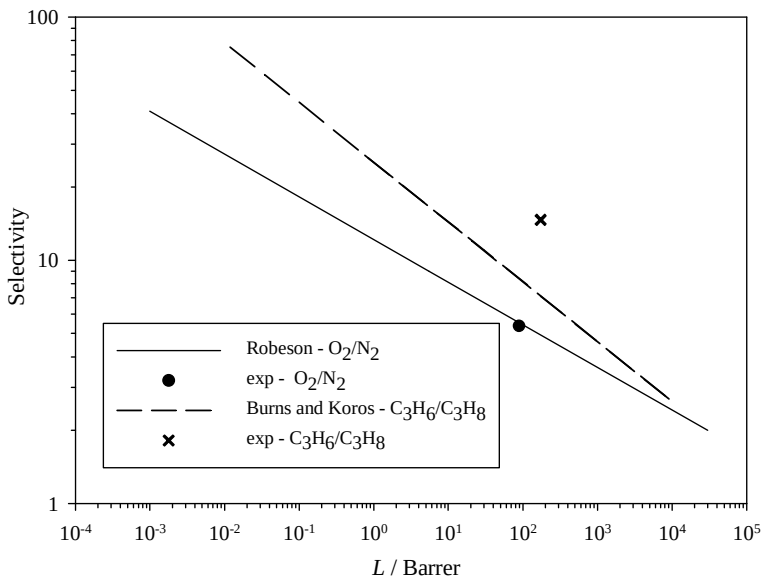

Figure 3.15 – Comparison of the experimental results achieved with the c-CMSM (at 400 kPa feed pressure) and the state of the art plots for O_2/N_2 and C_3H_6/ C_3H_8 separations (lines – state of the art plots; symbols – experimental data).

3.5 Conclusions

A composite carbon membrane derived from phenolic resin loaded with boehmite nanoparticles was successfully prepared in a single dipping-drying-carbonization step. After pyrolysis at 550 ºC, boehmite nanoparticles originated nanowires of Al_2O_3 10-30 nm long and 1-2 nm thick, greatly dispersed into the carbon matrix. The composite membrane is more suitable for separating bulkier molecules such as C_3H_6 and C_3H_8 and less suitable for separating O_2 from N_2. The membrane exhibited high C_3H_6 permeability and considerable C_3H_6/C_3H_8 ideal selectivities, positioning well above the state-of-the-art plot for polymeric membranes for this separation.

3.6 Acknowledgments

Miguel Teixeira, Margot Llosa and Marta Campo are grateful to the Portuguese Foundation for Science and Technology (FCT) for their grants (references SFRH/BD/24768/2005, SFRH/BD/61898/2009 and SFRH/BPD/65377/2009). The authors also acknowledge financing from FCT through the projects POCTI/EQU/59344/2004 and POCTI/EQU/59345/2004. The authors are thankful to CEMUP for the SEM analyses (REEQ/1062/CTM/2005 and REDE/1512/RME/2005 funding provided by FCT).

3.7 Nomenclature

Variables	Definition	Units
A	Surface area	$m^2 \cdot kg^{-1}$
b	Langmuir constant	Pa^{-1}
d	d-spacing between graphitic layers	m
E	Characteristic energy	$J \cdot mol^{-1}$
f	Volume fraction of pores	-
ℓ	Average micropore width	m
L	Membrane permeability	$mol \cdot m \cdot m^{-2} \cdot s^{-1} \cdot Pa^{-1}$
n	SIPS equation parameter	-
P_0	Vapor pressure of the free liquid	Pa
p	Partial pressure	Pa
P	Total pressure	Pa
q	Surface concentration	$mol \cdot kg^{-1}$
q^{max}	Maximum surface concentration	$mol \cdot kg^{-1}$
$\Re$	Gas constant	$Pa \cdot m^3 \cdot mol^{-1} \cdot K^{-1}$
S	Permselectivity	-
T	Absolute temperature	K
V	Pore volume	$m^3 \cdot kg^{-1}$
W_0	Total micropore volume	$m^3 \cdot kg^{-1}$

Greek	Definition	Units
θ	Fractional coverage of the pore surface	-
Φ	Potential energy	$Pa \cdot m^3 \cdot mol^{-1}$
ε	Porosity	-
τ	Tortuosity	-
δ	Membrane thickness	m
ρ	Density	$kg \cdot cm^{-3}$

Subscripts	**Definition**
i	Species i
j	Species j
μ*p*	Micropores
mp	Meso and macropores
app	Apparent
s	Solid
pore	Relative to the pore
r	Radius

3.8 References

[1] A.F. Ismail, K. Li, From Polymeric Precursors to Hollow Fiber Carbon and Ceramic Membranes, in: R. Mallada, M. Menéndez (Eds.) Inorganic Membranes Synthesis, Characterization and Applications, Elsevier Science, 2008.
[2] R. Ash, R.M. Barrer, R.T. Lowson, Transport of Single Gases and of Binary Gas-Mixtures in a Microporous Carbon Membrane, J Chem Soc Farad T 1, 69 (1973) 2166-2178.
[3] A. Soffer, J. Koresh, New Approach to Pore Development in Molecular-Sieve Carbon, Carbon, 18 (1980) 51-51.
[4] J.E. Koresh, A. Soffer, Mechanism of Permeation through Molecular-Sieve Carbon Membrane .1. The Effect of Adsorption and the Dependence on Pressure, J Chem Soc Farad T 1, 82 (1986) 2057-2063.
[5] A.F. Ismail, L.I.B. David, A review on the latest development of carbon membranes for gas separation, J Membrane Sci, 193 (2001) 1-18.
[6] S.M. Saufi, A.F. Ismail, Fabrication of carbon membranes for gas separation - a review, Carbon, 42 (2004) 241-259.
[7] V.C. Geiszler, W.J. Koros, Effects of polyimide pyrolysis conditions on carbon molecular sieve membrane properties, Ind Eng Chem Res, 35 (1996) 2999-3003.
[8] K.M. Steel, W.J. Koros, Investigation of porosity of carbon materials and related effects on gas separation properties, Carbon, 41 (2003) 253-266.
[9] K. Wang, H. Suda, K. Haraya, The characterization of CO_2 permeation in a CMSM derived from polyimide, Sep Purif Technol, 31 (2003) 61-69.
[10] A.B. Fuertes, I. Menendez, Separation of hydrocarbon gas mixtures using phenolic resin-based carbon membranes, Sep Purif Technol, 28 (2002) 29-41.
[11] F.K. Katsaros, T.A. Steriotis, A.K. Stubos, A. Mitropoulos, N.K. Kanellopoulos, S. Tennison, High pressure gas permeability of microporous carbon membranes, Microporous Mater, 8 (1997) 171-176.
[12] M.B. Shiflett, H.C. Foley, Reproducible production of nanoporous carbon membranes, Carbon, 39 (2001) 1421-1425.
[13] Y.D. Chen, R.T. Yang, Preparation of Carbon Molecular-Sieve Membrane and Diffusion of Binary-Mixtures in the Membrane, Ind Eng Chem Res, 33 (1994) 3146-3153.
[14] M.C. Campo, F.D. Magalhaes, A. Mendes, Carbon molecular sieve membranes from cellophane paper, J Membrane Sci, 350 (2010) 180-188.
[15] J. Gilron, A. Soffer, Knudsen diffusion in microporous carbon membranes with molecular sieving character, J Membrane Sci, 209 (2002) 339-352.
[16] T.A. Centeno, A.B. Fuertes, Supported carbon molecular sieve membranes based on a phenolic resin, J Membrane Sci, 160 (1999) 201-211.

[17] T.A. Centeno, A.B. Fuertes, Carbon molecular sieve membranes derived from a phenolic resin supported on porous ceramic tubes, Sep Purif Technol, 25 (2001) 379-384.
[18] J.N. Barsema, J. Balster, V. Jordan, N.F.A. van der Vegt, M. Wessling, Functionalized Carbon Molecular Sieve membranes containing Ag-nanoclusters, J Membrane Sci, 219 (2003) 47-57.
[19] J.N. Barsema, J. Balster, N.F.A. Van der Vegt, G.H. Koops, V. Jordan, M. Wessling, Ag functionalized Carbon Molecular Sieves membranes for separating O_2 and N_2, Membranes-Preparation, Properties and Applications, 752 (2003) 207-212.
[20] Y.C. Xiao, M.L. Chng, T.S. Chung, M. Toriida, S. Tamai, H.M. Chen, Y.C.J. Jean, Asymmetric structure and enhanced gas separation performance induced by in situ growth of silver nanoparticles in carbon membranes, Carbon, 48 (2010) 408-416.
[21] S. Yoda, A. Hasegawa, H. Suda, Y. Uchimaru, K. Haraya, T. Tsuji, K. Otake, Preparation of a platinum and palladium/polyimide nanocomposite film as a precursor of metal-doped carbon molecular sieve membrane via supercritical impregnation, Chem Mater, 16 (2004) 2363-2368.
[22] H.B. Park, C.H. Jung, Y.K. Kim, S.Y. Nam, S.Y. Lee, Y.M. Lee, Pyrolytic carbon membranes containing silica derived from poly(imide siloxane): the effect of siloxane chain length on gas transport behavior and a study on the separation of mixed gases, J Membrane Sci, 235 (2004) 87-98.
[23] H.B. Park, S.Y. Lee, Y.M. Lee, Pyrolytic carbon membranes containing silica: morphological approach on gas transport behavior, J Mol Struct, 739 (2005) 179-190.
[24] Q.L. Liu, T.H. Wang, J.S. Qiu, Y.M. Cao, A novel carbon/ZSM-5 nanocomposite membrane with high performance for oxygen/nitrogen separation, Chem Commun, (2006) 1230-1232.
[25] X.Y. Yin, J.Q. Wang, N.B. Chu, J.H. Yang, J.M. Lu, Y. Zhang, D.H. Yin, Zeolite L/carbon nanocomposite membranes on the porous alumina tubes and their gas separation properties, J Membrane Sci, 348 (2010) 181-189.
[26] C.F. Zeng, L.X. Zhang, X.H. Cheng, H.T. Wang, N.P. Xu, Preparation and gas permeation of nano-sized zeolite NaA-filled carbon membranes, Sep Purif Technol, 63 (2008) 628-633.
[27] C.L. Kong, J.Q. Wang, J.H. Yang, J.M. Lu, A.F. Wang, Q.Y. Zhao, Thin carbon-zeolite composite membrane prepared on ceramic tube filter by vacuum slip casting for oxygen/nitrogen separation, Carbon, 45 (2007) 2848-2850.
[28] H. Marsh, F. Rodríguez-Reinoso, Activated carbon, Elsevier, Amsterdam ; London, 2006.
[29] M. Ottaway, Use of Thermogravimetry for Proximate Analysis of Coals and Cokes, Fuel, 61 (1982) 713-716.

[30] M.C. Campo, F.D. Magalhaes, A. Mendes, Comparative study between a CMS membrane and a CMS adsorbent: Part I-Morphology, adsorption equilibrium and kinetics, J Membrane Sci, 346 (2010) 15-25.
[31] D. CazorlaAmoros, J. AlcanizMonge, A. LinaresSolano, Characterization of activated carbon fibers by CO_2 adsorption, Langmuir, 12 (1996) 2820-2824.
[32] M.M. Dubinin, V.A. Astakhov, Development of Ideas of Volume Filling of Micropores during Adsorption of Gases and Vapours by Microporous Adsorbents .1. Carbonaceous Adsorbents, B Acad Sci Ussr Ch+, (1971) 5-&.
[33] M.M. Dubinin, V.A. Astakhov, Development of Ideas of Volume Filling of Micropores during Adsorption of Gases and Vapours by Microporous Adsorbents .2. General Fundamentals of Theory of Gas and Vapour Adsorption on Zeolites, B Acad Sci Ussr Ch+, (1971) 11-&.
[34] M.M. Dubinin, Zolotare.Pp, K.M. Nikolaev, N.S. Polyakov, L.I. Petrova, Radushke.Lv, Study of Adsorption Dynamics in Broad Range of Brake down Concentrations .4. Theoretical Analysis of Experimental-Data, B Acad Sci Ussr Ch+, (1973) 293-297.
[35] D.D. Do, Adsorption analysis: equilibria and kinetics, Imperial College Press, London, 1998.
[36] S. Lagorsse, F.D. Magalhaes, A. Mendes, Carbon molecular sieve membranes - Sorption, kinetic and structural characterization, J Membrane Sci, 241 (2004) 275-287.
[37] K.M. Steel, W.J. Koros, An investigation of the effects of pyrolysis parameters on gas separation properties of carbon materials, Carbon, 43 (2005) 1843-1856.
[38] C. Nguyen, D.D. Do, Adsorption of supercritical gases in porous media: Determination of micropore size distribution, J Phys Chem B, 103 (1999) 6900-6908.
[39] C. Nguyen, D.D. Do, K. Haraya, K. Wang, The structural characterization of carbon molecular sieve membrane (CMSM) via gas adsorption, J Membrane Sci, 220 (2003) 177-182.
[40] L.M. Robeson, Correlation of Separation Factor Versus Permeability for Polymeric Membranes, J Membrane Sci, 62 (1991) 165-185.
[41] R.L. Burns, W.J. Koros, Defining the challenges for C_3H_6/C_3H_8 separation using polymeric membranes, J Membrane Sci, 211 (2003) 299-309.

Chapter 4: **Carbon-Al_2O_3-Ag composite carbon molecular sieve membranes for gas separation**

(Teixeira, M., Campo, M., Tanaka, D., Llosa, M., Magen, C., Mendes, A., submitted to Separation and Purification Technology, 2011)

4.1 Abstract

Phenolic resins were loaded with two different inorganic fillers: boehmite (γ-AlO(OH)) and silver (Ag). Polymer solutions with γ-AlO(OH) and $AgNO_3$ were prepared as well as polymer solutions where only γ-AlO(OH) was present, so as to assess the effect of Ag on the transport properties of the membrane. The polymer solutions were coated on α-Al_2O_3 tubes and carbonized in a single dipping-drying-pyrolysis step. After pyrolysis at 550 ºC, γ-AlO(OH) yielded γ-Al_2O_3 and Ag nanoparticles were formed. γ-Al_2O_3 was present as nanowires of around 20 nm length and Ag as spherical nanoparticles of 30 nm in diameter. Ag loading enhanced the carbon membrane performance for several gas pairs of interest, especially for C_3H_6/C_3H_8 separation, where the C_3H_6/C_3H_8 permselectivity increased from a maximum of 15 to 38.

4.2 Introduction

Polymer membranes are successfully implemented in several industrial processes [1-2]. However, polymer membranes are chemically and thermally unstable. Moreover, their performance for each gas separation is limited by an upper bound curve which relates permeability and selectivity, as reported by Robeson [3-4]. Meanwhile, inorganic membranes such as carbon membranes [5] have emerged as potential candidates for gas separations. These membranes present high

permeabilities and excellent selectivities, overcoming the Robeson upper bound for polymers. However, they are brittle, lack mechanical stability and exhibit low reproducibility [6]. Mixed matrix membranes, which combine the processability of polymers with the enhanced performance of inorganics in a single membrane, offer a promising alternative. This concept was first introduced for hybrid organic/inorganic membranes, but has been recently extended to composite carbon/inorganic membranes [7-9].

Chapter 3 detailed the preparation of a c-CMSM with Al_2O_3 nanowires well distributed in the carbon matrix. The present chapter focuses on a new c-CMSM obtained incorporating two types of nanoparticles: Al_2O_3 and Ag. Several characterization techniques such as scanning electron microscopy, high-resolution transmission electron microscopy and x-ray diffraction confirmed the presence and dispersion of the Ag and Al_2O_3 nanoparticles in the carbon matrix. Permeation experiments were performed to assess the permeability towards N_2, O_2, CO_2, He, C_3H_6 and C_3H_8.

4.3 Experimental

4.3.1 Materials

The chemicals used were supplied by Euroresinas (phenolic resin), Acros Organics (N-Methyl-2-pyrrolidone, for analysis), Kawaken Fine Chemicals Co., Ltd (10 wt.% γ-AlO(OH) aqueous dispersion, particle size 8-20 nm) and Merck ($AgNO_3$ for analysis, ($C_2H_4(NH_2)_2$) (Ethylenodiamine) for synthesis). The permanent gases used in this work were supplied by Air Liquide (99.999 %). C_3H_8 and C_3H_6 were supplied by Praxair (99.5 %).

γ-AlO(OH) nanoparticles were added to the resin and the dispersion diluted with NMP (*N*-Methyl-2-pyrrolidone) up to 13 wt.% phenolic resin and 0.88 wt.% γ-AlO(OH) (and 0.2 wt.% of $AgNO_3$, for the membranes featuring the two

inorganic fillers). $AgNO_3$ was used as Ag source because it has been shown to lead to well dispersed Ag nanoparticles in the carbon matrix [10]. Ethylenodiamine ($C_2H_4(NH_2)_2$) was added in molar excess to $AgNO_3$ to prevent Ag reduction by free formaldehyde before pyrolysis. The solutions were prepared in the absence of light to avoid Ag reduction by UV light.

4.3.2 Membrane Preparation

The membrane preparation method is detailed in the previous chapter. Briefly, a membrane was prepared by dip coating of the composite solution onto α-Al_2O_3 support tubes. This supported film was dried in a rotating oven at 40 ºC for two hours and left overnight at 90 ºC. Pyrolysis was performed under N_2 atmosphere with a gas flow rate of 100 $mL \cdot min^{-1}$ PTN. A heating rate of 1 $ºC \cdot min^{-1}$ up to 550 ºC and a soaking time of 2 hours were used. In parallel, dry films were also prepared to characterize the morphology and structure of the composite membrane. The samples used for adsorption studies were made from a 12.5/0.5 wt.% resin/γ-AlO(OH) dispersion and a 12.5/0.5/0.2 wt.% resin/γ-AlO(OH)/$AgNO_3$ dispersion. Two types of membranes were prepared, carbon-Al_2O_3 membranes (named hereafter C-Al) and carbon-Al_2O_3-Ag membranes (C- Al-Ag).

4.3.3 Morphological and Structural Characterization

The microporosity of both materials was assessed from the CO_2 adsorption isotherm at 293 K, determined in the Rubotherm® magnetic suspension balance ($\pm 10^{-5}$ mg precision) described in Chapter 2. The carbonized films were crushed into small flakes before being placed in the balance.

Thermogravimetric analyses (TGA) were carried in a Netzsch TG 209 F1 Iris thermogravimetric balance in the temperature range between 20-900 ºC and

under N_2 flow. X-ray diffraction (XRD) analyses were performed in a PAN'Alytical X'Pert Pro, with CuKα 0.15418 nm radiation, X'Celerator detector and secondary monochromator. XRD was used to confirm the amorphous nature of the carbon structure. The average *d*-spacing between the individual layers of the carbon membrane was calculated adopting Bragg's Law, with the *d*-spacing of graphite (0.335 nm) taken as reference. XRD was also used to give insight into the size of the Ag nanoparticles. SEM was performed in a FEI Quanta 400 FEG/EDAX Genesis X4M with 1.2 nm resolution. SEM was used to analyze the cross section of the carbonized membranes, the dispersion of Ag in the membrane and to assess the composite layer thickness. High-resolution transmission electron microscopy (HRTEM) was performed in a FEI Titan Cubed microscope operated at 300 kV. This instrument is equipped with an image aberration corrector that provides 0.8 Å resolution. This technique was used to give insight into the size and distribution of the two inorganic fillers: Al_2O_3 and Ag.

4.3.4 Permeation Experiments

The sieving properties of the c-CMSMs were evaluated by gas permeation. Monocomponent permeabilities were determined in the stainless steel shell and tube apparatus described in Chapter 3. Briefly, the gases were introduced in the shell side and the permeating flow rate determined by mass flow meters. The shell side was kept at fixed relative pressure (100-400 kPa) by means of a pressure controller and the permeate side was left at atmospheric pressure. Experiments were performed at 293 K.

4.4 Results

4.4.1 Microporosity analysis

For characterizing the microporosity of the C-Al and C-Al-Ag composite materials, the CO_2 adsorption isotherm was determined at 293 K. Afterwards, the Dubinin-Raduschkevisch (DR) equation (equation (4.1)), derived from the theory for volume filling of micropores, was used to provide information on the pore network.

$$\theta = \frac{W}{W_0} = \exp^{\left[-\left(\frac{\phi}{\beta E_0}\right)^2\right]} \tag{4.1}$$

where W is the micropore volume filled at pressure P, W_0 is the total micropore volume, θ is the fractional uptake of micropore volume, ϕ is the potential energy, E_0 is the characteristic energy and β is the affinity coefficient for CO_2 (assumed to be the affinity coefficient towards carbon [11]). The potential energy ϕ was determined using:

$$\phi = \Re T \ln \frac{P_0}{P} \tag{4.2}$$

where P_0 is the vapor pressure of the free liquid, P is the pressure of the gas phase, $\Re$ is the gas constant and T is the absolute temperature. Figure 4.1 shows that the DR equation provides a good fit to the experimental data. The micropore volume and characteristic energy were determined by fitting equation (4.1) to the experimental data. The average micropore width (ℓ) was estimated by Stoeckli's empiric correlation:

$$\ell = \frac{10.8}{E_0 - 11.4} \tag{4.3}$$

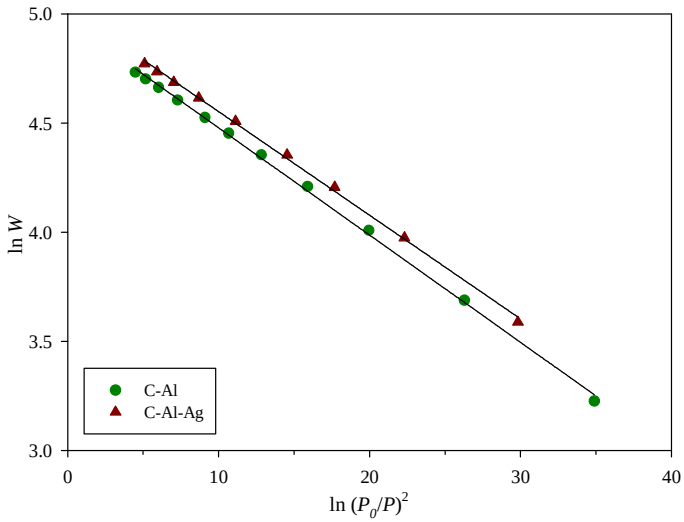

Figure 4.1 – DR plots for C-Al and C-Al-Ag samples.

The estimated parameters are summarized in Table 4.1. It can be concluded that the presence of Ag yields only small changes in the pore network. An increase in the total pore volume (consistent with the work of Barsema *et al.* [12]) is interestingly followed by a small decrease in average pore width. So, a more porous structure with a tighter size distribution is obtained for C-Al-Ag.

Table 4.1 – Structural parameters determined from the DR and Stoeckli equations.

Membrane	W_0 ($cm^3 \cdot kg^{-1}$)	E_0 ($kJ \cdot mol^{-1}$)	ℓ (nm)
C-Al	144	31.0	0.551
C-Al-Ag	153	31.5	0.536

4.4.2 Thermogravimetric analyses (TG)

TG runs were performed on dry films of C-Al and C-Al-Ag in the temperature range between 20-900 ºC. The dry basis mass loss curves (corrected for solvent loss) are shown in Figure 4.2.

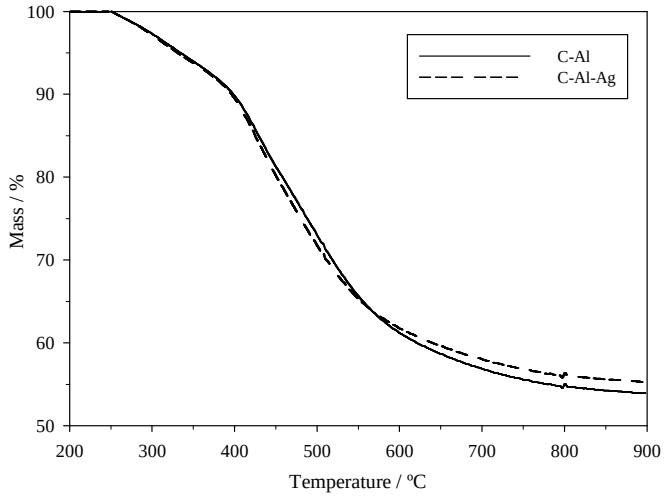

Figure 4.2 – TGA of carbon-Al_2O_3 and carbon-Al_2O_3-Ag c-CMSMs.

The TG curves for C-Al and C-Al-Ag membranes are fairly similar because the relative content of $AgNO_3$ is low. At 900 °C, the mass loss of the C-Al-Ag membrane is slightly smaller than the mass loss of the C-Al membrane.

4.4.3 X-ray and microscopic analyses

Wide angle X-ray diffraction was used to analyse the structures of C-Al and C-Al-Ag samples. The XRD diffraction patterns of both membranes are plotted in Figure 4.3. The XRD pattern of C-Al shows no Bragg lines suggesting that Al_2O_3 is too small and/or too spread in the matrix to be detected. The pattern of C-Al-Ag shows five diffraction peaks for Ag, corresponding to five diffraction planes. The size of the Ag nanoparticles was estimated by refinement of the experimental diffraction data with the spectrum of pure Ag; it was determined a mean particle diameter of 28 nm. Both spectra show a wide peak at 2θ between 15 and 30, characteristic of highly disordered amorphous carbon. The *d*-spacing - interlayer distance in the carbon structure - was computed applying Braggs Law to the amorphous peak related to the (002) plane. The *d*-value did not changed significantly upon introduction of Ag (for C-Al was 0.45 nm and for C-Al-Ag

was 0.44 nm) so the porous network of the carbon membrane should not be significantly different after adding Ag. The intensity of the d_{002} peak was somewhat lower for C-Al-Ag, indicating a less ordered microstructure arrangement.

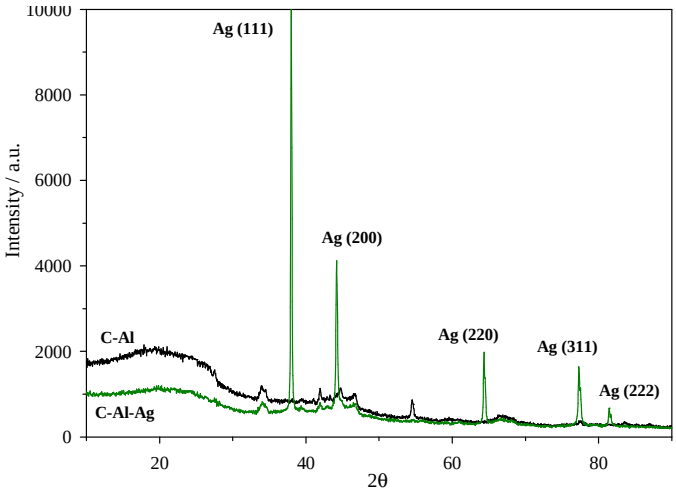

Figure 4.3 – X-ray diffraction spectrum of two composite membrane samples; dark line – C-Al; grey line – C-Al-Ag.

Scanning electron microscopy (SEM) analyses provided insight concerning the structure of the composite film. Cross sectional views of C-Al and C-Al-Ag membranes are shown in Figure 4.4A and Figure 4.4B, respectively. Both C-Al and C-Al-Ag membranes exhibit uniform film thickness. Yet, while the C-Al film has a thickness around 2.5 μm, the C-Al-Ag membrane exhibits a slightly higher thickness (3.3 μm). This might be attributed to the different rheology of the two precursor dispersions. Figure 4.4B also shows Ag nanoparticles (white dots) homogeneously distributed in the carbon matrix of the C-Al-Ag membrane, asserting the effective role of the ethylenodiamine complexant in preventing Ag agglomeration before pyrolysis. Traces of Ag are found in the Al_2O_3 support because the polymer solution was made to contact with the support by vacuum assisted dip coating.

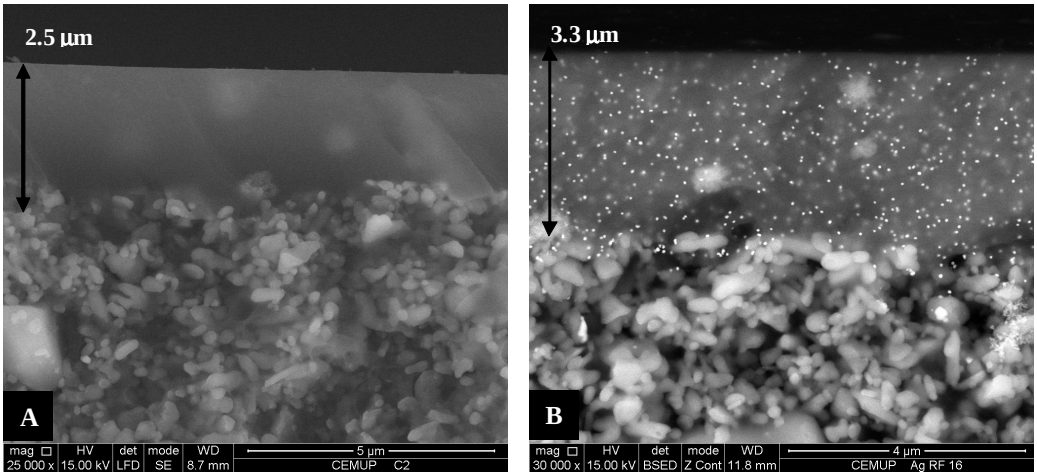

Figure 4.4 – SEM pictures of the cross sectional region of the c-CMSMs; A – C-Al membrane; B – C-Al-Ag membrane.

HRTEM analyses of the C-Al-Ag membrane allowed understanding the distribution of the Al_2O_3 and Ag nanoparticles in the carbon matrix. Figure 4.5 shows TEM images of the c-CMSM.

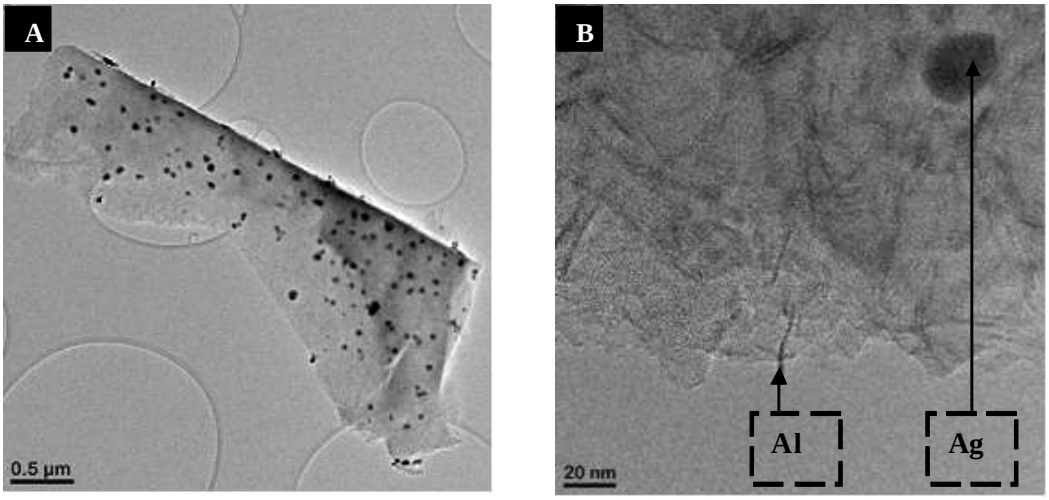

Figure 4.5 – HRTEM pictures of C-Al-Ag membrane; (A) Low magnification view; (B) High magnification view.

Figure 4.5A shows the distribution of Ag in the matrix, which resembles that of the supported membrane observed by SEM. Ag appears as a Gaussian

distribution of quasi-spherical nanoparticles of sizes ranging from 10 to 40 nm, with an average size of around 30 nm in diameter, a result consistent with the values determined by XRD refinement. A high resolution image (Figure 4.5B) details the structure of the c-CMSM. In addition to the Ag nanoparticles, nanowires of Al_2O_3 of about 20-30 nm length can also be found randomly distributed, as observed previously.

4.4.4 Permeation Experiments

The transport properties of the c-CMSMs prepared were analyzed in terms of permeability towards gases of different kinetic diameters: He (0.260 nm), CO_2 (0.335 nm), O_2 (0.346 nm), N_2 (0.378 nm), C_3H_6 (0.468 nm) and C_3H_8 (0.512 nm). This allowed ascertaining the relative importance of sieving and adsorption mechanisms on the overall transport and to conclude about the most promising gas separation applications. Figure 4.6 shows pure gas permeability of two sets of C-Al and C-Al-Ag membranes; it can be concluded that membranes are fairly reproducible. Also, the permeability values of C-Al and C-Al-Ag membranes do not differ much for the gases tested. Roughly, for the permanent gases, there is a decrease in permeability with the kinetic diameter, thus the sieving effect should be the controlling transport mechanism for these gases. The exception is He/CO_2, where similar permeability values are observed despite helium's smaller species size, indicative of the higher adsorption affinity of the membranes towards CO_2. For the hydrocarbons there is also a decrease in permeability with kinetic diameter, indicating that the sieving effect is controlling. On the other hand, the permeabilities of the membranes towards C_3H_6 are higher than the permeabilities towards N_2; this is attributed to a higher adsorption affinity towards the hydrocarbon.

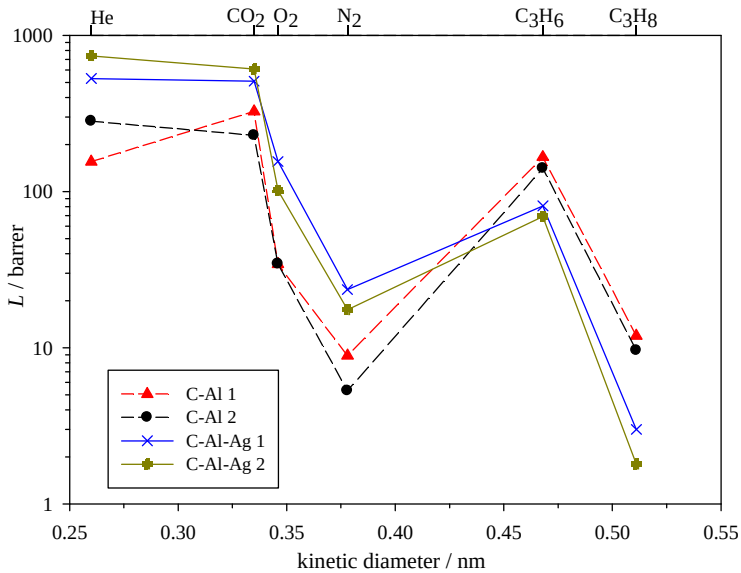

Figure 4.6 – Effect of kinetic diameter on the permeability of the c-CMSMs: dashed lines – C-Al; solid lines – C-Al-Ag.

Table 4.2 shows the permeabilities of the C-Al and C-Al-Ag membranes towards the probe gases and Table 4.3 the ideal selectivities (ratio of monocomponent permeabilities) for the same membranes.

Table 4.2 – Permeability of the c-CMSM for gas probe species.

Membrane	Permeability / barrer					
	He	CO_2	O_2	N_2	C_3H_6	C_3H_8
C-Al 1	155.5	326.2	34.3	8.9	166.2	11.9
C-Al 2	281.9	228.6	34.4	5.3	140.7	9.6
C-Al-Ag 1	529.3	508.5	155.9	23.6	80.9	3
C-Al-Ag 2	740	609.3	101.5	17.5	69.3	1.8

Table 4.3 – Ideal selectivities of the c-CMSMs for gas pairs of interest.

Membrane	Ideal selectivities			
	He/N_2	CO_2/N_2	O_2/N_2	C_3H_6/C_3H_8
C-Al 1	17.4	36.6	3.8	13.9
C-Al 2	53.4	43.3	6.5	14.9
C-Al-Ag 1	22.4	21.5	6.6	26.7
C-Al-Ag 2	42.3	34.8	5.8	37.8

The effect of Ag-ethylenodiamine on the permeability and permselectivity for the pairs O_2/N_2, He/N_2 and CO_2/N_2 are all quite similar: the permeability increases while ideal selectivity stays roughly constant. Yet, for C_3H_6/C_3H_8 it is observed a decrease in permeability towards C_3H_6 and a noticeable increase in permselectivity. The presence of Ag nanoparticles affects the membrane performance because it affects the PSD.

Changes in the number and size of both ultramicropores (constrictions, in the range of 0.3–0.5 nm) and larger micropores (in the range of 0.5–0.8 nm) influence the permeability and permselectivity. The ultramicropores (constrictions) are responsible for most of the permselectivity while both ultramicropres and micropores are responsible for the permeability. Because C_3H_6 and C_3H_8 should have diameters close to the tail end of the ultramicropores size distribution, only a small fraction of these pores should be available to the hydrocarbons. Hence, a small shift in the pore size distribution can have a large impact in the permeabilities towards C_3H_6 and C_3H_8. Figure 4.7 shows a hypothetical ultramicropores size distribution that is supported by the porosity parameters reported before.

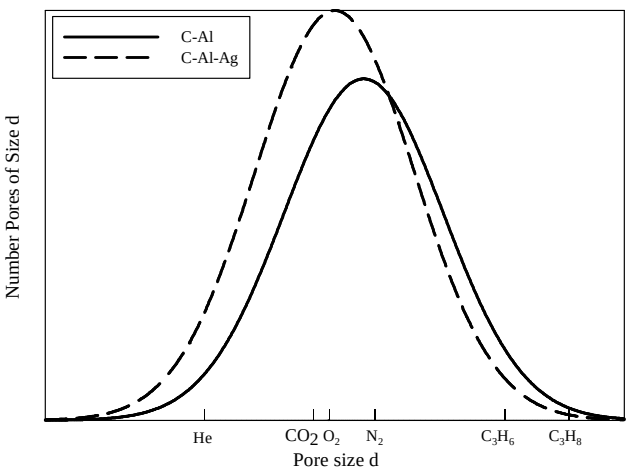

Figure 4.7 – Hypothetical size distribution of the ultramicropores in the c-CMSMs (C-Al, dashed line; C-Al-Ag, solid line).

It is proposed that Ag loading increases the number of ultramicropores and slightly decreases their average size (cf. Figure 4.7). This explains the increase in C_3H_6/C_3H_8 permselectivity and slight decrease in hydrocarbon permeability. Moreover, it also accounts for the permeability increase towards the permanent gases and the approximately constant ideal selectivities. The permeabilities and ideal selectivities obtained were inserted into the semi-empirical plots devised by Robeson [4]. For the C_3H_6/C_3H_8 separation, an upper bound plot suggested by Burns and Koros [13] is used since Robeson has not focused on this separation. Figure 4.8 illustrates the upper bound limits for O_2/N_2, He/N_2, CO_2/N_2 and C_3H_6/C_3H_8 separations and the experimental ideal selectivities.

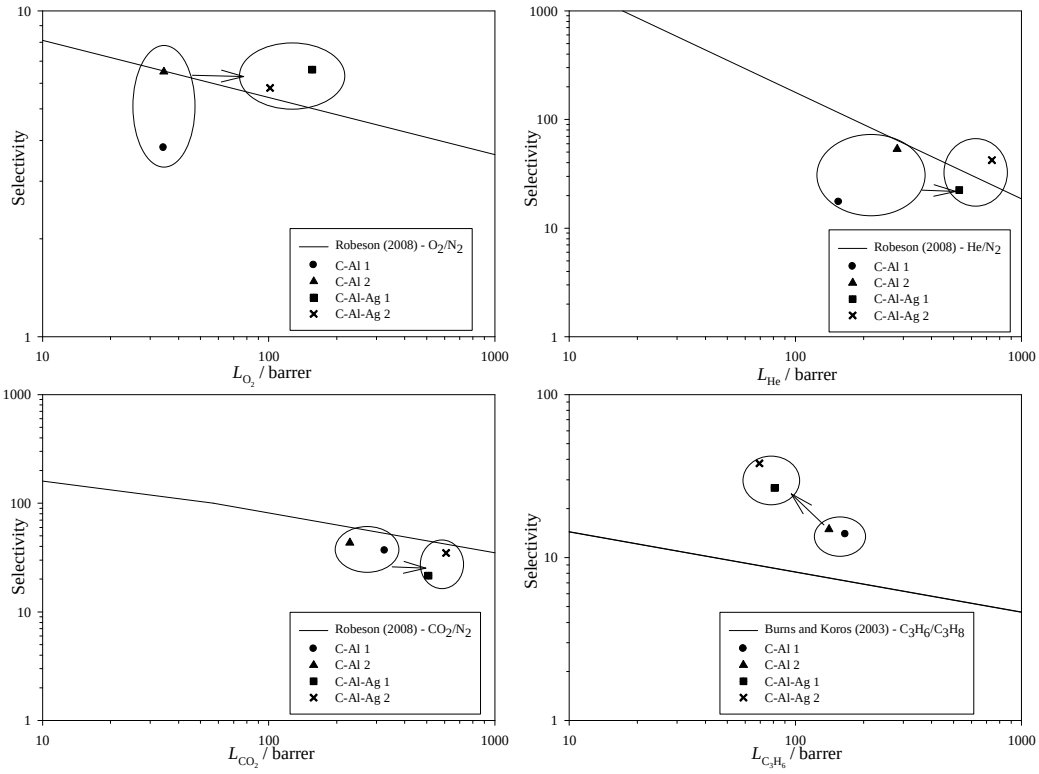

Figure 4.8 – Gas permeation results for 4 gas pairs of interest in C-Al and C-Al-Ag membranes and comparison with the respective upper bound plots.

The synthesized membranes performed particularly well for the separation of C_3H_6 from C_3H_8, largely surpassing the Burns and Koros plot. While C-Al membranes only yield promising results for the separation of the hydrocarbons, C-Al-Ag membranes place above the upper bound plots for O_2/N_2 and He/N_2 separations as well.

4.5 Conclusions

A new composite carbon membrane is proposed, featuring a low cost polymer (phenolic resin) and two inorganic fillers, Al_2O_3 nanowires and Ag nanoparticles. Thin composite membranes with uniform thickness and well-distributed fillers were synthesized in a single dipping-drying-carbonization step. The porous network of carbon-Al_2O_3 and carbon-Al_2O_3-Ag composite membranes is fairly similar and only small changes arise from the presence of Ag nanoparticles. The effects of Ag presence in the porous network were evaluated by gas permeation. The performances of the two types of composite membranes were analyzed in terms of permeability and ideal selectivity towards several gas pairs of commercial interest. Carbon-Al_2O_3-Ag membranes performed better for all separations analyzed and are particularly promising for the C_3H_6/C_3H_8 separation, where their performance overcame by far the best polymer membranes.

4.6 Acknowledgements

Miguel Teixeira and Margot Llosa are grateful to the Portuguese Foundation for Science and Technology (FCT) for their doctoral grants (references SFRH/BD/24768/2005 and SFRH/BD/61898/2009). Marta Campo is grateful to FCT for her post-doctoral grant (SFRH/BPD/65377/2009). The authors also acknowledge financing from FCT through the projects POCTI/EQU/59344/2004 and POCTI/EQU/59345/2004. The authors are thankful to CEMUP for the SEM

analysis (REEQ/1062/CTM/2005 and REDE/1512/RME/2005 funding provided by FCT). Finally, the authors acknowledge Prof. Pedro Tavares from UTAD (Universidade de Trás-os-Montes e Alto Douro) for the valuable discussions on XRD.

4.7 Nomenclature

Variables	Definition	Units
d	d-Spacing between graphitic layers	m
E	Characteristic energy	$J \cdot mol^{-1}$
ℓ	Average micropore width	m
P_0	Vapor pressure of the free liquid	Pa
P	Total pressure	Pa
p	Partial pressure	Pa
$\Re$	Gas constant	$Pa \cdot m^3 \cdot mol^{-1} \cdot K^{-1}$
T	Absolute temperature	K
W_0	Total micropore volume	$m^3 \cdot kg^{-1}$

Greek Symbols	Definition	Units
θ	Fractional coverage of the pore surface	-
Φ	Potential energy	$Pa \cdot m^3 \cdot mol^{-1}$
β	Affinity coefficient towards CO_2	-

4.8 References

[1] S.P. Nunes, K.V. Peinemann, Gas Separation with Membranes, in: S.P. Nunes, K.V. Peinemann (Eds.) Membrane Technology in the Chemical Industry, Wiley, Weinheim, 2006, pp. 53-75.
[2] A.K. Fritzsche, J.E. Kurz, The Separation of Gases by Membranes, in: M.C. Porter (Ed.) Handbook of Industrial Membrane Technology, Noyes Publications, Westwood, New Jersey, U.S.A., 1990, pp. 559-593.
[3] L.M. Robeson, Correlation of Separation Factor Versus Permeability for Polymeric Membranes, J Membrane Sci, 62 (1991) 165-185.
[4] L.M. Robeson, The upper bound revisited, J Membrane Sci, 320 (2008) 390-400.
[5] A.F. Ismail, L.I.B. David, A review on the latest development of carbon membranes for gas separation, J Membrane Sci, 193 (2001) 1-18.
[6] W.J. Koros, R. Mahajan, Pushing the limits on possibilities for large scale gas separation: which strategies?, J Membrane Sci, 181 (2000) 141-141.
[7] X.F. Zhang, T.H. Wang, H. Liu, K.L. Yeung, Preparation of composite carbon-zeolite membranes using a simple method, J Mater Sci, 39 (2004) 5603-5605.
[8] C.L. Kong, J.Q. Wang, J.H. Yang, J.M. Lu, A.F. Wang, Q.Y. Zhao, Thin carbon-zeolite composite membrane prepared on ceramic tube filter by vacuum slip casting for oxygen/nitrogen separation, Carbon, 45 (2007) 2848-2850.
[9] J.N. Barsema, N.F.A. van der Vegt, G.H. Koops, M. Wessling, Ag-functionalized carbon molecular-sieve membranes based on polyelectrolyte/polyimide blend precursors, Adv Funct Mater, 15 (2005) 69-75.
[10] J.N. Barsema, J. Balster, V. Jordan, N.F.A. van der Vegt, M. Wessling, Functionalized Carbon Molecular Sieve membranes containing Ag-nanoclusters, J Membrane Sci, 219 (2003) 47-57.
[11] D. CazorlaAmoros, J. AlcanizMonge, A. LinaresSolano, Characterization of activated carbon fibers by CO_2 adsorption, Langmuir, 12 (1996) 2820-2824.
[12] J.N. Barsema, J. Balster, N.F.A. Van der Vegt, G.H. Koops, V. Jordan, M. Wessling, Ag functionalized Carbon Molecular Sieves membranes for separating O_2 and N_2, Membranes-Preparation, Properties and Applications, 752 (2003) 207-212.
[13] R.L. Burns, W.J. Koros, Defining the challenges for C_3H_6/C_3H_8 separation using polymeric membranes, J Membrane Sci, 211 (2003) 299-309.

Chapter 5: **Composite carbon molecular sieve membranes – adsorption, kinetic and permeation studies – Part I**

(Teixeira, M., Campo, M., Tanaka, D., Llosa, M., Sousa, J., Madeira, L. M., Mendes, A., submitted to Journal of Membrane Science, 2011)

5.1 Abstract

Composite carbon molecular sieve membranes (c-CMSM) prepared from phenolic resin solutions (10-15 wt.%) loaded with boehmite nanoparticles (0.5-1.2 wt.%) in a single dipping-pyrolysis step were tested for gas separation. Equilibrium isotherms of N_2, O_2 and CO_2 (at 293 K), and propane (C_3H_8) and propylene (C_3H_6) (in the temperature range 293-453 K) were determined on c-CMSM flakes (resin/boehmite = 12.5/0.5 wt.%). The c-CMSM exhibited kinetic and adsorption selectivity towards O_2/N_2, CO_2/N_2 and particularly for C_3H_6/C_3H_8. The separation of C_3H_6 from C_3H_8 is controlled by the ratio of the diffusivity coefficients of the hydrocarbons, which is highest at 293 K.

The optimum composition of resin and boehmite for the separation of O_2 from N_2 and C_3H_6 from C_3H_8 was determined. The best performing c-CMSM exhibited O_2/N_2 and C_3H_6/C_3H_8 permselectivities up to 6 and 19, respectively. The performance of the c-CMSM for the pair C_3H_6/C_3H_8 was above the upper bound curve for polymeric membranes.

5.2 Introduction

Carbon membranes have a complex pore structure that combines the sieving effects of the smaller pores with preferential adsorption on its larger ones. This bi-modal distribution can lead to high selectivities while maintaining good permeabilities [1]. However, carbon membranes also have drawbacks, such as brittleness and poor reproducibility [2]. Moreover, when exposed to air or to impurities such as large organics and water vapor they are known to exhibit a decrease in performance [3-6]. In this context, new materials have been proposed. Namely, the concept of composite carbon molecular sieve membranes (c-CMSM) - incorporation of nanoparticles in the carbon matrix - has appeared as an alternative to improve the permeation performance, chemical and thermal stability of CMSMs.

c-CMSMs were prepared using polymer/boehmite dispersions with different compositions (keeping the same carbonization conditions) and their separation properties for several gas pairs of interest were compared. The stability of the most promising membranes was analyzed by studying the effect of exposure to atmospheric air on the decrease in performance of the membranes (aging).

5.3 Experimental

5.3.1 Membrane Synthesis

The precursors were prepared by mixing an industrial phenolic resin diluted in NMP (N-Methyl-2-pyrrolidone) with a 10 wt.% aqueous dispersion of boehmite nanoparticles in different proportions. Table 5.1 lists the composition of the prepared dispersions used to prepare the c-CMSM. Membranes M1 to M4 were prepared with the same resin content (12.5 wt.%) and different boehmite amounts (from 0.5 to 1.2 wt.%). On the other hand, the precursors of membranes M5, M3

and M6 were all prepared with 1 wt.% of boehmite and the resin content ranged from 10 to 15 wt.%. These two sets of membranes allowed understanding the effect of Al_2O_3 and resin contents in the permeation properties of the carbonized membranes.

After preparation, the dispersions were dip coated to the external surface of α-Al_2O_3 support tubes, as explained in Chapter 3. Additionally, films of these solutions were also prepared for characterization/adsorption studies. The supported membranes and films were carbonized at 550 ºC.

Table 5.1 – Composition of the precursors used to prepare the c-CMSM.

Membrane	Phenolic Resin (wt.%)	Boehmite (wt.%)
M1	12.5	0.5
M2	12.5	0.75
M3	12.5	1
M4	12.5	1.2
M5	10	1
M6	15	1

5.4 Morphological and structural characterization of the membranes

Mass loss curves (or characteristic curves) were determined in a thermogravimetric balance under a N_2 atmosphere in the temperature range 20-900 ºC (heating rate 10 ºC·min^{-1}). Scanning electron microscopy (SEM) was used to analyze the cross section of the carbonized membranes and determine the composite layer thickness. The specifications of the thermogravimetric balance and the microscope can be found in Chapter 3.

5.4.1 Adsorption isotherms/uptake experiments

Flakes of membrane M1 were used in all adsorption and uptake experiments. The adsorption isotherms of CO_2, O_2 and N_2 at 293 K were determined using a

Rubotherm® magnetic suspension balance. The adsorption kinetics of each equilibrium point was used to determine the gas diffusivities (uptake curves). Before use and whenever the adsorbed gas was changed, the adsorbent samples were degassed in cycles of high pressure helium and vacuum (ca. 10 Pa) for up to 36 hours at 343 K. Adsorption equilibrium isotherms of C_3H_8 and C_3H_6 were determined at 293, 343, 393 and 453 K in a VTI sorption analyzer equipped with a microbalance with a precision of 1 μg. Before the isotherm measurements, the adsorbent samples were degassed at vacuum (ca. 10 Pa) for up to 4 hours at 573 K.

5.4.2 Permeation Experiments

Mono and bicomponent permeabilities were determined in a shell and tube membrane apparatus, as shown in Figure 5.1.

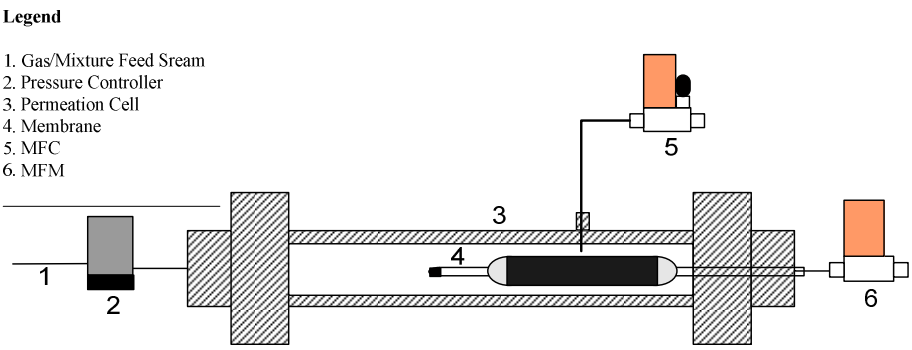

Figure 5.1 – Scheme depicting the permeation setup.

The gas/mixture stream was fed at 200-500 kPa at the shell side and the tube (permeate) side was kept at 100 kPa. The permeating flow rate of the gas/mixture was measured using mass flow meters (Bronkhorst, ranges 0-1, 0-10 and 0-100 $mL_N \cdot min^{-1}$). For mixed gas permeation experiments, a stainless steel tank was used to prepare equimolar C_3H_6/C_3H_8 mixtures and a mass flow controller (Bronkhorst, 0-1 $L_N \cdot min^{-1}$) was used to set the retentate flow rate at about ten

times the value of the permeate flow rate, to guarantee that the feed composition in the shell was uniform. The composition of the feed and permeating streams were determined using a GC (Dani 1000) equipped with a ValcoPlot column, a FID detector and a split/splitless injector.

5.5 Results and Discussion

5.5.1 Thermogravimetric analysis

Curves depicting the mass loss of membranes M1 to M6 as a function of temperature are seen in Figure 5.2. Table 5.2 lists the burn off percentage for all membranes as well as their composition. The contents of carbon and Al_2O_3 of the carbonized membranes could be estimated because the composition of M1 had been previously determined by proximate analysis in Chapter 3. The shape of the mass loss curve is similar for all membranes, implying that a similar carbonaceous structure is present in all cases.

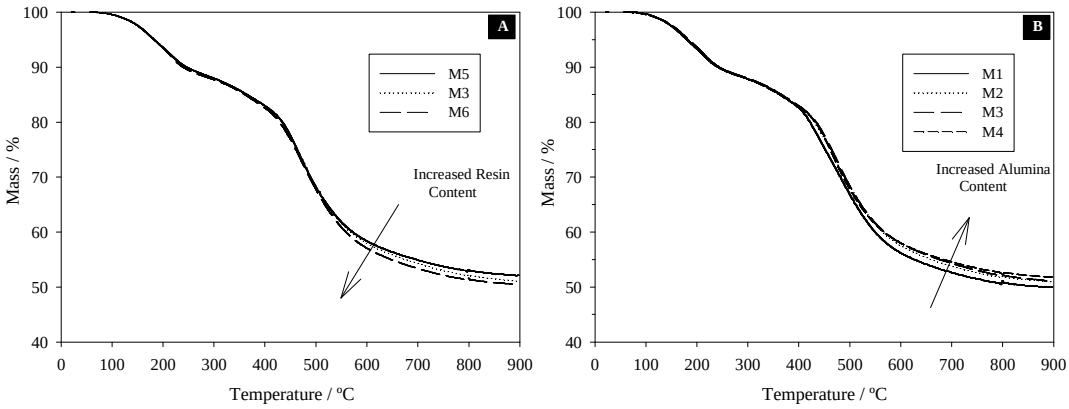

Figure 5.2 – Characteristic curves for two sets of membranes. In Figure 5.2A the boehmite composition is constant and the phenolic resin content is changed from 10 to 15 wt.% (wet basis). In Figure 5.2B the resin content remains at 12.5 wt.% while boehmite content is varied from 0.5 to 1.2 wt.% (wet basis).

There is a trend for higher burn off with higher resin and lower boehmite contents, so clearly the mass loss of the phenolic resin during carbonization is larger than the mass loss due to the dehydroxylation of boehmite to Al_2O_3. Yet, the differences are small because the content of Al_2O_3 when compared to carbon is also small (cf. Table 5.2).

Table 5.2 – Burn off of several c-CMSM prepared with different phenolic resin and boehmite contents in a 20-900 ºC run under N_2 atmosphere.

Membrane	Precursor composition (wt.%)		c-CMSM composition (wt.%)		Burn off (%)
	Phenolic Resin	Boehmite	Carbon[a]	γ-Al_2O_3[a]	
M1	12.5	0.5	88.0	12.0	50.3
M2	12.5	0.75	83.0	17.0	49.0
M3	12.5	1.0	78.6	21.4	48.9
M4	12.5	1.2	75.3	24.7	48.2
M5	10.0	1.0	74.6	25.4	47.9
M6	15.0	1.0	81.5	18.5	49.5

[a] Values based on the carbon and Al_2O_3 percentages determined previously for a membrane with the same composition as membrane M1 in Chapter 3.

5.5.2 SEM/EDS

Figure 5.3 shows SEM cross sectional images of the composite membrane M3. It is observed that a uniform ca. 2 μm thick composite layer is formed on top of a α-Al_2O_3 support tube. The white patches observed in Figure 5.3 correspond to Barium, a common component of industrial phenolic resins. The thickness of all membranes prepared was approximately the same and no noticeable trend was observed when the ratio phenolic resin/boehmite changed. Figure 5.3B also shows the concentration profile of Al_2O_3 along the composite layer. It is seen that Al_2O_3 is distributed uniformly throughout.

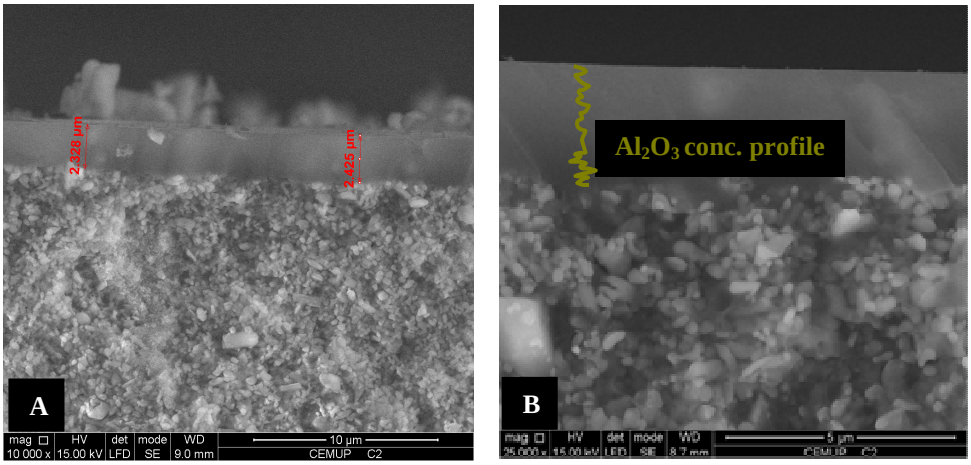

Figure 5.3 – SEM images of the cross-section of membrane M3, after pyrolysis; (A) 10 000 x magnification (B) 25 000 x magnification. In (B) it is displayed the concentration profile of alumina throughout the membrane.

5.5.3 Adsorption Isotherms and Uptakes

5.5.3.1 Adsorption of O_2, N_2 and CO_2

The adsorption equilibrium isotherms of O_2, N_2 and CO_2 on c-CMSM flakes were measured at 293 K over the pressure range 0-700 kPa. The isotherms are of type I and the experimental data was fitted to the Langmuir and SIPS equations (eqs. (5.1) and (5.2), respectively):

$$q = q^{\max} \frac{bP}{1+bP} \tag{5.1}$$

$$q = q^{\max} \frac{(bP)^{1/n}}{1+(bP)^{1/n}} \tag{5.2}$$

where q is the gas adsorbed amount (mol·kg^{-1}), $q^{\max}$ is the adsorption saturation capacity, b is the equation parameter (kPa^{-1}) , P is the pressure (kPa) and n is a parameter related to the deviance from the monolayer assumption. Figure 5.4 shows both the experimental data (symbols) and the respective fittings (lines).

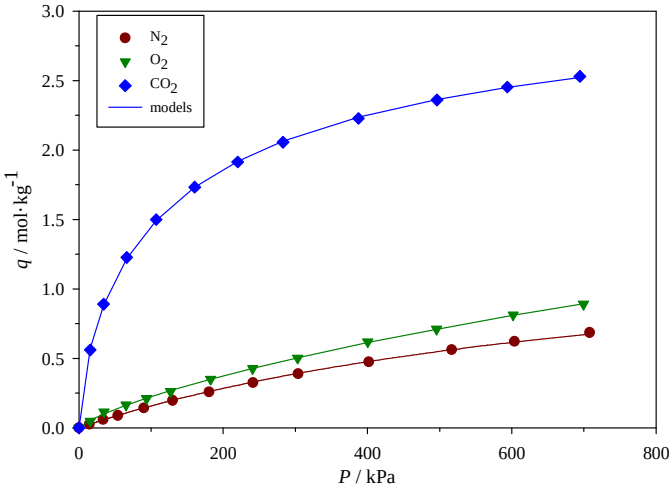

Figure 5.4 – Adsorption isotherms of N_2, O_2 and CO_2 at 293 K and corresponding fittings. The experimental values are represented by symbols and the SIPS fit model by lines.

Table 5.3 summarizes the Langmuir and SIPS isotherm parameters, calculated by minimizing the fitting error, *Err*, defined as:

$$Err = \frac{1}{n_v}\sum_{i=1}^{n_v}\left(\frac{q_i^{\text{model}} - q_i^{\text{exp}}}{q_i^{\text{exp}}}\right)^2 \tag{5.3}$$

where n_v refers to the number of experimental values, q^{exp} is the adsorbed concentration and q^{mod} is the adsorbed concentration given by the model. To determine the most adequate model a model selection criterion (MSC) was used [7]:

$$MSC = \ln\left(\frac{\sum_{i=1}^{m}\left(q_i^{\text{exp}} - q_{avg}^{\text{exp}}\right)^2}{\sum_{i=1}^{m}\left(q_i^{\text{exp}} - q_i^{\text{model}}\right)^2}\right) - 2\frac{n_p}{n_v} \tag{5.4}$$

where q_{avg}^{exp} is the average of all experimental q values and n_p is the number of parameters of each model. The model selection criterion weights the deviation to the experimental values as well as the number of parameters and both are minimized for higher MSC values.

Table 5.3 – Fitting parameters of the adsorption experimental data with the Langmuir and SIPS equations and corresponding fitting errors and MSC values.

		N_2	O_2	CO_2
Langmuir	q^{max} (mol·kg^{-1})	1.47	1.35	2.57
	b (kPa^{-1})	1.2x10^{-3}	2.1x10^{-3}	1.6x10^{-2}
	Err	1.4x10^{-4}	7.3x10^{-3}	3.1x10^{-3}
	MSC	7.56	3.69	3.33
SIPS	q^{max} (mol·kg^{-1})	1.62	2.35	3.28
	b (kPa^{-1})	1.0x10^{-3}	7.5x10^{-4}	7.4x10^{-3}
	n	1.02	1.17	1.37
	Err	6.0x10^{-5}	2.5x10^{-4}	3.1x10^{-5}
	MSC	9.17	4.99	7.95

Table 5.3 shows that the SIPS equation fits better the adsorption isotherm for all three gases, displaying higher MSC values and lower fitting errors. Parameter n (which is related to the deviance from the monolayer assumptions) was 1.17 and 1.37 for O_2 and CO_2, indicating some multilayer and/or multisite adsorption for these gases.

Besides the adsorption equilibrium conditions, the transient uptake curves of O_2, N_2 and CO_2 were also determined and the apparent diffusivity coefficients computed. The mass uptake at any time t was normalized by the mass uptake at equilibrium (t=∞) and the fractional uptake was calculated as:

$$F = \frac{m_t - m_0}{m_\infty - m_0} \tag{5.5}$$

where m_0 is the mass at t = 0. The fractional uptake was correlated to diffusivity coefficient (D) by a suitable model. When the uptake is controlled by micropore diffusion the fractional uptake is expressed by equation (5.6) [8] for a slab geometry:

$$F = 1 - \frac{2}{\pi^2} \sum_{v=1}^{\infty} \frac{1}{(v-0.5)^2} \exp\left(-(v-0.5)^2 \pi^2 \frac{D}{\Lambda^2} t \right) \tag{5.6}$$

where Λ is half of the slab thickness (an approximate value of 150 μm was determined using a caliper). On the other hand, when the gas diffusion is controlled by the pore mouth barrier, a LDF (linear driving force) model is used instead [9], represented by equation (5.7) [10], where *k* represents a mass transfer coefficient.

$$F = 1 - \exp(-kt) \tag{5.7}$$

Figure 5.5 shows the plots of the uptake curves for N_2, O_2 and CO_2 at 15 kPa. It can be seen that the micropore diffusion model provides a better depiction of the uptake behavior at high times. Yet, at low time values, the experimental curves are not perfectly described by either model. This suggests the mass transport is being controlled by a combined effect of the diffusion in the pore mouth and micropores.

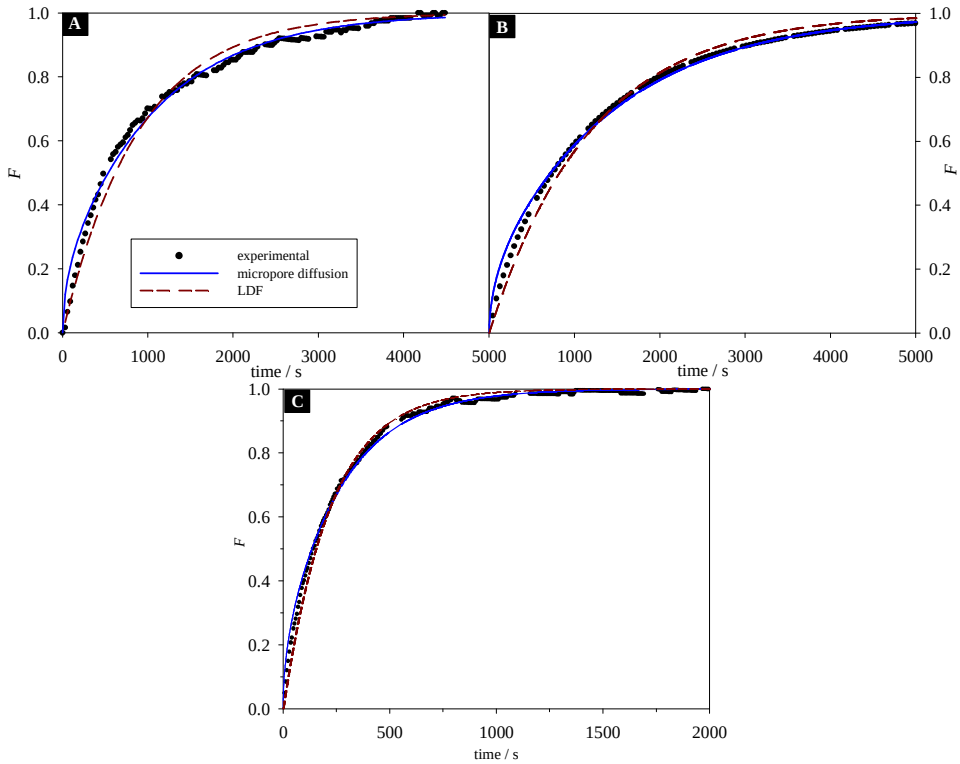

Figure 5.5 – Experimental and model fittings for the uptake curves of N_2 at P = 15 kPa(A), CO_2 at P = 15 kPa (B) and O_2 (C) at P = 35 kPa (micropore diffusion model – solid line; LDF model – dotted line).

Therefore, a pore mouth/micropore diffusion model would probably provide a more accurate depiction of the uptake behavior. Since the implementation of this model would require some computation effort and because at higher times the fitting provided by the micropore diffusion model was much better, it was considered that the mass transport was controlled by the diffusion in the micropores.

For O_2, an initial fast uptake (F appears to reach a plateau at 2000 s) is followed by a very slow increase, and the system is not at equilibrium even after 72 h. This behavior is consistent with chemisorption and Elovich's kinetic law has been reported to describe the uptake of chemisorption phenomena [11]:

$$r_c = \frac{dF_c}{dt_c} = \xi \exp(-\zeta F_c) \tag{5.8}$$

where r_c is the rate of O_2 chemisorption, t_c is the chemisorption time and ξ and ζ are constants. Finally, F_c is chemisorption uptake, i.e. the experimental uptake after subtracting the physical adsorption to the total amount adsorbed. The Elovich equation describes well the experimental chemisorption uptake rate, as illustrated in Figure 5.6, confirming that O_2 chemisorption occurs.

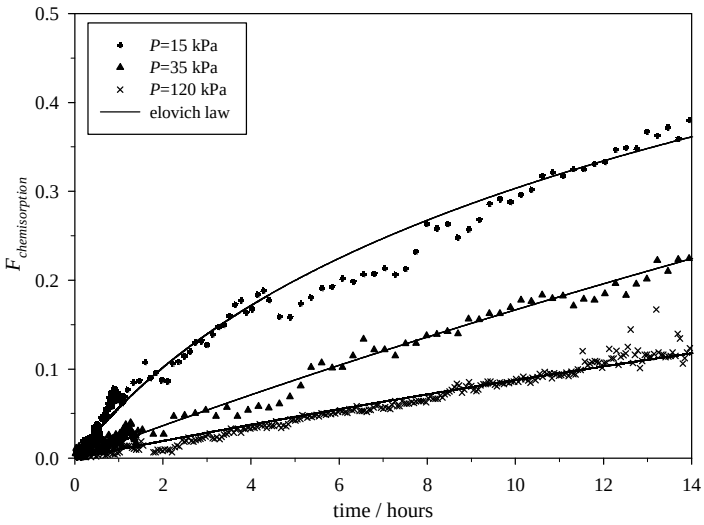

Figure 5.6 – Uptake chemisorption history of O_2 for three different pressure values; symbols – experimental data; lines – Elovich kinetic law ($1.31 < \zeta < 4.49$; $2.7\text{x}10^{-6} < \xi < 1.8\text{x}10^{-5}$ s^{-1}).

The decrease in the amount adsorbed for higher pressures is also indicative of chemisorption. Hence, the diffusivity of O_2 was determined using the physical adsorption data values. Because O_2 chemisorbs on the c-CMSM, it was decided to determine its desorption isotherm curve. Figure 5.7 plots both the adsorption and desorption branches of the isotherm curve of O_2, which took approximately 3 weeks to obtain. Unsurprisingly, around 10 % of the O_2 adsorption capacity was not restored. This is consistent with the findings by Sarah *et al.* [5], which studied O_2 chemisorption in hollow fiber CMSM. Additionally, Sarah *et al.* observed that vacuum in-situ regenerations at 343 K were unsuccessful to restore the original O_2 adsorption capacity. So, the adsorbent was regenerated *in-situ* at 343 K in a He atmosphere for two days followed by determination of the adsorption capacity towards N_2 (instead of O_2). Interestingly, the adsorption capacity of the regenerated c-CMSM sample towards N_2 was the same as that of the fresh sample, indicating that the relevant adsorption area for N_2 did not change much.

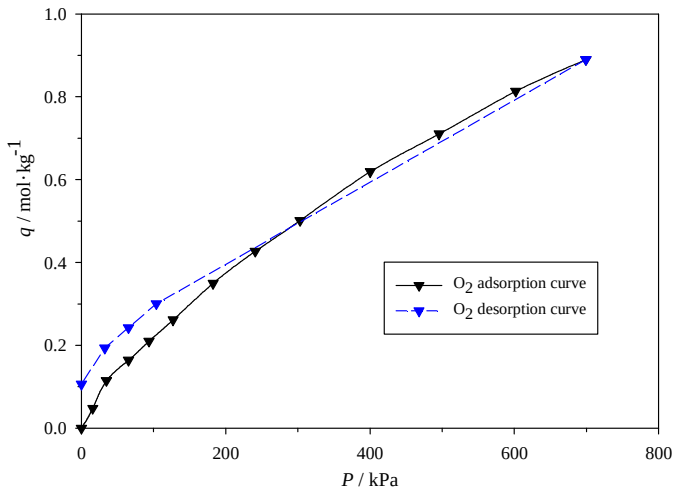

Figure 5.7 – O_2 adsorption /desorption equilibrium isotherm at 293 K.

5.5.3.1.1 Pressure dependence of diffusivity

According to the Darken equation, the diffusivity is given by [8]:

$$D = D_0 \Gamma \tag{5.9}$$

$$\Gamma = \frac{\partial \ln P}{\partial \ln q} \tag{5.10}$$

where D_0 is the diffusivity at zero loading and Γ is the thermodynamic correction factor. For a SIPS isotherm, it becomes:

$$D = D_0 n\left(1+\left(bP\right)^{1/n}\right) = D_0 \frac{n}{1-\theta} \tag{5.11}$$

where θ is the fractional loading. These equations were used to fit the dependence of the diffusivity coefficients with pressure (loading). Figure 5.8 shows that the N_2 diffusivity obeys to the Darken-SIPS relationship but the diffusivities of CO_2 and O_2 are not accurately described by this relation. Chen and Yang [12] have proposed a model where the pore blocking effect explains the behaviour of gases that do not exhibit monotically increasing diffusivities with pressure. They report that such behaviour is possible when sorbate-sorbate bonds are stronger than sorbate-surface bonds. This model features an additional parameter (λ), to account for the effect of the pore blockage:

$$D = D_0^{'} \frac{1-\theta+\lambda/2\theta\left(2-\theta\right)+H\left(1-\lambda\right)\left(1-\lambda\right)\lambda/2\theta^2}{\left(1-\theta+\theta\lambda/2\right)^2} \tag{5.12}$$

where H is the Heaviside function. When $\lambda = 0$ (there is no blocking effect) equation (5.12) becomes the Darken relation. Figure 5.8 shows that this model described much better the diffusivities as a function of pressure for O_2 and CO_2. Figure 5.8 also shows that the order of the diffusivities $O_2 > CO_2 > N_2$ does not follow the order of the kinetic diameters $CO_2 < O_2 < N_2$ [13], which is consistent with other reports in the literature [14-16]. However, differences in molecular shape are just as important. The 3D structure of a molecule impacts on its rotational, translational and vibrational degrees of movement in the constrictions [17].

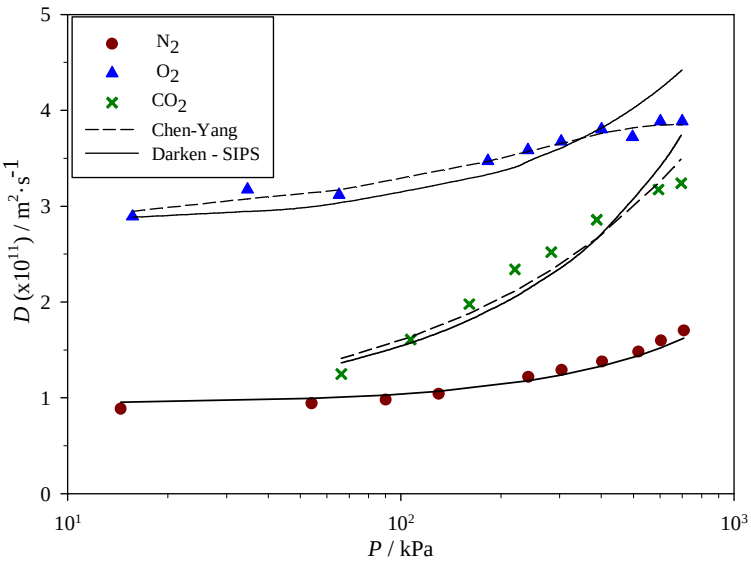

Figure 5.8 – Dependence of diffusivities of N_2, O_2 and CO_2 with pressure; symbols – experimental diffusivities with the micropore diffusion model; lines – fitting models ($D_0^{N_2} = 9.20x10^{-12}$; $D_0^{O_2} = 2.86x10^{-11}$; $\lambda = 1.63$; $D_0^{CO_2} = 8.19x10^{-12}$; $\lambda = 0.62$) .

Moreover, gas electronic properties, which influence the specific adsorbate-adsorbent interactions, have also been reported to affect the gas diffusivity [15]. Figure 5.9 summarizes the adsorption and diffusion O_2/N_2 and CO_2/N_2 selectivities for M1 in the pressure range 0-700 kPa.

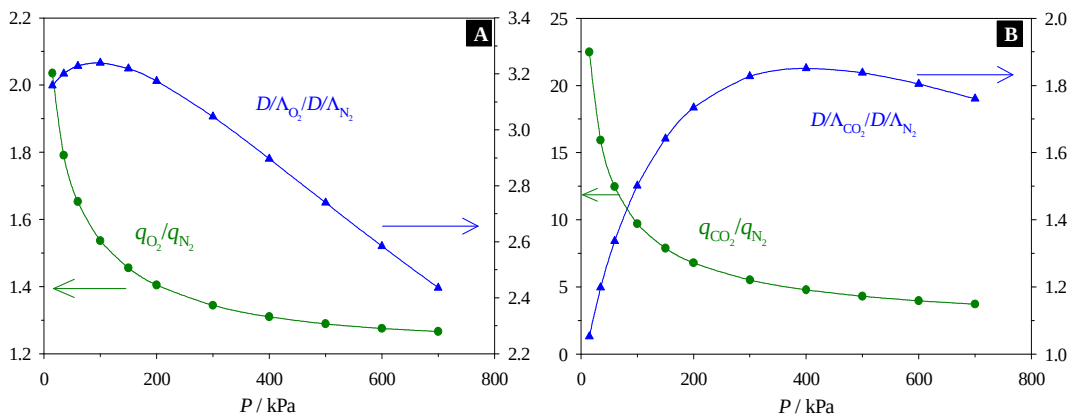

Figure 5.9 – Pressure dependence of the ratio of adsorption and diffusion coefficients for pairs O_2/N_2 and CO_2/N_2. Lines were added for readability.

The adsorption and diffusion coefficients of each gas correspond to the best fitting models of the equilibrium isotherm and adsorption uptake experiments. This c-CMSM sample combines adsorption and diffusion selectivity for O_2/N_2 and CO_2/N_2 separations.

5.5.3.2 Adsorption of C_3H_8 and C_3H_6

Adsorption equilibrium isotherms of C_3H_8 and C_3H_6 at 293, 343, 393 and 453 K for the pressure range 0-300 kPa are shown in Figure 5.10.

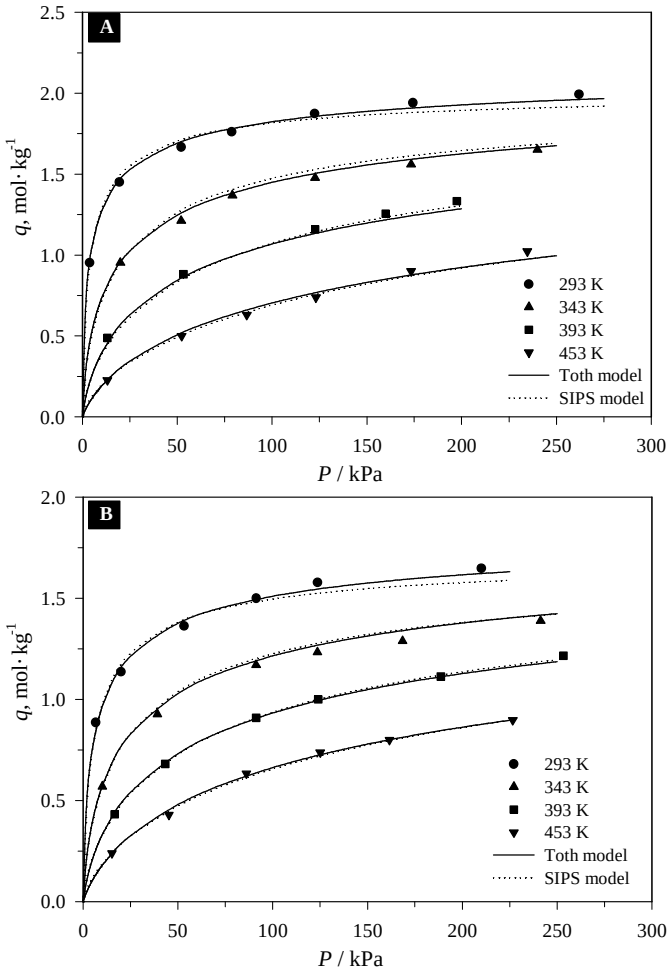

Figure 5.10 – Adsorption isotherms of C_3H_6 (A) and C_3H_8 (B) in c-CMSM1 at 293, 343, 393 and 453 K. The symbols refer to experimental data, the solid lines the fitting by the Toth equation and the dotted lines the fitting by the SIPS equation.

The adsorption equilibrium data was fitted using the Toth equation:

$$q = q^{\max} \frac{(bP)}{\left(1+(bP)^{u}\right)^{1/u}} \tag{5.13}$$

where u is the Toth model parameter. Figure 5.10 shows that the Toth equation provides a slightly better depiction of the adsorption behavior on sample M1 than the SIPS equation, particularly for 293 K. The isosteric heats of adsorption computed from both models are similar (Table 5.4).

Table 5.4 – Model parameters determined from fitting the experimental adsorption isotherms.

		C_3H_6	C_3H_8
Toth	q^{max} (mol·kg^{-1})	2.22	1.91
	u	0.49	0.52
	-ΔH (kJ·mol^{-1})	28.1	23.1
	b_0 (kPa^{-1})	1.4x10^{-5}	4.02x10^{-5}
	MSC	5.36	5.08
SIPS	q^{max} (mol·kg^{-1})	2.04	1.73
	n	1.47	1.43
	-ΔH (kJ·mol^{-1})	28.1	23.3
	b_0 (kPa^{-1})	2.20x10^{-6}	1.02x10^{-5}
	MSC	4.78	4.70

The diffusion coefficients were determined by fitting the experimental fractional uptake data to the isothermal micropore diffusion model (equation (5.6)). Figure 5.11 plots the experimental uptake curves of C_3H_8 and C_3H_6 at 293 K together with the respective fitting. For each temperature, the dependence of the diffusivity coefficients with pressure was well described by the Darken relation, which for a Toth isotherm is given by:

$$D = D_0 \frac{1}{1-\theta^{u}} \tag{5.14}$$

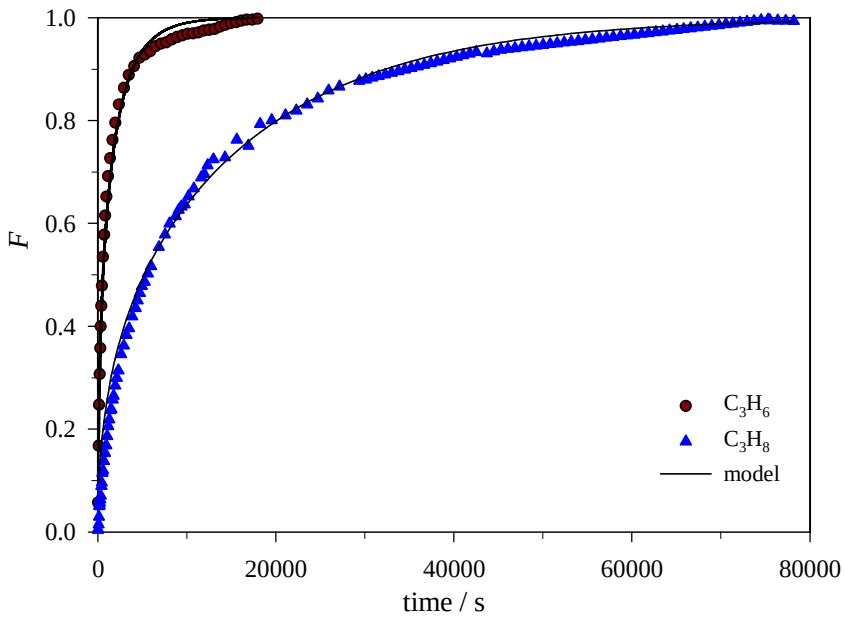

Figure 5.11 – Uptake curves of C_3H_8 and C_3H_6 in the c-CMSM M1 sample at 293 K ($P \approx 120$ kPa); points – experimental data; lines – micropore diffusion model.

Afterwards, the diffusivity coefficients at zero loading for each temperature were determined. The micropore diffusion of C_3H_8 and C_3H_6 is consistent with an activated process, so the diffusion coefficients at zero loading for different temperatures were correlated by the Arrhenius equation:

$$D_{0(T)} = D_{0(T\to\infty)} \exp\left(-E_a/\Re T\right) \tag{5.15}$$

where $D_{0(T\to\infty)}$ is the zero loading diffusivity limit for very high temperatures, E_a is the diffusion activation energy and $\Re$ is the ideal gas constant. Table 5.5 shows the zero loading diffusivity coefficients for different temperatures and the activation energies for the diffusion of C_3H_6 and C_3H_8. Once the diffusivity coefficients were determined, the ratio of these coefficients (diffusion selectivity) was computed.

Table 5.5 – Diffusivity coefficients at zero loading and activation energies determined from uptake experiments.

Temp / K	C_3H_8		C_3H_6	
	D_0 ($m^2 \cdot s^{-1}$)	E_a ($kJ \cdot mol^{-1}$)	D_0 ($m^2 \cdot s^{-1}$)	E_a ($kJ \cdot mol^{-1}$)
293	8.37×10^{-14}	22.8	6.84×10^{-13}	20.7
343	3.26×10^{-13}		2.36×10^{-12}	
393	9.02×10^{-13}		5.94×10^{-12}	
453	2.27×10^{-12}		1.37×10^{-11}	

In CMSM the diffusion selectivity results from the contribution of the entropic and enthalpic selectivities [17], and can be expressed by equation (5.16):

$$\frac{D_{0,C_3H_6}}{D_{0,C_3H_8}} = \exp\left(\frac{-\left(E_{a,C_3H_6} - E_{a,C_3H_8}\right)}{\Re T}\right)\exp\left(\frac{\left(S_{d,C_3H_6} - S_{d,C_3H_8}\right)}{\Re}\right) \qquad (5.16)$$

where S_d refers to the activation entropy of diffusion. The enthalpic (or energetic) selectivity is related to differences in diffusion activation energy. Meanwhile, the entropic selectivity expresses the restrictions in motion that each molecule faces as it diffuses along the constriction. Table 5.6 lists the impact of both contributions on the overall diffusion selectivities. It can be seen that both effects contribute to the overall diffusion selectivity, yet entropic selectivity is the most relevant.

Table 5.6 – Contribution of entropic and enthalpic selectivities to the overall C_3H_6/C_3H_8 diffusion selectivity.

Temp / K	D_{0,C_3H_6} / D_{0,C_3H_8}		
	Total	**Enthalpic effect**	**Entropic effect**
293	8.17	2.37	3.46
343	7.24	2.09	
393	6.58	1.90	
453	6.05	1.75	

5.5.4 Permeation experiments

All the permeability values shown in this section were calculated considering that the membrane thickness was 2 μm for all membranes (supported by SEM results).

5.5.4.1 Experimental and predicted permeabilities

Gas permeation experiments were carried out at 293 K, temperature at which membrane M1 displayed good sieving properties for the pairs O_2/N_2, CO_2/N_2, and C_3H_6/C_3H_8. The experimental results of membrane M1 were compared with the permeabilities (and permselectivities) computed from the adsorption and diffusion coefficients determined. One must recall that the permeability (L_i) is expressed as the ratio between the permeating flux and the driving force, normalized by the membrane thickness:

$$J_i = \frac{L_i}{\delta} \Delta P \qquad (5.17)$$

where δ is the membrane thickness and ΔP the permeation driving force (pressure difference between retentate and permeate). On the other hand, the flux (J_i) across the membrane can be expressed by:

$$J_i = -D_i \rho_s \frac{dq}{dz} \qquad (5.18)$$

where ρ_s is the skeleton density of the material (previously determined in Chapter 3), D_i is the fickian diffusivity coefficient of component *i*, *q* is the adsorbed amount and *z* is the spatial coordinate of the selective membrane (equal to zero for retentate surface and to δ, for permeate surface). Because $q = q^{\max}\theta$ and $D = D_0^{'} f(\theta)$, one can determine the permeability coefficients for each component *i* applying the following equation:

$$L_i = \frac{-q_i^{\max} \rho_s D_{0,i}^{'}}{\Delta p_i} \int_{\theta_i, z=0}^{\theta_i, z=\delta} f(\theta_i) d\theta \qquad (5.19)$$

where $f(\theta)$ is the thermodynamic correction factor, which has different expressions depending on the fitting model used for the diffusivities (cf. equations (5.11) and (5.12)). These expressions can be found in Appendix. Predicted O_2/N_2, CO_2/N_2 and C_3H_6/C_3H_8 permselectivities, plotted in Figure 5.12 as a function of feed pressure, were determined integrating equation (5.19).

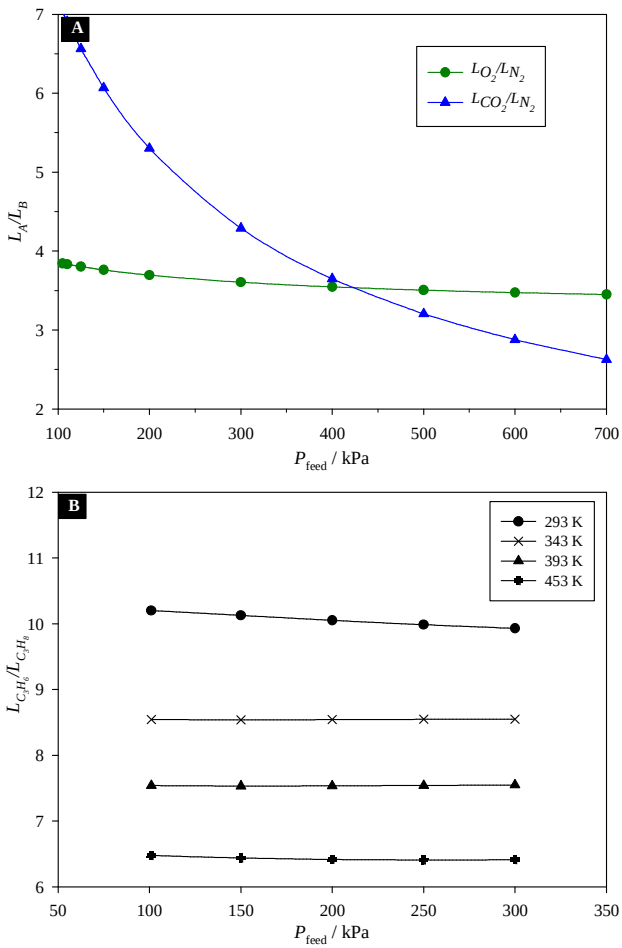

Figure 5.12 – Predicted permselectivities of c-CMSM1 as a function of feed pressure (permeate pressure = 100 kPa); (A) O_2/N_2 and CO_2/N_2 at 293 K; (B) C_3H_6/C_3H_8 permselectivities at different temperatures.

Figure 5.12A shows that the O_2/N_2 permselectivity does not depend much on pressure. Yet, the CO_2/N_2 permselectivity decreases with pressure, because the ratio of the sorption coefficients of CO_2 and N_2 is significantly higher for lower pressures. In the feed pressure range 100-700 kPa, the permselectivites range from 3.6-3.9 for O_2/N_2 and 2.7-7 for CO_2/N_2. The C_3H_6/C_3H_8 permselectivities (cf. Figure 5.12B) increase for lower temperatures, where the diffusion selectivity is the highest. It is also important to notice that the C_3H_6/C_3H_8 permselectivitity is mostly pressure independent for all temperatures, being roughly 10 at 293 K, 8.5 at 343 K, 7.5 at 393 K and 6.5 at 453 K. Clearly, the separation of C_3H_6/C_3H_8 mixtures should be carried out at low temperatures.

Table 5.7 shows the permeabilities (and permselectivities) determined experimentally for M1 and compares them with the predicted values from adsorption/diffusion studies. The permeation values are determined in steady-state conditions and only gas diffusion in wall-to-wall pores is relevant. Meanwhile, in adsorption experiments the diffusion coefficients are calculated by fitting the transient uptake curve, which is affected by the diffusion of the molecules in both the dead-end pores and wall-to-wall pores. This accounts for the differences in permeabilities. Additionally, the average size of these dead-end pores will likely differ from the average size of the wall-to-wall pores. So, the diffusion selectivities observed will be different for the two types of pores, which accounts for the differences in permselectivities observed.

Table 5.7 – Permeabilities and permselectivities of membrane M1 towards O_2, N_2, C_3H_6 and C_3H_8 determined by permeation and adsorption/diffusion experiments (293 K, feed pressure 400 kPa and permeate pressure 100 kPa).

Method	**Permeability (barrer)**				**Ideal selectivities (*S*)**	
	N_2	**O_2**	**C_3H_8**	**C_3H_6**	**O_2/N_2**	**C_3H_6/C_3H_8**
Permeation	11.5	64.0	17.8	108	5.6	6.1
Adsorption	51.5	195	2.56	25.5	3.4	9.9

5.5.4.2 Effect of composition of c-CMSM on gas permeation properties

The permeabilities and ideal selectivities of membranes M1 to M6 for several gases are summarized in Table 5.8 and Table 5.9 . The permeability towards all gases exhibited little dependence with the transmembrane pressure difference so all the results presented are for feed pressure 400 kPa and permeate pressure 100 kPa.

Table 5.8 – Permeability of membranes M1 to M6 towards probe gases at 293 K (feed pressure = 400 kPa; permeate pressure = 100 kPa).

Memb	Permeability (barrer)					
	N_2	O_2	He	CO_2	C_3H_8	C_3H_6
M1	11.5	64.0	-	-	17.8	108
M2	5.3	34.4	282	229	9.5	141
M3	8.9	34.3	156	326	11.9	166
M4	31.7	107	235	629	40.4	225
M5	1.3	7.56	-	-	7.9	39.5
M6	256	954	-	-	31.2	593

Table 5.9 – Ideal selectivity of membranes M1 to M6 for gas pairs of interest at 293 K (feed pressure = 400 kPa; permeate pressure = 100 kPa).

Memb	Ideal Selectivities (*S*)			
	O_2/N_2	CO_2/N_2	He/N_2	C_3H_6/C_3H_8
M1	5.6	-	-	6.1
M2	6.5	43.3	53.4	14.9
M3	3.8	36.6	17.4	13.9
M4	3.4	19.8	7.4	5.6
M5	6	-	-	5
M6	3.7	-	-	18.9

Figure 5.13 illustrates the effect of the precursor contents of boehmite and resin on the sieving properties of the carbonized membranes. Membrane permeabilities and ideal selectivies for O_2/N_2 and C_3H_6/C_3H_8 as a function of the boehmite content are shown in Figure 5.13A and Figure 5.13B, respectively. On the other hand, Figure 5.13C and Figure 5.13D show, respectively, the effect of the resin content on permeabilites and ideal selectivities.

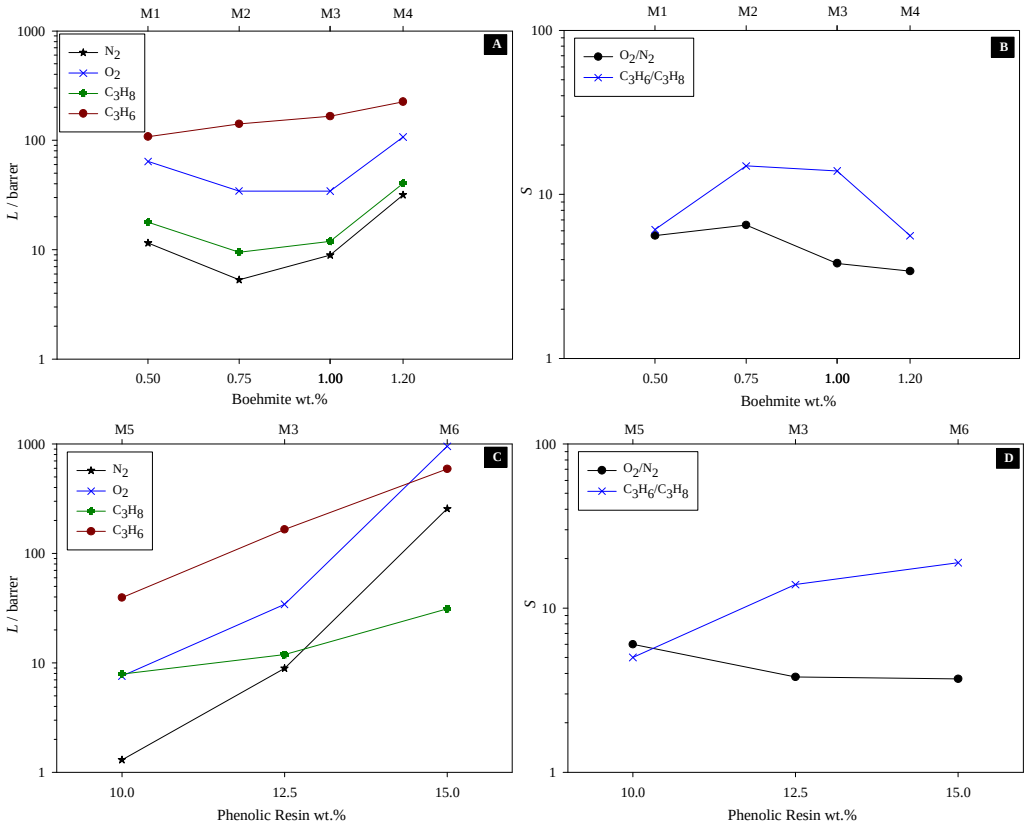

Figure 5.13 – Dependence of the membrane permeabilities and ideal selectivities with the precursor content of boehmite (A and B, respectively) and phenolic resin (C and D, respectively) at 293K. Lines are used for readability.

Roughly, when the boehmite content is between 0.75 and 1 wt.% the membrane permeability towards all gases is minimum, while the O_2/N_2 and C_3H_6/C_3H_8 ideal selectivities are maxima. At the same time, when resin content is 15 wt.%, the

permeability of the membranes towards O_2 is the highest, while O_2/N_2 selectivity is the lowest. All these results are consistent with the behavior observed by Robeson for the performance of polymer membranes [18]; an increase in selectivity occurs at the expense of a decrease in permeability and vice-versa. Yet, for C_3H_6/C_3H_8 separation, both the membrane permeability towards C_3H_6 and C_3H_6/C_3H_8 selectivity are maxima when the resin content is 15 wt.%.

The results obtained were plotted with the semi-empirical upper bound curves devised by Robeson [19] (for O_2/N_2 separation) and Burns and Koros [20] (for C_3H_6/C_3H_8 separation) – Figure 5.14. These plots, built with permeation data of polymer membranes, are widely acknowledged as the state-of-the art curves for gas separation by polymer membranes.

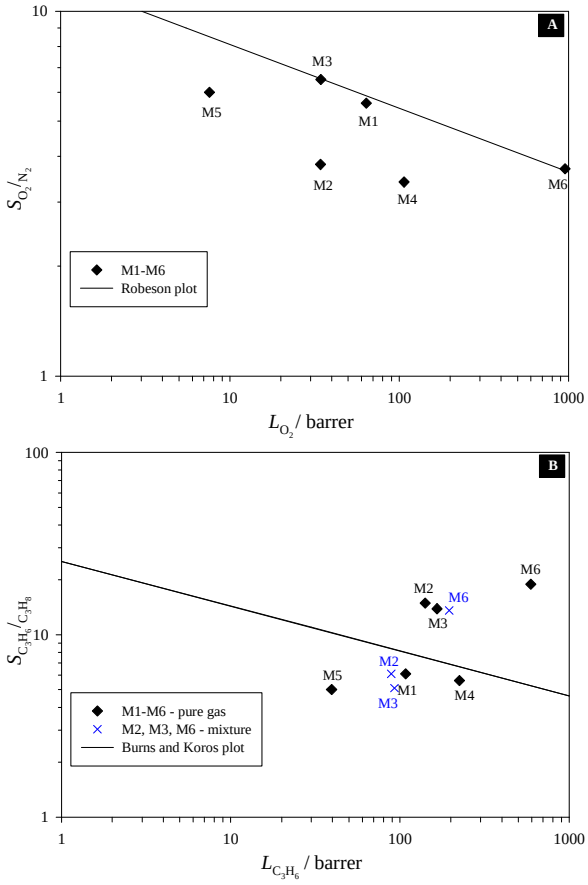

Figure 5.14 – Comparison of permeation results of membranes M1 to M6 with upper bound curves for O_2/N_2 and C_3H_6/C_3H_8 separations [19-20].

The results for O_2/N_2 separation are below the Robeson upper bound for all membranes. However, the results for C_3H_6/C_3H_8 are above the Burns and Koros upper bound plot, for membranes M2, M3 and M6. Hence, the composite membrane is less suitable to separate pairs of molecules of smaller kinetic diameters, such as O_2/N_2 and more suitable to separate larger molecules, such as C_3H_6/C_3H_8.

As the composite membranes exhibited good results for the separation of C_3H_6 and C_3H_8, mixed gas experiments were carried out with the most promising membranes (M2, M3 and M6). Table 5.10 shows the steady state results achieved when an equimolar mixture of C_3H_8 and C_3H_6 was fed. Moreover, these results are also plotted in Figure 5.14. The separation factors obtained are below the ideal selectivity values and the permeability towards both hydrocarbons decreases. This result is consistent with the findings of Chng *et al.* [21]. These results imply that the interactions between the molecules of C_3H_8 and C_3H_6 differ from C_3H_8/C_3H_8 or C_3H_6/C_3H_6 interactions. In a mixture feed, C_3H_8 and C_3H_6 should impact negatively the diffusion of each other to the constrictions, causing a decrease in permeability. This competition causes a bigger decrease in the diffusion of C_3H_6, the faster species, so selectivity also decreases. For gas mixtures, membrane M6 is still well above the trade-off line, but membranes M2 and M3 are now slightly below.

Table 5.10 – C_3H_6 permeability and C_3H_6 /C_3H_8 separation factor of membranes M2, M3 and M6 using an equimolar feed of C_3H_6 and C_3H_8 (293K, mixture feed pressure = 400 kPa).

Membrane	C_3H_6 Permeability / barrer	C_3H_6 /C_3H_8 Separation Factor
M2	89	6.1
M3	93	5.1
M6	196	13.6

5.5.5 Stability in air and Regeneration

After mono and bicomponent experiments, membrane M3 was exposed for 15 days to ambient air (humidity not controlled). Afterwards, the membrane permeability towards N_2 was re-determined. The permeability was 10 % of the value measured for the fresh membrane, indicative of pore clogging with O_2 and/or water vapor [5]. However, when membrane M3 was regenerated for two hours at 550 ºC in N_2 atmosphere, the membrane recovered 80 % of its initial permeability value. The use of higher soaking times did not improve this result and temperatures higher than 550 ºC were not considered, since the membrane pyrolysis temperature was 550 ºC. At the moment, passivation treatments with hydrogen are being studied to decrease the hydrophilic nature of the surface of the CMSM and improve their long-term stability.

5.6 Conclusions

Phenolic resin-based carbon molecular sieve membranes loaded with boehmite nanoparticles were prepared for adsorption and kinetic studies and as supported membranes for permeation studies. Adsorption isotherms and diffusion uptake rates for N_2, O_2 and CO_2 were determined at 293 K; the CMS exhibited kinetic and adsorption selectivity for O_2/N_2 and CO_2/N_2. The adsorption and kinetic study concerning C_3H_6 and C_3H_8 was performed between 293 and 453 K. The best results were for 293 K, where the ratio of the diffusivity constants of C_3H_6 and C_3H_8 was the highest.

Membranes were prepared from composite solutions with different amounts of phenolic resin (from 10 to 15 wt.%) and boehmite nanoparticles (0.5 to 1.2 wt.%). The optimum composition of the precursor for O_2/N_2 and C_3H_6/C_3H_8 gas separation was determined. For O_2/N_2 separation higher selectivities were obtained at the expense of lower permeabilities and no clear correlation could be

established between the resin and boehmite contents and the performance of the membranes. For C_3H_6/C_3H_8 the membrane performed best when boehmite content was between 0.75 and 1 wt.% and phenolic resin content was 15 wt.%; ideal selectivities up to 19 and real selectivites up to 13.6 were obtained, with high C_3H_6 permeability values. The performance of the CMSM for the pair C_3H_6/C_3H_8 was above the upper bound curve for polymeric membranes, making it promising for olefin purification. Aging effects were observed after 15 days of exposure to ambient air, but treatment in N_2 atmosphere at 550 ºC regenerated 80 % of the membrane's initial performance.

5.7 Appendix – Permeability expressions

5.7.1 Darken-SIPS (N_2)

$$f(\theta_i) = \frac{1}{1-\theta_i}$$

$$\int f(\theta_i) = -\ln\left(1-\theta_i\right)$$

$$L_i = \frac{q^{\max,i}\rho_s D_{0,i} n_i}{\Delta p_i} \ln\left[\frac{q^{\max,i} - q^{l,i}}{q^{\max,i} - q^{h,i}}\right]$$

Where q^h and q^l are the adsorbed amounts at the high (h) and low (l) pressure sides of the membrane.

5.7.2 Chen-Yang (CO_2, O_2)

$$f(\theta_i) = \frac{1-\theta_i + \lambda/2\theta_i\left(2-\theta_i\right) + H\left(1-\lambda\right)\left(1-\lambda\right)\lambda/2\theta_i^2}{\left(1-\theta_i+\theta_i\lambda/2\right)^2}$$

For λ >=1 it reduces to $f(\theta_i) = \dfrac{1-\theta_i+\lambda/2\theta_i\left(2-\theta_i\right)}{\left(1-\theta_i+\theta_i\lambda/2\right)^2}$

Integrating it becomes

$$\int f(\theta_i)d\theta = \frac{4\ln\left(abs\left(\theta_i\left(\lambda-2\right)+2\right)\right)\left(\lambda^2-\lambda+2\right)}{\left(\lambda-2\right)^3} + \frac{4\lambda^2}{\left(\theta_i\left(\lambda-2\right)+2\right)\left(\lambda-2\right)^3} - \frac{2\theta_i\lambda}{\left(\lambda-2\right)^2}$$

$$L_i = \frac{q^{\max,i}\rho_s D_{0,i}^{'}}{\Delta p_i}\left\{\left(\frac{4\ln\left(abs\left(\theta_{i,L}\left(\lambda-2\right)+2\right)\right)\left(\lambda^2-\lambda+2\right)}{\left(\lambda-2\right)^3} + \frac{4\lambda^2}{\left(\theta_{i,L}\left(\lambda-2\right)+2\right)\left(\lambda-2\right)^3} - \frac{2\theta_{i,L}\lambda}{\left(\lambda-2\right)^2}\right) - \right.$$

$$\left. -\left(\frac{4\ln\left(abs\left(\theta_{i,H}\left(\lambda-2\right)+2\right)\right)\left(\lambda^2-\lambda+2\right)}{\left(\lambda-2\right)^3} + \frac{4\lambda^2}{\left(\theta_{i,H}\left(\lambda-2\right)+2\right)\left(\lambda-2\right)^3} - \frac{2\theta_{i,H}\lambda}{\left(\lambda-2\right)^2}\right)\right\}$$

5.7.3 Darken-Toth (C_3H_8, C_3H_6)

$$f(\theta_i) = \frac{1}{1-\theta_i^t}$$

$$\int f(\theta_i) d\theta = \theta_i F\left(1;\frac{1}{t};1+\frac{1}{t};\theta_i^t\right)$$

Where $F\left(1;\frac{1}{t};1+\frac{1}{t};\theta^t\right)$ is a hypergeometric function, defined in the form of a hypergeometric series as:

$$F(a;b;c;z) = \sum_{n=0}^{\infty} \frac{(a)_n (b)_n z^n}{(c)_n n!} = 1 + \frac{abz}{1!c} + \frac{a(a+1)b(b+1)z^2}{2!c(c+1)} + \ldots$$

$$L_i = \frac{q^{\max,i}\rho_s D_{0,i}}{\Delta p_i}\left(\theta_{i,L} F\left(1;\frac{1}{t};1+\frac{1}{t};\theta_{i,L}^t\right) - \theta_{i,H} F\left(1;\frac{1}{t};1+\frac{1}{t};\theta_{i,H}^t\right)\right)$$

5.8 Nomenclature

Variables	Definition	Units
b	Adsorption affinity coefficient	Pa^{-1}
D	Diffusivity coefficient	$m^{-2} \cdot s^{-1}$
D_0	Diffusivity at zero loading	$m^{-2} \cdot s^{-1}$
Err	Fitting error	-
F	Fractional uptake (at a given time)	-
F_c	Chemisorption fractional uptake	-
$H()$	Heaviside function	-
J	Permeating flux	$mol \cdot m^{-2} \cdot s^{-1}$
k	LDF mass transfer coefficient	s^{-1}
L	Membrane permeability	$mol \cdot m \cdot m^{-2} \cdot s^{-1}$
MSC	Model selection criteria	-
m_t	Mass at instant t	kg
m_0	Initial mass	kg
m_∞	Equilibrium mass	kg
n	SIPS equation parameter	-
n_p	Number of parameters	-
n_v	Number of experimental values	-
p	Partial pressure	Pa
P	Total pressure	Pa
q	Surface concentration	$mol \cdot kg^{-1}$
q^{exp}	Experimental surface concentration	$mol \cdot kg^{-1}$
q_{avg}^{exp}	Average of experimental surface concentration	$mol \cdot kg^{-1}$
q^{max}	Maximum surface concentration	$mol \cdot kg^{-1}$
q^{model}	Surface concentration given by model	$mol \cdot kg^{-1}$
r_c	Chemisorption uptake rate	s^{-1}
$\Re$	Gas constant	$Pa \cdot m^3 \cdot mol^{-1} \cdot K^{-1}$

S	Permselectivity	-
S_d	Activation entropy of diffusion	
t	time	s
t_c	Chemisorption time	s
u	Toth equation parameter	-
T	Absolute temperature	K
z	Spatial coordinate	m

Greek	Definition	Units
λ	Blocking parameter	-
θ	Fractional coverage of the pore surface	-
δ	Membrane thickness	m
Γ	Thermodynamic correction factor	-
ζ	Elovich equation constant	-
ξ	Elovich equation constant	s^{-1}
Λ	Half of slab thickness	m
ρ_s	Solid Density	$mol \cdot kg^{-3}$

Subscript	Definition
i	species i

Superscripts	Definition
h	High pressure side of the membrane
l	Low pressure side of the membrane

5.9 Acknowledgments

Miguel Teixeira and Margot Llosa are grateful to the Portuguese Foundation for Science and Technology (FCT) for their doctoral grant (references SFRH/BD/24768/2005 and SFRH/BD/61898/2009, respectively). Marta Campo also acknowledges FCT for her post-doctoral grant (reference SFRH/BPD/65377/2009). The authors also acknowledge financing from FCT through the projects POCTI/EQU/59344/2004 and POCTI/EQU/59345/2004. Finally, the authors are thankful to CEMUP for the SEM analyses (REEQ/1062/CTM/2005 and REDE/1512/RME/2005 funding provided by FCT).

5.10 References

[1] S.M. Saufi, A.F. Ismail, Fabrication of carbon membranes for gas separation - a review, Carbon, 42 (2004) 241-259.
[2] W.J. Koros, R. Mahajan, Pushing the limits on possibilities for large scale gas separation: which strategies?, J Membrane Sci, 181 (2000) 141-141.
[3] C.W. Jones, W.J. Koros, Carbon Molecular-Sieve Gas Separation Membranes .2. Regeneration Following Organic-Exposure, Carbon, 32 (1994) 1427-1432.
[4] C.W. Jones, W.J. Koros, Characterization of Ultramicroporous Carbon Membranes with Humidified Feeds, Ind Eng Chem Res, 34 (1995) 158-163.
[5] S. Lagorsse, F.D. Magalhaes, A. Mendes, Aging study of carbon molecular sieve membranes, J Membrane Sci, 310 (2008) 494-502.
[6] I. Menendez, A.B. Fuertes, Aging of carbon membranes under different environments, Carbon, 39 (2001) 733-740.
[7] L. Brandao, D. Fritsch, L.M. Madeira, A.M. Mendes, Kinetics of propylene hydrogenation on nanostructured palladium clusters, Chem Eng J, 103 (2004) 89-97.
[8] D.D. Do, Adsorption analysis: equilibria and kinetics, Imperial College Press, London, 1998.
[9] S.W. Rutherford, J.E. Coons, Adsorption equilibrium and transport kinetics for a range of probe gases in Takeda 3A carbon molecular sieve, J Colloid Interf Sci, 284 (2005) 432-439.
[10] E. Glueckauf, Theory of Chromatography .10. Formulae for Diffusion into Spheres and Their Application to Chromatography, T Faraday Soc, 51 (1955) 1540-1551.
[11] I.S. Mclintoc, Elovich Equation in Chemisorption Kinetics, Nature, 216 (1967) 1204-1205.

[12] Y.D. Chen, R.T. Yang, Concentration-Dependence of Surface-Diffusion and Zeolitic Diffusion, Aiche Journal, 37 (1991) 1579-1582.
[13] D.W. Breck, Zeolite Molecular Sieves, Krieger Publishing Company, 1974.
[14] S.W. Rutherford, D.D. Do, Characterization of carbon molecular sieve 3A, Langmuir, 16 (2000) 7245-7254.
[15] Y.S. Bae, C.H. Lee, Sorption kinetics of eight gases on a carbon molecular sieve at elevated pressure, Carbon, 43 (2005) 95-107.
[16] C.R. Reid, K.M. Thomas, Adsorption of gases on a carbon molecular sieve used for air separation: Linear adsorptives as probes for kinetic selectivity, Langmuir, 15 (1999) 3206-3218.
[17] A. Singh, W.J. Koros, Significance of entropic selectivity for advanced gas separation membranes, Ind Eng Chem Res, 35 (1996) 1231-1234.
[18] L.M. Robeson, Correlation of Separation Factor Versus Permeability for Polymeric Membranes, J Membrane Sci, 62 (1991) 165-185.
[19] L.M. Robeson, The upper bound revisited, J Membrane Sci, 320 (2008) 390-400.
[20] R.L. Burns, W.J. Koros, Defining the challenges for C_3H_6/C_3H_8 separation using polymeric membranes, J Membrane Sci, 211 (2003) 299-309.
[21] M.L. Chng, Y.C. Xiao, T.S. Chung, M. Toriida, S. Tamai, Enhanced propylene/propane separation by carbonaceous membrane derived from poly(aryletherketone)/2,6-bis(4-azidobenzylidene)-4-methyl-cyclohexanone interpenetrating network, Carbon, 47 (2009) 1857-1866.

Chapter 6: **Composite carbon molecular sieve membranes – adsorption, kinetic and permeation studies – Part II**

(Teixeira, M., Campo, M., Tanaka, D., Llosa, M., Sousa, J., Madeira, L. M., Mendes, A., submitted to Journal of Membrane Science, 2011)

6.1 Abstract

Composite carbon molecular sieve membranes (c-CMSM) were prepared from phenolic resins loaded with boehmite (γ-AlO(OH)) and silver (Ag) nanoparticles. The resin/γ-AlO(OH) ratio was kept constant and precursors with $0 < AgNO_3 < 1$ wt.% were prepared. After pyrolysis at 550 ºC, silver loaded c-CMSMs ($0 < Ag < 13.8$ wt.%) were obtained. The effect of the Ag content on the separation properties of the pyrolysed c-CMSMs was investigated. Carbon-Al_2O_3-Ag membranes exhibited higher O_2/N_2, CO_2/N_2 and C_3H_6/C_3H_8 permselectivities than carbon-Al_2O_3 ones when Ag content was between 3.1 and 6.0 wt.% but not for silver content higher than 6.0 wt.%. The optimum membrane performance correlated with the size of Ag nanoclusters; smaller Ag clusters originated higher permselectivities. After silver doping, the C_3H_6/C_3H_8 permselectivity increased from 8 to 38 (3.1 wt.% Ag) and 30 (6.0 wt.% Ag). The C_3H_6/C_3H_8 separation factor was 20.5 (3.1 wt.% Ag) and 14.1 (6.0 wt.% Ag) and the permeabilities towards C_3H_6 decreased 20-30 %, yet they still placed well above the upper bound curve for polymer membranes. Adsorption studies showed that the C_3H_6/C_3H_8 permselectivity was mainly related to the diffusion selectivity.

6.2 Introduction

Membrane based gas separations are becoming viable alternatives to consolidated processes such as pressure swing adsorption or distillation [1-2]. Carbon molecular sieve membranes (CMSM) are one of the most promising alternative materials but still face some obstacles towards their commercial implementation. The only company to commercialize CMSM was the Israeli company Carbon Membranes, which bankrupted in 2001. The strategy defined by Carbon Membranes included a laborious post-treatment step involving several CVD and activation steps resulting in expensive membranes. It is clear that a successful transition of CMSM from laboratory to industrial scale requires the simplification of the preparation procedure (e.g., removing some pre- or post- treatments) without compromising their stability and sieving properties. One possible strategy to overcome some of the current limitations is the synthesis of composite carbon molecular sieve membranes (c-CMSM); it has been reported an increase in the selectivity and/or permeability of the CMSM upon addition of metal ions [3-5], silica [6-7] and zeolites [8-11], among others. This increase in performance may avoid the need of some pre- or post-treatments steps, hence making this strategy economically more feasible.

This work proposes the incorporation of inorganic nanofillers (γ-AlO(OH) and Ag) in a phenolic resin to synthesize a c-CMSM. Gas permeation experiments were conducted on c-CMSM with different amounts of Ag (in the same carbonization conditions) so determine the effect of Ag on the separation of several gas pairs of interest. Adsorption isotherms/uptake rates were carried out for O_2, N_2, CO_2, C_3H_6 and C_3H_8 to assess the controlling mass transport mechanism (diffusion or adsorption) responsible for O_2/N_2, CO_2/N_2 and C_3H_6/C_3H_8 separations.

6.3 Experimental

6.3.1 Membrane Synthesis

The precursor dispersions were prepared as indicated in Chapter 4. Briefly, the precursors were prepared by mixing a diluted phenolic resin with an aqueous dispersion of γ-AlO(OH) nanoparticles. Afterwards, $AgNO_3$ (Merck) was added in different proportions. A complexant (ethylenodiamine) was also added to prevent silver agglomeration. Table 6.1 shows the composition of the precursor dispersions used and of the resulting composite membranes. The ratio between carbon and alumina in the carbonized membranes was estimated from the results of the immediate analysis on a Carbon-Al_2O_3 membrane (Chapter 3). The final compositions were determined assuming that $AgNO_3$ decomposes completely originating a mass loss of 37 %. After preparation, the dispersions were dip coated to α-Al_2O_3 supports or cast upon Teflon dishes. Carbonization was carried out under N_2 at 550 ºC.

Table 6.1 – Mass composition of the dispersion precursors and the resulting composite membranes.

Membrane	Precursor (wt.%)			c-CMSM (wt.%)		
	Resin	γ-AlO(OH)	$AgNO_3$	C	γ-Al_2O_3	Ag
M1	13	0.88	0	81.3	18.7	0
M2	13	0.88	0.2	78.7	18.2	3.1
M3	13	0.88	0.4	76.4	17.6	6.0
M4	13	0.88	0.6	74.2	17.1	8.7
M5	13	0.88	0.8	72.1	16.6	11.3
M6	13	0.88	1.0	70.1	16.2	13.7

6.3.2 Morphological and Structural Characterization

Mass loss curves were determined in a thermogravimetric balance under a N_2 atmosphere in the temperature range 20-900 ºC (heating rate 10 ºC·min^{-1}). Scanning electron microscopy (SEM) was used to provide information on the distribution of Ag in the carbon matrix and the thickness of the c-CMSM. The specifications of the thermogravimetric balance and the microscope can be found in Chapter 3.

6.3.3 Permeation Experiments

For gas permeation experiments, the c-CMSMs were placed in the permeation cell detailed in Chapter 5. Briefly, the feed side was pressurized, while the permeate side was left at atmospheric pressure and mass flow meters were used to measure the steady state permeating fluxes for the gas/mixtures being studied. In bicomponent experiments, the composition of the feed and permeating streams was determined with a GC. The permeability towards each component *i* (*L*) was determined from:

$$L_i = J_i \frac{\delta}{\Delta p_i} \tag{5.20}$$

where *J* is the permeating flux (measured by flow meter), Δp is the partial pressure difference between the retentate and permeate and δ the membrane thickness (determined from SEM). The permselectivity (*S*) expressed the ratio of the pure-gas permeability towards two components (*i* and *j*)

$$S = \frac{L_{i,pure\ gas}}{L_{j,pure\ gas}} \tag{5.21}$$

and the separation factor (S_f) the ratio of mixed-gas permeability towards the same components.

$$S_f = \frac{L_{i,mixed\ gas}}{L_{j,mixed\ gas}} \tag{5.22}$$

6.3.4 Adsorption Isotherms/Uptake Experiments

Adsorption experiments were performed on a carbon-Al_2O_3-Ag sample either using a Rubotherm® balance (for the adsorption isotherms of CO_2, O_2 and N_2 at 293 K) or a VTI sorption analyzer equipped with a microbalance (for the adsorption equilibrium isotherms of C_3H_6 and C_3H_8 at 293, 343, 393 and 453 K). For all gases, the transient uptake curves were used to determine the diffusion coefficients and models were used to fit the dependence of the diffusion coefficients with loading.

6.4 Results

6.4.1 Thermogravimetric analyses

Figure 6.1 shows the mass loss curves corrected for solvent loss for membranes M1, M2, M4 and M6 in the temperature range 250-900 ºC.

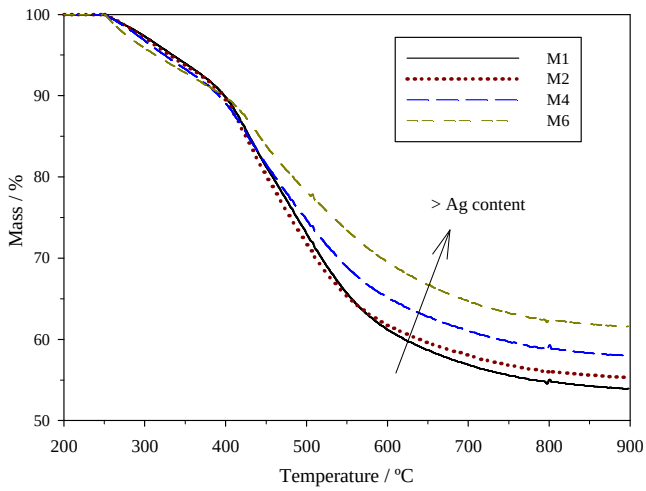

Figure 6.1 – Characteristic curves for membranes M1, M2, M4 and M6.

It can be seen that the shape of the curve is similar for all membranes and that the burn-off decreases as the Ag content increases. The mass derivative curves observed in Figure 6.2 show that the pyrolysis mass loss peak shifts from around 475 ºC for the membrane without Ag (M1) to around 450 ºC for the membranes with Ag.

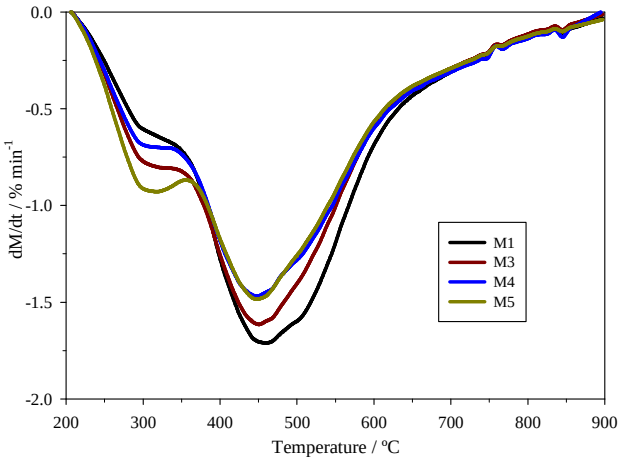

Figure 6.2 - Mass derivative curves for membranes M1, M3, M4 and M5.

6.4.2 XRD

Figure 6.3 shows X-ray diffraction spectra of membranes M1, M2, M3 and M4. The pattern of the Ag functionalized membranes exhibits five diffraction peaks, corresponding to the five diffraction planes of Ag. The size of the Ag nanoclusters, determined by refinement of the experimental diffraction data with the spectrum of pure Ag, is shown in Table 6.2. Clearly, Ag aggregates into smaller clusters when the Ag content in the c-CMSM ranges between 3.1 and 6.0 wt. %. In all XRD spectra a broad peak is observed at ca. $2\theta \approx 20$ º, characteristic of amorphous carbon.

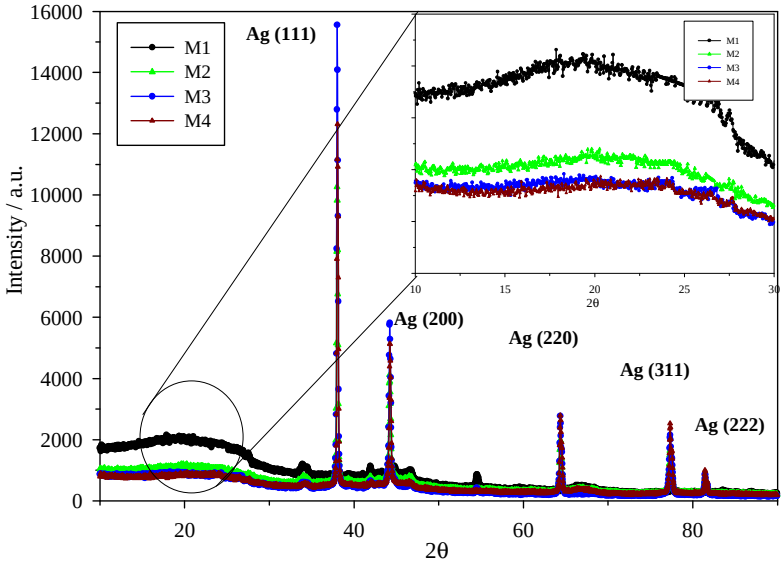

Figure 6.3 – XRD diffraction spectra of membranes M1, M2, M3 and M4.

As the Ag content increases, the intensity of this peak decreases because the structure arrangement becomes less graphitic. Moreover, the angle of the broad peak also increases as the Ag content increases. However, the differences are small (within experimental error) and for membranes M3 and M4, the peak is not unambiguously distinguishable – Figure 6.3. So, a similar average pore size should be expected.

Table 6.2 – Ag cluster size in membranes M1 to M6 determined from XRD refinement.

Membrane	Ag Cluster Average Size (nm)
M1	-
M2	28
M3	30
M4	47
M5	44
M6	42

6.4.3 SEM/EDS

SEM images of membranes M1, M2, M3 and M5 are pictured in Figure 6.4. In all cases, a uniform 2.5-3.5 μm thick composite membrane is observed on top of an α-Al_2O_3 support tube. The thickness of the Ag-functionalized membranes (M2, M3 and M5) is approximately the same and no noticeable trend is observed when Ag content changes. The SEM images show small white dots, confirmed from EDS analysis to be Ag nanoclusters, homogeneously distributed in the carbon matrix.

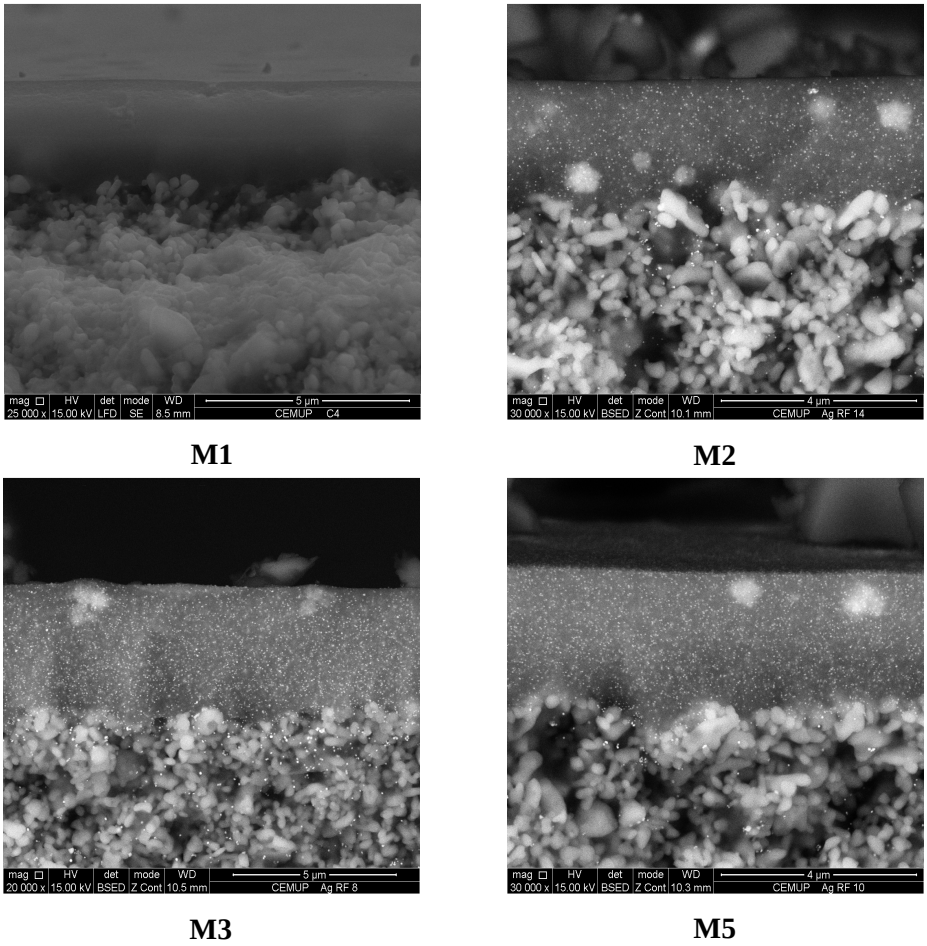

Figure 6.4 – SEM images of the cross-section of membranes M1, M2, M3 and M5.

6.4.4 Permeation experiments

The effect of Ag loading on mono and bicomponent permeation experiments at 293 K was assessed using several probe gas species: He, N_2, O_2, CO_2, C_3H_8, and C_3H_6. The permeability of membranes M1 to M6 towards the above mentioned species and ideal selectivities for O_2/N_2, CO_2/N_2, He/N_2 and C_3H_6/C_3H_8 are shown in Figure 6.5 as a function of Ag wt.%.

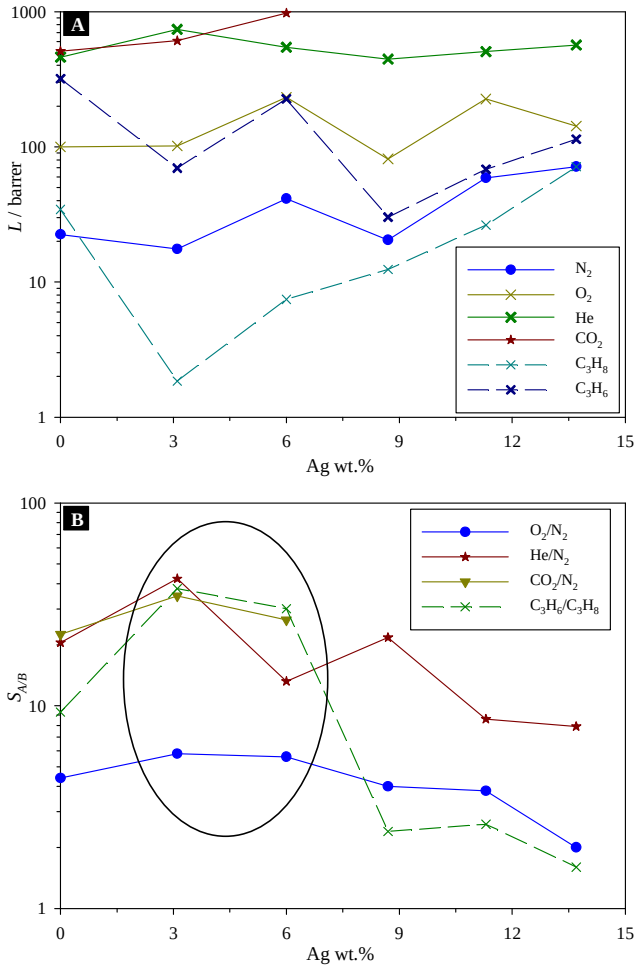

Figure 6.5 – Effect of the content of Ag on the permeabilities towards He, N_2, O_2, CO_2, C_3H_8, C_3H_6 (A) and on the O_2/N_2, He/N_2, CO_2/N_2 and C_3H_6/C_3H_8 permselectivities (B) (feed pressure = 500 kPa; permeate pressure = 100 kPa, T=293 K).

It can be seen that for all gas pairs, with the exception of He/N_2, the highest permselectivities are for membranes M2 and M3 (3.1 < Ag wt.% < 6.0). For the permanent gases this increase in selectivity did not occur at the expense of a decrease in permeability but for the hydrocarbons an average decrease is observed up to 6.0 wt.% of Ag. A possible explanation is that the pore network of membranes M2 and M3 has a smaller amount of larger constrictions than membrane M1, which impacts negatively on the permeability towards the two hydrocarbons but has a smaller impact on the permeability of the smaller penetrants. This also accounts for the fact that the relative increase in C_3H_6/C_3H_8 ideal permselectivity is higher than the increase in He/N_2, CO_2/N_2 and O_2/N_2 permselectivities. However, for membranes with higher Ag contents, the performance becomes poorer. This should be related to the size of the Ag clusters that increases with the Ag concentration. These results were compared to the semi-empirical curves devised by Robeson [12] for O_2/N_2, CO_2/N_2 and He/N_2 separations and by Burns and Koros [13] for C_3H_6/C_3H_8 separation - Figure 6.6.

The results of membranes M2 and M3 for CO_2/N_2, He/N_2 and O_2/N_2 are close to the upper bound curve but for C_3H_6/C_3H_8 are well above the upper bound plot. Because M2 and M3 exhibited particularly promising C_3H_6/C_3H_8 separation properties, they were tested with equimolar C_3H_6/C_3H_8 feed streams. Table 6.3 summarizes the results achieved.

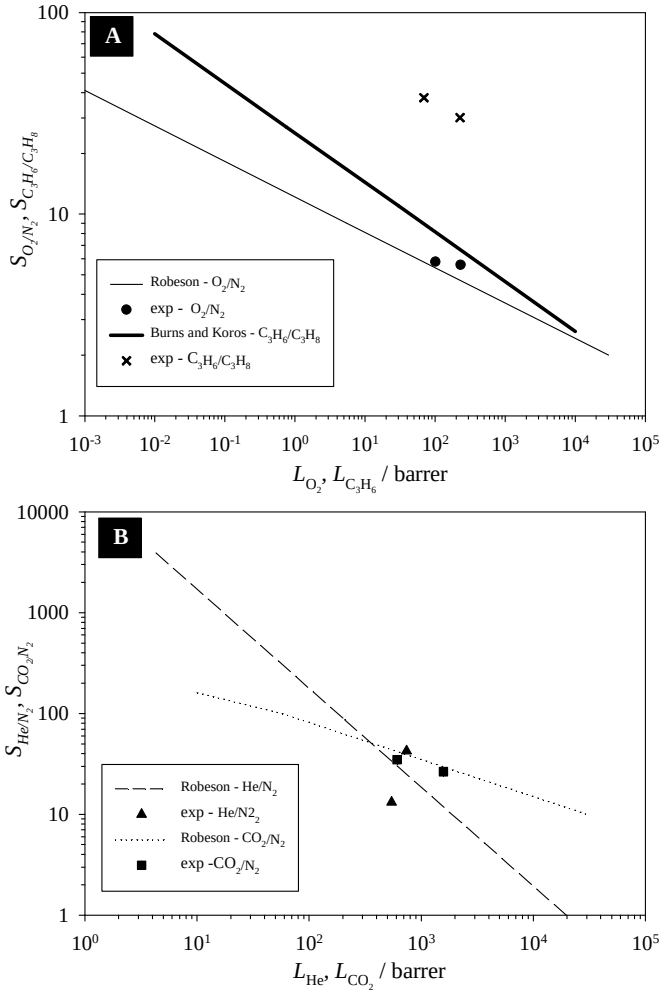

Figure 6.6 – Comparison of permeation results of membranes M2 and M3 with upper bound curves for O_2/N_2 and C_3H_6/C_3H_8 separations (A) and He/N_2 and CO_2/N_2 separations (B) [12-13].

Table 6.3 – C_3H_6 permeability and C_3H_6/C_3H_8 separation factor of membranes M2 and M3 using an equimolar feed of C_3H_6 and C_3H_8 (293K, mixture feed pressure = 400 kPa).

Membrane	$L_{C_3H_6}$ / barrer	$S_{f\ C_3H_6/C_3H_8}$
M2	46.5	20.5
M3	168.5	14.1

These results are plotted in Figure 6.7 together with the corresponding pure gas permeance data, for comparison purposes. The separation factors obtained are below the ideal selectivity values and the permeabilities towards C_3H_6 are also smaller, while the permeabilities towards C_3H_8 are slightly higher.

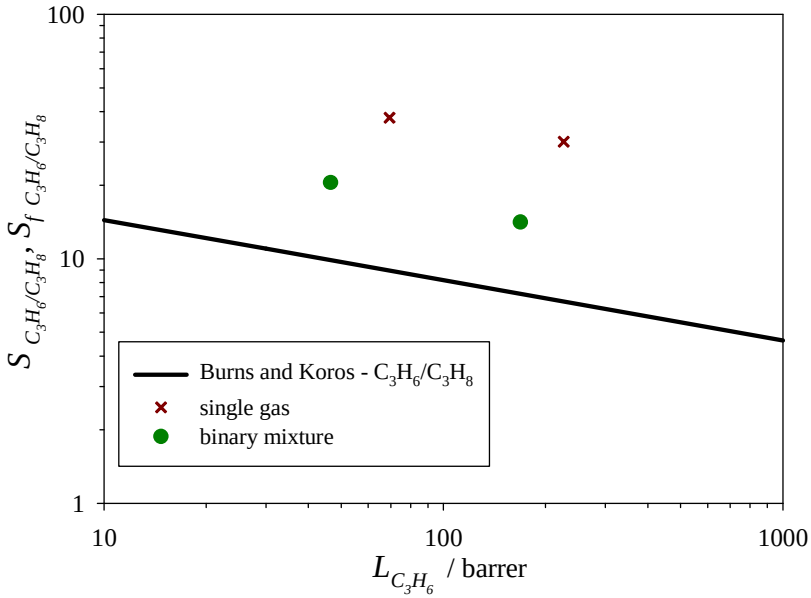

Figure 6.7 – Permeation results of membranes M2 and M3 for C_3H_6/C_3H_8 separation in single gas and mixed gas experiments.

The decrease in permeability towards C_3H_6 and in the separation factor as compared with the ideal selectivity values is consistent with the findings of Chng *et al.* [14], Hagg *et al.* [15], as well as results previously reported in Chapter 5. Yet, membranes M2 and M3 are still clearly above the trade-off line.

6.5 Adsorption Isotherms and Uptakes

Adsorption isotherms were carried out with gas species of interest (O_2, N_2, CO_2, C_3H_6 and C_3H_8) on a c-CMSM loaded with Ag. The c-CMSM used for the adsorption studies resulted from the pyrolysis of a precursor with 12.5 wt.% of resin, 0.5 wt.% of boehmite and 0.2 wt.% of $AgNO_3$. The resin/boehmite ratio

(12/0.5) was chosen for comparing the results with those determined in Chapter 5. At the same time, this precursor originated a membrane with 3.7 wt.% of Ag, a value that is between the Ag content of membranes M2 and M3.

6.5.1 O_2, N_2 and CO_2

The adsorption equilibrium isotherms of O_2, N_2 and CO_2 on c-CMSM at 293 K and up to 600 kPa were fitted by the SIPS model and are shown in Figure 6.8. Table 6.4 summarizes the isotherm parameters of the SIPS equation that minimizes the fitting errors (*Err*), defined as the sum of the square root of relative errors.

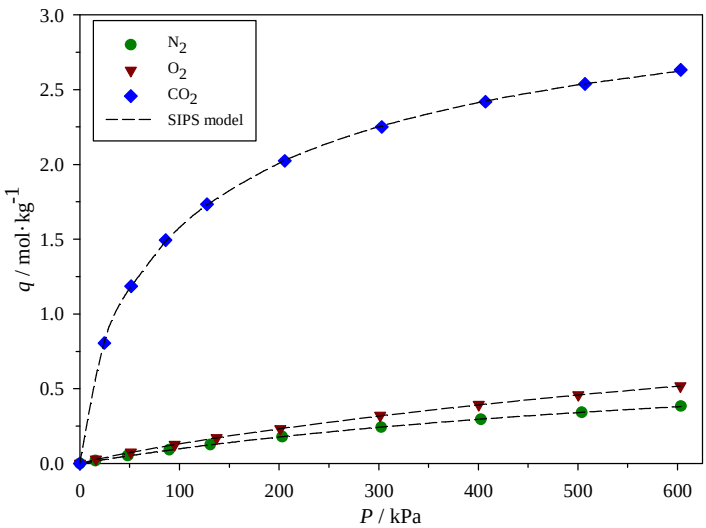

Figure 6.8 – Adsorption isotherms of N_2, O_2 and CO_2 at 293 K (symbols) and correspondent SIPS model fittings (dashed lines).

Table 6.4 – Fitting parameters of the adsorption experimental data with the SIPS equations and the corresponding fitting errors.

Gas	SIPS Model			
	q^{max}(mol·kg^{-1})	b (kPa^{-1})	n	*Err*
N_2	1.06	9.2x10^{-4}	1.06	2.0x10^{-6}
O_2	1.60	6.8x10^{-4}	1.11	2.2x10^{-4}
CO_2	3.49	7.8x10^{-3}	1.39	6.9x10^{-6}

Additionally, the uptake curves (F) of O_2, N_2 and CO_2 were recorded and the diffusivity coefficients (D) computed by applying equation (5.23):

$$F = 1 - \frac{2}{\pi^2} \sum_{v=1}^{\infty} \frac{1}{(v-0.5)^2} \exp\left(-(v-0.5)^2 \pi^2 \frac{D}{\Lambda^2} t \right) \tag{5.23}$$

valid when micropore diffusion in a slab is the controlling mass transport mechanism [16]. Λ refers to half of the slab thickness and an approximate value of 120 μm was determined using a caliper. Figure 6.9 shows that the micropore diffusion model provides an adequate fit for the uptake curves of O_2, N_2 and CO_2. The gas diffusion coefficients determined at different pressures were then correlated by the Darken-SIPS equation [16]:

$$D = n \frac{D_0}{1-\theta} = \frac{D_0^{'}}{1-\theta} \tag{5.24}$$

where D_0 is the gas diffusion at zero loading, θ is the fractional loading and n the SIPS model parameter.

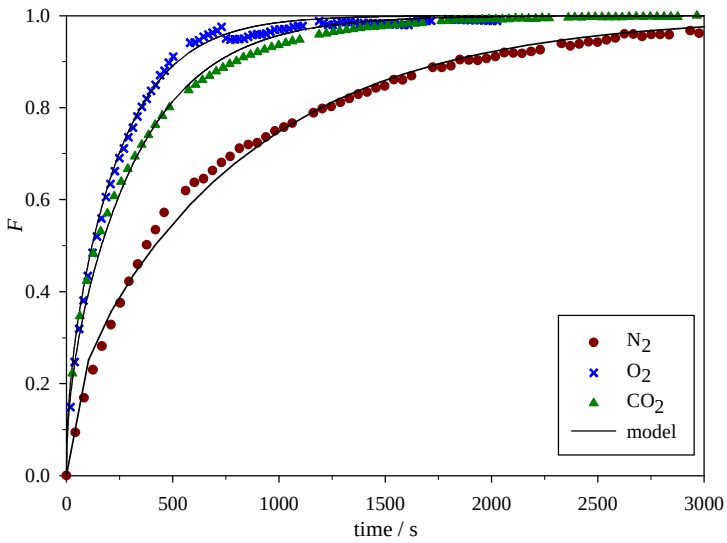

Figure 6.9 – Experimental uptake curves of N_2, O_2 and CO_2 with the respective fit by the micropore diffusion equation ($P \approx 130$ kPa).

Yet, for sieving materials, the Darken relation does not always describe well the pressure dependence of the diffusivity coefficients. In fact, it is not uncommon to

observe a decrease in diffusivity for higher loadings. Chen and Yang [17] have proposed a model that attributes this decrease to the blockage of the pores by the adsorbed molecules. This model, described by equation (5.25), features a pore blockage parameter λ and reverts back to the Darken relation when λ=0.

$$D = D_0^{'} \frac{1-\theta+\lambda/2\theta(2-\theta)+H(1-\lambda)(1-\lambda)\lambda/2\theta^2}{(1-\theta+\theta\lambda/2)^2} \qquad (5.25)$$

Both equations were used to fit the dependence of the diffusivity coefficients with pressure for the three adsorbate species. Figure 6.10 shows the diffusivity coefficients of N_2, O_2 and CO_2 as a function of the pressure.

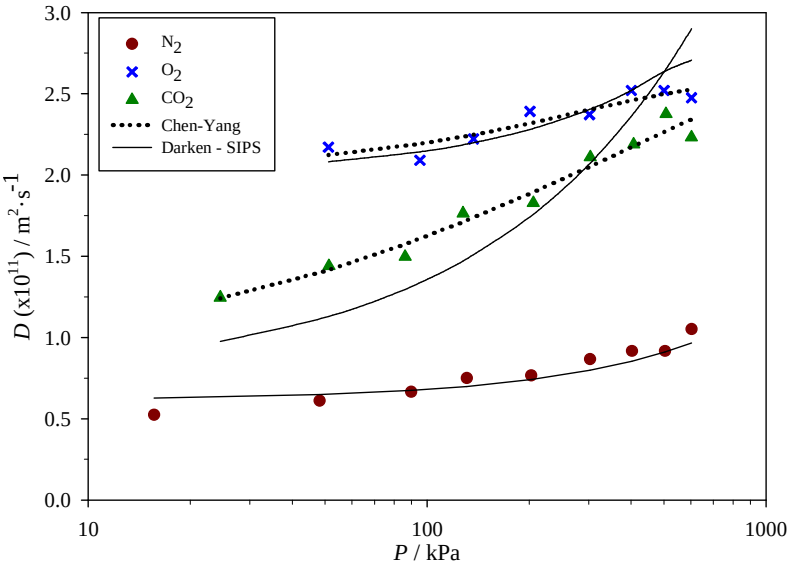

Figure 6.10 – Diffusivity coefficients as a function of the N_2, O_2 and CO_2 pressure. Symbols represent the experimental diffusivities determined with the micropore diffusion model and the lines the fitting models.

The diffusion of N_2 obeys to the Darken equation but the diffusion of O_2 and CO_2 was best described by the Chen and Yang equation. Despite N_2 having the largest kinetic diameter, no pore blocking was observed in the pressure range studied because of its low adsorption affinity. Table 6.5 summarizes the diffusion parameters of each model.

Table 6.5 – Model parameters obtained fitting the diffusion coefficients at different loadings for N_2, O_2 and CO_2 at 293 K.

Gas	Darken-SIPS	Chen-Yang	
	D_0 ($m^2 \cdot s^{-1}$)	D_0 ($m^2 \cdot s^{-1}$)	λ
N_2	5.82×10^{-12}	-	
O_2	1.73×10^{-11}	1.96×10^{-11}	1.89
CO_2	4.75×10^{-12}	9.07×10^{-12}	0.92

From the diffusion and adsorption parameters determined, theoretical permeabilities were calculated using the following equation:

$$L_i = \frac{-q^{max} \rho_s D_0'}{\Delta p_i} \int_{\theta, z=0}^{\theta, z=\delta} f(\theta) d\theta \qquad (5.26)$$

where ρ_s refers to the density of the membrane (determined by helium pycnometry to be 1550 $kg \cdot m^{-3}$), z the spatial coordinate and $f(\theta)$ has the expressions shown in equations (5.24) and (5.25)). The permselectivities computed (based on the permeabilities given by equation (5.26)) are shown in Figure 6.11, for the feed pressure range 100-600 kPa.

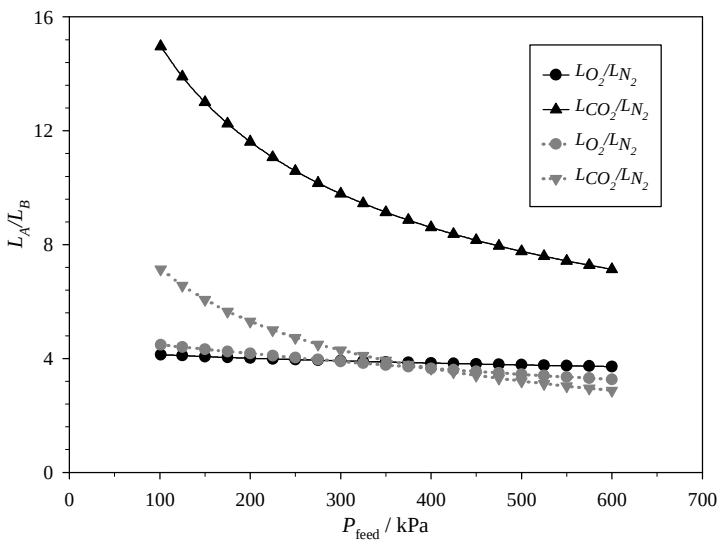

Figure 6.11 – O_2/N_2 and CO_2/N_2 ideal permselectivities determined from equation (5.26) as a function of the feed pressure (permeate pressure = 100 kPa); black – carbon-Al_2O_3-Ag sample; grey – carbon-Al_2O_3 sample analyzed in Chapter 5.

For comparison purposes, the permselectivities obtained previously for the carbon-Al_2O_3 adsorbent studied in Chapter 5 are also plotted in Figure 6.11. The O_2/N_2 permselectivity ranged from 4.0 to 4.3 and the CO_2/N_2 permselectivity from 7.4 to 15.0 (for the carbon-Al_2O_3-Ag adsorbent). The O_2/N_2 ideal permselectivities do not differ much for both adsorbents but the Ag functionalized adsorbent performs significantly better for the CO_2/N_2 separation.

6.5.2 C_3H_6 and C_3H_8

Adsorption equilibrium isotherms of C_3H_8 and C_3H_6 at 293, 343, 393 and 453 K in the pressure range 0-300 kPa are shown in Figure 6.12.

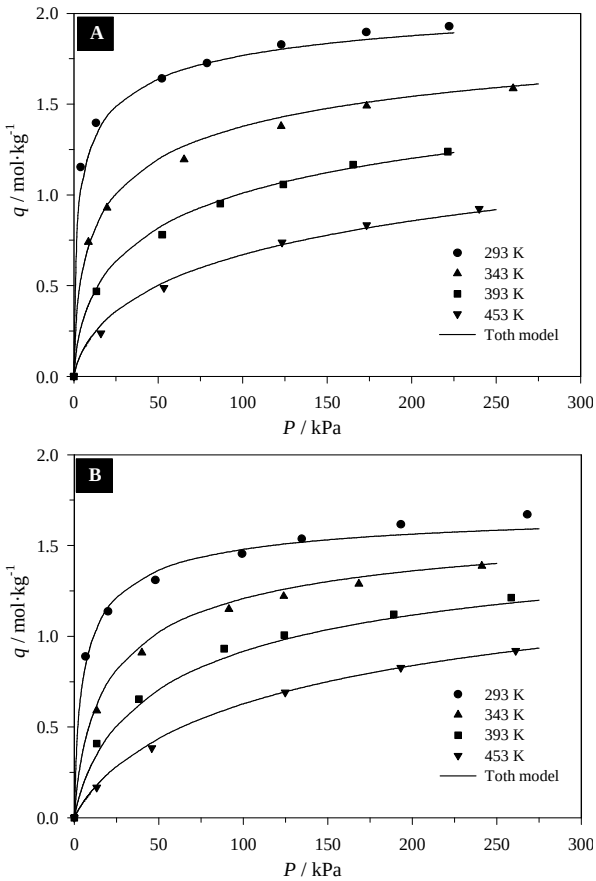

Figure 6.12 – Adsorption isotherms of C_3H_6 (A) and C_3H_8 (B) at 293, 343, 393 and 453 K (symbols **–** experimental data; solid lines **–** Toth equation).

The Toth model [18] was used to fit the experimental adsorption equilibrium data and the fitting parameters are shown in Table 6.6. These results are similar to the ones reported in Chapter 5 for the carbon-Al_2O_3 sample. Hence, it can be concluded that the adsorption selectivity of the carbon material does not change much upon silver loading. The diffusion coefficients of C_3H_6 and C_3H_8 were also determined, by fitting the experimental uptake data to the micropore diffusion model.

Table 6.6 – Toth equation parameters for the adsorption of propane and propylene on a carbon-Al_2O_3-Ag sample.

Gas	q^{max} (mol·kg^{-1})	u	-ΔH (kJ·mol^{-1})	b_0 kPa^{-1}
C_3H_6	2.29	0.40	30.7	9.5x10^{-6}
C_3H_8	1.74	0.62	23.5	2.4x10^{-5}

The experimental diffusion curves of the hydrocarbons and correspondent fitting are observed in Figure 6.13.

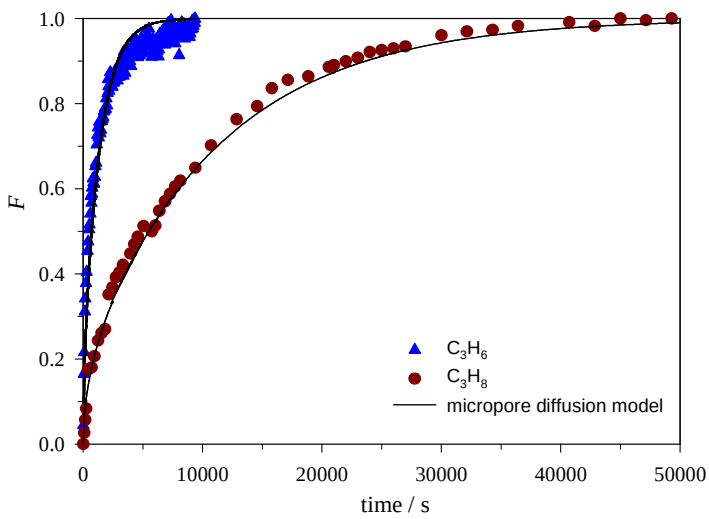

Figure 6.13– Experimental fractional uptake values of C_3H_8 and C_3H_6 in the carbon-Al_2O_3-Ag at 343 K and $P \approx 120$ kPa (experimental points – symbols; model – lines).

Then, the diffusion coefficients as a function of pressure for both hydrocarbons were fitted using the Darken relation with Toth isotherm:

$$D = D_0 \frac{1}{1-\theta^u} \tag{5.27}$$

The zero loading diffusion coefficients (D_0) determined at each temperature were correlated by the Arrhenius equation ($D_{0(T)} = D_{0(T\to\infty)} \exp\left(-E_a/\Re T\right)$). Table 6.7 shows the zero loading diffusion coefficients of C_3H_6 and C_3H_8 for different temperatures, their ratio and the diffusion activation energies.

Table 6.7 – Diffusion parameters of C_3H_6 and C_3H_8 in the temperature range 293-453 K.

Temp (K)	**C_3H_8**		**C_3H_6**		**D_{C3H6}/D_{C3H8}**	
	D_0 ($m^2 \cdot s^{-1}$)	**E_a ($kJ \cdot mol^{-1}$)**	**D_0 ($m^2 \cdot s^{-1}$)**	**E_a ($kJ \cdot mol^{-1}$)**	**C-Al-Ag**	**C-Al**
293	2.52×10^{-14}	20.8	3.10×10^{-13}	19.3	12.4	8.2
343	8.74×10^{-14}		9.85×10^{-13}		11.4	7.2
393	2.22×10^{-13}		2.33×10^{-12}		10.6	6.6
453	5.14×10^{-13}		5.10×10^{-12}		9.9	6.1

The diffusion selectivities (ratio of diffusion coefficients) are higher (9.9-12.4) for the carbon-Al_2O_3-Ag sample when compared to the carbon-Al_2O_3 sample analyzed in Chapter 5 (6.1–8.2). Also, the diffusivities of both gases decrease. These results allow interpreting better the gas permeation results. In gas permeation experiments, it was observed that in the presence of Ag, permeability decreases and permselectivity increases. The adsorption studies showed that the sorption capacity of the membrane towards the hydrocarbons remains roughly unchanged after Ag loading. Yet, the diffusivity of both gases decreases, supporting the idea that the pore network of the composite membrane in the presence of Ag is composed of slightly smaller pores. The ideal selectivity of the

Ag-containing membrane increases because the diffusivity decrease is more substantial for C_3H_8.

6.6 Conclusions

Composite carbon molecular sieve membranes loaded with Al_2O_3 and Ag nanoparticles were prepared. It was analyzed the effect of the content of Ag towards the molecular sieving properties of the composite membranes. The better performing membranes for separating gas pairs such as O_2/N_2, CO_2/N_2 and C_3H_6/C_3H_8 were prepared with 3 < Ag wt.% < 6; these membranes exhibited the smallest clusters of Ag. The better performing membranes surpass the current upper bound plots, particularly in the case of C_3H_6/C_3H_8. C_3H_6 permeabilities between 69 and 226 barrer and permselectivities between 30 and 38 were observed. When a binary mixture of C_3H_6/C_3H_8 was used, C_3H_8 negatively impacted the diffusion of C_3H_6. Nonetheless, the performance of the carbon-Al_2O_3-Ag for this mixture was still well above the upper bound curve for polymeric membranes, permeability towards C_3H_6 was 47 and 169 barrer and separation factors were 20.5 and 14.1 respectively for membranes M2 and M3.

Adsorption and kinetic studies showed that the carbon-Al_2O_3-Ag composite membrane was more selective than the carbon-Al_2O_3 membrane towards CO_2/N_2 and C_3H_6/C_3H_8 separations. For C_3H_6/C_3H_8, this increase in selectivity was due to the fact that the diffusivity of C_3H_8 decreased significantly than the diffusivity of C_3H_8. Consequently, in the silver-containing carbon material, the ratio of diffusivities for the pair C_3H_6/C_3H_8 was higher than in the plain Carbon-Al_2O_3 membrane.

6.7 Acknowledgements

Miguel Teixeira and Margot Llosa are grateful to the Portuguese Foundation for Science and Technology (FCT) for their doctoral grant (references SFRH/BD/24768/2005 and SFRH/BD/61898/2009, respectively). Marta Campo also acknowledges FCT for her post-doctoral grant (reference SFRH/BPD/65377/2009). The authors also acknowledge financing from FCT through the projects POCTI/EQU/59344/2004 and POCTI/EQU/59345/2004. Finally, the authors are thankful to CEMUP for the SEM analyses (REEQ/1062/CTM/2005 and REDE/1512/RME/2005 funding provided by FCT).

6.8 Nomenclature

Variables	Definition	Units
b	Adsorption affinity coefficient	Pa^{-1}
D	Diffusivity	$m^{-2} \cdot s^{-1}$
D_0	Diffusivity at zero loading	$m^{-2} \cdot s^{-1}$
F	Fractional uptake	-
$H()$	Heaviside function	-
J	Permeating flux	$mol \cdot m^{-2} \cdot s^{-1}$
L	Membrane permeability	$mol \cdot m \cdot m^{-2} \cdot s^{-1} \cdot Pa^{-1}$
m_t	Mass at instant t	kg
m_0	Initial mass	kg
m_∞	Equilibrium mass	kg
n	SIPS equation parameter	-
p	Partial pressure	Pa
P	Total pressure	Pa
q	Surface concentration	$mol \cdot kg^{-1}$
q^{max}	Maximum surface concentration	$mol \cdot kg^{-1}$

$\Re$	Gas constant	$Pa \cdot m^3 \cdot mol^{-1} \cdot K^{-1}$
S	Permselectivity	-
t	time	s
u	Toth equation parameter	-
T	Absolute temperature	K
z	Spatial coordinate	m

Greek	**Definition**	**Units**
λ	Blocking parameter	-
θ	Fractional coverage of the pore surface	-
δ	Membrane thickness	m
Λ	Half of slab thickness	m
ρ_s	Solid Density	$mol \cdot kg^{-3}$

Subscript	**Definition**
i	species i

6.9 References

[1] P. Bernardo, E. Drioli, Membrane gas separation progresses for process intensification strategy in the petrochemical industry, Petrol Chem+, 50 (2010) 271-282.
[2] P. Bernardo, E. Drioli, G. Golemme, Membrane Gas Separation: A Review/State of the Art, Ind Eng Chem Res, 48 (2009) 4638-4663.
[3] Y.C. Xiao, M.L. Chng, T.S. Chung, M. Toriida, S. Tamai, H.M. Chen, Y.C.J. Jean, Asymmetric structure and enhanced gas separation performance induced by in situ growth of silver nanoparticles in carbon membranes, Carbon, 48 (2010) 408-416.
[4] J.N. Barsema, J. Balster, V. Jordan, N.F.A. van der Vegt, M. Wessling, Functionalized Carbon Molecular Sieve membranes containing Ag-nanoclusters, J Membrane Sci, 219 (2003) 47-57.
[5] J.N. Barsema, N.F.A. van der Vegt, G.H. Koops, M. Wessling, Ag-functionalized carbon molecular-sieve membranes based on polyelectrolyte/polyimide blend precursors, Adv Funct Mater, 15 (2005) 69-75.
[6] H.B. Park, C.H. Jung, Y.K. Kim, S.Y. Nam, S.Y. Lee, Y.M. Lee, Pyrolytic carbon membranes containing silica derived from poly(imide siloxane): the effect of siloxane chain length on gas transport behavior and a study on the separation of mixed gases, J Membrane Sci, 235 (2004) 87-98.
[7] H.B. Park, S.Y. Lee, Y.M. Lee, Pyrolytic carbon membranes containing silica: morphological approach on gas transport behavior, J. Mol. Struct., 739 (2005) 179-190.
[8] Q.L. Liu, T.H. Wang, J.S. Qiu, Y.M. Cao, A novel carbon/ZSM-5 nanocomposite membrane with high performance for oxygen/nitrogen separation, Chem. Commun., (2006) 1230-1232.
[9] Y. Li, T.S. Chung, Exploratory development of dual-layer carbon-zeolite nanocomposite hollow fiber membranes with high performance for oxygen enrichment and natural gas separation, Microporous Mesoporous Mater., 113 (2008) 315-324.
[10] Q.L. Liu, T.H. Wang, C.H. Liang, B. Zhang, S.L. Liu, Y.M. Cao, J.S. Qiu, Zeolite married to carbon: A new family of membrane materials with excellent gas separation performance, Chem. Mater., 18 (2006) 6283-6288.
[11] Q.L. Liu, T.H. Wang, H.C. Guo, C.H. Liang, S.L. Liu, Z.G. Zhang, Y.M. Cao, D.S. Su, J.S. Qiu, Controlled synthesis of high performance carbon/zeolite T composite membrane materials for gas separation, Microporous Mesoporous Mater., 120 (2009) 460-466.
[12] L.M. Robeson, The upper bound revisited, J Membrane Sci, 320 (2008) 390-400.
[13] R.L. Burns, W.J. Koros, Defining the challenges for C_3H_6/C_3H_8 separation using polymeric membranes, J Membrane Sci, 211 (2003) 299-309.

[14] M.L. Chng, Y.C. Xiao, T.S. Chung, M. Toriida, S. Tamai, Enhanced propylene/propane separation by carbonaceous membrane derived from poly (aryl ether ketone)/2,6-bis(4-azidobenzylidene)-4-methyl-cyclohexanone interpenetrating network, Carbon, 47 (2009) 1857-1866.
[15] M.B. Hagg, J.A. Lie, A. Lindbrathen, Carbon molecular sieve membranes - A promising alternative for selected industrial applications, Ann Ny Acad Sci, 984 (2003) 329-345.
[16] D.D. Do, Adsorption analysis: equilibria and kinetics, Imperial College Press, London, 1998.
[17] Y.D. Chen, R.T. Yang, Concentration-Dependence of Surface-Diffusion and Zeolitic Diffusion, Aiche Journal, 37 (1991) 1579-1582.
[18] J. Toth, State Equations of Solid-Gas Interface Layers, Acta Chimica Academiae Scientarium Hungaricae, 69 (1971) 311-328.

PART IV:

CATALYTIC MEMBRANE REACTORS

Chapter 7: **Improving propyne removal from propylene streams using a catalytic membrane reactor – a theoretical study**

(Teixeira, M.; Madeira, L. M.; Sousa, J.; Mendes, A., Journal of Membrane Science, Volume 375, Issues 1-2, 15 June 2011, Pages 124-133)

7.1 Abstract

Typical industrial propylene streams contain 2-5 molar % of alkynes, which must be removed. Traditionally, this is carried out through hydrogenation. However, the deeper hydrogenation to alkanes is a drawback of such process. The use of a catalytic membrane reactor (MR) featuring a propyne permselective membrane and a catalyst selective to the propyne hydrogenation loaded on the permeate side membrane surface is proposed; plug-flow pattern and segregated feed of reactants are considered. This strategy should improve the selective hydrogenation, as the permselective membrane enhances the propyne/propylene ratio at the catalyst surface.

The combined process was analyzed using a mathematical model. The MR performance was compared to a conventional fixed-bed catalytic reactor (FBCR) with the same feed and reaction conditions, in terms of the propyne molar fraction. The performance of the MR was characterized by the conversion of propyne and selectivity towards propylene as a function of some model parameters. The MR showed to be more efficient in performing the required purification.

7.2 Introduction

Alkenes produced by steam cracking are inevitably contaminated with alkynes, which must be removed from the product stream since they interfere with the downstream polymerisation processes [1-3]. As a monomer for the production of polypropylene, the purified propylene should contain less than 5 ppm of propyne. Among the methods known for alkynes removal, the selective catalytic hydrogenation is the most appropriate process [4-5], carried out in a fixed-bed catalytic reactor [5]. However, the over-hydrogenation of propylene to propane is a drawback of such process, which should be avoided.

An alternative approach for propylene purification is the combined use of chemical reaction and separation modules in a single processing unit – *i.e.*, employing a membrane reactor (MR). Very recently, it has been shown that when properly functionalized [6-8], membranes can become highly selective towards alkynes. This should have several advantages over the conventional arrangement of a chemical reactor followed by a separation unit [9], since combining the reaction and separation in a single stage simplifies the process, according to the strategy of process intensification [10]. Additionally, the use of MRs can enhance the selectivity and yield towards the desired product, either through the selective removal of a reaction product, *i.e.*, yield-enhancement [3, 11-13], or through the distributive feed of reactants, i.e., selectivity enhancement [14-18]. These selectivity and/or yield enhancement may also decrease downstream separation costs [19].

The interest in the use of membrane reactors has increased among the scientific community, according to the number and diversity of papers available in the open literature [20-21]. The applications of membrane reactors have been mainly focused on dehydrogenation reactions [14, 22-24], hydrogenation reactions [5, 9, 13, 20-21]) and oxidative coupling [22-24]). Nevertheless, the concept has yet to find large scale industrial applications, mainly due to the high manufacturing

costs and limited lifetime of the membranes themselves [19, 25]. The synthesis of defect-free membranes, the membrane thickness reduction and the long-term stability are challenges to overcome in the development of membrane reactors [26].

Different designs of membrane reactors have been proposed for the hydrogenation of alkynes and alkenes. While Liu *et al.* [5] reported the use of a hollow fiber membrane reactor, Ziegler *et al.* [21] studied the application of porous polymeric membranes loaded with palladium clusters. More recently, Mendes and co-workers studied the use of a catalytic PDMS matrix built-in with palladium nanoclusters, both experimentally [13] and theoretically [9]. The reactants (hydrocarbons and hydrogen) were fed in the same stream to the retentate side (high pressure side), and the purified stream exited through the low-pressure permeate side. In the present work, a MR combining the selective permeation of propyne and its consumption on a selective catalyst placed on the low-pressure permeate chamber is proposed. This improves the driving force for permeation, and takes advantage of the catalyst selective hydrogenation at low pressures.

To the best of our knowledge, this MR design featuring a catalytic layer dispersed on the surface of a propyne permselective membrane was not proposed yet for this application. The use of a segregated feed minimizes the undesired deeper hydrogenation to propane and the highly purified propylene stream exits at high-pressure from the retentate side. Furthermore, the present work aims not only at proposing an alternative membrane reactor design, but also studying its theoretical feasibility in removing propyne below the 5 ppm threshold. In order to analyze in which conditions the proposed MR may outperform the conventional fixed bed catalytic reactor (FBCR) in terms of the propyne concentration reduction and propylene selectivity, a 1D mathematical model was developed, described in the following section.

7.3 Model

The membrane reactor considered in this study has the general features of the one depicted in Figure 7.1.

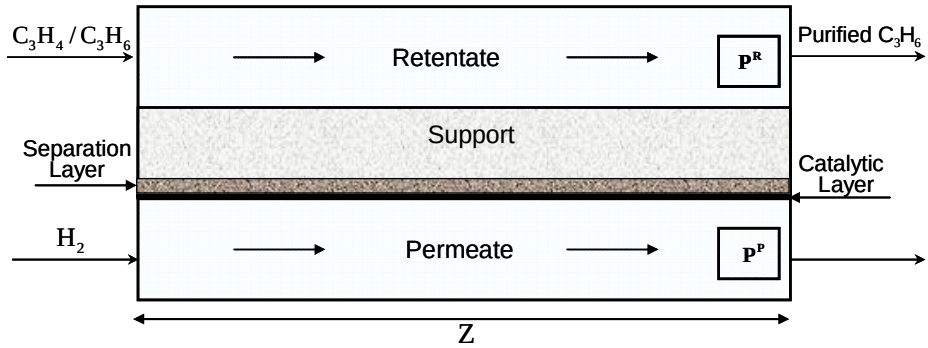

Figure 7.1 – Schematic diagram of the membrane reactor (MR).

It consists of a tube (permeate) and shell (retentate) type module, with the chambers at different (but constant) total pressures and separated by a composite membrane. This membrane is composed by a porous support and a permselective layer with thickness δ on the internal side and a hydrogenation catalyst homogeneously dispersed on the surface of the selective layer. Due to the low thickness of this layer, it can be considered flat. This assumption simplifies the model equations and doesn't compromise the main conclusions. The reactants are fed in a segregated way, with the hydrocarbon mixture (propyne and propylene) being fed to the retentate chamber and the hydrogen stream fed to the low-pressure permeate side in a co-current arrangement.

This work consisted on the development of a mathematical model to study the feasibility of the proposed MR for the purification of industrial propylene streams; it focused on the consecutive-parallel reaction system propyne→propylene→propane (equations (7.1) and (7.2)):

$$C_3H_4 + H_2 \rightarrow C_3H_6 \qquad (7.1)$$

$$C_3H_6 + H_2 \rightarrow C_3H_8 \qquad (7.2)$$

The mathematical model comprises steady-state mass balance equations for the retentate and permeate sides, as well as the respective boundary conditions. Its main assumptions are the following:

1) Ideal gas behavior and isothermal conditions.
2) Plug flow pattern on both chambers without radial dispersion and constant total pressures.
3) Absence of internal and external mass transfer resistances (kinetic regime).
4) The transport through the selective membrane layer is considered to be described by an "overall" permeability coefficient (assumed constant for the ranges of compositions of this work). The porous support doesn't impose any mass transfer resistance (the gas composition and pressure at the interface selective layer/porous support are the same as the ones on the retentate chamber).
5) Homogeneous distribution of the catalytic particles over the selective layer surface, which is considered to be part of the permeate chamber.
6) The kinetic equations are considered valid for all the operating conditions.
7) Negligible film mass transport resistance in both retentate and permeate chambers.
8) Both hydrogenation reactions are assumed to be irreversible [4]. It has been reported that specific catalyst active sites can directly hydrogenate propyne to propane [27-28]. This study assumes that such active sites are not present in the catalyst and thus it neglects the direct hydrogenation of propyne to propane.
9) The catalytic activity is considered constant. The rate of deactivation of a hydrogenation catalyst is determined by the rate of green-oil formation, which depends on many factors (catalyst support acidity, dispersion of the catalyst, temperature, hydrogen/propyne ratio). Hence, it is very hard to estimate the rate of green-oil formation and consequently the catalytic

deactivation. Thus, it was decided not to consider the impact of this parameter in this study. Yet, it should be noted that the use of well dispersed catalysts on neutral supports should minimize catalyst deactivation.

7.3.1 Mass Balances

The mass balance equations are:

7.3.1.1 Partial and Total Mass Balances to the Retentate Side

$$\frac{1}{\Re T}\frac{d\left(p_i^R Q^R\right)}{dz}+\frac{2\pi r^t L_i\left(p_i^R-p_i^P\right)}{\delta}=0 \tag{7.3}$$

$$\frac{P^R}{\Re T}\frac{dQ^R}{dz}+\frac{2\pi r^t \sum_i L_i\left(p_i^R-p_i^P\right)}{\delta}=0 \tag{7.4}$$

The respective boundary conditions are as follows:

$$z=0: p_i^R = p_i^{F,h} \text{ and } Q^R = Q^{F,h}$$

where the subscript i refers to the ith component (hydrogen, propyne, propylene, propane), Q is the volumetric flow rate, L is the permeability coefficient, P and p are total and partial pressures, respectively, r^t is the external tube radius, z is the membrane axial coordinate, δ is the selective membrane thickness, $\Re$ is the gas constant and T is the temperature. The superscripts R, P and F refer to the retentate, permeate and feed stream conditions, respectively, and h refers to the high pressure chamber (retentate).

7.3.1.2 Partial and Total Mass Balances to the Permeate Side

$$\frac{1}{\Re T}\frac{d\left(p_i^P Q^P\right)}{dz}-\frac{2\pi r^t L_i\left(p_i^R-p_i^P\right)}{\delta}-2\pi r^t\left(\nu_{i,1}k_1^g f_1\left(p_i^P\right)+\nu_{i,2}k_2^g f_2\left(p_i^P\right)\right)=0 \quad (7.5)$$

$$\frac{P^P}{\Re T}\frac{dQ^P}{dz}-\frac{2\pi r^t\sum_i L_i\left(p_i^R-p_i^P\right)}{\delta}-2\pi r^t\sum_i\left(\nu_{i,1}k_1^g f_1\left(p_i^P\right)+\nu_{i,2}k_2^g f_2\left(p_i^P\right)\right)=0 \quad (7.6)$$

The respective boundary conditions are as follows:

$$z=0:\ p_i^P=p_i^{F,l} \text{ and } Q^P=Q^{F,l}$$

where the superscript l refers to the low pressure (permeate) chamber. In equations (7.5) and (7.6) (and in all the subsequent ones), $\nu_{i,j}$ is the stoichiometric coefficient of species i in reaction j ($j=1$ for propyne's hydrogenation and $j=2$ for propylene's hydrogenation), taken negative for reactants, positive for reaction products and null for the components that do not take part in the reaction. k_1^g and k_2^g are the reaction rate constants in reactions 1 and 2, respectively, based on the gas-phase reaction conditions (temperature and partial pressures) and catalyst amount. f_1 and f_2 are the local reaction rate functions expressed by equations (7.7) and (7.8) (below there is a detailed discussion about their choice):

$$f_1\left(p_i^P\right)=\left(p_{C_3H_4}^P\right)^{0.25}\left(p_{H_2}^P\right) \quad (7.7)$$

$$f_2\left(p_i^P\right)=\left(p_{C_3H_6}^P\right)\left(p_{H_2}^P\right) \quad (7.8)$$

7.3.2 Mass Balances – Dimensionless Form

Equations (7.3) to (7.8) were made dimensionless with respect to the feed conditions, $Q^{F,h}$ and $P^{F,h}$, to component propylene, $L_{C_3H_6}$, and to the reactor length, Z. The reference temperature was set to 298 K. Changing for

dimensionless variables and introducing suitable dimensionless parameters, the mass balances and respective boundary conditions became as follows.

7.3.2.1 Partial and Total Mass Balances for the Retentate Side

$$\frac{d\left(Q^{R*}p_i^{R*}\right)}{dz^*}+\Gamma L_i^*\left(p_i^{R*}-p_i^{P*}\right)=0 \tag{7.9}$$

$$P^{R*}\frac{dQ^{R*}}{dz^*}+\Gamma\sum_i L_i^*\left(p_i^{R*}-p_i^{P*}\right)=0 \tag{7.10}$$

$$z^*=0:\ p_i^{R*}=p_i^{F*,h} \text{ and } Q^{R*}=Q^{F*,h}$$

7.3.2.2 Partial and Total Mass Balances for the Permeate Side

$$\frac{d\left(Q^{P*}p_i^{P*}\right)}{dz^*}-\Gamma L_i^*\left(p_i^{R*}-p_i^{P*}\right)-Da\left(\nu_{i,1}f_1\left(p_i^{P*}\right)+\nu_{i,2}R_r f_2\left(p_i^{P*}\right)\right)=0 \tag{7.11}$$

$$P^{P*}\frac{dQ^{P*}}{dz^*}-\Gamma\sum_i L_i^*\left(p_i^{R*}-p_i^{P*}\right)-Da\sum_i\left(\nu_{i,1}f_1\left(p_i^{P*}\right)+\nu_{i,2}R_r f_2\left(p_i^{P*}\right)\right)=0 \tag{7.12}$$

$$z^*=0:\ p_i^{P*}=p_i^{F*,l} \text{ and } Q^{P*}=Q^{F*,l}$$

where $p^*=p/P_{ref}$; $Q^*=Q/Q_{ref}$; $L^*=L/L_{ref}$; $z^*=z/Z$; $f_1\left(p_i^{P*}\right)=p_{H_2}^{P*}\left(p_{C_3H_4}^{P*}\right)^{0.25}$;

$f_2\left(p_i^{P*}\right)=p_{H_2}^{P*}p_{C_3H_6}^{P*}$; $Da=\dfrac{k_1^g A^M \Re T P_{ref}^{0.25}}{Q_{ref}}$; $\Gamma=\dfrac{A^M \Re T L_{ref}}{\delta Q_{ref}}$; $R_r=\dfrac{k_2^g}{k_1^g}P_{ref}^{0.75}$

The superscript * refers to dimensionless conditions, *Da* is the Damköhler number (based on the propyne hydrogenation reaction), Γ is a dimensionless contact time (ratio between the maximum possible flux across the membrane for the reference component, that is, permeation of pure species against null permeate pressure, and its molar feed flow rate [9]), A^M is the selective membrane surface area and R_r is the ratio of the reaction rate constants.

7.3.3 Solution of the model equations

The general strategy used for solving the equations is the same as used previously [29]. A time derivative term was added to the right-hand side of equations (7.9) and (7.11), transforming this problem into a pseudo-transient one. The resulting partial differential equations, combined with equations (7.10) and (7.12), were spatially discretised using orthogonal collocation [30]. A suitable variable transformation of the collocation points in the axial direction as a function of the Damköhler number was applied, in order to obtain a solution with high accuracy and low computational effort [31]. For all simulations, 11 internal collocation points were used. The time integration routine LSODA [32] was used to integrate the resulting set of equations until a steady-state solution was reached. The solution is considered to be in steady state when the time derivative of each dependent variable, for each spatial coordinate, is smaller than a pre-defined value [31].

7.3.4 Model Reaction System and Parameters

An effective way to analyze and compare the performance of our MR with the FBCR is to measure the extent of the two-hydrogenation reactions, by calculating the conversion of propyne and hydrogen, as well as the selectivity and overall yield to the desired intermediate propylene. The conversion of a component *i*, X_i, can be expressed by:

$$X_i = 1 - \frac{Q^{P*} p_i^{P*} + Q^{R*} p_i^{R*}}{Q^{F*,l} p_i^{F*,l} + Q^{F*,h} p_i^{F*,h}} \tag{7.13}$$

In our work, the selectivity is defined as the ratio of net moles of propylene produced per mole of propyne reacted [14] and is given by:

$$\sigma_{C_3H_6} = \frac{Q^{P*} p_{C_3H_6}^{P*} + Q^{R*} p_{C_3H_6}^{R*} - Q^{F*,h} p_{C_3H_6}^{F*,h}}{Q^{F*,h} p_{C_3H_4}^{F*,h} - (Q^{P*} p_{C_3H_4}^{P*} + Q^{R*} p_{C_3H_4}^{R*})} \tag{7.14}$$

The overall yield to propylene is defined as the ratio of net moles of propylene produced per mole of propyne fed and can be given by:

$$Y_{C_3H_6} = \frac{Q^{P*} p^{P*}_{C_3H_6} + Q^{R*} p^{R*}_{C_3H_6} - Q^{F*,h} p^{F*,h}_{C_3H_6}}{Q^{F*,h} p^{F*,h}_{C_3H_4}} = \sigma_{C_3H_6} X_{C_3H_4} \qquad (7.15)$$

A systematic study on the effect of the most important operating variables and parameters was also made. In this study, a 2 % propyne/ 98 % propylene feed stream was considered [33], even though propadiene can also normally be found in industrial streams [4-5]. However, data for propadiene hydrogenation kinetics was not as readily available in the literature as for propyne. Table 7.1 summarizes the ranges of values for other parameters used in the simulations.

Table 7.1 – Parameter ranges used in the simulations.

Parameter	Value	Parameter	Value
P^{P*}	0.005	Γ	0.01-TPC[a]
Ψ	1-5	Da	$1 - 2\times10^3$
$L^*_{C_3H_4}$	$1 - 10^2$	R_r	0.1-10
$L^*_{C_3H_6}$, $L^*_{C_3H_8}$, $L^*_{H_2}$	1	T	298 K

[a] – Total Permeation Condition

A range of two orders of magnitude was selected for the dimensionless contact time value (Γ), accounting for a possible wide range of feed volumetric flow rates. Low dimensionless permeate pressure values were used in order to maximize the driving force for propyne permeation, minimize the driving force for hydrogen permeation to the retentate and increase the selectivity. Because of its low permeation driving force, hydrogen's permeability coefficient (with respect to propylene) had a negligible impact on the model results. Hence, a constant value for hydrogen's permeability coefficient (equal to one) was considered in all simulations presented. In the following sections, details

regarding the criteria used for selection of the most important parameters will be given.

7.3.5 Reaction Kinetics

This study considers the kinetics of selective propyne hydrogenation towards propylene as well as the undesired deeper hydrogenation towards propane. A thorough literature review on the kinetics for alkynes and alkenes hydrogenations was done and summarized in Table 7.2.

Table 7.2 – Reported data on kinetics of alkynes and alkenes hydrogenations under different operating conditions and using different catalysts.

Ref	Gas	Kinetic Equation	Cat	Temp. (K)	Pressure, Composition
[4]	C_3H_4	$r = kp_{H_2}$	Pd	343-373	$\frac{H_2}{\sum_{i=4,6,8} C_3H_i} = 0.25 - 0.75$
[13]	C_3H_4	$r = k\left(p_{C_3H_4}\right)^{-0.44}\left(p_{H_2}\right)^{1.02}$	Pd	308	P^R=1.2 bar P^P=0.1 bar
	C_3H_6	Langmuir-Hinshelwood			
[33]	C_3H_6	$r = kp_{H_2}$	Pd	293-353	$\frac{H_2}{\sum_{i=4,6,8} C_3H_i} = 0.02 - 0.07$
[34]	C_3H_4	$r = kp_{H_2}$	Pd	298	H_2/C_3H_4=1
[35]	C_3H_4	$r = k\left(p_{C_3H_4}\right)^{-0.02}\left(p_{H_2}\right)^{0.6}$	Pt	333	P=1 bar
[36]	C_3H_4	$r = k\left(p_{C_3H_4}\right)^{0.03}\left(p_{H_2}\right)^{0.93}$	Pd	298	P=2 bar; H_2/C_3H_4=0.5-3
[37]	C_3H_4	$r = kp_{H_2}$	Ni Pd Pt	348-363	$p_{C_3H_4}$ = 60 mmHg p_{H_2} = 30-300 mmHg
		$r = k\left(p_{H_2}\right)^{1.53}$	Fe	347-387	

While some kinetic models use up to 5 different parameters [13, 27], others consist of power-law kinetic equations that fit well the experimental data with much less parameters [4, 35-36, 38]. So, it was decided to consider power-law type equations, simplifying the problem without compromising the main

conclusions. Because the proposed MR features a low-pressure reaction chamber, the reported kinetic expressions are not always applicable and a qualitative analysis was performed to choose the adequate rate expressions, valid for the operating range of conditions considered. Table 7.2 shows that it has been frequently reported a zero order dependence relative to propylene on the account of this reactant being present in large excess; however, in the present study the propylene/propyne ratio near the active sites is dependent on the permeation rates, thus a first order dependence was considered instead. It was also decided to use a first order dependence for hydrogen in both reactions, as reported in most studies found. The reaction rate order of propyne has been reported to be lower than propylene's and hydrogen's (cf. Table 7.2), because most catalysts show adsorption selectivity towards propyne [1, 13, 35]. Since the propyne concentration on the catalyst surface could potentially be near zero, a negative reaction rate order was discarded and values ranging between zero and first order dependence were considered, more specifically 0.25. On one hand, a zero order dependence is unreasonable to be considered, since for very low propyne concentrations and large excess of hydrogen the hydrogenation of propyne could potentially (numerically speaking) continue after the depletion of propyne in the permeate chamber. On the other hand, a first order dependence would not illustrate the adsorption selectivity of the catalyst towards propyne, for reasonable propyne concentration values.

7.3.6 Propyne/Propylene Separation Factor ($L^*_{C_3H_4}$)

The propyne/propylene separation factor is defined as the ratio of the membrane permeability of propyne to propylene for bicomponent mixtures. Since the permeability coefficients were made dimensionless for the permeability of propylene, this separation factor can be expressed simply as $L^*_{C_3H_4}$. Until now, the

potential benefits of using MRs for the hydrogenation of alkynes have been limited by the low separation factor of reported membranes and adsorbents and quick degradation of the performance of these materials [38, 39]. It has been reported that alkynes adsorb irreversibly in silver and copper functionalized adsorbents [39] and the alkyne/alkene adsorption selectivity ratio in nickel (II) functionalized adsorbents is below 2 [40]. However, Jung et al. [6-8] have recently reported pyrrolidinium-based ionic liquids as highly selective alkyne carriers (alkyne/alkene selectivities over 20 [8]) due to the interaction between the acidic hydrogen of the alkyne and the basic anion of the ionic liquid. The range of separation factor values (1 to 100 - cf. Table 7.1) considered in the present study reflects this recent breakthrough in membrane technology for the separation of alkynes and our expectations for further improvements.

7.3.7 Reaction Rate Ratio (R_r)

The reaction rate ratio is defined as the ratio of the kinetic constants of the undesirable and desirable reactions, respectively. The rate expressions considered for the two hydrogenations are:

$$-r_1 = k_1^g \, p_{\mathrm{H_2}} \left(p_{\mathrm{C_3H_4}} \right)^{0.25} \tag{7.16}$$

$$-r_2 = k_2^g \, p_{\mathrm{H_2}} \, p_{\mathrm{C_3H_6}} \tag{7.17}$$

Based on reported studies and on the conditions used in our study, it was possible to estimate the ratio of the kinetic constants (R_r). Values of one order of magnitude above and below the estimated value of the reaction rate ratio parameter for palladium catalysts were considered, to account for the possibility of using different catalysts (cf. Table 7.2).

7.3.8 Hydrogen/Propyne Molar Inlet Ratio (Ψ)

The ratio of the molar feed flows of hydrogen and propyne (Ψ):

$$\Psi = \frac{p_{\mathrm{H_2}}^{F*,l} Q^{F*,l}}{p_{\mathrm{C_3H_4}}^{F*,h} Q^{F*,h}} \tag{7.18}$$

is a key parameter of this MR, since one wishes to effectively remove propyne while consuming the smallest possible amount of hydrogen. The molar feed flow rate of hydrogen must exceed the molar feed flow rate of propyne, to avoid hydrogen depletion before the exit of the permeate chamber. However, and because high retentate output flow rates are desired, Ψ values slightly greater than 1 assure an effective propyne removal.

In the case of the FBCR, higher Ψ ratios had to be considered since lower propyne/propylene ratios at the catalyst surface can be observed, which in turn favors the consumption of hydrogen through the undesired reaction. Values in the range 1 – 5 have been considered (cf. Table 7.1).

7.4 Results and Discussion

7.4.1 Model Validation

The MR model proposed for the alkyne hydrogenation was validated using data of selective hydrogenation of front-end steam-cracking C_2-C_3 mixtures in a packed bed catalytic reactor from the open literature [3]. In order to make the MR loosely equivalent to a fixed bed catalytic reactor (FBCR), it was considered that the membrane was not permeable (Γ = 0), and all species are fed at high pressure in the same side. Moreover, it was also considered the same feed reported by Godinez *et al*. [3]. Since C_2 species were present in the feed, the mass balance equations were modified accordingly, including also the kinetic equations for hydrogenation reactions of ethyne and ethene. As a result, two additional

dimensionless parameters, Rr_2 and Rr_3, were introduced, defined as the reaction rate ratios for the hydrogenations of ethyne and ethene with respect to propyne's. The simulation runs used the reaction rate orders determined by Godinez *et al.* [3]. The dimensionless parameters (*Da*, *Rr*, Rr_2 and Rr_3) were determined by optimization, minimizing the sum of the relative errors between the conversion and selectivity values observed experimentally and those calculated by the model. Figure 7.2 compares the effect of two parameters (CO content and $H_2/(C_2H_2+C_3H_4)$ ratio) on the experimental conversion of alkynes (ethyne and propyne) with the model results. The model showed to fit quite well the experimental data by Godinez *et al*.

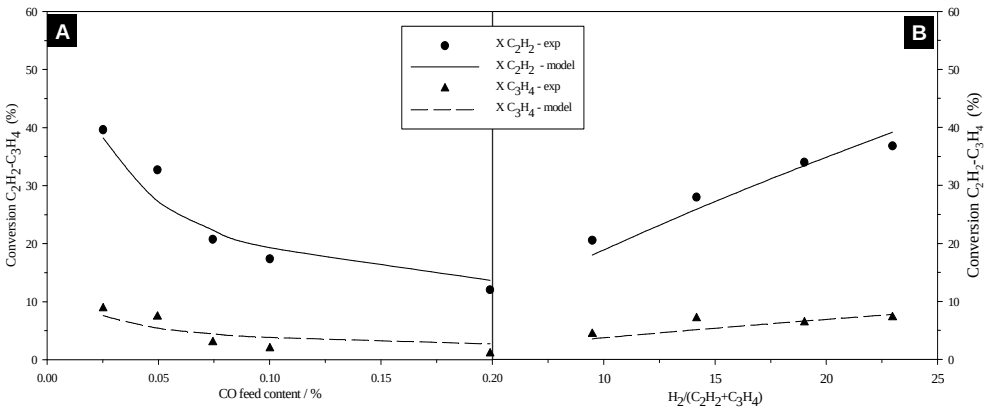

Figure 7.2 – Comparison between experimental [3] conversion of propyne and ethyne as a function of CO content (A) and the ratio $H_2/(C_2H_2 + C_3H_4)$ (B) (symbols) and the results of the model (lines). The parameters determined from optimization of the experimental data were $Da = 2.1\text{x}10^{-4}$; $Rr = 0.09$; $Rr_2 = 14.18$; $Rr_3 = 1.3$.

7.4.2 Fixed Bed Catalytic Reactor (FBCR)

Figure 7.3 shows the dependence of the outlet molar fraction of propyne (A) and propane (B) with *Da*, for different hydrogen/propyne molar ratios (Ψ). As a monomer for the production of polypropylene, the purified propylene should contain less than 5 ppm of propyne. To reach this value, the FBCR requires a minimum Ψ value of 1.35 and high Damköhler numbers, because hydrogen is

also being significantly consumed through the undesired deeper hydrogenation to propane – Figure 7.3. In fact, the propylene selectivity observed is around 70 % (data not shown), regardless of Ψ hence about 23 % of the reacted hydrogen is being consumed in the hydrogenation of propylene. This constitutes also a drawback of this reactor, because the propylene stream should have a maximum propane content of 0.5 % [41] in order to be considered a polymer grade stream and be used for the synthesis of polypropylene. In fact, Figure 7.3B shows that for Ψ = 1.35 and for the high Damköhler numbers region, the molar fraction of propane is as high as 0.7 %. This constitutes a big disadvantage for the FBCR and either more selective catalysts or an additional separation unit for propane removal is required.

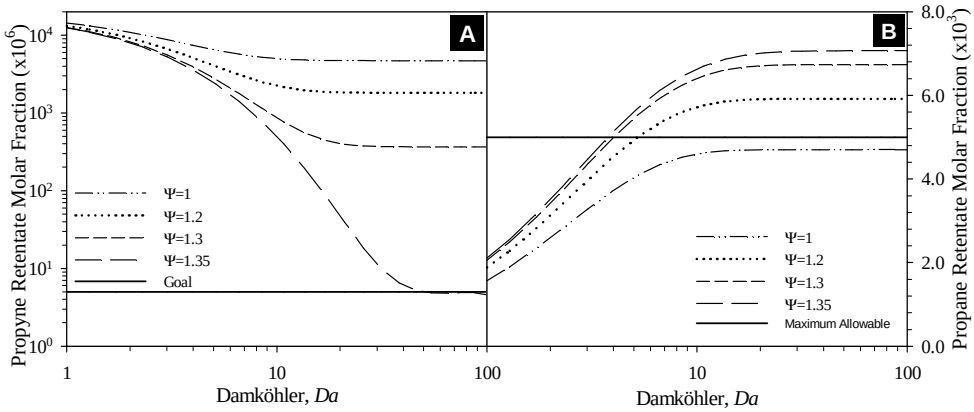

Figure 7.3 – Propyne retentate molar fraction (A) and propane molar fraction (B) as a function of the *Da* number, for different hydrogen/propyne molar feed ratios (Ψ), in the FBCR with a reaction rate ratio (*Rr*) value of 0.1.

7.5 Membrane Separation System (MS)

The performance of a permselective membrane without reaction (a membrane based separation – MS) is shown in Figure 7.4. The retentate composition of propyne exhibits a monotonically decreasing trend with Γ, regardless of the propyne/propylene separation factor ($L^*_{C_3H_4}$). An increase in Γ increments the

stage-cut value (ratio between the permeating and feed flow rates), thus enhancing the flux of the hydrocarbons to the permeate side (and of hydrogen to the retentate side), leading to retentate streams poorer in propyne. An increase of $L^*_{C_3H_4}$ leads to an increase of this flux, favoring the effective propyne removal. Yet, increasing Γ or $L^*_{C_3H_4}$ also leads to permeate streams enriched in propyne, and consequently to progressively lower driving force values for its permeation. For highly permselective membranes (e.g. $L^*_{C_3H_4} = 100$), as one moves axially along the MS, the driving force begins to decrease very quickly and, under these conditions, the permeation begins to be limited by the low driving force values. So, further increases in $L^*_{C_3H_4}$ have little effect on the improvement of the separation.

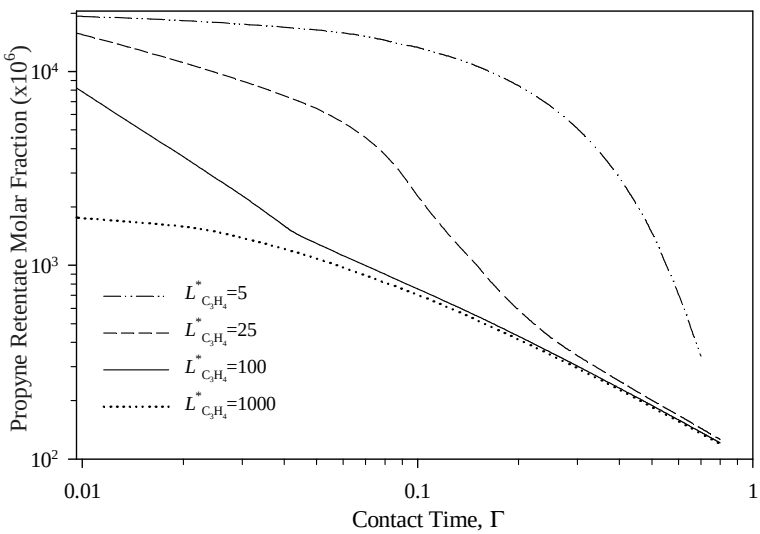

Figure 7.4 – Propyne retentate concentration as a function of the dimensionless contact time, for different propyne/propylene separation factor values, in a membrane based separation system (MS) for Ψ = 1.

The most important conclusion that can be drawn from Figure 7.4 is that even very highly selective membranes are unable to achieve the desired propylene

purity on the retentate stream (maximum of 5 ppm). It was analyzed also the possibility of improving the MS performance by using higher Ψ values, because such an enhancement decreases the hydrocarbon fractions on the permeate, thus increasing the permeation driving force and, as a consequence, decreasing the retentate propyne composition. However, even with Ψ values up to 5, it was not possible to attain propyne retentate concentration values below the 5 ppm threshold.

7.6 Membrane Reactor (MR)

With the MR proposed in this work, several advantages relatively to the conventional approach for removing propyne from industrial propylene streams are expected to be obtained. In order to evaluate the efficiency of the MR, it was analyzed the effect of the parameters Γ and *Da* on the concentration of propyne in the retentate and permeate streams, on the conversion of propyne and on the selectivity and yield towards propylene, for different values of separation factor ($L^*_{C_3H_4}$) and Ψ.

7.6.1 Effect of Membrane Permeability Coefficients

The propyne/propylene separation factor is an important factor when evaluating the performance of the MR. The first approach to assess its effect was to study the performance of the proposed reactor with a non-selective membrane. Regardless of Γ and *Da* values, the partial pressure of propyne at the retentate exit was similar to its feed value, hence much higher than the desired one. Thus, an effective propyne removal requires the synergetic effect of the selective permeance and the selective hydrogenation of propyne. Figure 7.5 shows the propyne retentate and permeate molar fractions at the exit of the MR for three

different propyne/propylene separation factor values; Figure 7.5A and Figure 7.5C show the retentate and permeate propyne molar fractions when operating in the low *Da* region, while Figure 7.5B and Figure 7.5D illustrate the propyne composition patterns in both streams in the high *Da* region. These results consider a highly selective catalyst to the desired reaction, R_r=0.1. In such conditions, the consumption of hydrogen in the undesired hydrogenation of propylene was negligible. Hence, an equimolar feed of hydrogen and propyne (Ψ = 1) was considered.

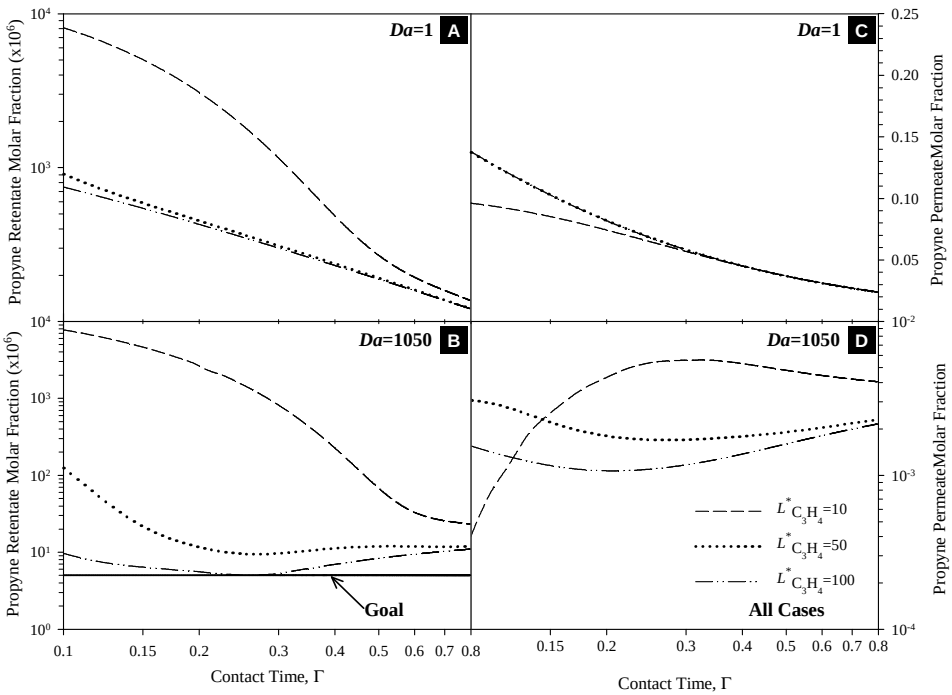

Figure 7.5 – Propyne retentate molar fraction (A and B) and propyne permeate molar fraction (C and D) as a function of Γ, for different values of L^*_{C3H4}. Figures A and C are relative to the low *Da* region and Figures B and D to the high *Da* region. R_r = 0.1, Ψ = 1. The other parameters used have the values listed in Table 7.1.

When the reaction extent is negligible (low *Da*), the composition in the retentate and permeate streams is essentially dependant on the permeation rate through the membrane. Increasing the contact time Γ increases the stage-cut, thus enhancing the permeating flux of the hydrocarbons relatively to the feed flow rate. Since

propyne is more permeable than propylene, the retentate stream becomes poorer in propyne (and richer in propylene) - Figure 7.5A.

On the other hand, the permeate composition of propyne passes through a maximum, albeit at very low Γ values (Γ << 0.1), not observed in Figure 7.5C. When Γ is very low (Γ << 0.1), only a small fraction of propyne permeates and its retentate molar fraction is practically constant along the reactor. Thus, small increases in Γ enhance significantly the ratio of the propyne and propylene fed that permeates, leading to permeate streams richer in both hydrocarbons and poorer in hydrogen. However, Figure 7.5A shows that for Γ=0.1 most of the propyne has already effectively permeated. So, further increases in Γ only have a small effect on the enhancement of the amount of propyne that permeates. Conversely, the enhancement in the permeation of propylene is much bigger, leading to permeate streams progressively richer in propylene and poorer in propyne.

Figure 7.5A and Figure 7.5C also show the effect of $L^*_{C_3H_4}$ on the propyne composition/concentration patterns, arising from the fact that the composition of the permeating stream depends directly on $L^*_{C_3H_4}$. When more selective membranes are used, the permeation of propyne is enhanced so the retentate concentration diminishes - Figure 7.5A - and the permeate one increases – Figure 7.5C.

In the high *Da* region, the propyne concentration in the permeate (and consequently in the retentate) is the result of the combined effect of reaction and permeation. When more highly selective membranes are used, the permeating stream becomes richer in propyne, which also favors its own conversion (equation (7.7)). The concentration of propyne in the permeate results from the balance between those two factors and is shown in Figure 7.5D. Since lower molar fractions of propyne are observed in the permeate side when more selective

membranes are used (except for very low contact times), we can conclude that the conversion of propyne is enhanced by the use of more selective membranes. These results demonstrate a clear synergetic effect of reaction and permeation, which is the main objective of the proposed membrane reactor. For high *Da* values and a propyne separation factor value ranging from 50 to 100, the conversion of propyne is close to one (> 99.9 %) and the undesired reaction is virtually nonexistent (propylene yield > 99.8 % - data not shown). Furthermore, it can be concluded from Figure 7.5B that a MR with $L^*_{C_3H_4} = 100$ and $Da = 1050$ achieves the required propylene purity, albeit in a small range of contact time values (0.23-0.28). On the other hand, a MR with $L^*_{C_3H_4} < 15$ is unable to perform the desired separation, regardless of Γ. Below the trade off between Γ, *Da* and $L^*_{C_3H_4}$ is explored in greater detail.

7.6.2 Hydrogen/Propyne Ratio Effect

Besides the separation factor, it is also important to analyze the effect of the hydrogen/propyne molar ratio (Ψ) on the MR performance. In the previous section, an equimolar feed of hydrogen and propyne (Ψ = 1) was considered for all simulations because hydrogen consumption in the hydrogenation of propylene was negligible (R_r = 0.1). However, when hydrogen is being consumed both by propyne and propylene, higher Ψ values are required to guarantee the maximum conversion of propyne. The amount of hydrogen available at the permeate side can be increased either by increasing the feed flow rate and/or its feed pressure value. In this study, it was decided to use progressively higher flow rate values, since increasing the pressure enhances the driving force for hydrogen permeation and favors the hydrogenation of propylene – cf. Eqs. (7.7) and (7.8).

Figure 7.6A shows the effect of increasing Ψ on the retentate concentration of propyne in a MR loaded with a catalyst with higher kinetic selectivity towards the undesired reaction, R_r = 10.

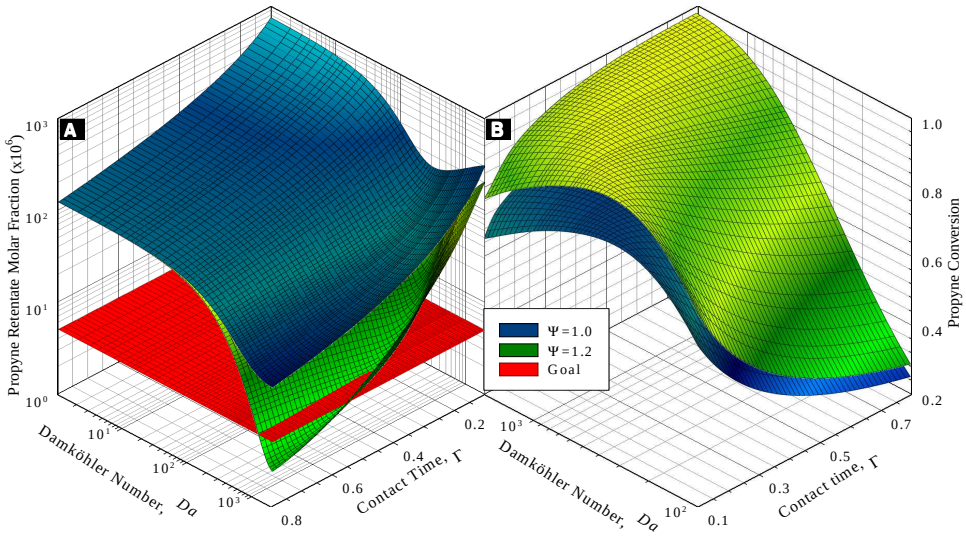

Figure 7.6 - Propyne retentate profiles (A) and propyne conversion curves (B) illustrating the effect of hydrogen/propyne molar flow ratio for a MR with separation factor 100 and R_r=10. In Figure 7.6B only the high *Da* region is represented since little effect is felt at lower *Da* values.

While this MR cannot perform the desired purification with Ψ = 1, after a 20 % increase in the hydrogen flow rate it proves to be effective in removing propyne. For Ψ > 1.2 the MR performs the desired purification with lower Γ requirements (e.g., lower membrane area). However, the use of higher hydrogen flow rates is associated with higher costs. In the present work, the optimum Ψ is defined as the minimum value of Ψ that guarantees an effective removal of propyne in a MR operating at Γ < 0.2. Following this criteria, the optimum value of Ψ is 1.25. Figure 7.6A also shows that, for low Damköhler numbers, the propyne retentate concentration is not very sensitive to the increase of Ψ. The use of higher hydrogen flow rates decreases the permeate concentration of propyne and, consequently, the retentate concentration, but its effect is minimal. An increase of Ψ has its biggest impact on the extent of both reactions, which is dependant on

the Damköhler number and on the reactants concentration, as seen in equations (7.11) and (7.12). Figure 7.6B shows the effect of increasing Ψ on the conversion of propyne in the same MR. An increase in the conversion of propyne is observed upon increasing the flow rate of hydrogen. When Ψ increases, the permeate is impoverished in propyne and propylene and enriched in hydrogen. The consumption rate of propyne is more sensitive to changes in the composition of hydrogen as compared to changes in hydrocarbon concentration (cf. equation (7.7)), so propyne's conversion increases – Figure 7.6B.

The effect of *Da* in the conversion of propyne is also displayed in Figure 7.6B. An increase in *Da* leads to an increase in catalytic activity, which enhances the consumption of propyne. Yet, this leads to a decrease in molar fraction of propyne and hydrogen, which has a negative impact on conversion. So, the overall impact of *Da* on conversion is a result of these two combined effects. It can be observed in Figure 7.6B that the conversion of propyne passes through a maximum in the low Γ region, for $Da \approx 350$. For $Da > 350$ the effect of the decrease in reactants concentration due to the increase in reaction extent is greater than the effect of the increase in the Damköhler number itself. As a consequence, the concentration of propyne in the permeate (and thus in the retentate – Figure 7.6A) also passes through a minimum, for the same conditions of Γ and *Da*.

7.6.3 Damköhler-Separation factor-Stage Cut Trade-Off

The use of a MR targets to achieve the desired propylene purity with low requirements of catalytic activity, contact time (low membrane area, for example) and propyne/propylene separation factor. This trade-off is illustrated in Figure 7.7, where the minimum Damköhler number required to achieve 5 ppm of propyne on the retentate stream is plotted as a function of Γ, for separation factor values between 40 and 100. Although the desired propyne purity can be achieved with separation factors lower than those shown in Figure 7.7 (as low as 15), it

occurs at the expense of high stage cuts and high catalytic activity requirements and is not represented therein.

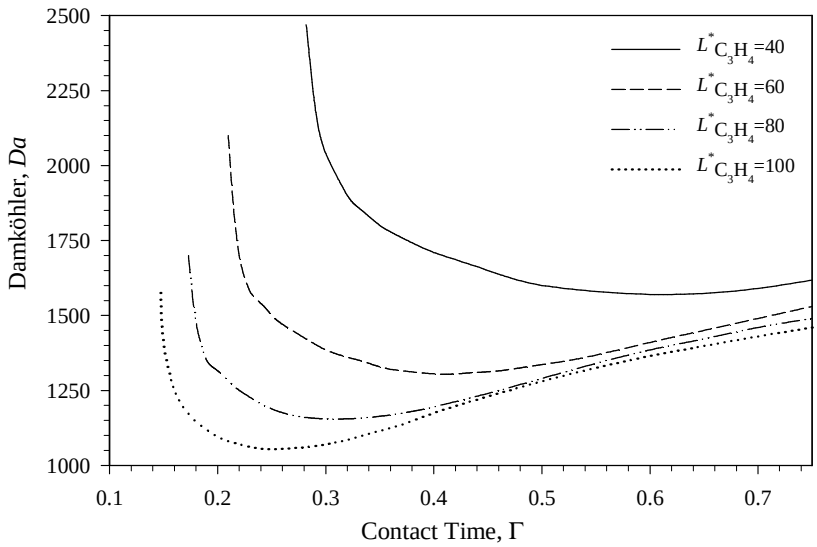

Figure 7.7 - Minimum Damköhler (*Da*) numbers to achieve 5 ppm of propyne on the retentate stream as a function of Γ, for different separation factors.

The shape of the Damköhler requirement curves shown in Figure 7.7 results from the combined effect of Γ and *Da* on the extension of the conversion of propyne, for each separation factor value. An increase in Γ leads to retentate streams poorer in propyne, progressively approaching the desired propyne purity. Thus, the extent of the hydrogenation of propyne on the permeate side that is required to decrease the propyne molar fraction to 5 ppm is smaller. However, eqs. (7.5) and (7.7) show that the reaction extent is the product of *Da* and the reactants concentrations raised to their respective reaction orders. Since an increase in Γ also decreases the permeate molar fraction of hydrogen, the Damköhler requirements to achieve the desired separation might either increase or decrease with Γ. Nonetheless, it is observed in all curves the existence of a minimum Γ value (Γ_{min}) for effective propyne removal, and as Γ approaches Γ_{min} the Damköhler requirements reveals an asymptotic behavior, increasing very

significantly. Furthermore, it is seen that in MRs with higher separation factors, the same retentate concentration can be attained at lower Γ values. The results shown in Figure 7.7 allow us to conclude that a MR with separation factor of 100 for propyne performs satisfactory propylene stream purification, operating at a contact time value of 0.15 ($Q^{R*} = 0.85$).

Since the permeate stream is also a highly purified propylene stream, with virtually no propane, the strategy of mixing it with the retentate stream was analyzed. For a MR with $L^*_{C_3H_4} = 100$, $Q^{R*} = 0.85$ and $Da = 1600$, the combined stream has a propyne concentration higher than 5 ppm. So, much higher Damköhler values are required to reach the 5 ppm threshold in the mixed stream. Furthermore, this approach features the additional cost of re-compressing the permeate stream. The required values of Da and Γ to sucessfully remove propyne were correlated with values of permeance and catalytic activities found in the literature [3-4, 8, 13]. It was concluded that typical permeance values for ionic liquid membranes correlate very well with Γ-values used in the present study. Furthermore, existing catalysts achieve the catalytic activity required by our system. It was also concluded that the membrane area required to implement the proposed MR in a typical refinery (annual flow rate of 200 000 tonnes/year) is quite large, which means that a shell and tube configuration featuring a high number of membrane tubes would be required, for an effective propyne removal. Developments in membrane technology, namely in more permeable and more permselective membranes (e.g. ionic liquid-based), will decrease heavily the needed area making this strategy even more appealing.

7.7 Conclusions

It was simulated the removal of propyne from an industrial propylene stream, by selective hydrogenation, using a conventional fixed bed catalytic reactor and a

membrane reactor equipped with a propyne selective membrane and a hydrogenation catalyst on the permeate side. It was concluded that the FBCR required a minimum hydrogen/propyne ratio of 1.35 to perform the desired purification (maximum outlet propyne concentration of 5 ppm). However, the catalytic hydrogenation selectivity towards propylene is low, thus propane is also formed, which hinders the possibility of attaining propylene polymer grade streams in a single stage using a FBCR.

The effect of propyne/propylene separation factor and of the hydrogen/propyne molar ratio on the performance of a MR was analyzed. It was concluded that operating at higher separation factors enhances the permeation of propyne to the reaction chamber, hence boosting the conversion of propyne and lowering its retentate output molar fraction. While a membrane reactor was able to perform the desired purification with a separation factor value as low as 15, higher separation factor values are required to effectively remove propyne at lower stage cut values; a MR with separation factor 100 performed the purification with a stage cut of 0.15. Moreover, more selective membranes also had lower catalytic activity requirements to achieve the desired purity. It was also seen that the MR operating with higher hydrogen/propyne ratios could perform the desired purification at lower Γ values. The permeate stream from the MR contains virtually no propane, however it contains some hydrogen and propyne. Combining the permeate with the retentate stream requires a deeper removal of propyne from the permeate stream, which can only be achieved for very high Damköhler values.

The proposed MR is a promising alternative to the current technology employed (fixed bed catalytic reactors) that takes advantage of the recent breakthroughs in the synthesis of propyne permselective membranes.

7.8 Acknowledgements

Miguel Teixeira is grateful to the Portuguese Foundation for Science and Technology (FCT) for his doctoral grant (reference SFRH/BD/24768/2005). The authors also acknowledge financing from FCT through the projects POCTI/EQU/59344/2004 and POCTI/EQU/59345/2004.

7.9 Nomenclature

Variables	Definition	Units
A	area	(m^2)
Da	Damköhler number	$(-)$
k_1^g	gas-phase propyne hydrogenation kinetic constant	$(\mathrm{mol}\cdot\mathrm{m}^{-2}\cdot\mathrm{s}^{-1}\cdot\mathrm{Pa}^{-1.25})$
k_2^g	gas-phase propylene hydrogenation reaction rate constant	$(\mathrm{mol}\cdot\mathrm{m}^{-2}\cdot\mathrm{s}^{-1}\cdot\mathrm{Pa}^{-2})$
L_i	Permeability coefficient of the component i	$(\mathrm{mol}\cdot\mathrm{m}\cdot\mathrm{m}^{-2}\cdot\mathrm{s}^{-1}\cdot\mathrm{Pa}^{-1})$
p_i	partial pressure of species i	(Pa)
P	total pressure	(Pa)
Q	volumetric flowrate	$(\mathrm{m}^3\cdot\mathrm{s}^{-1})$
r^t	tube radius	(m)
R_r	reaction rate ratio	$(-)$
$\Re$	universal gas constant	$(\mathrm{J}\cdot\mathrm{mol}^{-1}\cdot\mathrm{K}^{-1})$
T	absolute temperature	(K)
$X_{C_3H_4}$	propyne conversion	$(-)$
z	axial coordinate	(m)
Z	reactor length	(m)
$Y_{C_3H_6}$	propylene yield	$(-)$

Greek Symbols	Definition	Units
δ	membrane thickness	(m)
Γ	dimensionless contact time	$(-)$
Γ_{TPC}	dimensionless contact time for the total permeation condition	$(-)$
ν_i	stoichiometric coefficient of the component *i*	$(-)$
$\sigma_{C_3H_6}$	propylene selectivity	$(-)$
Ψ	hydrogen/propyne feed molar ratio	$(-)$

Superscript	Definition
M	relative to the membrane
*	dimensionless variable
F	relative to feed stream conditions
R	relative to retentate stream conditions
P	relative to permeate stream conditions
h	relative to high pressure stream conditions
l	relative to low pressure stream conditions

Subscript	Definition
i	species i
j	reaction j
ref	relative to the reference conditions or component

7.10 References

[1] J.T. Wehrli, D.J. Thomas, M.S. Wainwright, D.L. Trimm, N.W. Cant, Selective Hydrogenation of Propyne over Supported Copper-Catalysts - Influence of Support, Appl. Catal., 70 (1991) 253-262.
[2] M.L. Derrien, J.W. Andrews, P. Bonnifay, J. Leonard, IFP Selective Hydrogenation Process, Chem. Eng. Prog., 70 (1974) 74-80.
[3] C. Godinez, A.L. Cabanes, G. Villora, Experimental-Study of the Front-End Selective Hydrogenation of Steam-Cracking C-2-C-3 Mixture, Chem. Eng. Process., 34 (1995) 459-468.
[4] J.C. Fajardo, C. Godinez, A.L. Cabanes, G. Villora, Kinetic analysis of rate data for propylene and methylacetylene hydrogenation, Chem. Eng. Process., 35 (1996) 203-211.
[5] C.Q. Liu, Y. Xu, S.J. Liao, D.R. Yu, Y.K. Zhao, Y.H. Fan, Selective hydrogenation of propadiene and propyne in propene with catalytic polymeric hollow-fiber reactor, J. Membr. Sci, 137 (1997) 139-144.
[6] J.M. Lee, J. Palgunadi, J.H. Kim, S. Jung, Y.S. Choi, M. Cheong, H.S. Kim, Selective removal of acetylenes from olefin mixtures through specific physicochemical interactions of ionic liquids with acetylenes, Phys. Chem. Chem. Phys., 12 (2010) 1812-1816.
[7] J. Palgunadi, H.S. Kim, J.M. Lee, S. Jung, Ionic liquids for acetylene and ethylene separation: Material selection and solubility investigation, Chem. Eng. Process., 49 (2010) 192-198.
[8] S. Jung, J. Palgunadi, J.H. Kim, H. Lee, B.S. Ahn, M. Cheong, H.S. Kim, Highly efficient metal-free membranes for the separation of acetylene/olefin mixtures: Pyrrolidinium-based ionic liquids as acetylene transport carriers, J. Membr. Sci., 354 (2010) 63-67.
[9] J.M. Sousa, A. Mendes, Consecutive-parallel reactions in nonisothermal polymeric catalytic membrane reactors, Ind. Eng. Chem. Res., 45 (2006) 2094-2107.
[10] R. Mallada, M. Menendez, Inorganic membranes: synthesis, characterization and applications, Elsevier, Amsterdam ; Oxford, 2008.
[11] A. Julbe, D. Farrusseng, C. Guizard, Porous ceramic membranes for catalytic reactors - overview and new ideas, J. Membr. Sci., 181 (2001) 3-20.
[12] S. Miachon, J.A. Dalmon, Catalysis in membrane reactors: what about the catalyst?, Top. Catal., 29 (2004) 59-65.
[13] L. Brandao, L.M. Madeira, A.M. Mendes, Propyne hydrogenation in a continuous polymeric catalytic membrane reactor, Chem. Eng. Sci., 62 (2007) 6768-6776.
[14] A.G. Dixon, Analysis of intermediate product yield in distributed-feed nonisothermal tubular membrane reactors, Catal. Today, 67 (2001) 189-203.

[15] H.W.J.P. Neomagus, G. Saracco, H.F.W. Wessel, G.F. Versteeg, The catalytic combustion of natural gas in a membrane reactor with separate feed of reactants, Chem. Eng. J., 77 (2000) 165-177.
[16] G. Saracco, V. Specchia, Catalytic combustion of propane in a membrane reactor with separate feed of reactants. IV. Transition from the kinetics- to the transport-controlled regime, Chem. Eng. Sci., 55 (2000) 3979-3989.
[17] M.P. Harold, C. Lee, Intermediate product yield enhancement with a catalytic inorganic membrane 2: Nonisothermal and integral operation in a back-mixed reactor, Chem. Eng. Sci., 52 (1997) 1923-1939.
[18] M.P. Harold, V.T. Zaspalis, K. Keizer, A.J. Burggraaf, Intermediate Product Yield Enhancement with a Catalytic Inorganic Membrane .1. Analytical Model for the Case of Isothermal and Differential Operation, Chem. Eng. Sci., 48 (1993) 2705-2725.
[19] S.S. Ozdemir, M.G. Buonomenna, E. Drioli, Catalytic polymeric membranes: Preparation and application, Appl. Catal., A, 307 (2006) 167-183.
[20] L. Brandao, D. Fritsch, A.M. Mendes, L.M. Madeira, Propylene hydrogenation in a continuous polymeric catalytic membrane reactor, Ind. Eng. Chem. Res., 46 (2007) 5278-5285.
[21] S. Ziegler, J. Theis, D. Fritsch, Palladium modified porous polymeric membranes and their performance in selective hydrogenation of propyne, J. Membr. Sci., 187 (2001) 71-84.
[22] Y.K. Kao, L. Lei, Y.S. Lin, Optimum operation of oxidative coupling of methane in porous ceramic membrane reactors, Catal. Today, 82 (2003) 255-273.
[23] H.H. Wang, Y. Cong, W.S. Yang, Oxidative coupling of methane in $Ba_{0.5}Sr_{0.5}Co_{0.8}Fe_{0.2}O_{3-d}$ tubular membrane reactors, Catal. Today, 104 (2005) 160-167.
[24] X. Tan, Z. Pang, S. Liu, Catalytic perovskite hollow fibre membrane reactors for methane oxidative coupling, J. Membr. Sci., 302 (2007) 109-114.
[25] N.N. Li, Advanced membrane technology and applications, Wiley-Blackwell, Oxford, 2008.
[26] I.F.J. Vankelecom, P.A. Jacobs, Dense organic catalytic membranes for fine chemical synthesis, Catal. Today, 56 (2000) 147-157.
[27] A. Borodzinski, A. Cybulski, The kinetic model of hydrogenation of acetylene-ethylene mixtures over palladium surface covered by carbonaceous deposits, Appl. Catal., A, 198 (2000) 51-66.
[28] D.R. Kennedy, G. Webb, S.D. Jackson, D. Lennon, Propyne hydrogenation over alumina-supported palladium and platinum catalysts, Appl. Catal., A, 259 (2004) 109-120.
[29] J.M. Sousa, A. Mendes, Modelling a catalytic membrane reactor with plug flow pattern and a hypothetical equilibrium gas-phase reaction with Dn not equal 0, Catal. Today, 104 (2005) 336-343.
[30] B.A. Finlayson, Nonlinear Analysis in Chemical Engineering, Mcgraw Hill, London, 1980.

[31] J.M. Sousa, A. Mendes, Simulating catalytic membrane reactors using orthogonal collocation with spatial coordinates transformation, J. Membr. Sci., 243 (2004) 283-292.
[32] L.R.H. Petzold, A.C.; LSODA, Computing and Mathematics Research Division; Lawrence Livermore National Laboratory; Livermore, CA, (1997).
[33] J.T. Wehrli, D.J. Thomas, M.S. Wainwright, D.L. Trimm, N.W. Cant, Selective Hydrogenation of Propyne over an Ion-Exchanged Copper on Silica Catalyst, Appl. Catal., 66 (1990) 199-208.
[34] L. Groschel, R. Haidar, A. Beyer, H. Colfen, B. Frank, R. Schomacker, Hydrogenation of propyne in palladium-containing polyacrylic acid membranes and its characterization, Ind. Eng. Chem. Res., 44 (2005) 9064-9070.
[35] S.D. Jackson, G. Kelly, Hydrogenation of Propyne to Propene over Platinum Silica, J. Mol. Catal., 87 (1994) 275-285.
[36] R. Marshall, G. Webb, S.D. Jackson, D. Lennon, Propyne hydrogenation: characteristics of a carbon-supported palladium catalyst that exhibits a kinetic discontinuity effect, J. Mol. Catal. A: Chem., 226 (2005) 227-230.
[37] R.S. Mann, D.E. To, Catalytic Hydrogenation of Allene, Can. J. Chem., 46 (1968) 161-166.
[38] M.J. Vincent, R.D. Gonzalez, A Langmuir-Hinshelwood model for a hydrogen transfer mechanism in the selective hydrogenation of acetylene over a Pd/gamma-Al_2O_3 catalyst prepared by the sol-gel method, Appl. Catal., A, 217 (2001) 143-156.
[39] R.T. Yang, R. Foldes, New adsorbents based on principles of chemical complexation: Monolayer-dispersed nickel(II) for acetylene separation by p-complexation, Ind. Eng. Chem. Res., 35 (1996) 1006-1011.
[40] A.J. Kodde, J. Padin, P.J. van der Meer, M.C. Mittelmeijer-Hazeleger, A. Bliek, R.T. Yang, $NiCl_2$ on gamma-alumina as selective adsorbents for acetylene over ethylene, Ind. Eng. Chem. Res., 39 (2000) 3108-3111.
[41]http://www.petkim.com.tr/eng/Trade/Products/Products.aspx?urunId=73 , acessed in July 2010

Chapter 8: **Conclusions and Future Work**

8.1 General Conclusions

This thesis focused on the purification of propylene streams using membranes and membrane reactors. Membranes were used to separate propylene from propane and a membrane reactor was proposed to selectively remove propyne from such streams. The olefin/paraffin separation was carried out with two types of inorganic membranes (zeolite and carbon molecular sieve) in order to establish the main advantages/weaknesses of each membrane type. Finally, the results with both membranes were compared with the state-of-the art.

Faujasite (Y) zeolites were prepared in powder form, for adsorption equilibrium analysis, and as supported membranes, for gas permeation experiments. Faujasite membranes were synthesized hydrothermally by the seeding and secondary growth method on top of α-Al_2O_3 supports; thin, defect free membranes were obtained by repeating the synthesis cycle 3 times. The adsorbents/membranes were ion-exchanged with silver (Ag^+) and their separation performance assessed before and after ion-exchange. In single gas experiments, the propylene/propane permselectivity was below 1 for the plain and silver-exchanged forms of the faujasite zeolite. The membranes adsorbed propylene to a greater extent, but propane diffused faster on the porous network and its permeability was also higher. In mixed gas experiments, propylene (the more adsorbed species) partially blocked the permeation of propane and the membranes were selective towards propylene. Because the silver-exchanged form of the zeolite exhibited significantly higher affinity towards propylene than the plain form, higher propylene/propane separation factors were achieved. At 298 K and using an undiluted equimolar feed, the separation factor of the best performing

silver-exchanged zeolite membrane was 6.0 and the permeability towards propylene was 712 barrer. However, when propylene/propane feeds were diluted, the separation factor was higher (S_f = 9.0) as well as the membrane permeability towards propylene (1685 barrer). The best performing zeolite membranes placed above the present trade-off line for polymer membranes, yet their long-term stability was hindered by Ag^+ reduction to Ag^0. Moreover, following reoxidation, only a partial recovery in performance was observed. Besides these stability limitations, synthesis reproducibility was poor.

Motivated by the poor reproducibility and limitations of the functionalized zeolite membranes, composite carbon molecular sieve membranes (c-CMSM) were also studied for the propylene/propane separation. To provide mechanical strength to the membranes, they were supported on α-Al_2O_3 tubes (~1 cm outside diameter). Because cost limitations are one of the biggest obstacles towards implementation of carbon membranes on an industrial scale, it was used a cheap polymer (phenolic resin) loaded with relatively cheap nanofillers (boehmite). Moreover, no pre- or post-treatments were considered and all membranes were prepared in a single dipping-carbonization step. Carbonization was performed under nitrogen atmosphere, with a heating rate of 1 $^{o}C \cdot min^{-1}$ up to 823 K and a soaking time of 2 hours at this final temperature. After pyrolysis, boehmite nanoparticles originated nanowires of Al_2O_3 10-30 nm long and 1-2 nm thick, greatly dispersed into the carbon matrix. From the adsorption isotherm of CO_2 at 273 K it was determined a microporous volume of 150 $cm^3 \cdot kg^{-1}$ and an average pore width of 0.58 nm for the composite material. A more detailed knowledge of the c-CMSM microporosity was acquired by using a structure-based method that allowed determining the micropore size distribution; a bi-modal distribution composed of small micropores (0.35 - 0.45 nm) and larger micropores (0.5 - 0.8 nm) was observed. Monocomponent permeabilities were determined at ambient

temperature. The membrane exhibited high propylene permeability (160 barrer) and considerable propylene/propane ideal permselectivities (14.5).

After establishing the validity of the proposed strategy, composite membranes were prepared with different resin/boehmite proportions and the optimum composition of the precursor for propylene/propane gas separation was determined. The c-CMSMs that exhibited the better performances for propylene/propane separation were prepared from precursors with boehmite content between 0.75 and 1 wt.% and phenolic resin content of about 15 wt.%; permselectivities up to 19 and separation factors up to 13.5 were obtained, with high propylene permeability values (593 barrer in single gas experiments and 196 barrer in mixed gas experiments). The decrease in performance for mixed gas experiments showed that propylene and propane negatively impacted the diffusion of each other in the pore constrictions. It was also studied the aging of the membranes (decrease in performance with time) because the adsorption studies had showed that O_2 chemisorbed on the membrane, a phenomenon known to lead to water vapor adsorption and consequent clogging of the pores. After 15 days of exposure to ambient air the membrane permeability towards N_2 decreased 90 %, showing a fast aging on these composite membranes. However, treatment in N_2 atmosphere at 823 K regenerated the membrane to about 80 % of its initial performance.

Adsorption isotherms/ diffusion uptake rates were also determined in carbon/Al_2O_3 composite membrane films to assess the mass transfer mechanism responsible for the membrane selectivity towards propylene/propane and two more gas pairs: O_2/N_2 and CO_2/N_2. While both O_2/N_2 and propylene/propane permselectivities were essentially due to a transport kinetic selectivity, the CO_2/N_2 permselectivity was attributed to the combined effect of diffusion and adsorption selectivities. The adsorptive and transport kinetic study for propylene and propane was performed in the temperature range between 293 and 453 K.

The most promising results were for 293 K, where the ratio of the diffusion coefficients of propylene and propane (8.2) was the highest.

After demonstrating the good separation results of a carbon/Al_2O_3 composite membrane, a new composite carbon membrane featuring two inorganic fillers (Al_2O_3 nanowires and Ag nanoclusters) was studied. Membranes were prepared from dispersions with different amounts of $AgNO_3$ (from 0 to 1 wt.%) and the effect of Ag evaluated from CO_2 adsorption isotherms and gas permeation experiments. The porous network of carbon-Al_2O_3 and carbon-Al_2O_3-Ag composite membranes were observed to be fairly similar and only small changes arose from the presence of Ag nanoparticles; the pore volume increased a little but the average size of the pores decreased. This small change explained the observed decrease in permeability towards the two hydrocarbons and significant increase in propylene/propane selectivity. The adsorption capacity of the carbon/Al_2O_3/Ag sample towards propane and propylene was similar to that of the carbon/Al_2O_3 sample; hence, the increase in selectivity was due to an increase in diffusion selectivity. The better performing composite membranes were observed to be the ones where Ag aggregated into smaller nanoparticles (~30 nm in size), when 3.1 < Ag wt.% < 6.0. As the content of Ag was increased beyond 6.0 wt.% Ag particles became larger and the separation results significantly worse. Propylene permeabilities between 69 and 226 barrer and permselectivities between 30 and 38 were obtained for the best performing membranes. When mixed gas streams were used, it was again observed that propane had a negative impact on the diffusion of propylene through the membrane. Nonetheless, the performance of the c-CMSMs with mixed gas streams (permeability towards propylene between 47 and 169 barrer and separation factor between 14.0 and 20.5) still placed well above the upper bound curve for polymer membranes.

The final chapter of the thesis focused on analyzing theoretically the feasibility of a new membrane reactor (MR) configuration envisioned for the selective

hydrogenation of propyne present in propylene streams. Typical industrial propylene streams contain 2-5 molar % of alkynes (and dienes), whose concentration should be decreased below 5 ppm in hydrogenation reactors. Yet, the deeper hydrogenation to alkanes is a drawback of such traditional processes. In order to overcome this disadvantage and decrease the catalytic requirements of the traditional fixed bed catalytic reactor (FBCR), it was proposed to use a membrane reactor (MR) featuring a propyne permselective membrane and a catalyst selective to the propyne hydrogenation loaded on surface of the permeate side of the membrane. In this MR, propylene exits from the retentate as a highly purified stream (polymer grade purity) and by finely tuning the hydrogen/propyne reactor ratio it is also possible to achieve a highly purified (albeit not polymer grade) permeate stream.

The performance of the MR was compared to that of a FBCR for the same feed and reaction conditions using a 1-D mathematical model. The MR showed to be more efficient in performing the required purification. The catalytic hydrogenation selectivity towards propylene of the MR (above 99 %) was much higher than that of the FBCR (about 70 %) and the catalytic requirements were smaller. Moreover, the MR was able to perform the desired purification with a propylene/propane membrane selectivity as low as 15. Yet, higher membrane selectivities were required to effectively remove propyne at lower stage cuts. When operating at lower stage cuts, one minimizes the fraction of propylene fed that permeates and exits from the reactor in the non-purified low pressure stream, hence decreasing the recompression costs associated with recycling that stream to the MR feed. It was also observed that the propyne/propylene selectivities and propyne catalytic activities required to perform the desired purification in the MR correlated well with membranes and catalysts found in the literature. Hence, the proposed MR showed to be a promising alternative to the current hydrogenation reactors,

8.2 Overview and Future Work

Concerning the two inorganic materials tested for propylene/propane separation, it is clear that both classes of membranes have stability issues that need to be solved before either can become a viable alternative to distillation. However, the use of c-CMSMs seems to be more promising. Besides being more reproducible, c-CMSMs also exhibited much higher separation factors (20.5 vs. 6, for undiluted equimolar feeds at ambient temperatures). Moreover, many variables that have a potentially big effect on the final properties of the composite membranes were kept constant in this study, namely the pyrolysis temperature, gas flow rate, soaking time, heating rate, etc. It is reasonable to expect that an optimization of these parameters will yield significantly better results.

Another obstacle to overcome towards industrialization is the high costs of the membranes themselves. This work proposed to use tubular ceramic supports to confer mechanical stability to the membrane, but the added cost of the ceramic support used is very significant. Aware of this problem, future research should focus on cheaper supports. If cheap carbon supports are used, not only will the costs be inferior but the thermal expansion coefficients of the support and selective layer will be similar and consequently defect formation during pyrolysis less likely. This research line is now being explored at LEPAE.

Finally, much of the future work should focus on understanding and preventing the aging of the membranes. The phenolic resin-based carbon membranes pyrolyzed at 823 K exhibited poor stability in the presence of oxygen. The use of higher pyrolysis temperatures is expected to help preventing oxygen chemisorption and this analysis will be performed soon. Nonetheless, if phenolic resin-based carbon membranes pyrolyzed at higher temperatures continue to exhibit poor stabilities, then other precursors should be considered, namely cellulose (a precursor which is known to lead to stable carbon membranes).

Concerning the removal of propyne from propylene streams, the next step is to select a propyne selective membrane, where a hydrogenation catalyst should be loaded, and to assemble an experimental apparatus to test the MR configuration proposed. So far, ionic liquid membranes have presented the best propyne/propylene results, but in a recent experiment performed in our lab a carbon/Al_2O_3 composite membrane yielded a propyne/propylene permselectivity of 7, showing the potential of these membranes towards this application.

APPENDIX A: GAS PERMEATION EXPERIMENTAL APPARATUS

For measuring mono and multicomponent gas permeances of supported zeolite membranes it was assembled an experimental setup (pictured in Figure A.1). Later, the same setup was adapted for measuring the permeances of tubular carbon membranes by using a different permeation cell. The setup offers robust and versatile operation; it was designed to handle combustible, inert and oxidant gases in a wide range of temperature (293-453 K) and feed pressure (100-700 kPa) values.

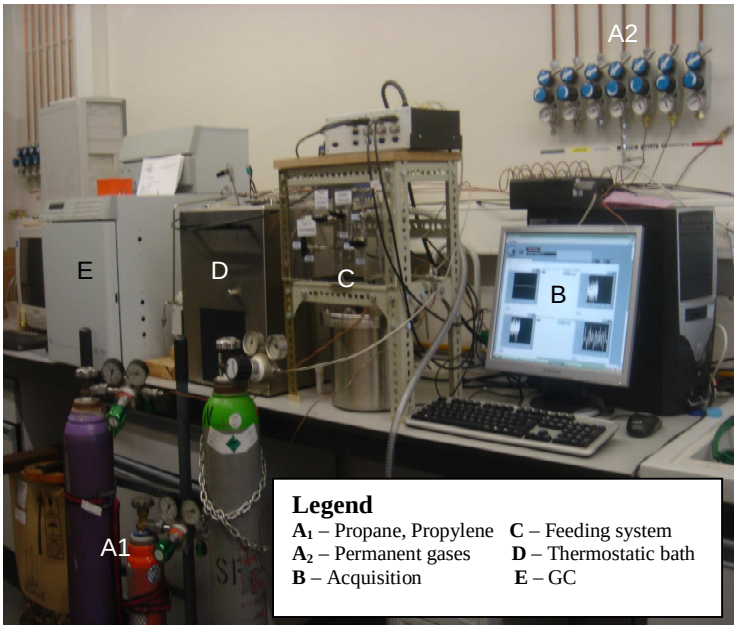

Figure A.1– Picture of the gas permeation apparatus assembled.

The setup consisted of the gases used (A), an acquisition system (B), a feeding system (C), a thermostatic system (D) and an analysing unit (E). Praxair supplied propane and propylene (99.5 %) and Air Liquide the permanent gases (99.999 %). The valves, tubes and tanks used in the feeding system were in stainless steel; Swagelok supplied the valves and tubing and Neves & Neves the

tanks. It was used an oil pump (Edwards RV 5) equipped with an oil trap to perform vacuum on the feed tank (ultimate vacuum below 1 kPa) and a membrane pump (Ilmvac MPC 201 Tp) to perform vacuum to the permeate tank (ultimate vacuum below 0.2 kPa). Pressure transducers (Druck series PMP 4010, accuracy 0.04 % full scale) were placed in the feed tank (0-700 kPa), retentate (0-700 kPa) and permeate (permeate - 0-200 kPa or 0-35 kPa). A pressure controller (LINDE, range 0-1500 kPa) was placed between the feed tank and permeation cell to control the feed pressure. Mass flow meters were used to determine the permeating flow rate (Bronkhorst, ranges 0-10 or 0-100 $ml \cdot min^{-1}$) and a mass flow controller to control the output flow rate of the retentate stream for multicomponent experiments (Bronkhorst 0-1 $L \cdot min^{-1}$). The accuracy of the Bronkhorst mass flow meters/controllers was ± 0.8 % RD (read value error) plus ± 0.2 % FS (full scale error).

An acquisition board (Advantech 8710 HG) was used to acquire the signal from the pressure sensors and mass flow meters/controllers and a Labview program was used for signal treatment. A GC (Dani 1000) was used to determine the composition of the retentate and permeate streams; it was equipped with a Valcoplot column (VP 30 m x 53 mm x 20 μm), a FID 86/10 detector and a split/splitless Injector. A thermostatic bath (Huber; CC1-K25) provided thermostatic control in the temperature range 273-368 K (accuracy ~ 0.1 º C). Figure A.2 pictures the permeation setup immersed in the thermostatic bath. A series of arrows illustrates the direction of flow during permeation experiments.

For temperatures higher than 368 K it was assembled in-house a heating system consisting of two resistances and one fan, pictured in Figure A.3 – designed by Prof. José Sousa. The temperature of this system was controlled by means of a Eurotherm temperature controller 3216L, connected to a thermocouple, which was in contact with the gas inside the membrane cell. This system provided ± 1ºC homogeneity throughout the permeation membrane cell.

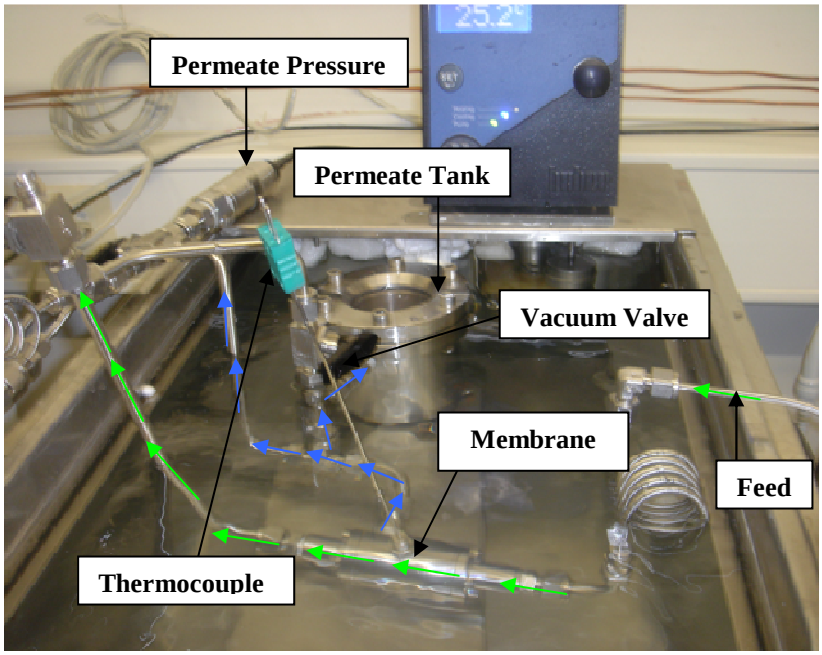

Figure A.2 – Picture of the membrane cell and permeate tank immersed in the thermostatic bath. The arrows depict the direction of flow: green – feed/retentate stream; blue – permeate stream.

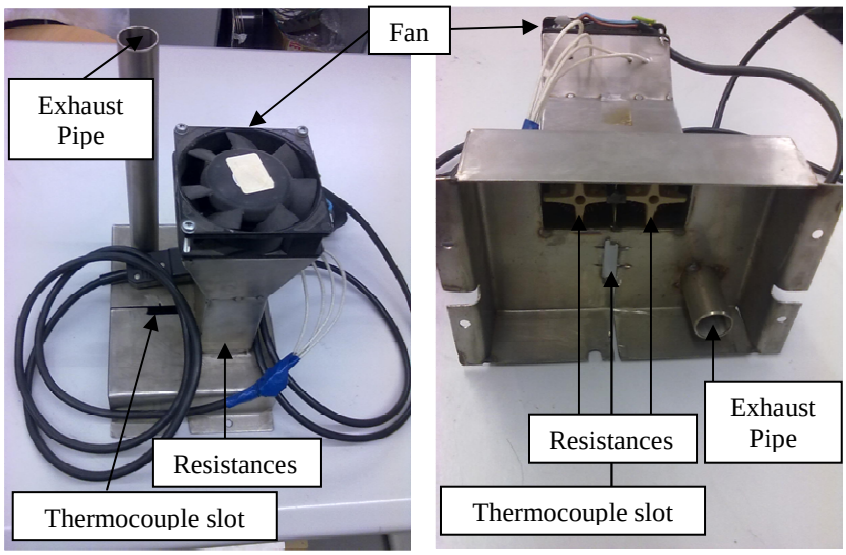

Figure A.3 – Pictures of the heating system assembled (left – top view; right – bottom view). The resistances were placed inside a conical metal structure and are seen in the bottom view picture. The thermocouple (whose slot is seen in the pictures) was connected to a temperature controller.

The permeation membrane cell, designed for receiving ceramic tubular membranes, is pictured in Figure A.4A. In Figure A.4B it is seen the zeolite ceramic membranes.

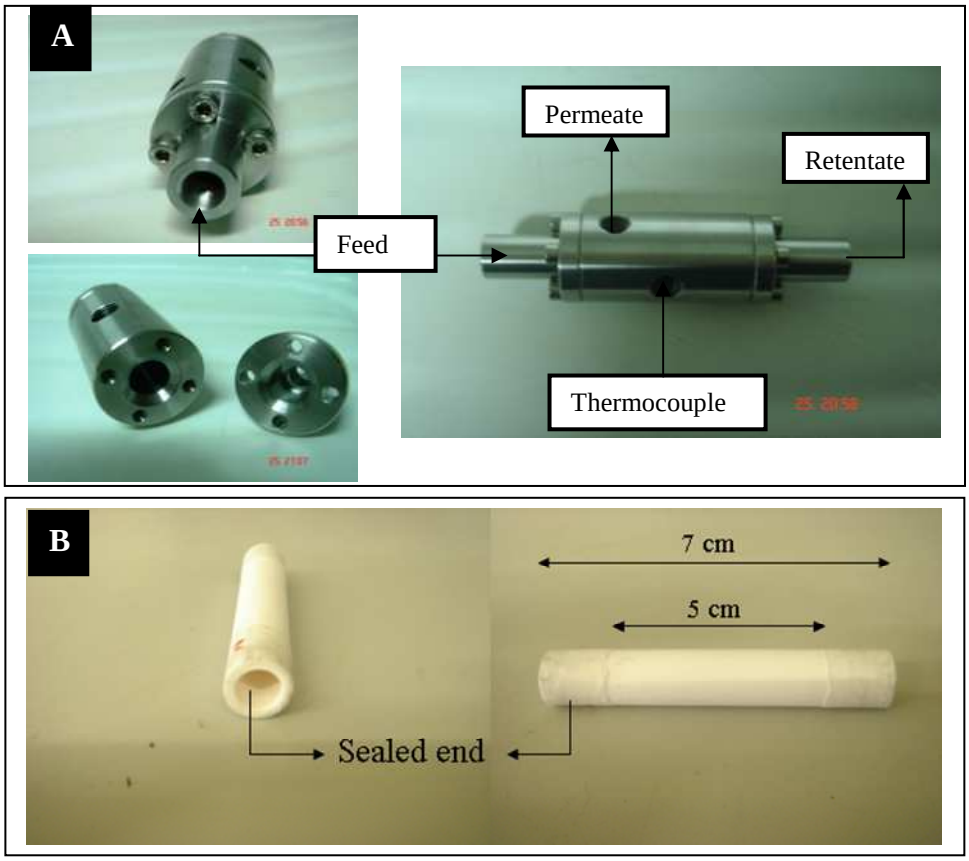

Figure A.4 – Membrane permeation cell from various views (A) and ceramic zeolite membranes used (B).

The sealing of the membranes in the permeation cell was done by o-rings. The adequacy of the sealing was tested by performing permeation tests in a cylindrical stainless steel tube geometrically identical to the ceramic membranes; no permeation could be detected even at high temperatures (180 ºC) ensuring that the membrane/o-ring interface was leak free. The ceramic zeolite membranes received from CICECO were made impermeable on the ends so that the effective

length of the membrane (5 cm) matched the distance between the two o-rings of the membrane cell. Figure A.4B pictures a membrane after sealing. The sealing was performed with a silicone polymeric rubber (RS Amidata, Reference 555588). The effectiveness of the sealant was confirmed because the permeance of a completely impermeabilized membrane towards nitrogen, helium, propane and propylene was three to four orders of magnitude below the permeance of a defect-free faujasite zeolite membrane. To prevent silver reduction by exposure to light, the silver-functionalized membranes were sealed in a dark environment.